

NOVEL MECHANICAL TEST METHODS APPLIED TO BULK METALLIC GLASSES

Phillip Simon Mahoney

February 2016

A thesis presented for the degree of
Doctor of Philosophy



Department of Materials Science and Engineering
The University of Sheffield

Abstract

By their nature Bulk Metallic Glasses (BMGs) are generally available with limited volumes. Therefore, to understand their mechanical behaviour, innovative small scales tests are required. Here aspects of mechanical behaviour covering elastic, time dependent and plastic deformation are explored.

For indentation (elastic moduli and hardness measurements), test data contained displacement burst signals; dependent on indentation load and loading rates; hypothesised to be due to shear bands and Shear Transformation Zones (STZs). Measurements of the energy associated with these signals were heavily influenced by data smoothing. Nevertheless, shear banding is seen to be more energetic process than STZ activation, and STZ activation during loading is more energetic than in load-hold or unloading.

Teter's empirical relationship [1] provided the best estimate of elastic properties from hardness data. Whilst indentation size effects made the method unreliable for bulk estimates, these effects are suggested as a means to map free volume distributions within BMG structures.

Poor reproducibility of indentation creep data and the influence of analysis methods led to the conclusion that indentation creep measurements are unreliable. Practices to improve this reliability are given, however the fundamentals of the test limits its usefulness.

Finally, shear banding of BMGs was explored through a new testing methodology based on the dynamic measurement of resistivity. Two types of signal were detected; both accountable through the shear band process. Analysis of the signals indicated that thermal and structural changes were required to explain the observed resistivity changes. Monte-Carlo and Ising based models were used to relate the observed signals to structure and temperature. Whilst these require further work, the method provides the means to measure shear band structure evolution.

Acknowledgements

Firstly I would like to thank Dr Russell Goodall for his guidance, enthusiasm, advice and patience; all of which have kept both myself and this project on course and under control. There are not many academic supervisors who put the level of time and effort into their students as he does, despite his other extensive responsibilities. Therefore on behalf of all his students, both present and past, I would like to express my appreciation and gratitude for all his efforts. In addition I would also like to express my thanks to Prof. Iain Todd. His questioning ways and enthusiasm for my work has pushed me to do things that I would not have necessarily have tried. I hope this document reflects this, and I look forward to working in his research group in the future.

I would also like to thank the Technical staff of the Materials Science department, in particular Michael Bell, Andrew Mould, Ben Palmer and Dean Haylock; who have all contributed to both my research and motivation for carrying on in the darkest of days. As any other Ph.D. student will tell you, it is people like these that get you through to the end.

I would also like to express my gratitude to Dr Claire Hinchliffe. She has kept our CDT cohort running straight and true and is rarely thanked as a result. Without her, all the lives of the Advanced Metallics CDT Ph.D. students would have been a lot harder, less enjoyable and less rewarding.

Finally I would like to express my utmost admiration for Dr Claire Warner. Despite the inputs and influences of all the great people in the department, it is truly down to her that I have made it this far. Her level of support and understanding is something that I, nor anybody, could ever reciprocate in kind.

Contents

| | | |
|----------|--|-----------|
| 1 | Introduction | 9 |
| 2 | BMG formation, structure and classification | 11 |
| 2.1 | Metallic glass formation | 11 |
| 2.1.1 | Thermodynamics and kinetics of metallic glass formation | 13 |
| 2.2 | Metallic glass structure | 21 |
| 2.2.1 | Tools for describing structures of BMGs | 21 |
| 2.2.2 | Tools for observing BMG structures | 24 |
| 2.2.3 | Tools for further understanding BMG structures | 24 |
| 2.2.4 | Key structural features observed in BMGs | 25 |
| 2.2.5 | Structure models of BMGs | 27 |
| 2.3 | Classification of BMGs | 30 |
| 2.3.1 | Chemical classification | 30 |
| 2.3.2 | Electromagnetic property classification | 30 |
| 2.3.3 | Mechanical classification | 30 |
| 3 | Selected BMG properties | 33 |
| 3.1 | Electrical properties | 33 |
| 3.1.1 | Drude model | 33 |
| 3.1.2 | Ziman theory | 35 |
| 3.2 | Mechanical properties of BMGs | 37 |
| 3.2.1 | Microscopic mechanisms behind BMG deformation | 37 |
| 3.2.2 | Elastic behaviour | 43 |
| 3.2.3 | Plastic behaviour | 46 |
| 3.3 | Details surrounding current theories of shear band formation | 51 |
| 3.3.1 | Shear banding mechanisms | 52 |
| 3.3.2 | Shear band dependences | 58 |
| 3.4 | Methods for assessing mechanical behaviours of BMG materials | 68 |
| 3.4.1 | Ultrasonic testing | 68 |
| 3.4.2 | Nano-indentation | 69 |
| 4 | Experimental Methods | 76 |
| 4.1 | Sample synthesis, preparation and confirmation | 76 |
| 4.1.1 | Arc melting and casting | 76 |
| 4.1.2 | XRD structure verification | 78 |
| 4.2 | Local mechanical testing | 80 |
| 4.2.1 | Nano-indentation tests | 80 |
| 4.3 | Bulk mechanical tests | 84 |

| | | |
|----------|--|------------|
| 4.3.1 | Micro indentation tests | 84 |
| 4.4 | Resistivity Characterisation | 84 |
| 4.4.1 | Static resistivity measurements | 84 |
| 4.4.2 | Dynamic resistivity measurements | 86 |
| 5 | Local mechanical property assessments of BMGs through Nano-indentation | 88 |
| 5.1 | Measuring elastic modulus and hardness | 88 |
| 5.2 | Nano-indentation derived values and related properties | 97 |
| 5.2.1 | H_v and ν in crystalline materials. | 98 |
| 5.2.2 | H_v and ν in BMG materials. | 100 |
| 5.3 | Conclusions | 103 |
| 6 | Probing creep behaviour in crystalline and BMG materials. | 105 |
| 6.1 | Observations of nano-indentation creep data | 108 |
| 6.1.1 | Creep data analysis | 110 |
| 6.1.2 | Other factors for consideration | 117 |
| 6.1.3 | Optimal method and limitations | 119 |
| 6.2 | Conclusions | 120 |
| 7 | Probing inhomogeneous yield behaviour in BMGs | 122 |
| 7.1 | Use of cross property characterisation of inhomogeneous yield | 122 |
| 7.1.1 | Using an electrical response to probe shear banding behaviour | 123 |
| 7.1.2 | Wheatstone bridge calculations and expected signals | 124 |
| 7.2 | Shear band detection limits through the Shear Band Electronic Detection System (SBESD) | 126 |
| 7.2.1 | Shear band lifetime | 126 |
| 7.2.2 | Shear band energy and its effect on resistance | 127 |
| 7.3 | Prototype and development of the SBESD system | 129 |
| 7.3.1 | Sensitivity analysis and noise reduction of the SBESD system | 134 |
| 7.4 | SBESD results and critical analysis | 138 |
| 7.4.1 | Positive detection events | 138 |
| 7.5 | Signal analysis and enthalpy/entropy implications | 146 |
| 7.5.1 | SBESD events and enthalpic processes | 147 |
| 7.5.2 | SBESD events and entropic processes | 161 |
| 7.5.3 | Application of entropic models on observed SBESD events. | 183 |
| 7.5.4 | False result analysis | 186 |
| 7.6 | Conclusions | 187 |
| 8 | Conclusions | 189 |
| 8.1 | Local mechanical property assessments of BMGs through nano-indentation | 189 |
| 8.2 | Probing creep behaviour in crystalline and BMG materials | 191 |
| 8.3 | Probing inhomogeneous yield behaviour in BMGs | 191 |
| 9 | Appendix | 194 |
| 9.1 | Wheatstone bridge theory | 194 |
| 9.1.1 | Calculations regarding the relationship between the Wheatstone bridge voltage, and changes in resistance | 194 |
| 9.2 | Kauzmann's paradox | 196 |

| | | |
|-------|--|-----|
| 9.3 | XRD results | 197 |
| 9.4 | LabView program | 203 |
| 9.5 | Fitting resistivity data to a temperature profile equation | 205 |
| 9.6 | Chapter 7 results | 206 |
| 9.6.1 | Microstructure of Tin tested for indentation creep | 206 |
| 9.6.2 | Indentation creep results and fitting equations | 206 |

Equation terms

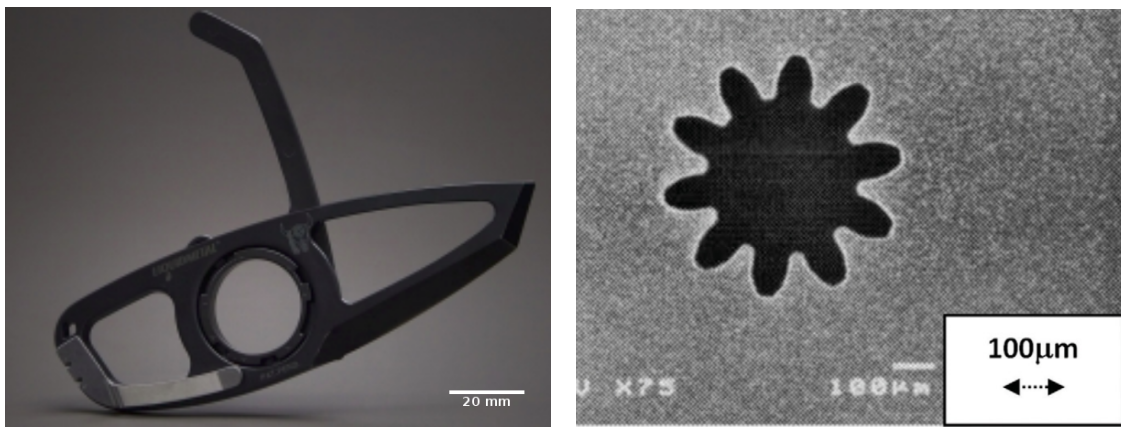
| Term | Description. |
|------------------|--------------------------------------|
| k_b | Boltzmann's Constant |
| E | Elastic Modulus |
| G | Shear Modulus |
| K | Bulk Modulus |
| ν | Poisson's Ratio |
| ΔU_{sys} | Change in internal energy |
| ΔW_{sys} | Work put into a thermodynamic system |
| ΔQ_{sys} | Heat put into a thermodynamic system |
| F | Applied force |
| P | Load |
| A | Area |
| T | Temperature |
| V | Volume |
| C_V | Heat capacity at constant volume |
| C_P | Heat capacity at constant pressure |
| R | Molar gas Constant |
| n_{mol} | Number of moles |
| S_{tot} | Entropy |
| R_c | Critical cooling rate |
| d_c | Critical cooling diameter |
| H_f | Enthalpy of melting/fusion |
| S_f | Entropy of melting/fusion |
| G_E | Gibbs free energy |
| T_g | Glass Transition temperature |
| T_{rg} | Reduced glass transition temperature |
| m | Fragility |
| T_m | Melting temperature |
| T_l | Liquidus temperature |
| T_x | Crystallisation temperature |
| η | Viscosity |
| Q_0 | Free energy for STZ activation |
| Ω_0 | STZ volume |
| τ_0 | Shear stress at STZ activation |
| $G(T)$ | Temperature dependent shear modulus |
| $P(r)$ | Probability distribution function |

| | |
|----------------------------------|---|
| h | Planck's constant |
| $\varepsilon, \dot{\varepsilon}$ | Strain, Strain rate |
| σ | Stress |
| V^* | Shear activation volume of Chen's entropy model |
| α_θ | Thermal diffusivity |
| H | Enthalpy |
| α_Ω | Thermal coefficient of resistivity |
| $R(T_o)$ | Resistance at room temperature (293K) |
| V_G | Gate voltage for a Wheatstone bridge |
| V_S | Supply voltage to a Wheatstone Bridge |
| $R_{SB}(t)$ | Dynamic electrical resistance contribution from a Shear band |
| a_n | Radius of a neck in a BMG machined sample |
| N | Total Number of atoms in a system |
| $S(q)$ | Structure Factor |
| σ_r | Structure Factor (PDF) |
| λ_L | Wavelength of light |
| α_x | Thermal coefficient of expansion |
| ξ | Correction factor for the evaluation of h_c in nano-indentation |
| S | Stiffness |
| ν_D | Debye Frequency |
| Q_{STZ} | Activation energy of a shear transformation zone |
| β_ν | Ratio of dilation to shear strain |
| Q | Activation energy term |
| b | Burgers vector |
| d_g | Grain size |
| p_g | Grain size dependence exponent |
| σ_i | (effective) stress |
| n | Stress exponent |
| D_i | Diffusion constant for vacancy diffusion in mode i |
| Q_i | Activation energy for vacancy diffusion in mode i |
| ρ_ω | Resistivity |
| ρ | Density |
| θ_i | Angle of an indenter tip |
| A, B | Fitting constants |
| Ψ | Tip area function factor |

Table 1: Equation terms used throughout this thesis.

Chapter 1

Introduction



(a) Metallic glass created by Liquidmetal for use as a surgical blade that is 25% harder than stainless steel [2].

(b) Micro electromechanical gear processed through extruding $\text{La}_{55}\text{Al}_{15}\text{Ni}_{20}$ bulk metallic glass [3].

Figure 1.1: Present commercial applications of metallic glasses.

Metallic glasses hold a wide array of industrially exploitable properties, such as high strength, good formability, corrosion resistance, damping characteristics, amongst many others, and have therefore attracted substantial academic interest. However, poor understanding of the factors affecting their physical properties, in particular their mechanical properties, has led to metallic glasses until recently only being commercially utilised in niche applications, such as sport equipment and jewellery, where failure of the material, whilst not ideal, has no catastrophic consequences.

A key limitation to developing metallic glass materials is the volumes of material that can be formed during processing. These volumes are limited for the vast majority of glass forming compositions, and therefore characterisation of these materials through standard testing techniques is often not possible. It is only with the introduction of small scale characterisation techniques such as TEM and nano-indentation that advances in understanding of metallic glass behaviours began to yield results. This can be seen in the chronology of metallic glass developments which, from its discovery in the 1960s to the late 1990s, was focussed on developing larger and larger volumes of the material. From the turn of the millennium onwards however, the research focus became shifted to the specific physical behaviours of these materials through the availability of these new small scale testing techniques. Significant advances over the last decade or so in understanding the structure and behaviour of these materials has led to the material being processed in a range of different ways and being used in more important roles, such as surgical equipment [2] and micro

electromechanical systems (MEMs: microscopic gears, etc.) [3]. However load bearing applications, which would benefit from the high yield strength of such materials, have yet to be exploited due to the poorly understood catastrophic failure mechanism of metallic glasses when plasticity is initiated under unconstrained modes of loading. As such this has become a key focus area for metallic glass research with several review papers on the subject being published over the last decade summarising the current state of knowledge in this field [4–6].

This thesis provides an overview of the mechanical behaviours of metallic glass materials and the techniques used to mechanically characterise them. Previously used methodologies have been scrutinised regarding their validity in measuring the mechanical behaviour of these unique materials, and a new testing methodology is proposed, developed and validated, capable of providing vital information regarding the poorly-understood catastrophic shear banding phenomena that occurs in metallic glasses under high strain/ low temperature conditions. The breakdown of this work is presented as follows:

- Chapter 2 outlines bulk metallic glass formation and structure, providing a basis upon which mechanical behaviours can be related to and explained.
- Chapter 3 provides the current state of knowledge pertaining to the mechanisms and characteristics of deformation in bulk metallic glasses as well as covering some of the testing methodologies required to probe these properties.
- Chapter 4 outlines standard experimental investigations carried out in order to evaluate both the mechanical behaviour of metallic glasses and the performance of the testing methodologies themselves.
- Chapter 5 investigates the use of novel indentation techniques for probing elastic properties of metallic glasses including the application of the elastic-plastic relationship provided by Chen [7] and Zorzi and Perottoni [8].
- Chapter 6 probes visco-elastic/creep in both crystalline and metallic glass systems through room temperature nanoindentation.
- Chapter 7 introduces a new test methodology for probing inhomogeneous flow (shear banding) in metallic glasses, which provides a potential technique for measuring temperature, lifespan, structural state and thickness of shear bands both as an absolute change and change during the process providing the essential experimental evidence required to bridge the gap between the atomistic scale processes to the macro-scale observations.

Chapter 2

BMG formation, structure and classification

2.1 Metallic glass formation

Metallic glasses (MGs), first discovered by Klement et al. in 1960 through splat quenching of a $\text{Au}_{75}\text{Si}_{25}$ eutectic melt [9], are a class of material characterised by the lack of long range order (LRO) in atomic structure (outlined in Fig.(2.1)). This yields numerous favourable material behaviours, including high yield strength, wear resistance, high corrosion resistance and high formability [10]. After the initial discovery of MGs, efforts were initially focused on developing MG materials with ever greater volumes [11]. The first metallic glasses were produced by quenching of melts at cooling rates of the order of 10^6Ks^{-1} [9]. Other processes were also investigated including solid state amorphisation and heat treatment processes [12, 13], and mechanical alloying [14]. These initial efforts only yielded MGs with bulk cross-sectional dimensions from $10\ \mu\text{m}$ to $100\ \mu\text{m}$. From 1974, Chen and Turnbull [15] began to consider MG compositions with slow crystallisation kinetics, allowing glasses to be formed from cooling melts at rates of $< 10^4\text{Ks}^{-1}$. This provided the recipe for the formation of the first Bulk Metallic Glasses (BMGs); metallic glasses with bulk cross-sectional dimensions $\geq 1\text{mm}$, with which practical industrial applications could be envisaged. Melt compositions of Pd-Cu-Si, Pd-Ni-P and Pt-Ni-P [15–17] were amongst the first amorphous alloy families to be produced in bulk form, however new BMG compositions continued to emerge for the

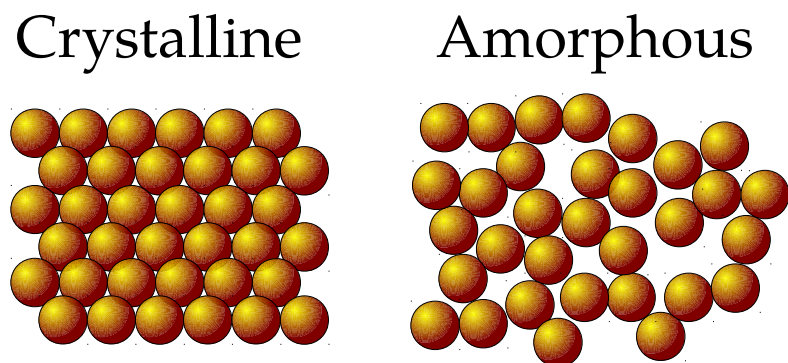


Figure 2.1: A 2D schematical representation of crystalline and amorphous atomic structures.

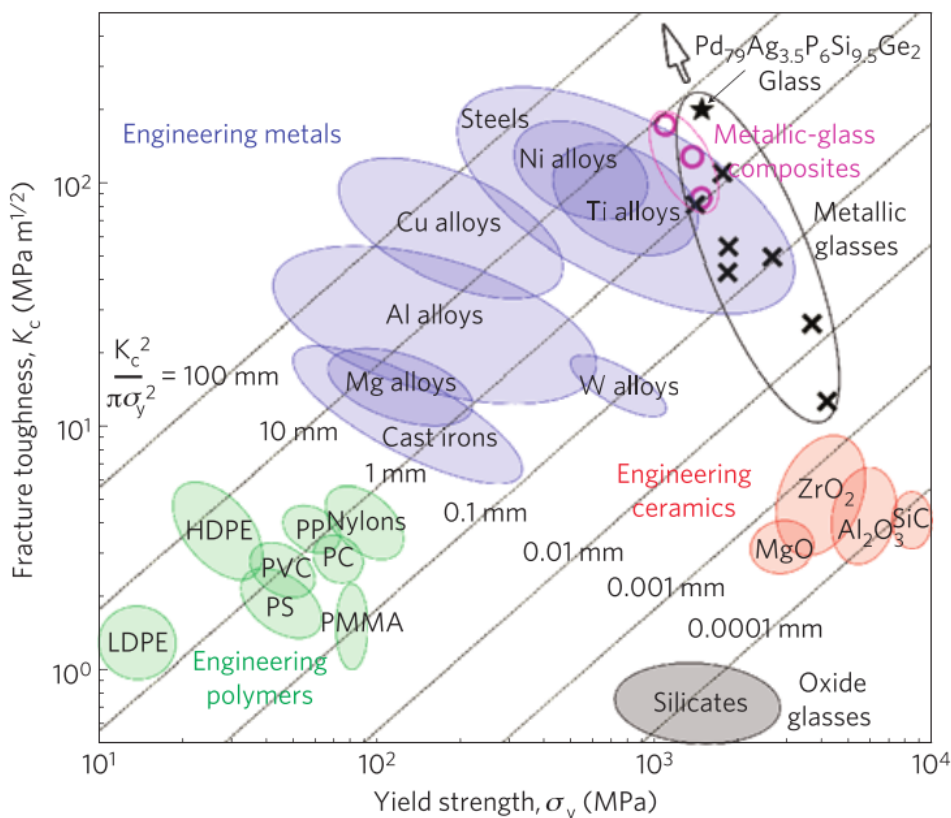


Figure 2.2: A property map showing the mechanic performance of a range of materials including metallic glasses, metallic glass composites and a carefully designed ultra-tough, ultra-strong BMG (reproduced from [21]).

next few decades, allowing for the unique properties of metallic glasses to begin to be both tested and investigated. Up until the 1990s, research efforts focussed on producing larger and larger glassy materials through retardation of crystallisation during quenching [11]. As a result, BMG materials are now commercially sold in rod and plate form with bulk cross sectional dimensions of the order of 10mm [18], and research specimens have been observed to reach length scales of ≈ 80 mm [11]. The focus on BMG casting sizes has diminished over recent years, with the dawn of processes such as additive layer manufacturing [19] and vapour deposition methodologies [20] effectively circumventing the limitations previously put on BMG geometries from cooling rates of BMG melts.

At the turn of the millennium, focus began to shift towards understanding the factors affecting physical properties of BMGs and how to improve them [11]. Mechanical properties became a particular focus of this effort [4] due to the poor plasticity typically exhibited by BMGs under standard conditions making them non-viable for a wide range of load bearing applications. Great strides have been made since the formation of the first BMGs, with the development of composite glass-crystalline structures rivalling strength to toughness ratios of the strongest of steels [22], and the discovery of certain Pd rich BMG compositions that outperform even these carefully designed composites [21], as shown in Fig.(2.2). Despite this progress, current models for predicting possible BMG compositions are largely empirical [23] with loose influences from atomic packing models providing clues for new avenues of investigation. As such, development of new BMG materials has adopted approaches ranging from incremental changes of already well known BMG compositions with the aim of improving properties [5], to full combinatorial alloy library investigations through

the use of additive layer manufacturing capabilities [24]. A notable study into BMG forming compositions of Zr-Cu system was performed by Li et al. [25] who used the differences in glassy and crystalline densities to determine glassy phase compositions by observing deflections of silicon wafers when coated with different composition melts and cooled rapidly. In any case, to understand the factors affecting BMG behaviours, a clear understanding of the current state of metallic glass formation theory is required.

2.1.1 Thermodynamics and kinetics of metallic glass formation

Beyond the basic amorphous nature, MG atomic structure can be described as a densified liquid phase, whose atoms have been ‘frozen’ into a disordered configuration, often during rapid solidification [5,9]. The ability for a MG melt to subvert crystallisation in favour of forming a disordered glassy state is known as the glass forming ability (GFA). In the case of forming a BMG through rapid quenching of a liquid melt, the GFA is characterised by a balance of the thermodynamics and kinetics of the melt during cooling, whereby the driving force for crystallisation (ΔG) remains small enough to allow supercooling of the liquid melt to a point whereby the temperature dependence of viscosity of the melt restricts the rearrangement of atoms to form a crystalline structure [5,26].

The competing processes of thermodynamics and kinetics can be quantitatively analysed in order to identify GFA and its affecting factors. Thermodynamics of the melt are assessed through the driving force for crystallisation; Gibbs free energy (ΔG_E), whilst the kinetics of the melt are determined through the state of atomic mobility within the melt; viscosity (η).

Thermodynamics of GFA

The driving force for crystallisation is thermodynamically defined as the difference in G_E between the liquid and crystalline states [27].

$$|G_E^{liquid} - G_E^{crystalline}| = \Delta G_E = \Delta H_f - T\Delta S_f. \quad (2.1)$$

When forming a BMG, ΔG_E must remain as low as possible during supercooling of the melt. Therefore, to form a BMG with good GFA according to Eq.(2.1), the melt must have a large difference in the entropy of melting (ΔS_f) in order to offset the difference between the enthalpy of melting (ΔH_f) between the crystalline and liquid states. Based on these thermodynamic considerations, BMG compositions with good GFA have often been observed near eutectic points in the phase diagrams. Examples of this include some binary compositions of Zr-Cu and Ni-Nb [5,17,28–30], as well as a multitude of multi-component systems. Often hypo-eutectic (i.e. solute poor) BMG compositions give the best GFA, as these compositions often show slower crystalline growth kinetics compared to the hyper-eutectic case [31].

Kinetics of GFA

The kinetic behaviour (viscosity) of an ideal melt is ideally characterised through the Arrhenius equation [32]:

$$\eta = \eta_o \exp\left(\frac{Q}{k_b T}\right), \quad (2.2)$$

where Q defines the activation energy required for viscous flow (assumed to be constant and independent of the material temperature) [33] and η_o is the high temperature viscosity limit for the material [34]. All ideal liquids (and amorphous materials e.g. SiO₂) follow this relationship

closely, to produce a linear $\log(\eta)$ vs. $\log(1/T)$ relationship as detailed in Fig.(2.3a) [26, 32]. In the case of real BMGs, deviation for this Arrhenius behaviour is observed at temperatures typically $\lesssim 1.2T_g$, showing a decoupling in flow in favour of a rapid increase in viscosity [32]. Such non-Arrhenius behaviour is better described by the Vogel-Tammann-Fulcher equation (Eq.(2.3)); capable of describing several orders of viscosity magnitude change over the $T_g \leq T \lesssim 1.2T_g$ [32, 34, 35].

$$\eta = A \exp \left[\frac{B}{(T - T_o)} \right] \quad (2.3)$$

Despite the deviations in viscosity vs. temperature behaviours shown in Fig.(2.3a) over a range of BMG compositions, observations of glassy melts show that viscosities all converge to a critical value of 10^{12} Pa s [32] when the temperature drops below a material-specific critical value. Below this temperature viscosity remains constant, and the bulk flow of the material takes on the flow behaviour of a solid [32]. The temperature at which this convergence occurs for a given MG melt is defined as the glass transition temperature (T_g).

The magnitude of deviation of BMG melt viscosity from nominal flow behaviour differs for different BMG melt compositions. Work performed by Angell took this observation and characterised potential BMG melts in terms of the *fragility* of the melt [32]. Melts that show large deviations in viscosity behaviour from Eq.(2.2) have a high fragility and are therefore termed *fragile* melts, whilst melts whose viscosity behaviour correlates well with Eq.(2.2) have low fragility and are termed *strong* melts. It is worth noting, given the theme of this thesis, that the descriptions of strong and fragile glasses given here have no bearing on the mechanical strength of these materials. However, as discussed later, it is observed that melt fragility does indeed correlate with BMG mechanical performance, in particular, plasticity [17, 36].

The fragility (m) of a given melt can be mathematically quantified through considering the level of deviation of melt viscosity from the nominal behaviour [5]:

$$m = \left[\frac{d \log \eta(T/T_g)}{d(T/T_g)} \right]_{T=T_g}. \quad (2.4)$$

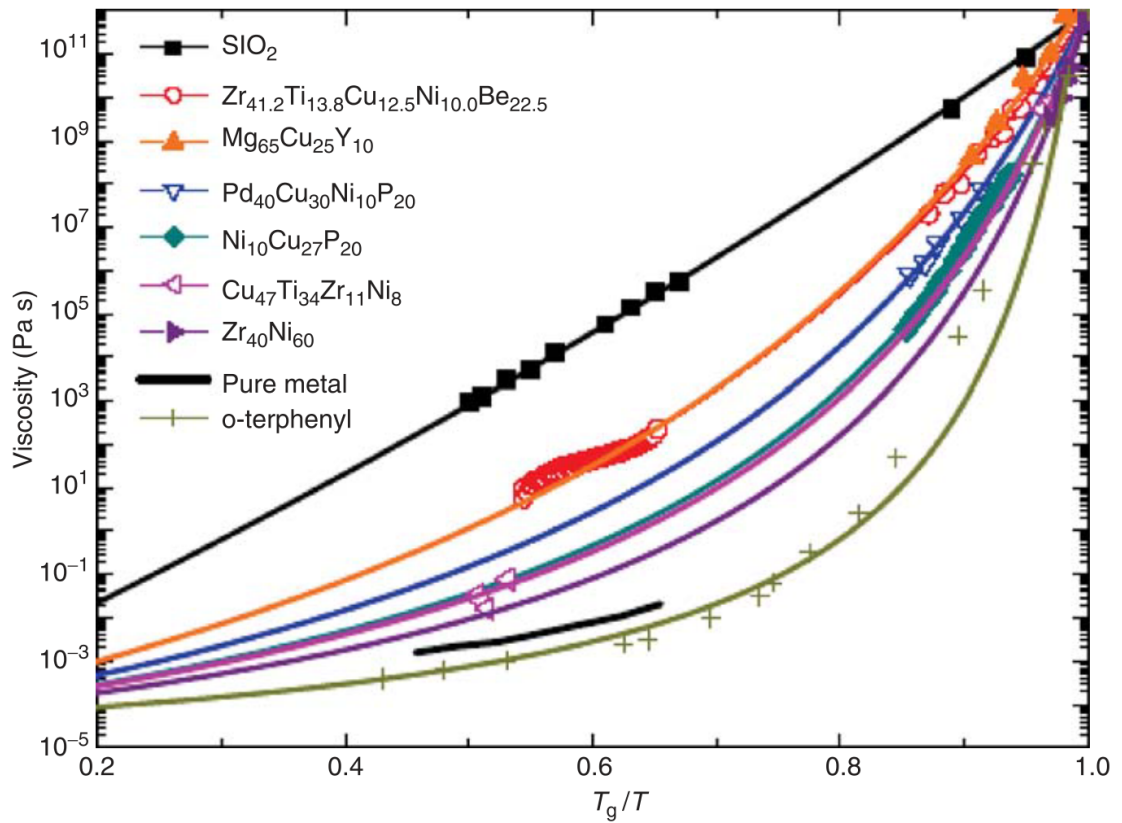
This equation uses a measure of the gradient of viscosity at T_g with respect to temperature to determine the fragility index, and therefore the nature of the BMG melt. This fragility behaviour is observed to scale well with GFA of BMGs for most BMG compositions, with low fragility indicating good GFA and *vice versa* [26]. Pd rich BMGs are an exception to this observation, demonstrating good GFA and fragile behaviour [37].

Linking thermodynamics and kinetics

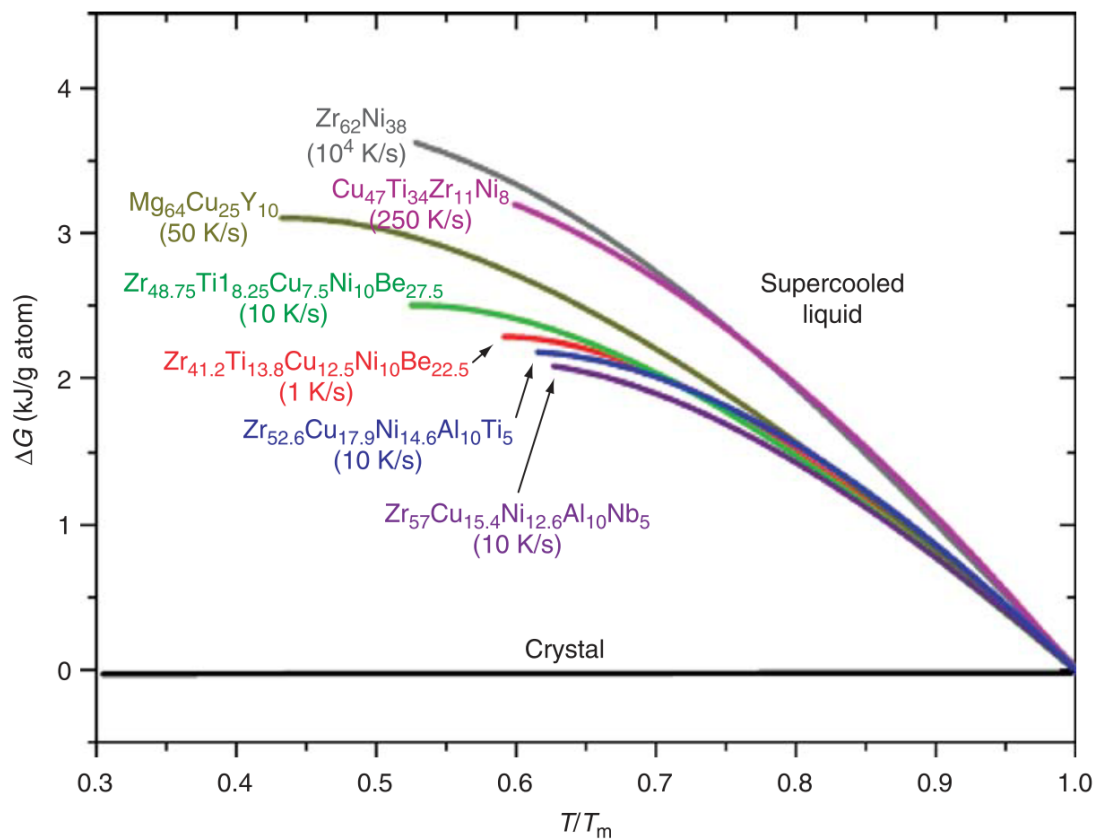
Relating thermodynamic and kinetic behaviour of a BMG melt to each other was first performed through the molecular kinetic theory of BMGs [38] through

$$t \text{ or } \eta = A \exp \left(\frac{B}{TS_c} \right) \quad (2.5)$$

where S_c is the configurational entropy which is related to the number of inherent structural states in a BMG (see the PEL in Sec.(2.1.1) for further details) [34]. According to this equation, the viscosity (or relaxation time) increases as the system approaches T_g due to the reduction in the number of available entropy states that atoms in the melt can sample [38]. In theory, if the temperature continues to decrease, the system will eventually reach a state where the atoms exist



(a) An Angell plot showing the strong glasses approaching an almost Arrhenius response with regards to viscosity below T_g .



(b) The Gibbs free energy of supercooled liquids for BMG candidates.

Figure 2.3: Angell plot and Gibbs free energies of some typical BMGs (reproduced from [26]).

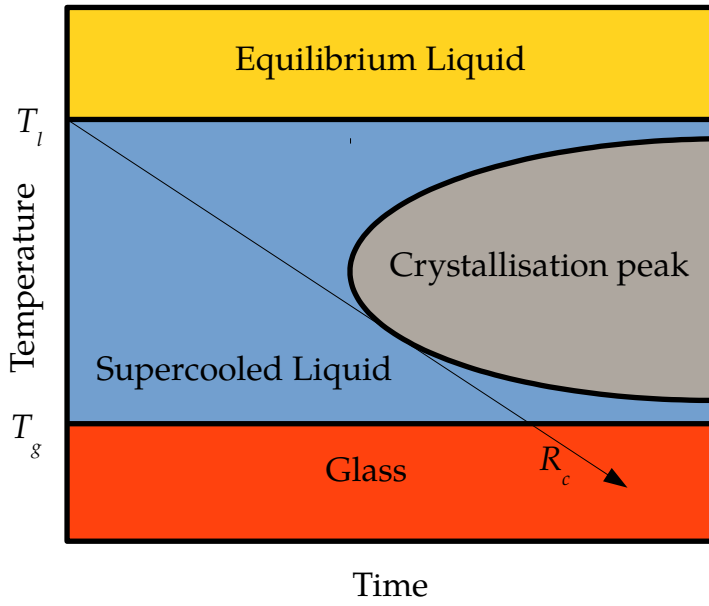


Figure 2.4: A schematic of a typical metallic glass TTT diagram.

in one ideal low energy glass structure. This temperature is known as the Kauzmann temperature, and defines the basis for what is known as the entropy crisis.

The entropy crisis arises from the fact that configurational entropy of a liquid phase is higher than that of the crystalline phase due to the higher number of degrees of freedom of atoms in the liquid structure [34]. Measurements of the configuration entropy can be determined through the heat capacity of the system:

$$\left(\frac{\delta S_c}{T}\right) = \frac{\Delta C_p}{T} \quad (2.6)$$

During the supercooling of the liquid, the higher heat capacity of the liquid structure indicates that ΔS_c must be consumed in order to maintain the ideal viscosity to the point whereby at a given temperature (T_k), the entropy of the system must vanish [34]. In reality, the presence of the kinetics of the system stops this occurring, whereby the formation of a glass at a temperature above T_k limits further reductions in the entropy state of the material, causing ΔS_c to become constant, and the viscosity of the system to deviate from the nominal behaviour to produce the final structural state of the glass [34].

Improving glass forming ability

Knowledge of how thermodynamics and kinetics contribute to the formation of a glassy structure can be used to create a Temperature-Time-Transformation (TTT) diagram, like that schematically outlined in Fig.(2.4). This diagram outlines the critical cooling rate (R_c) for which a melt can be cooled and still remain amorphous [5].

Enhancing the value of R_c of BMG melts has been the subject of focussed research in order to improve BMG component sizes [11]. Most successful BMGs formed for research purposes undergo

rapid quenching from a superheated melt in techniques such as arc-melting and suction casting into a water cooled copper mould [22]. Recent advances in production methods such as vapour deposition [20] and additive layer manufacturing techniques (ALM) [19] are starting to circumvent the limitations imposed by critical cooling rates, however these processes are still a work in progress in their application to glassy materials, and often rely on good GFA of a BMG in order to offset difficulties in the processing conditions required by such techniques. To that end, understanding the factors that are attributed to good GFA is still important in the development of new high performance BMGs.

Aside from extrinsic experimental factors, improving the GFA of a BMG in terms of the TTT diagram can be achieved altering the BMG melt composition such that [5]:

- The position of the crystallisation nose in the TTT diagram is pushed right, thereby delaying the onset of crystallisation
- The reduced glass transition temperature ($T_{rg} = T_g/T_l$) is increased such that the temperature range in which a stable liquid like structure can exist is maximised.

Senkov [39] used this information to produce a formulae from which the critical cooling rate can be predicted, providing information regarding both the kinetics (in the form of fragility of the system; m) and thermodynamics (in the form of the reduced glass transition temperature T_{rg}) of the melt are known.

$$F_1 = 2 \left[\frac{m}{m_{min}} \left(\frac{1}{T_{rg}} - 1 \right) + 2 \right]^{-1} \approx -\log_{10}(R_c) \quad (2.7)$$

The value of m_{min} corresponds to the fragility of the strongest possible melt. This value is set as the fragility of the melt if it obeys the Arrhenius behaviour outlined in Eq.(2.2) and Fig.(2.3); ≈ 17 , which represents a straight line between high temperature melt viscosities of 10^{-5} Pas and the glass convergence viscosity of 10^{12} Pas. Based on this relation, it can be seen that a combination of a high T_{rg} and a low m favours GFA. It is important to note that information regarding only one of these parameters is not enough to identify good GFA of a melt, as demonstrated in the case for the high GFA of the highly fragile Pd based BMGs composition melts [4, 40].

Whilst the described treatments are good for empirically identifying why a melt has a good or poor GFA, they are poor for predicting new BMG compositions, as they require prior knowledge of the thermodynamic and kinetic behaviour of a melt [17]. To solve this issue, multiple attempts at modelling BMG melts have provided useful insights regarding factors that are useful for identifying new BMG compositions, showing that melts with good GFA can be indicated by the empirical observations developed by Inoue [23]:

1. The melt must contain 3 or more elemental components.

This creates competition for the preferred crystallisation structure, thus destabilising the crystallisation process and lowering the driving force for crystallisation.

2. The atomic size ratios between the different components must be $\geq 12\%$ for the 3 main alloying elements.

This improves the packing efficiency of atoms in the melt, thus stabilising the liquid structure at lower temperatures, and reducing diffusion rates when crystallisation is thermodynamically favoured.

3. The enthalpy of mixing of the different components must be negative.

Improves the mixing ability of the melt such that chemical segregation does not occur, which could lead to individual phases crystallising upon cooling.

The first metallic glass structures produced by Klement required $R_c \approx 10^6 \text{Ks}^{-1}$. This is due to the violation of rule 1 (2 components) in Inoue's rules. However the melt composition had an atomic mismatch of 22.7% and a negative enthalpy of mixing of -30kJ/mol , allowing for the formation of a thin splat quenched glassy phase. New melt chemistries containing Zr, Cu, Pd, Pt, Ti, Mg, Ce, La and Ni as the dominant elements have been developed over the years [11], which satisfy all of Inoue's empirical rules.

The potential energy landscape (PEL) and BMG structure

The varied fragility behaviour of BMG compositions calls into question the cause of such behaviour and how this affects GFA and other BMG behaviours. In order to understand this more deeply, the concept of a Potential Energy Landscape (PEL) must be introduced [5, 34, 35, 41–44].

The PEL, created by Goldstein [35] and introduced by Stillinger [44] for use in explaining behaviours in BMG systems, introduces the idea that the sum of all the potential energies of a multi body system can be described through a potential energy landscape; a 2 dimensional plot outlining the potential energy associated with a set of particle coordinates which could describe the BMG structure, schematically represented by Fig.(2.5). Sharp, deep troughs in the PEL indicate a stable phase of material with well defined coordinate information, i.e. crystalline arrangements. Relatively deep, yet diffuse troughs, referred to as 'mega-basins' identify a stable material state over a range of potential atomic coordinates. These basins define the bulk short to medium range order state of a potential BMG melt of given energetic state, with the diffuse nature of the basin arising from the statistical variability that exists within the BMG structure [34]. Shallow basins are also observed in the PEL, which identify metastable atomic configurations of a BMG melt that can only be sampled if the melt with a particular PEL is quenched rapidly such that the atoms do not have enough time to sample a lower energy configuration. This produces frustrated BMG structures that will undergo relaxation processes during annealing. The peaks between all the basins within the structure are termed transitions or 'saddle points'. These define the energy required by a melt in order for an atomic configuration to change from one type to another.

The PEL illustrates the behaviour of atomic motion within a BMG. These motions are characterised as relaxation events. There are 2 kinds of relaxation process; β relaxations and α relaxations. β relaxations define minor relaxation events of a few atoms providing transitions from sub-basin to sub-basin. Such a process is attributed to the activation of shear transformation zones (covered in detail in Chap.(3)) [45]. α relaxations deal with transitions from mega basin to mega-basin, signifying a significant change in the atomic structure of the glass [45]. Such a change requires significant energy, which can be described as the energy associated with T_g . A system heated to above this temperature is no longer in a glassy state, thereby the atoms that were trapped in the PEL are released to behave as a nominal liquid as described by Eq.(2.2) [34, 45].

The PEL acts as a useful tool to identify the effect of thermomechanical processing on BMG structures. For example, atoms in a melt excited to energies greater than any feature outlined in Fig.(2.5) can sample every atomic configuration possible defined by the PEL. If the melt is slowly cooled to a lower energy state, atoms become trapped in the mega-basins of the PEL, but have time to escape the higher energy sub-basins. This provides a visual basis for the types of structure formation in BMGs and how they depend on processing history:

PEL structures for different BMG compositions depend on the fragility of the melt, as outlined in Fig.(2.6). In the case of a strong glass former, the relaxed amorphous phase is populated by

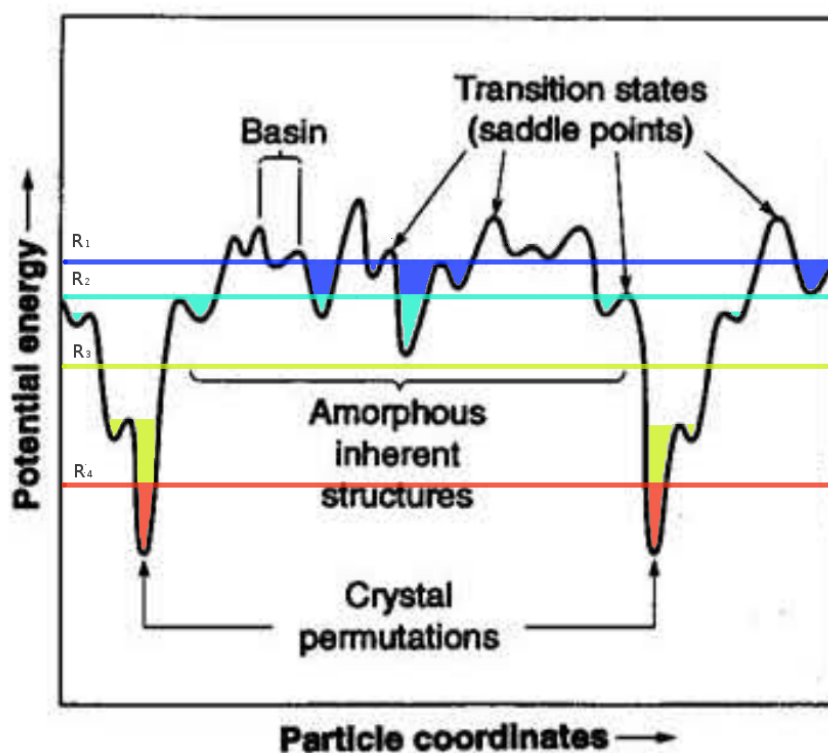
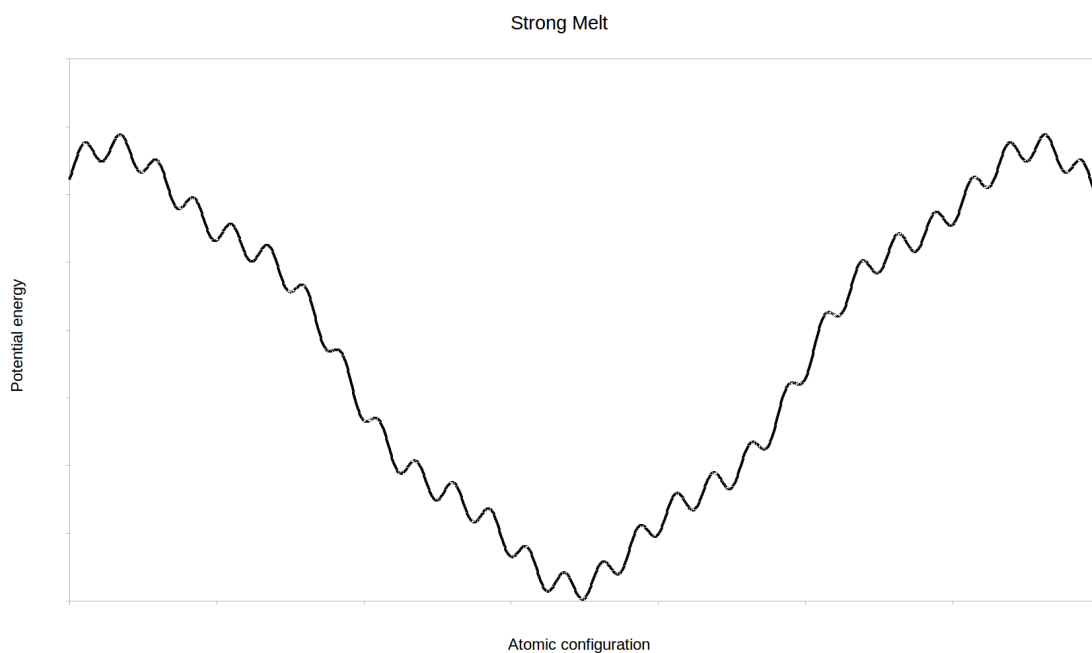
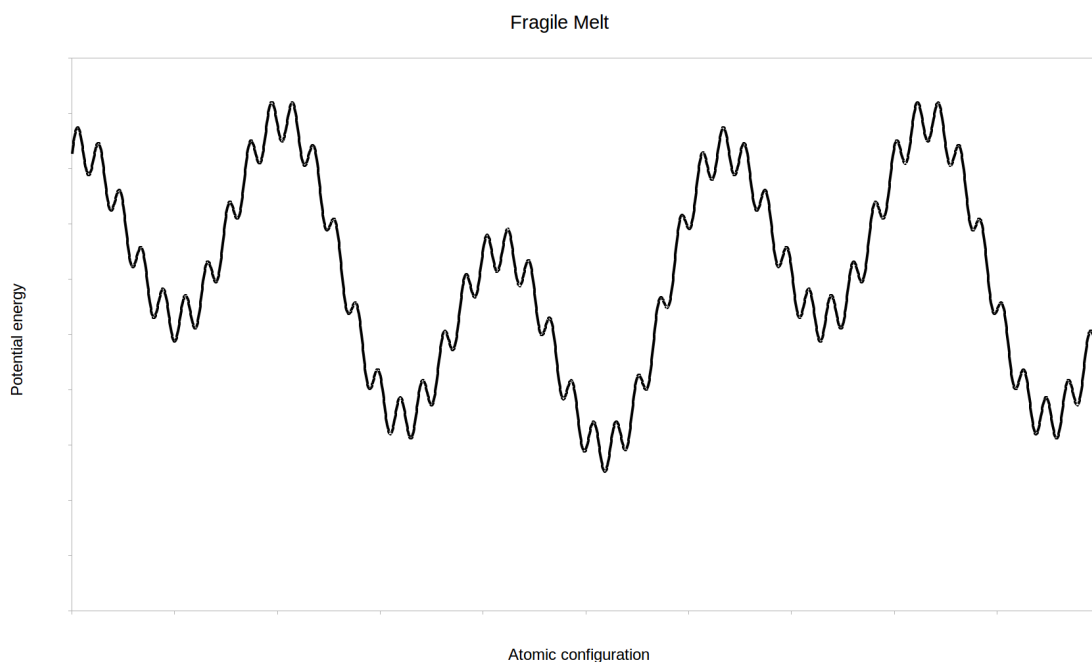


Figure 2.5: A schematic of a potential energy landscape. Each trough in the PEL is coloured corresponding to the atomic configurations that can be sampled if a system is quenched from an energy state defined by the corresponding lines of colour R_1 - R_4 (adapted from [34]).



(a) PEL of a strong BMG showing a deep mega-basin representing the ideal atomic configuration for a stable strong brittle glass BMG.



(b) PEL of a fragile BMG showing shallower and more frequent mega-basin than the strong melt indicating elevated atomic mobility and a more ductile BMG.

Figure 2.6: A schematic showing how PELs differ for strong and fragile melts.

small sub-basins that can be overcome with relative ease such that the lowest energy amorphous state (ideal metallic glass) can be sampled easily even at low cooling rates [5]. Compared to strong glass formers, fragile glass formers tend to have multiple, but shallower, mega-basins in addition to the sub-basins. As such α transitions are easier in these materials, which is manifested as enhanced atomic mobility in the fragile glasses. As such, this identifies why fragile glass formers tend to have poorer GFA for the most part, as atoms can sample the crystalline configuration in these melts easier than in the strong melts [35, 44, 46, 47]. The idea of this atomic mobility in the PEL and how they differ for different fragility glasses aids in the explanation of a multitude of BMG behaviours.

The PEL provides a good visual aid regarding the relaxation processes and time scales involved [34, 45]. It has been computationally and experimentally shown that whatever the exact nature of the transitions from basin to basin in the PEL, actual structural changes during deformation are due to the intense rearrangement of a few hot spots of atoms at low temperatures that are surrounded by elastically mobile, plastically immobile atoms [34]. It is the existence of these features in the PEL and the distribution of these features that determine the flow behaviour of a BMG and outline what separates a fragile and strong glass former [34].

There are several types of relaxation behaviour observed in the thermomechanical processing of a glass. Greer highlighted some of the key relaxation processes [45], which are summarised as irreversible relaxation, reversible relaxation near T_g , reversible relaxation below T_g , relaxation of the kinetic state, the memory effect and the quench rate effect.

2.2 Metallic glass structure

The amorphous nature of BMGs makes investigations into the factors affecting their properties difficult, as there are few obvious state variables to relate properties to. Whilst many properties of BMGs have been related to the extrapolation of properties of liquids, such as electron transport properties [48], other properties, such as mechanical properties, need a foundation in BMG structure. Therefore a clear outline of what is currently known and unknown regarding BMG atomic structures is required.

BMG structures can be thought of as densified liquid structures. Whilst liquid structures can be considered to be almost random (neglecting the presence of nearest neighbour packing), the dense atomic packing in BMGs must give rise to a certain amount of short range order (SRO) and medium range order (MRO) from geometrical considerations [5]. Whilst these structures cannot be used in the same way as the unit cells in crystalline material to predict absolute properties of materials, a statistical approach can be utilised with information of these SRO and MRO structures to estimate the bulk behaviour of BMGs. Measurement, describing and modelling of these ordered structures provides the foundations of understanding the factors affecting BMG properties and behaviours.

2.2.1 Tools for describing structures of BMGs

Descriptions of BMG structures have been approached in several different ways. However the successful descriptors all rely on the concept of SRO and MRO, the most common of which are as follows:

Pair distribution functions: $g(\mathbf{r})$

The pair distribution function (PDF) defines the statistical distribution of atomic positions of atoms surrounding any given central atom, For a mono and bi-atomic system, this is defined

respectively by:

$$g(r) = \frac{1}{4\pi r^2 \rho N} \sum_{i=1}^N \sum_{j=1, j \neq i}^N \delta(r - |\bar{r}_{ij}|), \quad (2.8)$$

$$g_{AB}(r) = \frac{N}{4\pi r^2 \rho N_A N_B} \sum_{i=1}^{N_A} \sum_{j=1}^{N_B} \delta(r - |\bar{r}_{ij}|). \quad (2.9)$$

These equations identify the probability of certain atom pairs within a BMG structure that lie within $r + \delta r$ of each other, as outlined in Fig.(2.7a). For multi-component systems with 3 or more constituents, Eq.(2.8) and Eq.(2.9) would define *partial* PDFs as they only describe the statistical spacial distribution of $A - A/B - B$ pairs in the case of Eq.(2.8), or $A - B$ atomic pairs in the case of Eq.(2.9). This allows for the investigation of chemical ordering within glassy alloys, an important factor governing the SRO and MRO structures that can form in BMG materials [5, 49].

SRO of BMGs is described by the first peak within a given PDF. Peaks beyond this value are beyond the nearest neighbour atoms, and thus quantify MRO atomic packing. Due to the amorphous nature of BMGs, these peaks typically extends no further than 1-2 nm [5], before the position information degenerates due to the pseudo-random packing in the glass structure.

Structure factor: $S(q)$

Partial PDFs are usually considered from diffraction experiments in order to obtain useful information. However metallic glasses are usually comprised of multicomponent systems, therefore there is a need to be able to deal with diffraction spectra that are comprised of multiple partial PDFs to give an overall description of the SRO and MRO of BMGs. The structure factor deals with this, whereby a sum of the Fourier transforms of the partial PDFs in reciprocal space is produced to fit diffraction spectra, which can then be separated into individual PDFs to describe the structure of a BMG. Mathematically, for a partial structure factor describing the distribution of A and B atoms, the structure factor can be described as

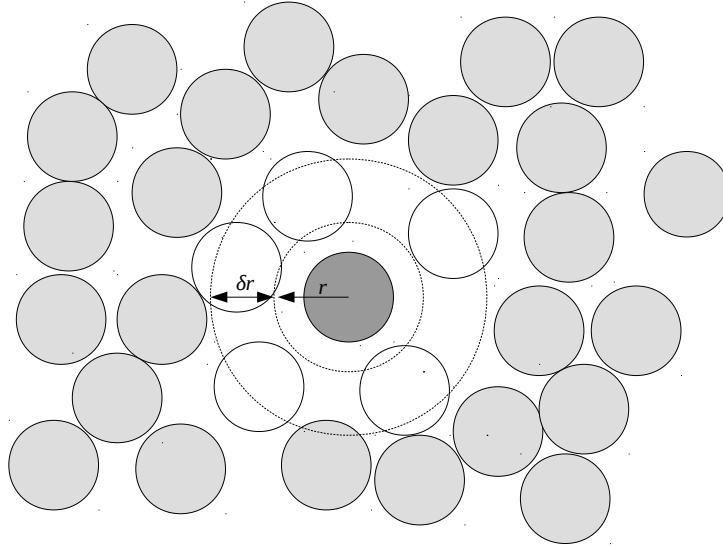
$$S_{AB}(q) - 1 = \frac{4\pi\rho}{q} \int_0^\infty r[g_{AB}(r) - 1] \sin(qr) dr. \quad (2.10)$$

Diffraction data can be related directly to this equation as q represents the magnitude of the diffraction vector defined as $4\pi \sin \theta / \lambda$. Therefore, through a data fitting exercise, the total structure factor can be determined through

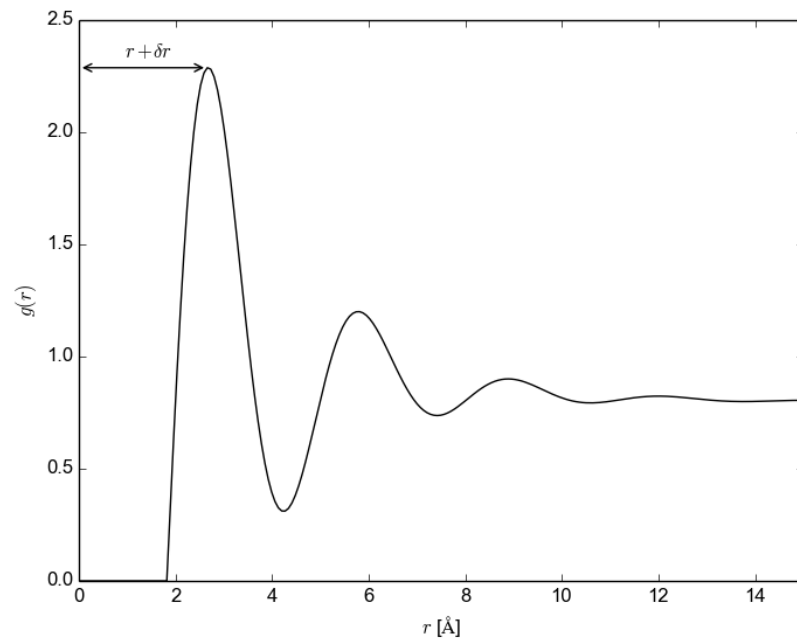
$$S(q) = \sum_A \sum_B \frac{c_A c_B f_A f_B}{(\sum_A c_a f_a)^2} S_{AB}(q) \quad (2.11)$$

A Fourier transform can be performed on $S(q)$ defined by real diffraction data to reveal the total PDF of a glassy material describing the distribution of atoms throughout the structure.

There are a number of other ways of defining and describing atomic structure in glassy materials, including coordination number, chemical SRO, bond angle distribution, bond orientation order, common neighbour analysis, and Voronoi tessellation; all of which have been reviewed in detail by Cheng and Ma [5].



(a) A 2D representation of a BMG structure showing the nearest neighbours responsible for the SRO peak in a given PDF.



(b) Schematic of a PDF of the structure in Fig.(2.7a) showing the peaks corresponding to SRO and MRO.

Figure 2.7: Schematic representation of an amorphous structure and its associated PDF.

2.2.2 Tools for observing BMG structures

X-ray/neutron diffraction

Diffraction experiments have been used since Rutherford in 1911 [50] to probe structures of materials. The short wavelengths associated with x-rays and the penetration properties associated with neutrons make both of these experimental techniques ideal for probing atomic structure of metals. X-ray diffraction (XRD) experiments are often used as the first verification technique to determine if an alloy is amorphous. Whilst the technique is ordinarily used to identify the structures of crystalline materials, it is just as powerful for identifying a lack of crystalline structure. In the case of glasses, a diffuse intensity of x-rays are detected often centred around a scattering angle of $2\theta \approx 40^\circ$ [5]. Such a signal indicates a lack of LRO within the material structure, and implies the presence of a glass to a first approximation. Standard X-ray diffraction experiments are only capable of probing a few microns into the test surface (material depending), making this a topological assessment method. Therefore tests using this method require the assumption that the surface is representative of the entire sample.

Neutron diffraction experiments work on the same principle as XRD, however the lack of electrostatic charge and higher momentum of neutrons allows neutron diffraction to probe deeper into materials [5]. These experiments can identify whether or not a structure is amorphous and can measure fine detail such as MRO of BMGs, as demonstrated by Scopigno et al. [51] who showed the presence of liquid-like structures in amorphous materials through this technique.

In addition to diffraction experiments, other techniques for directly measuring MG structure include X-ray absorption fine structure (EXAFS) [5], Fluctuation Electron Microscopy [52–54], Transmission electron microscopy (TEM) [55–57], Positron Annihilation Spectroscopy (PAS) [52, 58] and Nuclear Magnetic Resonance (NMR) [59, 60]. All these methodologies have their unique advantages and drawbacks. Therefore use of multiple techniques is often employed in literature in order to determine the best possible information regarding BMGs structures. This is reflected in the work of J3v3ari et al. [60], who successfully measured SRO in the $\text{Mg}_{60}\text{Cu}_{30}\text{Y}_{10}$ BMG through X-ray and neutron diffraction techniques as well as EXAFS, and confirmed with the aid of the Reverse Monte-Carlo technique (outlined in Sec.(2.2.3)) that SRO of this material is remarkably similar to that of the crystalline counterpart of the alloy of Mg_2Cu , with the Y additions aiding in the stabilisation of the glass structure during formation. This is an observation that was to become common place in BMGs, and resulted in a metallic glass modelling methodology known as efficient cluster packing (discussed in detail later).

2.2.3 Tools for further understanding BMG structures

To determine useful information regarding the effect of BMG structures on physical properties modelling methodologies have to be developed and tested. Unlike the crystalline case, BMGs do not have an exact synonym to the unit cell. As such, models require a statistical approach to describe the bulk BMG structure and how this correlates to property dependencies. To that end, investigations rely heavily on computational simulations, as a pseudo-random structure of BMGs requires numerical solutions to produce bulk behaviour from local atomic features. A plethora of computational methodologies have been reported in the literature which can be categorised into the following general approaches:

- Reverse Monte Carlo (RMC)

Using a Monte Carlo approach, this methodology places atoms within an atomic box in a pseudo-random manner, with atomic positions being chosen according to a probability

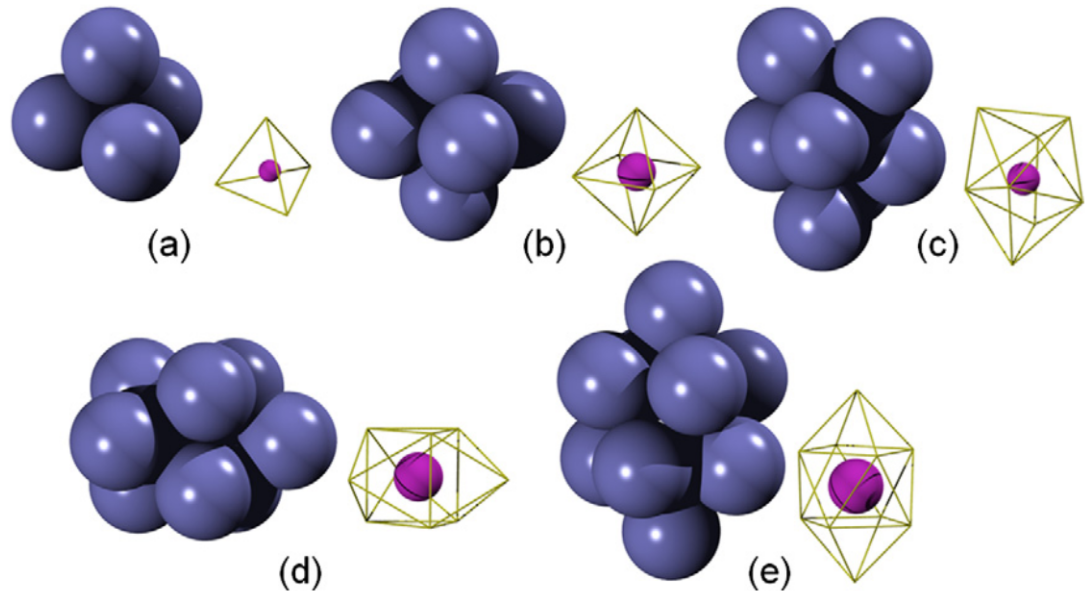


Figure 2.8: Bernal's holes showing schematically the different levels of free volume accommodated by different packing arrangements of atoms in ascending order of free volume fraction. a) Tetrahedron, b) octahedron, c) tetragonal dodecahedron, d) trigonal prism capped with three half octahedra e) Archimedean antiprism capped with two half octahedra. (reproduced from [5]).

function defined by the input of a PDF of a given BMG [5]. This methodology returns no singular solution as the pseudo-random nature of the model will return a distribution of structures that will average to the most common structure dictated by the input PDF. No consideration is given to the energetic state of the structures produced in this manner, which could be considered a weakness of the approach [5, 55, 61].

- Molecular dynamic simulations

Through the implementation of classical physics, these models simulate individual atoms as particles with given positions, trajectories and inter-atomic potentials (defined through modified Lennard-Jones potentials) [5]. Based on classical equations of motion and energy, the evolution of atomic structures are then predicted over small time intervals to produce new structures with atoms having new positions and trajectories [5].

- Quantum molecular dynamic simulations

Through the use of quantum theory, structures are produced through solutions to the Hamiltonian equation. The complexity however currently limits this method's application to structures with atoms whose electrons are in the ground state. In addition only very solute lean binary amorphous materials of 100 atoms have been confidently modelled in this way [5], with more complex structures requiring significant computational time.

2.2.4 Key structural features observed in BMGs

Based on experimental observations and computational simulations, structural features in amorphous materials have been identified which have successfully been related to a range of BMG properties. These features are identified as follows:

Free volume and short range order (Bernal packing clusters)

Free volume in BMGs is critical in identifying physical BMG properties and can be used as a state variable of the material. Free volume is characterised as the volume within a BMG that cannot be occupied by an atom. Different levels of free volume can be accommodated within BMG structures, which are described through Bernal's holes, shown in Fig.(2.8) [62]. These structures are derived through the dense random packing of hard spheres of equal/near equal sizes such that no long range order can be achieved by any of the structures, and the volume accommodated by any of the structures cannot be filled by atoms within the model. Tetrahedrally packed atoms have the lowest level of free volume and therefore the highest packing efficiency of all the clusters described. Therefore atoms prefer to cluster in this arrangement as it defines the lowest energy state of the system on a local scale.

Tetragonal packing of atoms is heavily featured in both crystalline and glassy structures. However, due to geometrical considerations, this packing regime cannot be accommodated over long distances (LRO). Therefore glass structures must contain a mixture of the 5 cluster types identified in Fig.(2.8) (in various distorted states) to produce a bulk glassy material. In fact, Bernal performed a macro-scale steel ball bearing experiment analogous to Argon's bubble raft experiment (discussed in Chap.(3)) and found that for the most relaxed mono-atomic amorphous structure, 73% of clustered atoms formed tetrahedral packing systems, 20.3% formed half octahedral clusters, and the rest of the structures were formed from the remaining structure types [62]. This has since been replicated in a number of DRPHS computer models [63, 64], and it has even been observed that these BMGs have a higher fraction of tetrahedral clusters than HCP or FCC structures, despite the lower density of BMG structures compared to crystalline materials. This is due to the fact that packing structures of 12 atoms can be described purely through linked tetrahedral structures and therefore can have a higher density than the crystalline materials over these volumes. However on larger scales, the lack of translational order of these clusters requires the need for other structural types with higher free volume fractions than the tetrahedral and the unit cells of FCC and HCP materials, making BMGs over bulk scale the less dense of the two material states [5]. By considering the packing of BMGs as a result of packing of tetrahedral structures, it can be seen how a common low energy state structural feature in BMGs is formed. Packing of tetrahedral clusters can be accommodated up until 12 atoms are packed closely together. This packing leaves a large portion of free volume that cannot quite accommodate a 13th atom. As such, the introduction of another atom either forces the atoms to rearrange to form a cluster representative of the HCP/FCC unit cell, or to redistribute the cluster evenly such that no single atom is in the low energy state of a perfect tetrahedra, but forms a slightly distorted tetrahedra. Such a cluster is known as an icosahedron, and it defines the first low energy structure that is common only to amorphous materials [5]. The structure is capable of forming more bonds, and has better rotational symmetry. Therefore this structure has been postulated to be the most common structure in liquids by Frank [65], and by extension a common feature in defining the free volume state in BMGs.

The introduction of icosahedra solves the atomic packing dilemma for a cooling liquid allowing the formation of a BMG. However further geometrical consideration reveals that even icosahedra suffer from the same packing frustration issue that was outlined for the tetrahedral atomic clusters. Therefore whilst (distorted) tetrahedral clusters identify SRO in BMGs and icosahedral clusters identify MRO in BMGs, a similar process regarding the distortion of MRO clusters to form LRO requires significant energy, and outlines the process of crystallisation. This identifies the point in the energetics and kinetics of a cooling MG system as to whether a stable glass is to be formed or not.

During the physical formation of a glass the energy of transforming a cluster of atoms from agitated tetrahedral to unit cells of FCC/HCP structure is far less than the energy required to transform clusters of icosahedra to bulk FCC/HCP structures. Therefore the icosahedral structures remain metastable, supported by what are termed broken icosahedra to accommodate any unoccupied space left by inefficient packing.

2.2.5 Structure models of BMGs

Modelling of BMG features and behaviours requires a basic level of understanding of how atoms or elements within the structure behave within the confines of the model. To that end, the key modelling approaches used to describe BMG structures and behaviours within them have been summarised as follows.

Dense Random Packing of Hard Spheres (DRPHS)

This self describing model identifies atoms within an atomic box simulation as densely and randomly packed atoms with no flexibility on the boundaries defining an atom's dimensions. This is a common approach used in simulations, often teamed up with the MD and RMC methodologies to simulate behaviours of BMGs [66].

It is noted that DRPHS has associated with it a certain degree of order. This is acceptable over short and medium ranges, however Torquato et al. has suggested that this is not the case and the inference of packing to the maximum density through a random approach ultimately leads to some degree of order over longer scales [67]. This has led to the introduction of the Maximum Jammed Random (MJR) state which puts emphasis on maintaining the random structure rather than density, unlike the DRPHS model which aims to maximise density through the random packing of atoms. Sheng and Ma have demonstrated that mono-atomic liquids follow this model better than the DRPHS model, indicating that whilst DRPHS is a good first approximation regarding BMG structures and behaviours, MRJ should be accommodated more in modelling approaches for a truer estimation of BMG structure and how they relate to material properties [68].

A modification to the DRPHS model could be described as the DRPSS (dense random packing of soft spheres). Here instead of using a hard limit to represent the interface of an atom's surface, inter-atomic potentials are utilised, whereby atomic radii are defined by minima in the potentials. A model set up to investigate structural behaviours through this method therefore uses the inter-atomic potentials to identify the lowest acceptable energy configuration such that maximum density structures can be identified without the hard limit of the atomic dimensions. This allows for more accurate modelling of metallically bonded materials through the summation of positive potentials of atoms being surrounded by the negative potential of electrons [5]. This approach is far more representative of a real metallic structure than that identified by the DRPHS model.

Different inter-atomic potentials have been utilised by a wide range of authors in efforts to model amorphous metals in this manner. The most notable examples of potentials include the Lennard-Jones, Morse and Dzugov potentials, all of which predict icosahedral clustering, and show that the energies of icosahedrally packed materials is lower than that of crystalline packed materials over localised scales, thereby providing the seed required for the formation of a glassy structure in the first instance [69–73].

Stereochemical modelling

Taking elements of the DRPHS model, Gaskell [74] proposed a model which at its core relies on the fact that short range order in BMG structures is chemically driven and therefore very similar

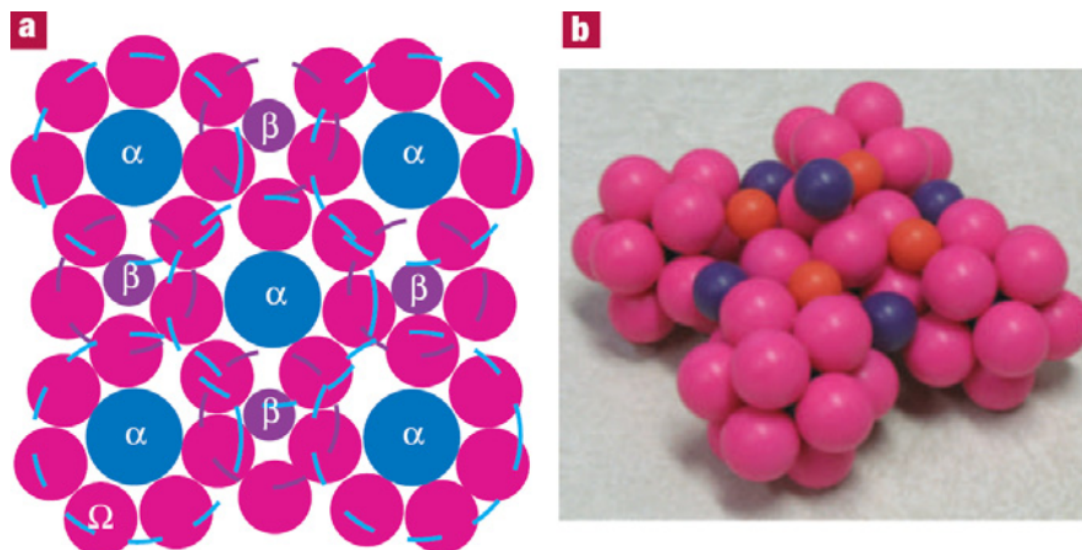


Figure 2.9: A figure demonstrating Miracle's approach of modelling BMG structures through the packing of amorphous SRO clusters into a FCC/HCP framework to provide a means to describe MRO (reproduced from [55]).

to that which exists in crystalline materials. It is only at MRO that significant differences between the two models arise. This model was applied to MG structures containing Ni-P, and predicted the presence of a tricapped trigonal pyramidal packing unit common in crystalline materials containing these elements (Ni_3P) was also present in BMGs. This agreed with results from neutron diffraction and EXFAS measurements, which provides further evidence that SRO in BMGs is similar to SRO in crystalline materials.

Efficient cluster packing model (ECP)

Unlike the dense packing models discussed up until now, work from Miracle provided the basis for what is now known as the Efficient Cluster Packing model (ECP) [55, 75]. This model attempts to accommodate MRO into the packing of atoms in a BMG structure, as opposed to the random placement models, which accommodate SRO only at best. The ECP model takes SRO atomic clusters (icosahedra, etc) and models them as spheres, which are then packed into an FCC or HCP packing framework such that dense packing is still achieved, but amorphicity is maintained. This allows the modelling of MRO clusters which are no more than a few SRO cluster diameters across, schematically represented in Fig.(2.9) [55].

In the model as used by Miracle, atomic sizes are the only criteria used for identifying MRO structures, with no considerations being given to chemical interactions beyond those involved with the formation of SRO clusters. As a consequence, the model uses the DRPHS approach in the formation of these MRO clusters, which whilst giving a good approximate starting point for the estimation of MRO, may introduce errors in the size, behaviour and even the form of MRO clusters. However, the framework set here provides the basis for other researchers to accommodate for factors such as chemical ordering over medium range order in future models.

Fractal packing

Accommodation of MRO is a significant weakness in the current methodologies for describing BMG structures. However Cheng et al. [76] have made a potential link between fractal behaviour and

SRO, MRO and possibly ‘long’ MRO. Through observations of PDFs, Chen noted that a power law applies between the position of the first peak of neutron and X-ray diffraction data for a range of MGs. They found through plotting the positions of the first sharp diffraction peaks scaled with the atomic volume of any give MG, with a fractal dimension of 2.31, indicative of fractal behaviour [76]. This is supported by observations from previous works which observed fractal behaviour in super-ionic glasses [77]. There are discrepancies between the fit and observations, indicating that there are other factors within BMG structures to be accounted for, however the use of Fractal mathematics to describe BMG structures is a powerful tool that could be used to predict BMG structures that have yet to be formed, or to investigate issues surrounding poor GFA for some amorphous compositions.

Tight bond cluster model (TBCM)

One of the first models to accommodate deformation with their descriptions of BMG atomic structure, Fan et al. [66,78] conceived the TBCM based on the idea that SRO clusters are infallible. Therefore deformation and free volume are processes and parameters that are accommodated between these SRO clusters and not within them. In the case of shear deformation, strain is accommodated through the rotation of SRO clusters which are loosely bound together compared to that atoms that make them up.

Core shell model

Described in detail in Chap.(3), the Core-shell model is the first model providing experimental evidence for the presence of shear transformation zones in BMGs. Reported by Ye et al. [79], observations of mechanical hysteresis were linked to the presence of free volume in nano-pillars of BMGs acting as bubbles of viscous fluid encased in a ‘springy’ shell, describing a Kelvin spring and dash-pot response. These bubbles have been likened to the structures required for the formation of a STZ, though difficulties surrounding in-situ observations means direct evidence for this is yet to be presented.

Structures of multicomponent systems

Thus far, considerations have been given to the structural state of mono-atomic liquid/glass structures for ease of explanation and modelling purposes. However as stated from Inoue’s empirical laws, BMGs are multicomponent alloys, whose structures are likely to show marked differences to those calculated for mono-atomic systems. To that end, to understand the factors affecting glass formation and mechanical behaviours, an understanding of how these structures are affected by a multicomponent array of atoms must be addressed.

In the case of multicomponent amorphous materials, the tetrahedra formed from the constituent atoms have a range of bond lengths which produce distorted tetrahedra. These distortions can be orientated in such a way that the packing frustration experienced in the mono-atomic modelling approach is alleviated or even eliminated, allowing for long range ordered structures, *disinclinations*, a rotational symmetry defect in icosahedra analogous to the dislocation imperfections in crystalline materials [80,81]. BMG structure that can be described as a polytetrahedrally packed structure with a low number of disinclinations is a structure are the most stable and strongest glass formers. The number of disinclinations, just like dislocations, in BMGs structures can be reduced through annealing processes or increased through other thermomechanical processes [5].

| Base metal | Binary pair | example BMG systems |
|------------|-------------|---|
| LTM | LTM+NM | Ni-P/ Pd-Si/ Au-Si-Ge/ Pd-Ni-Cu-P/ Fe-Cr-Mo-P-C-B |
| ETM or LTM | ETM+LTM | Zr-Cu/ Zr-Ni/ Ti-Ni/ Zr-Cu-Ni-Al/ Zr-Ti-Cu-Ni-Be |
| SM or RE | SM+RE | Al-La/ Ce-Al/ Al-La-Ni-Co/ La-(Al,Ga)-Cu-N |
| AM | AM+LTM | Mg-Cu/ Ca-Mg-Zn/ Ca-Mg-Cu |

Table 2.1: Table highlighting a simplified classification system of BMGs from which future work can refer back to (adapted from [5]). The abbreviations classifying different element types are: AM (alkaline metals), SM (simple metals), ETM (early transition metals), LTM (late transition metals) and RE (rare earths).

2.3 Classification of BMGs

Classification of BMGs is commonly done through chemical composition, however other works have classified BMGs with respect to their physical properties. Key approaches in this endeavour have been highlighted as follows:

2.3.1 Chemical classification

Efforts have been made to classify BMGs in terms of chemical composition, the earliest of which focused on the dominant element that makes up a BMG [5]. However, this was quickly found to be unsatisfactory due to the variability of behaviours and performances of BMGs in any given category of this type. More intricate classification methods evolved with time, with focus turning to the nature of the inter-atomic bonding and the constituent elements that populate a given BMG structure. The advent of Inoue's empirical rules for BMG formation saw the rise of a sophisticated chemical bonding-based classification system from Takeuchi and Inoue [23, 82], which not only classifies a given BMG, but aids in the prediction of further BMG compositions. This classification system consists of 7 key classification groups that describe all BMGs. A simplified version introduced by Cheng and Ma based on pairing a main alloying element with a strong glass forming binary system, and is outlined in Tab.(2.1) [5].

2.3.2 Electromagnetic property classification

Classification of BMGs through electromagnetic properties has been effectively summarised by Mizutani [83], who characterised BMG behaviours based on their Curie temperature, the nature of the conduction electrons (i.e. the ones at the Fermi surface) and their magnetic behaviour. Fig.(2.10), taken from Mizutani's work, outlines the 5 BMG groups that make up this classification methodology.

2.3.3 Mechanical classification

It has been observed by a multitude of authors [36, 84–87], and covered extensively in review articles [4–6] that plasticity of BMGs is dependent on the elastic behaviour of materials. BMGs that exhibit a high Poisson's ratio or a low Pugh's ratio appear to have a greater tendency for plasticity through the formation for multiple shear bands (covered in detail in Chap.(3)). Therefore there is a basis for characterising BMG materials in terms of their mechanical behaviour, a useful tool when attempting to design a BMG for mechanical applications.

| group | I ferromagnetism | II weak ferromagnetism | III spin-glass or Kondo state | IV paramagnetism | | V weak paramagnetism or diamagnetism |
|---------------------------------|------------------------------------|--------------------------------------|--|---|--|--|
| characteristic features | Curie temperature $T_C > 300$ K | Curie temperature $T_C \ll 300$ K | presence of the spin freezing temperature (spin-glass) Curie-Weiss-type temperature dependence of magnetic susceptibility (Kondo state) | $\chi \approx 10^{-4}/\text{mol}$ temperature dependence of the Pauli paramagnetism $\gamma > 3$ mJ/mol·K ² | $\chi \approx 10^{-5}/\text{mol}$ negligible temperature dependence of magnetic susceptibility $1.5 < \gamma < 3$ mJ/mol·K ² | $\chi < 10^{-6}/\text{mol}$ negligible temperature dependence of magnetic susceptibility $\gamma < 1.5$ mJ/mol·K ² |
| main carrier at the Fermi level | d electrons | d electrons | d electrons or (sp + d) electrons | d electrons | (sp + d) electrons | sp electrons |
| typical amorphous alloys | Fe-Co-Zr Co-B Fe-Co-B-Si | Fe-Zr Fe-Hf | Pd-Si-Mn Fe-Mn-B-Si Co-Mn-B-Si | Cu-Zr Cu-Ti Ni-Zr Y-Al La-Al | Ca-Al Ca-Mg Ni-P Mo-Ru-P | Mg-Zn-Ga Ag-Cu-Mg Ag-Cu-Ge Mg-Cu |

Figure 2.10: Classification of BMGs based on the charge carrier and magnetic behaviours (reproduced from [83]).

Previous attempts have been made to characterise crystalline metallic materials through such a methodology. Work from Brown and Ashby [88] and Frost and Ashby [33] first attempted this through normalising the data for materials such that both obvious and subtle trends in physical behaviours could be observed independently (or at least quasi-independently) from material structure and bonding [17]. Whilst Brown and Ashby successfully applied the method to identify classes of semiconductor [88], Frost and Ashby applied the method to the mechanical behaviour of materials and identified a relationship between elastic moduli and T_m [33] through:

$$M = \frac{Bk_bT_m}{\Omega} \quad (2.12)$$

where M is a given modulus value, and Ω is the atomic volume and B is a constant. When this was applied to materials, it was found that low values of B (≈ 20) corresponded to ductile materials, whilst higher values of B (≈ 95) corresponded to brittle materials [17]. Based on this, the parameter B could be used to identify different isomechanical groups of materials. Plummer [17] took this idea further and applied the method to BMG materials with the aim of identifying proportionality between shear and Young's modulus from which intrinsic toughness of BMGs could be found. As reports indicate that high Poisson's ratio BMGs have greater toughness [36], this parameter was used to identify different classes of BMG materials. It was found that despite BMGs all being described through the same SRO cluster modelling approach, that a range of isomechanical groups arises, indicating that BMGs must demonstrate differences in their atomic packing and bonding characteristics [17]. Further investigations into the data revealed that BMGs with high ν values when plotted on a Blackmann Diagram (diagram that plots the ratios of the elastic constants C_{12}/C_{11} against C_{44}/C_{11}), outlined in Fig.(2.11), produced a large deviation from the Cauchy pressure (arises from forces acting on a central atom within a structure that do not equate, best surmised through $C_{12} = C_{44}$), indicating low directionality of metallic bonding in a given BMG structure. However upon considering the elements involved with the ductile metallic glasses, metal-metalloid bonding appears to be a strong feature which produces highly directional bonds and is therefore at odds with what is being observed. Plummer, amongst others [66] therefore suggest that SRO in BMGs is not what governs the mechanical behaviour of these materials, rather the bonding between atomic clusters, as suggested by the tight cluster model outlined earlier. By

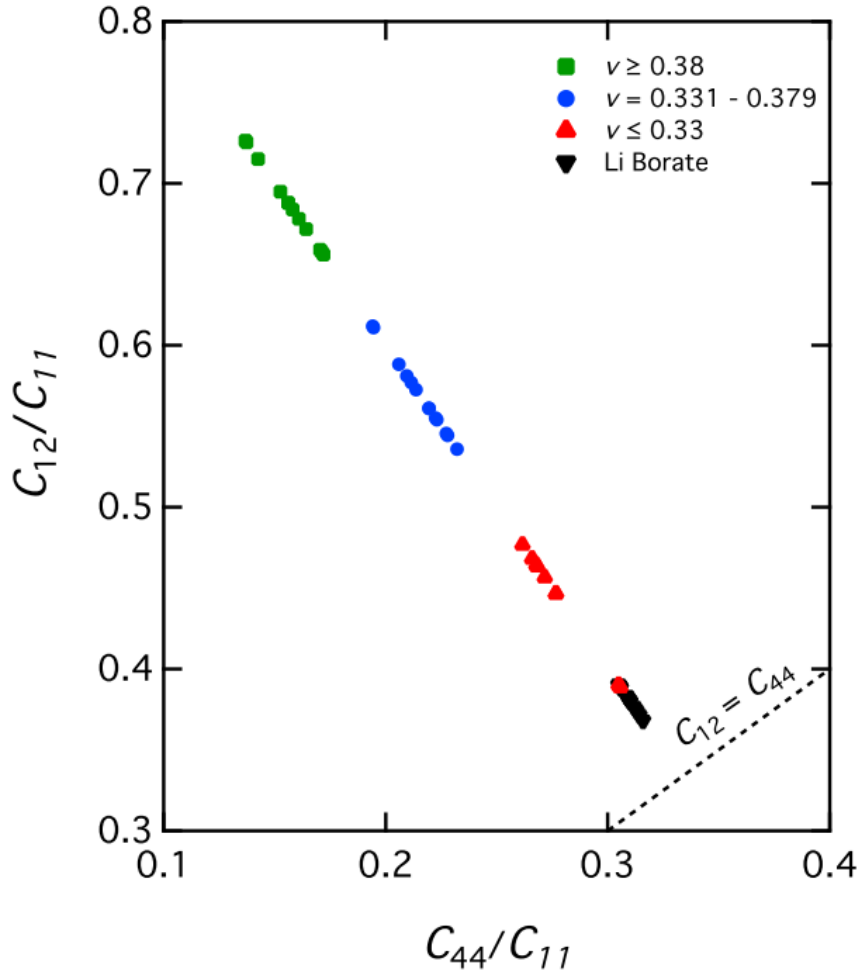


Figure 2.11: Blackmann Diagram demonstrating how differences in Cauchy pressure correlates with Poisson's ratio for a range of BMGs (reproduced from [17]).

considering this, with the high electron density and non directionality of atomic bonding between the dominant elements in the BMGs that make up the ductile alloys, it is suggested that although directional bonding exists in these materials from elements that are essential for the formation of a glassy structure, the non directional bonding of the dominant elements between atomic clusters accommodates the plasticity observed in these materials [17].

Chapter 3

Selected BMG properties

Properties of importance for this work include those relates to electrical and mechanical behaviour and these will be discussed here.

3.1 Electrical properties

Broadly speaking, conduction behaviour of BMGs reflects the conduction behaviour of most metals, exhibiting low resistivity compared to divalent materials. However upon closer inspection, the conductivity in BMGs shows unique characteristics that are not reflected in crystalline metals. In fact BMG conductivity appears to have more in common with liquid metals, as shown in Fig.(3.1) [83,89]. The differences in behaviours between glassy and crystalline materials are observed as the following:

- Standard resistivity values of amorphous alloys range from 5 to 100 times greater than their crystalline counterparts, but are comparable to the values of resistivity of the supercooled liquid state.
- Resistivity of amorphous alloys and liquids are only weakly dependent on temperature (above cryogenic temperatures [90]), unlike the crystalline case.
- The temperature coefficient of resistance (α_Ω) for liquid and amorphous alloys can be either positive, negative or close to zero depending on the composition of the metallic glass being considered. Crystalline metals however always have a positive α_Ω , providing the alloy does not have semiconductor properties (e.g. silicon rich alloys).

The mechanisms behind electrical conduction in amorphous metals are highly complex due to the lack of LRO. Without a crystalline structure, the standard practice of using Brillouin zones to determine the repeatable scattering behaviour of electrons passing through a material cannot be utilised as the momentum of scattering in a pseudo random matrix is not conserved in such a way that the process can be made up of repeatable units [83]. This being said, approaches to identifying conduction behaviour in liquid structures have been found to be broadly applicable to amorphous materials [83,91]. To that end, we present the basis of the two main electron transport theories used in describing conduction behaviours in BMGs.

3.1.1 Drude model

The Drude model represents a classical approach to electron transport theory, which determines the conductivity of a material based on the frequency and severity of scattering of charge carriers

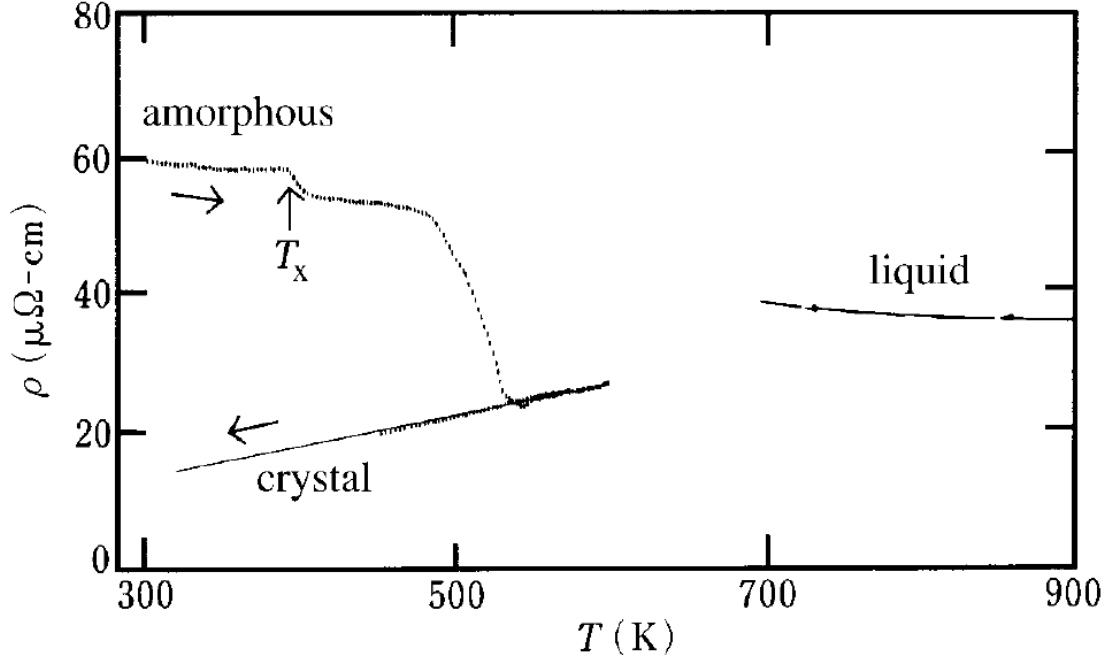


Figure 3.1: The resistivity behaviour of the composition $\text{Mg}_{70}\text{Zn}_{30}$ in its amorphous, liquid and crystalline states demonstrating the differences in absolute values and temperature dependencies of resistivity (reproduced from [83]).

placed in an electric field by phonons or impurity atoms in a material through a ‘billiard-ball’ style analysis [92]. This is defined as

$$m \left(\frac{d\mathbf{v}_D}{dt} + \frac{\mathbf{v}_D}{\tau} \right) = (-e)\mathbf{E}, (c.f. \mathbf{F} = m\mathbf{a}) \quad (3.1)$$

where

$$\mathbf{v}_D = \frac{\sum_{i=1}^n \mathbf{v}_i}{n} \quad (3.2)$$

Eq.(3.1) is comprised of an acceleration term $\frac{d\mathbf{v}_D}{dt}$ due to the applied field, and a scattering term $\frac{\mathbf{v}_D}{\tau}$. τ in the scattering term defines the relaxation time such that when the steady state current is achieved, if the field is switched off, then:

$$m \left(\frac{d\mathbf{v}_D}{dt} + \frac{\mathbf{v}_D}{\tau} \right) = 0 \quad (3.3)$$

$$\frac{d\mathbf{v}_D}{dt} = -\frac{\mathbf{v}_D}{\tau} \quad (3.4)$$

$$\mathbf{v}_D = \mathbf{v}_D(0) \exp\left(-\frac{t}{\tau}\right) \quad (3.5)$$

When steady state in the system has been reached, $\frac{d\mathbf{v}_D}{dt} \rightarrow 0$:

$$\mathbf{v}_D = \frac{(-e)\mathbf{E}\tau}{m} \quad (3.6)$$

By substituting into the electrical current density, $J = n(-e)v_D$,

$$\mathbf{J} = \left(\frac{ne^2\tau}{m} \right) \mathbf{E} \quad (3.7)$$

This can then be rearranged into an electrical conductivity formulae by assuming that the metal is isotropic:

$$\sigma = \frac{\mathbf{J}}{\mathbf{E}} = \left(\frac{ne^2\tau}{m} \right) \quad (3.8)$$

$$\rho = \frac{1}{\sigma} = \left(\frac{m}{ne^2\tau} \right) \quad (3.9)$$

This classical approach is good for a conceptual understanding of conduction in a metal, however the approach does not take account the Fermi surface or its interactions with the distribution of other electrons within the material, and so a more accurate approach is required. This gave rise to the Ziman theory.

3.1.2 Ziman theory

The Ziman theory is based on the free electron model of metals, which states that electrons that facilitate charge flow within a metal are not bound to any given atom [83]. Using this model, Ziman [83, 93] produced a theory that could predict the resistivity of liquid metals, which due to structural similarities, has been extended to glasses relatively successfully. Ziman theory is based on three assumptions [48]:

- Conduction electron kinetics are described by the Boltzmann equation:

This implies that the mean free path of conduction electrons must be greater than the inter-atomic distance within the structure, which limits the application of the theory to materials with large inter-atomic spacings.

- Conduction electrons interact with metallic ions through a pseudo-potential generated by the ion:

This is an accurate approximation to some BMGs such as the electrically classified group V BMGs (Sec.(2.3.2)).

- Conduction electrons are almost free from the metallic matrix, with the only binding factor being that of the sum of the psuedo-potentials produced by the metal ions:

This assumption indicates that elastic scattering is the dominant scattering effect on charge carriers

The result of this theory is an equation that can describe the resistivity state of the material:

$$\rho = \frac{3\pi\Omega}{4e^2\hbar v_f^2 k_f^4} \int_0^{2k_f} a(K)|U(K)|^2 K^3 dK \quad (3.10)$$

where Ω , v_f , k_f , $a(K)$, $U(K)$ are the atomic volume, Fermi velocity, Fermi radius, the PDF and the pseudo-potential respectively in wave space (K space). Use of this equation has been shown to replicate experimental results of group 1 periodic table metals the best, in particular Na and K, however other elements with strong metallic bonding characteristics, and some BMGs also agree well [83].

In the case of BMGs, the assumption of elastic scattering of electrons fails, resulting in the need to accommodate inelastic electron-phonon interactions. Baym-Miesel-Cote theory takes this into account, which still has the Ziman theory at its core, however Eq.(3.10) now takes into account the inelastic electron-phonon interactions through the substitution of the simplistic $a(K)$ with a frequency dependent structure factor:

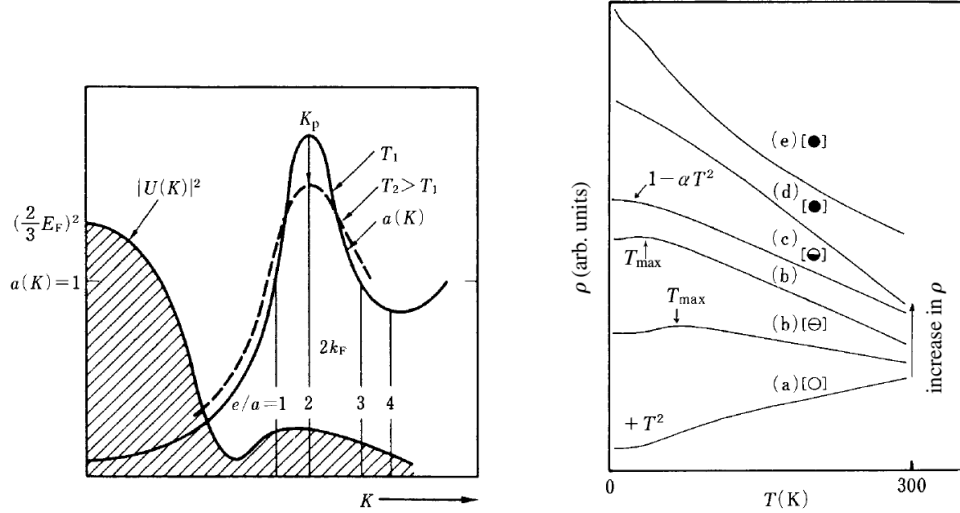
$$\rho = \frac{3\pi\Omega}{4e^2\hbar v_f^2 k_f^4} \int_0^{2k_f} \left[\int_{-\infty}^{\infty} \frac{(\hbar\omega/k_bT)}{\exp(\hbar\omega/k_bT) - 1} a(K, \omega) d\omega \right] |U(K)|^2 K^3 dK \quad (3.11)$$

It is noted that in high temperature conditions (where $T > \theta_D$), Eq.(3.11) reduces to Eq.(3.10), indicating that so long as the temperature of a BMG being tested is greater than the Debye temperature, Eq.(3.10) is a satisfactory equation to use to predict electrical conductivity [48,83,90].

The Ziman theory has proven to be a powerful theory for the description of BMG conductivity behaviour, which even accommodates for the negative values of α_Ω , common in many BMGs as shown in Fig.(3.1) and a feature usually associated with semiconductor materials. By substituting higher temperature values into Eq.(3.10), the resistivity ‘spectra’ predicted by Eq.(3.10) broadens to produce the dashed line in Fig.(3.2a). In the cases whereby the valency of a BMG (e/a)=1 or 3, an increase in the resistivity of the material is observed with increasing temperature, mirroring the behaviour commonly observed in standard crystalline metals. However for BMGs with an $e/a = 2$, resistivity is observed to decrease with temperature, which is seen to maximum effect when $2k = K_p$ [83]. The criteria of $2k/K_p = 1$ is a frequently criteria utilised by researchers to determine the general resistivity behaviour of melts and amorphous materials to gain an estimate on not only the direction, but the magnitude of the resistivity dependence on temperature [83,89,90].

In addition to electron valency, Eq.(3.10) predicts that resistivity is dependent on structure ($a(K)$). Bai et al. showed this through an in-depth study on the low temperature dependence of resistivity of BMGs from 4.2K-293K on BMGs annealed for 2 hours over a range of temperatures [90]. Bai found that different annealing treatments produced different resistivity behaviours with respect to test temperature. For example glasses annealed to temperatures less than T_g showed a generic decrease resistivity with increasing temperature, in contrast to that observed classically. However on increasing the temperature of their BMG to between T_g and T_x , they observed a marked change in the resistivity response such that the temperature dependence actually changed sign to give a positive resistivity dependence on temperature. In addition, annealing treatments at temperatures closer to T_x , gave a stronger resistivity-temperature dependence than those closer to T_g . This confirms the results derived from Eq.(3.10), whereby resistivity is observed to depend on the structural changes of BMGs ($a(K)$) as well as other factors such as valency.

Despite the success of the Ziman theory in its raw form, it is noted that the theory only accurately portrays resistivity behaviours for specific BMGs as the theory neglects other resistivity affecting factors. Contributions to the theory put forward by Anderson [94] (localisation theory) and Mott [95] (Mott’s scattering) aids the application to a wider array of BMGs, however the complexity of the describing conduction behaviour through a pseudo-random structure means that conductivity of BMGs can never be modelled to the same accuracy as that for the well defined and understood crystalline materials. As such the Ziman theory (plus modifications) remains to this day the best theory for linking structural characteristics of BMGs to resistivity. It is interesting to note that whilst both mechanical and electrical behaviours are reported to link to BMG structure [83,90,91,96], little effort has been made to directly link mechanical properties to electrical properties. This idea is explored in full in Chap.(7).



(a) Wave number dependence of $U(K)$ and $a(K)$ indicating showing how structure and valency can affect the resistivity behaviour of a BMG (determined through Eq.(3.10)). (b) Examples of different α_Ω values for different amorphous alloys.

Figure 3.2: Plots showing how temperature dependence of resistivity for BMGs is derived from Eq.(3.10) (reproduced from [83]).

3.2 Mechanical properties of BMGs

The mechanical behaviour of BMGs differs from that of crystalline metals (due to their lack of long range order in the atomic structure which removes defects such as those that govern plastic yield in crystalline materials) and from covalent glasses (due to the metallic bonding which minimises the directionality allowing for more freedom in MRO and the accommodation of strains on local scales without the need for charge imbalances [4]). This unique combination of structure and bonding yields a material capable of accommodating high stresses in the elastic regime amongst other interesting and favourable properties. However due to the complexities and uncertainties regarding amorphous structures outlined in Chap.(2), understanding and improving these properties is still a highly active field of research, with many theories and predictions still falling short of successfully describing observed mechanical behaviours. To that end, this section aims to provide an overview of the mechanical behaviours of BMGs, the current state of understanding of these behaviours, the methods with which these behaviours are assessed and the key factors known to affect these behaviours whether they are well understood or not.

Tab.(3.1) compares the key mechanical properties of BMGs to crystalline materials. Properties such as Bulk and Elastic modulus are comparable for both material states as these properties are fundamentally based on inter-atomic bonding. Differences in the mechanical behaviours such as plasticity and elastic strain arise from the micro/meso-structure [33]. This accounts for the variability in yield, the elastic limit, shear modulus and even the Poisson's ratio of these the materials.

To understand the factors affecting mechanical properties outlined in Tab(3.1), an understanding of the current state of deformation theory in BMGs is required.

3.2.1 Microscopic mechanisms behind BMG deformation

Understanding the mechanisms responsible for BMG mechanical behaviours is a challenge for a material whose atomic structure is seemingly featureless in contrast with polycrystalline materials.

| Property | Compared to the crystalline case | Causing factor |
|---------------------------|--|---|
| Shear and Elastic modulus | $\lesssim 30\%$ difference | As shear modulus deals with shape change of a material, the lower values are believed to be due to the presence of shear transformation zones, which provide a reversible plastic accommodation of strain, compared to the reversible elastic accommodation of strain of crystalline materials [4]. This means that BMGs can accommodate more elastic shear deformation for a given load. |
| Bulk modulus | $\lesssim 6\%$ difference | These parameters are derived through the inter-atomic bonds which are of the same nature regardless of the crystalline or amorphous nature. The small discrepancy in the values stems from the density of BMGs being generally slightly less than that of their crystalline counterparts, reducing bond strength and density. |
| Yield strength | Approaches theoretical limit in some cases | Without a dislocation mechanism present to weaken the BMG structure, bonds cannot be broken and reformed easily, so high stress can be supported. |
| Elastic strain | up to 2% | The same mechanism that gives high yield strength and low shear modulus leads to high levels of elastic strain prior to yield. |
| Poisson's ratio | 0.3-0.4 | Metallic glasses tend to exhibit roughly isotropic deformation behaviours due to the disordered nature of the structure providing no net preference for a particular direction of deformation. However, as discussed later, mechanical isotropy can be induced into BMGs through thermomechanical processing in the supposedly elastic regime. |
| Elastic response | visco-elastic | Unlike crystalline materials, BMGs have a viscous component to their deformation behaviour in addition to the elastic response, which originates from free volume rich regions that can be approximated to pockets of liquid in the atomic structure. This means that under high strain-rate cyclic loading, mechanical hysteresis loops are observed in BMGs, as demonstrated by Ye et al. [79]. |

Table 3.1: Basic outline of mechanical properties of BMGs compared to their crystalline counterparts.

However literature time and again reports mechanical property dependencies of factors such as thermomechanical processing history [56,97], which indicates that deformation of these materials is reliant on structural features that can be changed through certain treatments. Many authors have suggested that this feature is free volume, which can be used as a state variable to give a description of deformation behaviour of BMGs [56,97], whilst others suggest that other factors such as the exact changes in atomic packing must also be considered [98].

A lack of LRO in BMGs has led mechanical behaviour theories to be based on the summed effect of multiple localised flow events (which can be described by a single flow mechanism) that contribute to the bulk deformation behaviour of the material [4,99]. This flow mechanism has been postulated to follow one of two key mechanisms; the Shear Transformation Zones (STZs) model and the Free Volume model [4]. A good qualitative understanding of these models is useful for highlighting the issues surrounding the uncertainties in macroscopic deformation of BMGs, especially concerning how local atomic processes evolve to from macroscopic BMG deformation behaviours and features.

Shear Transformations Zone (STZ) Mechanism

First postulated by Becker and Orowan [100] and confirmed by an analogous bubble raft experiment performed by Argon [101], STZs can be described as flow defects or local inelastic shear strain transitions [4]. STZs are made up of clusters of atoms packed with a high fraction of free volume which are able to accommodate a shear strain through a small rearrangement of atoms within the cluster, moving the atomic cluster from one entropic configuration to another [101]. It is important to state that STZs, whilst being constructed of clusters of atoms, cannot be identified as a structural feature within the metallic glass matrix prior to its activation. This makes assessing the mechanical performance of a BMG difficult, as direct observations of STZs cannot be made in order to link the mechanical behaviour of a BMG to the density of potential STZs in a BMG structure for example (i.e. the presence of free volume does not necessarily mean the presence of an STZ) [41].

Argon was the first to produce an experiment to show how STZs behave in BMGs undergoing deformation through a proof of concept experiment constructed from a 2 dimensional raft of soap bubbles [101]. It was found that the attractive potential of the bubbles due to the free energy of the bubble surface approximated that of actual MGs, and also produced normalised pair distribution functions, which compared well to the normalised pair distribution functions of real BMGs [101]. Observations made regarding bubble motion when deformation of the bubble raft was performed revealed 2 kinds of localised flow event that have since been accepted as common place in MG structures (despite the 2D nature of the experiment) [101]; a sudden slip of closely packed bubbles in a ‘dislocation-like’ manner, and a more subtle complex rearrangement of bubbles surrounded by an equiaxed ring of closely packed bubbles in regions of high free volume. Argon also linked this bimodal observation to processes in real metallic glasses, with the disk shaped sudden dislocation like events occurring at low temperatures ($0 \leq T \leq 0.6T_g$), and the more subtle equiaxed events occurring at high temperatures ($0.6T_g \leq T \leq T_g$) [102].

A final observation surrounding Argon’s experiment was made regarding the free volume state of the bubble raft in that free volume had to be generated, even if only temporarily, in order to facilitate either of the shear transformation modes [101]. This is a factor that has later come to feature as the main potential cause for inhomogeneous deformation-induced catastrophic failure in these materials. Therefore, whilst the experiment acknowledges the shortfalls of comparing bubbles to atoms in an amorphous structure, many of the observations made within the study are

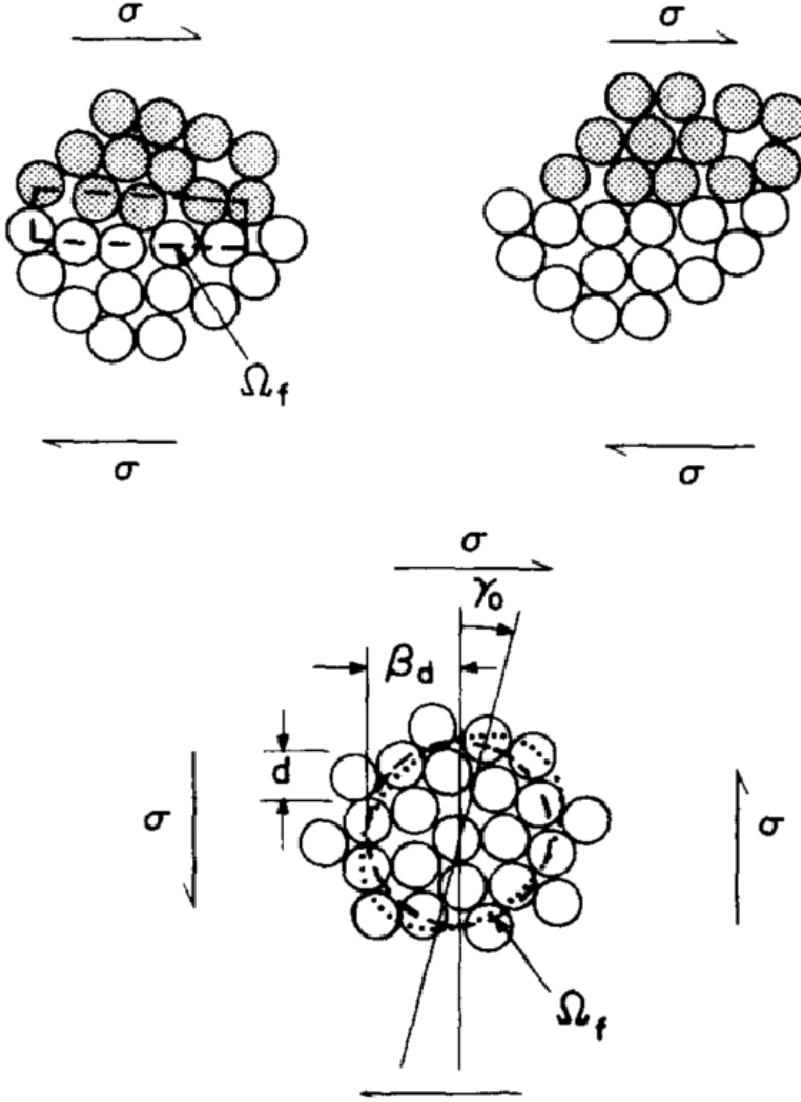


Figure 3.3: Schematic representations of the 2 different bubble arrangement behaviours observed in Argon's bubble raft experiment (reproduced from [101]).

still held to be valid phenomena, making this study a fundamental turning point in understanding the mechanical behaviour of BMGs.

Since STZs from Argon's work appear to be integral to the mechanical behaviour of BMGs, it is of key importance to understand the energies and behaviours of STZs. To that end, Argon himself took his work further and deduced that the free energy required for the activation of an STZ can be determined through Eq.(3.12) by modelling the BMG structure as an elastic medium populated with Eshelby inclusions (elastic inclusions with a different compliance to that of the surrounding elastic matrix).

$$\Delta Q_{STZ} = \left[\frac{7-5\nu}{30(1-\nu)} + \frac{2(1+\nu)}{9(1-\nu)} \beta_\nu^2 + \frac{1}{2\gamma_o} \cdot \frac{\tau_o}{G(T)} \right] \cdot G(T) \cdot \gamma_o^2 \cdot \Omega_o \quad (3.12)$$

Subsequent to Argon's initial work, computational simulations regarding STZs use this equation and have estimated that the free energy for STZ activation is $\approx 1-5\text{eV}$ ($20-120k_bT_g$) depending on

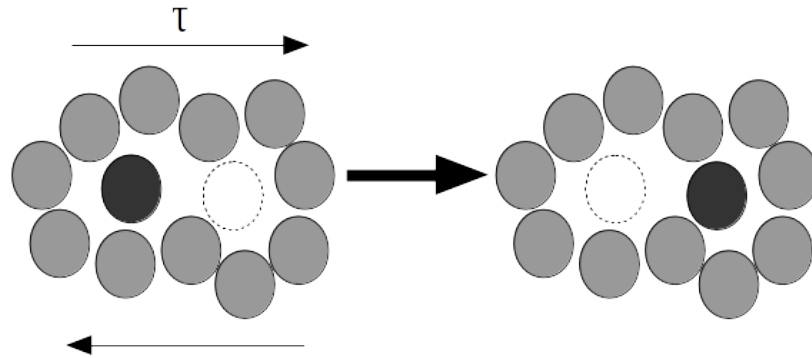


Figure 3.4: Schematic representation of the atomic jump mechanism from the free volume model.

the glass considered [4]. This value is dependent on the free volume component of a BMG as well as the chemical and topological short range order [103]. In addition, STZs have been shown to have a critical size of approximately 100 atoms [103], with actual sizes, structure and activation energies that are statistically distributed around a given value which differs for different glasses [4].

Free volume model

Developed by Turnbull and co-workers [104] and applied to BMGs by Spaepen [105], the free volume model is based on a diffusion controlled atomic jump mechanism that relies on the soft sphere approximation (outlined in Chap.(2)) to allow atoms within the metallic glasses matrix to move through gaps between atoms to high free volume sites that would otherwise be impossible to fill. These jumps are considered to occur uniformly throughout the MG material at any given time with a frequency determined by the structural and thermal state of the material [4]. When the MG structure is in a stressed state, a preference for a net atomic jumping direction arises due to the stressed state of the material in a particular direction. Whilst it can be envisaged how a normal stress state/ structural pressure gradient could potentially influence atomic motion through this model, the effect of a deviatoric stress in a singular defined atomic jump compared to the subtle rearrangement of a cluster of atoms in the STZ case is unclear [4]. However the simplicity of defining deformation through single atomic jump events provides a means to describe deformation through a single free volume state variable, which allows for further development of laws governing mechanical behaviour based on the creation and annihilation of free volume through a simplistic mechanism. The activation energies required to engage such a deformation mechanism have been estimated to reside at the lower end of that defined for the STZ model; $15-25k_bT_g$ [4,105].

Free volume vs. Shear transformation zones

Despite the significant differences between atomic ‘re-shuffle’ STZ model and the singularly-defined diffusion-controlled free volume model, both approaches may yield behaviours that are common to both mechanisms. Both models rely on discrete jump-like processes that are fully reversible [4], which has implications regarding the flow behaviour as well as the elastic/anelastic behaviour of the material (discussed later). In addition both models operate over similar activation energies, are

highly temperature dependent and have the capacity to accommodate both localised and homogeneous plastic flow, meaning, unlike for crystalline materials, the entirety of macro-scale mechanical deformation behaviours under all temperature and strain rate conditions can be accommodated through either of these mechanisms [4].

Beyond these similarities, differences in behaviours implied by each mechanism become apparent in the details surrounding how they relate to macroscopic mechanical observations and processes [4]. For example, the free volume model is expected to have a full range of energies and volumes associated with each atomic jump performed due to the local variability that exists in metallic glass structures [101]. This is also partly true for STZs for the same reason, however there is significant evidence that STZs have a maximum critical size that appears to be universal across all BMGs (≈ 100 atoms neglecting some small statistical variability) [103]. This has significant implications regarding the macroscopic deformation of BMGs. If STZs are the dominant deformation mechanism, then a defined number of STZs need to be nucleated in order to accommodate a given amount of shear strain. As individual STZ activations generate a certain amount of free volume, then there is the potential for a universal level of shear strain that can be accommodated for all BMGs prior to plastic yield (discussed later) [4]. This appears to be the case, with observations of Johnson and Samwer dictating a universal shear strain can be accommodated by BMGs prior to plastic yield [41], and is described by:

$$\tau_c = \gamma_c G \text{ where } \gamma_c = 0.0267 \pm 0.0020 \quad (3.13)$$

Other microscopic model approaches

There have been several attempts to model plastic flow in BMGs through dislocation theory based on the fact that the specific definition of a dislocation is described as regions of material shearing relative to each other. Therefore typical descriptions of dislocations, which usually involve defects in a periodic lattice, are not absolutely necessary for describing the presence of a dislocation in BMG structures [6]. This is supported by the idea that shear bands (a manifestation of localised unstable plastic flow, discussed later) have a stress concentration associated with the shear band front, which reduces the viscosity of the local material allowing for further propagation of the shear band in a way that is similar to that observed for dislocations in crystalline metals [106].

Cargill was the first to use the literal description of dislocations to characterise inhomogeneous localised deformation (i.e. shear banding) in materials as an analogy tool in order to extrapolate macroscopic plastic behaviours from the STZ process [107]. Evidence supporting the use of this idea was reported by Boborov and Khonik through observations of internal friction amplitude and temperature dependencies, as well as observations of work hardening of preloaded BMGs producing behaviours similar to those observed in crystalline materials, thereby indicating indirectly a dislocation-like behaviour is (at least if treated in a particular way [108]).

There are however issues surrounding the use of a dislocation-based model to describe deformation behaviour in BMGs, chief among which is the lack of work hardening behaviour in the material during deformation. Despite the claims made in Boborov and Khoniks work, it is widely recognised that BMGs work soften rather than work harden during deformation, with work hardening effects in BMGs only being observed in BMG structures which have crystalline phases within them [4]. In addition, tests performed through nano-indentation, show significant deviation of the hardness values obtained for crystalline materials from their bulk hardness behaviour compared to the difference observed in metallic glass macro and nano-hardness. It is known that crystalline materials, when deformed over very small scales, tend to show an uncharacteristic increase in strength due to an effect known as dislocation starvation, whereby the nearest dislocations capable of accom-

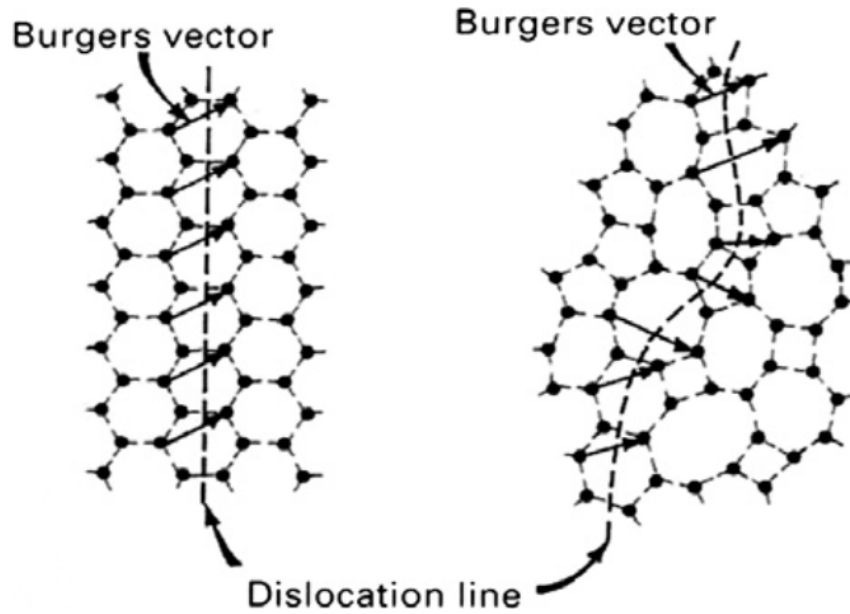


Figure 3.5: Schematic representation how a dislocation would be interpreted in a BMG structure compared to that of a crystalline structure (adapted from [6]).

modating plastic deformation are outside of the stress field imparted by the nano-indenter. In the case of BMGs, hardness values are reported to follow a rule of mixtures behaviour for the most part, which indicates that dislocation like behaviour cannot accommodate for this observation [4].

One of the biggest issues surrounding a full understanding of the deformation behaviour of BMGs is the lack of a robust mechanism that links nano-scale processes, such as STZs, to macro-scale deformation phenomena, such as shear bands (discussed below) [109]. To that end, a lot of research has been performed in order to understand these linkages better. The following outlines the key advances made in understanding this field, and the areas which require further work.

3.2.2 Elastic behaviour

Elastic behaviour of crystalline metals stems from the stretching and distortion of bonds in a reversible manner in order to accommodate strain [4]. This also must occur in BMG structures to some extent as the nature of the bonding in both materials are the same. However, unlike the crystalline materials, BMG structures have a wide range of inter-atomic bonding energies due to the lack of LRO. As such, the elastic nature of these materials harbours an extra level of complexity, as both the inter-atomic potentials over SRO and MRO needs to be accounted for. To that end, we highlight some of the key behaviours and studies into the elastic behaviour of BMG materials. BMGs have comparable elastic moduli to crystalline materials (Tab.(3.1)). Bulk moduli are $\approx 6\%$ less than crystalline materials, which has been calculated to be due to the reduced density of the material weakening the inter-atomic potential energy between atoms [110]. However elastic and shear moduli are $\approx 30\%$ less than crystalline materials, and therefore cannot be accommodated by the same explanation. Instead, with observations of structure-property changes [4, 5, 99, 110], deviations in the elastic modulus have been concluded to be due to the presence of free volume in the material allowing for subtle rearrangements of atoms to accommodate reversible shear strains. This

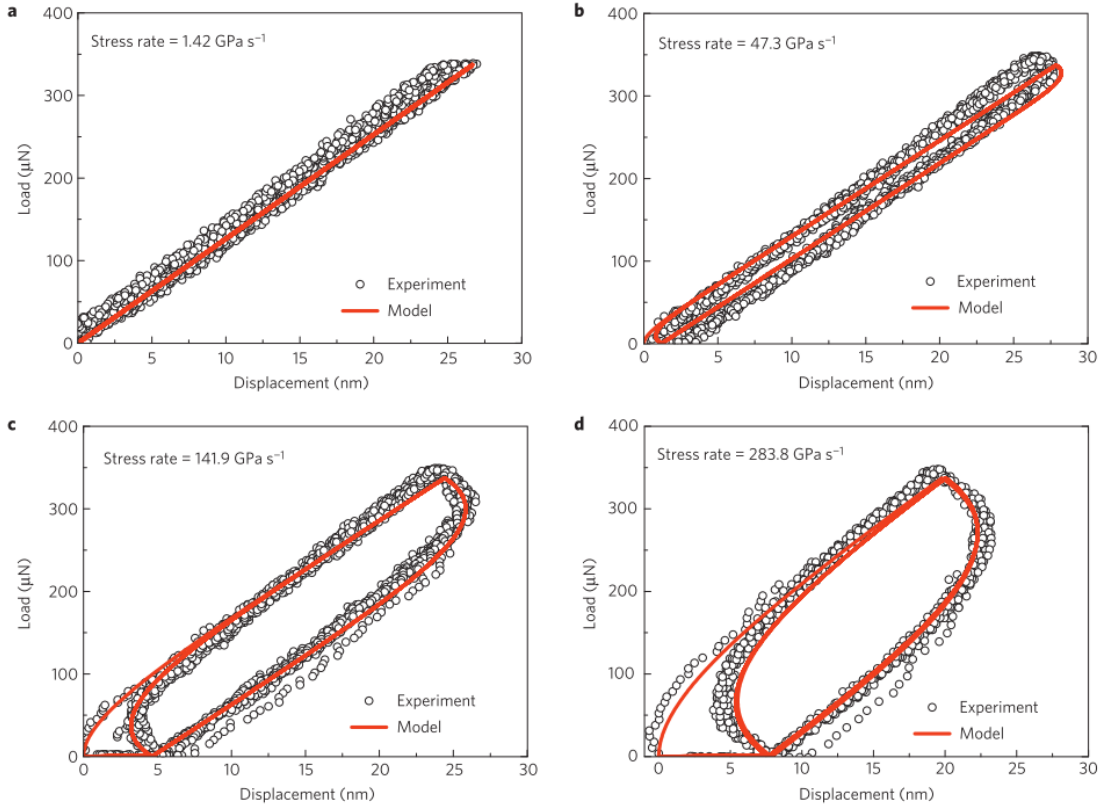


Figure 3.6: Plots showing the effect of increasing strain rate on a metallic glass with elastic loading (reproduced from [79]).

is noted to be markedly different from the processes governing the elastic behaviours of standard polycrystalline metals, as this is technically a reversible plastic process rather than an elastic one. This has implications for the elastic response behaviour of BMGs as a whole, as experimentally demonstrated by Ye et al. [79].

Ye et al. performed an experiment on tapered FIB machined micro-pillars of a $Zr_{55}Cu_{30}Ni_{15}Al_{10}$ BMG of diameters $0.6\ \mu\text{m}$ to $1.6\ \mu\text{m}$. The pillars were cyclically loaded at different frequencies, and mechanical hysteresis behaviour was observed in the stress-strain response, which became more prominent at higher frequencies as shown in Fig.(3.6). This behaviour is indicative of a visco-elastic material, often observed in polymers, whereby the combination of an elastic and viscous response is observed during the loading cycle of a material. Observations of such a bimodal response in BMGs indicates the presence of 2 processes occurring during so-called elastic deformation. By adopting the core-shell structure model of BMGs (described in Chap.(2)), this could be quantified as an elastic response of the hard shells combined with the viscous response of the soft cores. Ye et al. subsequently fitted the measured visco-elastic response of the material to a typical Kelvin spring and dash-pot model, and interestingly found that the viscous component of the response corresponded to the viscosity of the supercooled fluid of the same composition at vitrification temperature (T_g) [79]. This finding supports the Kauzmann paradox/ entropy crisis, outlined in Chap.(2), showing that the entropy state of the material effectively freezes during vitrification to provide the core-shell model structure commonly utilised in mechanical property modelling of BMGs today [79]. These findings are further supported by further investigations through Dynamic mechanical analysis (DMA) through indentation [111,112].

The reversible plastic deformation process responsible for the quasi-static elastic response of

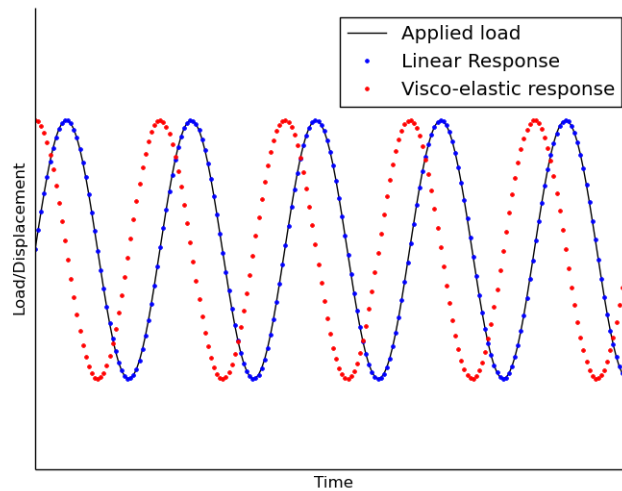


Figure 3.7: A Schematic showing the stress-strain response of a cyclically loaded perfect elastic and perfect visco-elastic material.

BMGs gives rise to a number of mechanical behaviours that are not observed in crystalline materials, namely a dependence of elastic behaviour on the ‘microstructure’ of BMGs. Weaire et al. were the first researchers to conclusively show this through modelling changes in local BMG environments to observe the effect of the elastic response of MGs [113]. They took a simplistic reverse Monte-Carlo modelling approach, whereby an ensemble of MG atoms were modelled as densely packed hard spheres and were agitated to give an approximate representation of a MG structure that produced pair distribution functions (see Chap.(2)) similar to that observed experimentally. Elastic constants were then determined for the relaxed and unrelaxed states, such that the difference between the elastic constants could be calculated from changes in the potential energy states of each case. Whilst it was recognised that the approach was simplistic and ignored many effects such as the validity of the inter-atomic potentials, the assumption that elastic constants could be directly extracted from pair potentials, etc. the difference in the calculated change in bulk and shear moduli corresponded to changes experimentally observed, with higher free volume structures showing reductions in elastic moduli and vice versa [113]. An extension to these observations is provided from the work of Concustell et al. [114], who showed that elastic loading of BMGs heated to near their glass transition temperature can induce a mechanical anisotropy in the BMG once it has been quenched back to room temperature. Such an effect is confusing in a supposedly structurally isotropic material [4, 5, 114], which should have no preferred direction of deformation when elastically loaded, regardless of previous processing conditions. However, Concustell found that Poisson’s ratio was heavily influenced through this process, indicating once again that the elastic loading of the BMG has a plastic process associated with it. An explanation of this effect can be found in the description for the PEL (introduced in Chap.(2)), whereby, when a BMG is heated and elastically deformed, higher energy atomic configurations can be sampled in order to accommodate the strain through minor β transitions in the PEL. When the material is cooled again, atomic configurations that were once explorable by atoms at high temperature become unavailable and trap atoms already in these high energy configurations in place. Therefore when the material is relaxed, the back-stresses of the BMG matrix are not enough to free the atoms from their high energy state, resulting in a residual stress in the amorphous material which is manifested

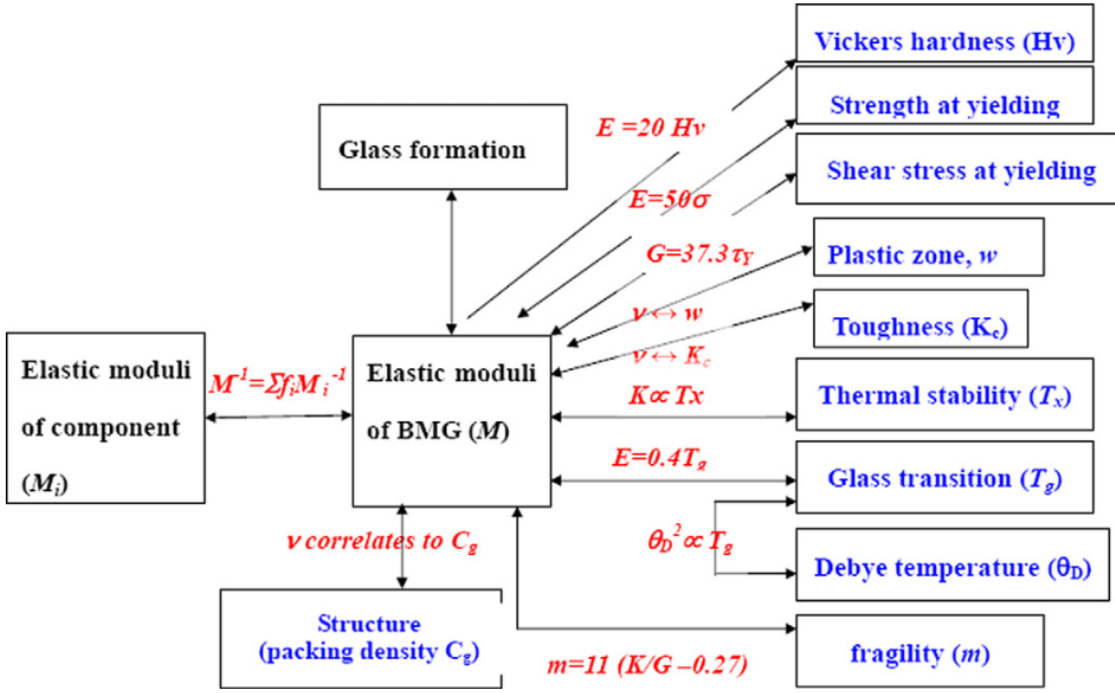


Figure 3.8: An overview of the known correlations between elastic properties and all other physical properties of BMGs (reproduced from [110]).

as a mechanical anisotropy [114].

The PEL is a useful tool for understanding both elastic and plastic processes in BMGs. In addition to the induced anisotropy phenomena outlined above, temperature dependencies of elastic properties can also be explained through the PEL [110]. By considering a BMG heated to higher energy states, the PEL shows that higher energy atomic configurations can be sampled by the BMG structure, thus allowing the accommodation of strain, thereby reducing the elastic moduli [36,110]. This hypothesis is supported by experimental observations of elastic property temperature dependence, which shows clearly that elastic moduli are negatively dependent on temperature [115].

Wang et al. recently published an article [110], which gives a comprehensive review of BMG elasticity, how elastic behaviours pertain to the PEL and all the known correlations between physical properties and elastic behaviours of BMGs. A summary of these correlations is outlined in Fig.(3.8), which shows that some elastic properties have an influence on the plastic behaviour of a material. In the case of Poisson's ratio, as outlined in Chap.(2), an elastic property has even been used to define a classification system of BMGs based on their plastic performance. To understand the potential reasons behind elastic-plastic relationships, current theories behind the mechanisms of plastic deformation need to be understood, and the factors perceived to affect these mechanisms need to be quantified.

3.2.3 Plastic behaviour

The previous section described how BMGs can potentially deform on an atomistic level, and how this pertains to elastic behaviours. However the details surrounding the progression of deformation beyond these localised processes to plastic behaviours are still an area of active research. Observations of deformation behaviour in BMGs have shown that they deform through 3 main modes, homogeneous bulk flow, inhomogeneous bulk flow, and inhomogeneous localised flow [4]. The deformation behaviour undertaken depends on a multitude of factors, not least of which are the test

conditions which the BMG is subjected to. However every mode of BMG deformation observed to date can be sampled with the correct combination of temperature and stress or strain rate, as defined by deformation maps outlined in Fig.(3.9b) and Fig.(3.9a) for a typical BMG [4].

Modes of Deformation: Homogeneous flow

During localised plastic flow events described by both the STZ and the free volume model, free volume is created, which is subsequently destroyed when the surrounding material relaxes through diffusional processes [101,104,105]. When the condition is such that temperatures allow for significant diffusional recovery (i.e. free volume annihilation) BMGs undergo homogeneous plastic flow as free volume can be generated at the same or similar rates at which it is destroyed [4,105]. Such a deformation mechanism is explicable through relatively simplistic statistical arguments based on an attempt frequency approach from rate theory [4,105]. At a given temperature, STZs can be activated at any given time in the absence of an external stress according to Eq.(3.14):

$$\dot{s} = \nu_D \exp\left(-\frac{Q_{STZ}}{k_b T}\right). \quad (3.14)$$

When a shear stress is applied to a BMG material, Eq.(3.14) is adjusted such that the energy required to activate an STZ or an atomic jump is changed. In the direction of the applied shear stress, the energy term is adjusted to $Q_-\tau V$ whilst STZ or atomic jump activation in the opposite direction to the applied requires an energy term of $Q_+\tau V$, where V is the STZ volume multiplied by the shear strain accommodated by an STZ or an atomic jump [105]. Taking into consideration the direction of the activated STZs and atomic jumps, Eq.(3.14) can be rewritten as

$$\dot{\gamma} = \alpha_o \nu_D \gamma_o \exp\left(-\frac{Q_{STZ}}{k_b T}\right) \sinh\left(\frac{\tau V}{k_b T}\right), \quad (3.15)$$

$$\text{or } \dot{\varepsilon} = \alpha'_o \nu_D \gamma_o \exp\left(-\frac{Q_{STZ}}{k_b T}\right) \sinh\left(\frac{\sigma V}{\sqrt{3}k_b T}\right) \text{ for the uniaxial case.} \quad (3.16)$$

The term α_o is used to encompass multiple terms to give a numerical constant within which the fraction of material capable of undergoing deformation is included. Work from Spaepen et al. [105] states that areas rich in free volume are the only areas which can contribute to significant deformation through either the free volume of the STZ models, which in turn can be related to the temperature state of the material through:

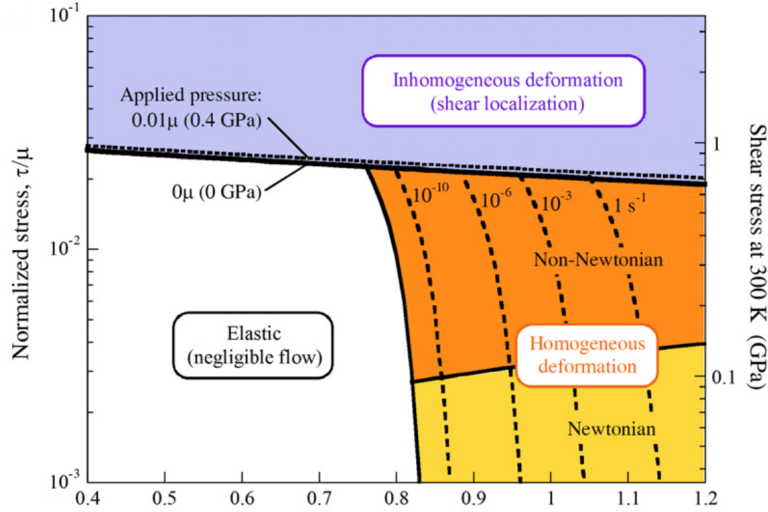
$$\alpha_o \propto \exp\left(-\frac{\xi v^*}{v_f}\right) = \exp\left(-\frac{\xi v^*}{\alpha_\Omega \bar{v}(T - T_o)}\right). \quad (3.17)$$

Eq.(3.15) and Eq.(3.17) defines a link between the fragility and structural state of a BMG to plasticity, with strong glass formers obeying Eq.(3.15) closely and weak glasses demonstrating a strong temperature dependence outlined in Eq.(3.17) [32].

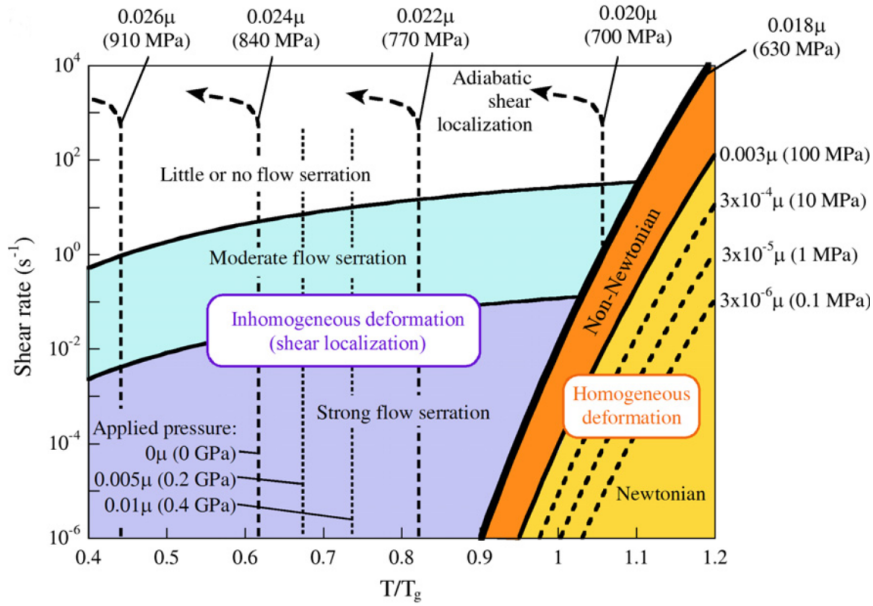
Homogeneous deformation has been observed to accommodate both Newtonian and non-Newtonian flow [4,6,101,105]. This is determined according to the relative temperature states of a stressed BMG and how this affects Eq.(3.15). In the case of high temperature, low stress environments, Eq.(3.15) can be reduced to:

$$\dot{\gamma} = \frac{\alpha_o \nu_o \gamma_o}{k_b T} \exp\left(-\frac{Q}{k_b T}\right) \tau \left(\tau \ll \frac{k_b T}{V}\right) \quad (3.18)$$

This indicates that the strain rate is proportional to the applied stress in this temperature con-



(a) A deformation map showing the different deformation responses with respect to the normalised stress and testing temperature.



(b) A deformation map showing the different deformation responses with respect to the shear strain rates and testing temperature.

Figure 3.9: Deformation maps indicating the different conditions required for the different deformation responses (reproduced from [4]).

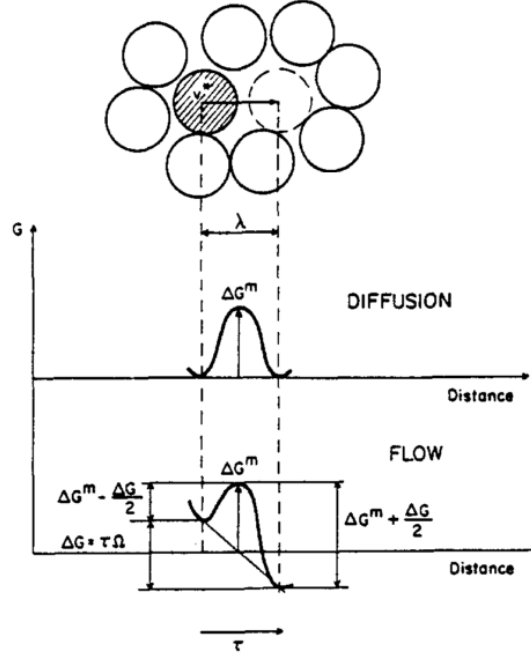


Figure 3.10: A schematic diagram showing the difference in energy states of activating an atomic jump, or equivalently an STZ, under an applied shear stress compared to the rest state of the material (reproduced from [105]).

dition, i.e. a Newtonian flow criteria. This is indicative of BMG behaviours observed in high temperature environments ($T \geq 0.8T_g$) [4, 101, 116]. Qualitatively, this is characterised by homogeneous activation of multiple STZs or atomic jumps throughout the BMG material at a rate low enough such that reductions in the viscosity of the material through free volume and thermal energy generation is dissipated quickly enough through free volume annihilation and thermal diffusion such that macroscopic strain softening and runaway deformation is circumvented [105].

In the case of high temperature high stress environments, homogeneous flow can still be accommodated through non-Newtonian flow. Here there is an imbalance in the rate of free volume generation/annihilation such that a net gain of free volume reduces the viscosity of the material allowing for localised deformation to occur for a short time. However the high temperature condition and high rate of recovery of the material leads to diffusional recovery of these localised areas of deformation which allows multiple localised deformation bands to form. Under these conditions, Eq.(3.15) can be reduced to:

$$\dot{\gamma} = \frac{1}{2} \alpha_o \nu_o \gamma_o \exp\left(-\frac{Q_{STZ} - \tau V}{k_b T}\right) \left(\tau \gg \frac{k_b T}{V}\right) \quad (3.19)$$

This indicates that the stress dependency that exists in the previous case diminishes to produce a non-Newtonian flow state. Between the Newtonian non-Newtonian states, the stress-strain rate relationship varies continuously according to [4]

$$\dot{\gamma} = A \tau^n. \quad (3.20)$$

Under non-Newtonian flow state, work from Lu et al. showed that for deformation performed in $Zr_{41.2}Ti_{13.8}Cu_{12.5}Ni_{10}Be_{22.5}$ at high strain rates at high temperatures revealed a stress overshoot, and sometimes even a stress undershoot. This has been attributed to an imbalance in the free

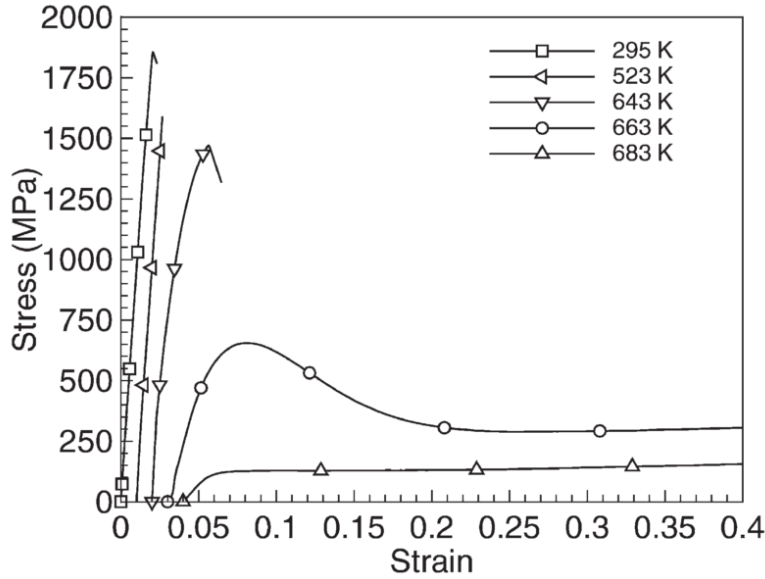


Figure 3.11: Demonstration of inhomogeneous flow in compression tested $Zr_{41.2}Ti_{13.8}Cu_{12.5}Ni_{10}Be_{22.5}$ over different temperatures (reproduced from [117]).

volume of the BMG. Upon STZ activation, free volume is produced which in normal BMG steady state flow is balanced by annihilation of free volume through atomic diffusion. At high strain rates, the annihilation of free volume cannot keep up with the rate of free volume generation, which results in the reduction of viscosity of the material, which in turn leads to increased rates of deformation, higher levels of free volume, and in turn higher levels of atomic mobility within the BMG structure. In low temperature conditions, this is thought to continue into catastrophic runaway deformation (see later), however the high temperature environment of this BMG and the increased atomic mobility allows free volume annihilation to catch up, and in some cases temporarily overtake free volume production, leading to the increase of flow stress and even produce a stress undershoot as a result [117].

Work from Steif et al. [118] correctly predicted such an effect with a mathematical description of free volume [4], which has provided support for the use of the free volume model to interpret homogeneous deformation in BMGs. This has been integrated with the work of Falk and Langer, who introduced the effect of chemical SRO into the work of Steif et al through the consideration of a simple molecular dynamics simulation with Lennard-Jones potentials to further improve the predictions set by Steif et al.'s model [119]. Whilst they acknowledge the issues surrounding the small system sizes utilised in their work, the outcome of these models suggests that the free volume and STZ models are relatively robust in describing homogeneous plastic behaviours in BMGs [119].

Plastic deformation: Inhomogeneous flow in BMGs (Shear bands)

Inhomogeneous deformation is the mode of deformation of the greatest academic and industrial interest for BMGs. This deformation mode occurs when a BMG is subjected to low temperature high strain rate environments, which hinder atomic mobility within a BMG structure during deformation. Therefore mechanisms that annihilate the free volume produced during STZ and atomic jump processes cannot balance the rate at which free volume is generated, resulting in a runaway deformation process. This produces features known as shear bands; $\approx 10\text{nm}$ thick planes of BMG material [58,120] that propagates over length scales of $1\mu\text{m}$ [99,121,122] over time scales of

1ms [123–127] that form close to the plane of critically resolved shear stress which accommodates the vast majority of any plastic deformation of the material during their activity. In addition, shear bands have been estimated to reach temperatures of up to 8600K [84] during the initial stages of activation, and (whilst remaining amorphous) have been observed to be structurally different to the surrounding amorphous material, with greater fractions of free volume compared to the bulk material through observations of TEM [57] and PAS [52,58], and preferential etching of the materials due to more open atomic cluster structures with greater freedom of atomic bonding with an attacking chemical agent [128].

The process of shear banding and how it comes into being from the activation of a STZ is still under scrutiny. As STZ and atomic jump processes can occur over time-scales of $\leq 10^{-12}$ s [109], the time delay between STZ activation and full shear band formation is a gap in the process that is still a mystery [4]. Some theories suggest that shear banding forms from a chain of STZs that activate in a cooperative manner [41]. Others suggest that shear bands form due to the propagation of a shear band front from a single or a cluster of shear bands. Therefore whilst it is generally accepted that a runaway softening mechanism is responsible for the formation and propagation of shear bands, it is unclear as to the lead cause of the softening and how this propagates to the formation of a shear band. A review article by Schuh et al. summarised the potential factors considered in the literature that could attribute to strain softening [4]:

- Local production of free volume due to the activation of an STZ.
- Local structure evolution upon the activation of an STZ, leading to the local softening of the material.
- Relief of internal stresses of the glassy system, that perpetuates the growth of a shear band.
- Thermal energy generated during the process reducing the viscosity of the surrounding material.

3.3 Details surrounding current theories of shear band formation

Beyond the general observed behaviours of shear banding, there are several areas regarding shear band formation that are poorly understood. These are outlined as:

- The exact mechanism behind how shear bands form from atomic scale processes is yet to be shown, as accurate atomistic simulations can only simulate up to the early stages of shear band initiation in a bulk material, and experimental observations are limited to time resolutions of micro/nano-seconds depending on the experimental treatment being utilised [4,109].
- Structural dependencies of shear band formation remain unclear, with indications of MRO playing a significant role in the formation of shear bands [66]; structural order that is only accurately characterised in the most simple of BMG structures [5].
- Structural evolution of shear banded material during the shear band process is poorly understood.

We outline some of the key studies that have shaped the current understanding of shear band formation, and identified the areas to be improved in which the work presented in the thesis may aid in.

3.3.1 Shear banding mechanisms

Shear band initiation

The cause of shear band initiation, whilst generally agreed to be due to local instabilities growing into a runaway deformation processes, fall into 2 camps. The first argument was introduced by Leamy et al. [129], who suggested that shear banding was an adiabatic process such that activation of STZs causes a sudden increase in temperature, which in turn causes a rapid reduction in viscosity. This leads to increased atomic mobility in the immediate vicinity of the STZ, allowing for further STZ activation events to take place with lower activation energies. The extreme rise in temperature of shear band material has been experimentally measured by Lewandowski and Greer, who noted localised melting of a tin coated MG ribbon in the vicinity of formed shear bands [84], however subsequent calculations revealed that the temperatures generated and the time-scales of melting are not indicative of adiabatic heating due to diffusional length scales of the observed temperature increases predicting shear band widths of 100 nm to 240 nm. As such, temperature increases during shear banding are believed to be a consequence rather than a cause of the process [84]. Despite these findings, researchers continually use the assumption of adiabatic heating of shear band material in models and predictions due to the simplicity of the calculation and reduction of modelling times for a small trade-off in model accuracy [4, 130].

The second theory of shear band formation is based on the idea of free volume generation increasing atomic mobility within the structure and therefore decreasing the viscosity of the material to allow for the formation of a runaway deformation mechanism. The mechanism was first introduced by Dalla Torre et al. [131] based on the observation of load-displacement serrations in BMGs under compression over a range of strain rates. Dalla Torre noticed that the effect is similar to the Portevin-Le Chatelier (PLC) effect in crystalline materials, a process governed by the diffusion of interstitial atoms that act as pins to dislocation motion. Using this comparison, Dalla Torre assumed that the serration effect is a similarly diffusion-controlled effect and explained the following serration behaviours in terms of diffusion processes in BMG materials:

- The number density of serration events are observed to have some positive proportionality to the applied strain rate and the amplitude of serration events are observed to decrease with increasing strain rate:

It has been stated that the activation of STZs or atomic jump events generate free volume [131]. This is observed in the presence of shear bands through a range of experimental methodologies such that shear bands have a greater fraction of free volume in their structure, with volume dilations estimated over 10% in some cases [58, 132]. This generation of free volume is in competition with diffusion processes suggested by Spaepen et al. [105] such that once a shear band has formed, there is a period of time after which the shear band structure relaxes to a state governed by the PEL of the BMG. If the strain rate of a BMG is high, then the level of relaxation of shear band structures is minimal compared to a lower strain rate experiment. As a result, the critical shear stress for STZ activation [41] and subsequent shear band formation is reached quicker for high strain rate experiments. In addition, the shear band material for higher strain rate tests do not have enough time to recover to a metastable state such that the critical strain rate is achieved for a lower level of applied stress, thereby storing less elastic energy to produce a significant load drop. This argument could be applied to Leamy's adiabatic (or even near adiabatic) model of shear band formation [129] whereby thermal diffusion rates in the material limit the viscosity recovery of the material post shear band formation to produce the same effect observed here. This model could

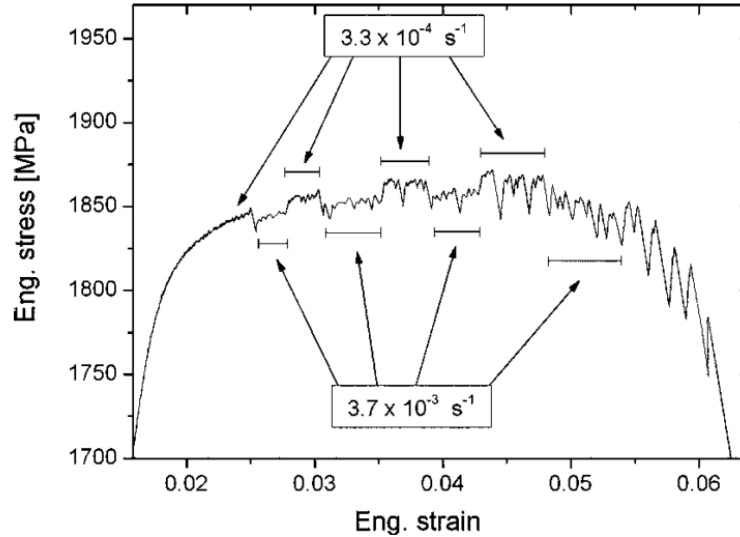


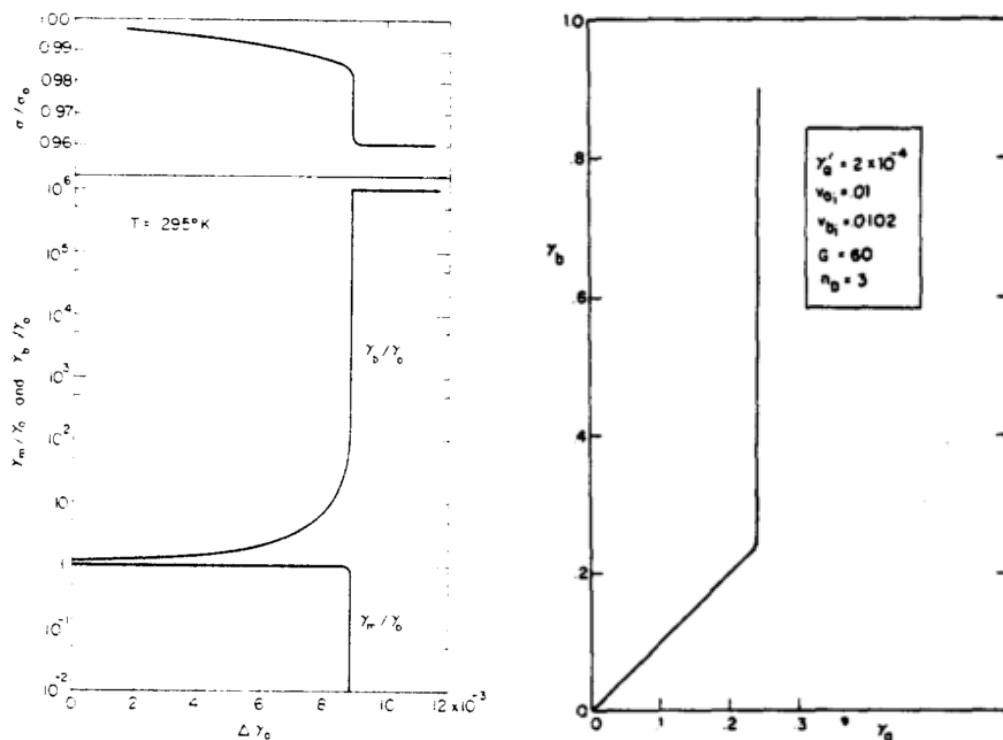
Figure 3.12: An example of flow serration behaviour of a compressed $\text{Zr}_{52.5}\text{Ti}_5\text{Cu}_{17.9}\text{Ni}_{14.6}\text{Al}_{10}$ showing how serration behaviour evolves with test time (reproduced from [131]).

be further brought into line with the findings of the free volume initiation model through the introduction of variable thermal diffusion rates due to differences in structure affecting thermal conductivity. Whilst this is unlikely, a lack of information regarding structural evolution during shear banding provides a reasonable doubt as to whether the adiabatic model can explain this effect.

- For compression tests at a given strain rate, BMGs exhibit serration events that increase in magnitude throughout the test and occur less frequently with test duration:

During multiple serration events, it is thought that shear bands tend to reactivate preferentially over old shear bands due to higher levels of free volume. As shear bands reform, more free volume is generated such that new potential STZ sites are formed making nucleation and formation of shear bands easier [133]. This ‘softens’ the material such that with each shear band event, more deformation is accommodated with less resistance, resulting in greater drops in load. In addition, the higher free volume state of the material increases the rate of material recovery due to increased atomic mobility within the material. Therefore whilst the shear band structure itself gets weaker with increasing numbers of activations, the recovery of the material also becomes quicker, thus the time between shear band initiation events increase. This effect cannot be explained through Leamy’s adiabatic rheological flow model, as in this model, structural state of shear bands is determined through melting and rapid cooling of shear band material. Such a heating and cooling process will initially increase the serration magnitude as observed in Dalla Torre’s work [131, 134], however as the process repeats, the structure of the shear band material will be governed by the PEL, and accumulation of free volume will be annihilated during the heating process.

It is now generally accepted that this is the likely cause of shear band initiation, with temperature rises being a by product of the process rather than the cause [84, 131].



(a) Bifurcation of strain rate due to strain rate fluctuations from Argon's calculations (reproduced from [102]).

(b) Bifurcation of strain rate due to Free volume fluctuations from Steif's calculations (reproduced from [118]).

Figure 3.13: Bifurcation of strain rate behaviour due to the accumulation of free volume from STZ operations calculated by Argon [102] and Steif [118].

Shear band propagation

Once a shear band is initiated through the activation of STZs, propagation needs to be considered. It is well accepted that the process is due to a softening of the material which leads to a runaway deformation process, which from the previous section is believed to be primarily caused through the accumulation of free volume. Work from Argon [101] showed this in Fig.(3.13a) through a mathematical description of strain localisation through the accumulation of free volume due to perturbations in strain rate from individual STZ activations. A similar effect is reported in the work of Steif et al. [118], shown in Fig.(3.13b), who approached the problem of shear localisation through modelling strain perturbations as a result of fluctuations of free volume within a BMG structure. Calculations from both models not only correctly predicted the expected bifurcation behaviour of strain rate with respect to shear strain, but also agree with the shear band formation times measured by Neuhäuser [127] through high speed cinematography.

Models proposed by Argon and Steif have both been based on the presence of a consistent applied strain, which in practice is not a valid assumption as shear bands dynamically accommodate strain, thereby momentarily changing the strain rate experienced by the bulk material and shear bands. An FEM based computational model put forward by Anand et al. is more sophisticated and is able take into account multiaxial loading [135]. The model has successfully captured the arrest of shear bands due to the accommodation of strain reducing the driving force of deformation, however work remains to be done in progressing the model to full failure and to accommodate high temperature deformation environments both in the localised and homogeneous states [4, 135]. Cao et al. performed an embedded atomic modelling (EAM) simulation for shear localisation and shear

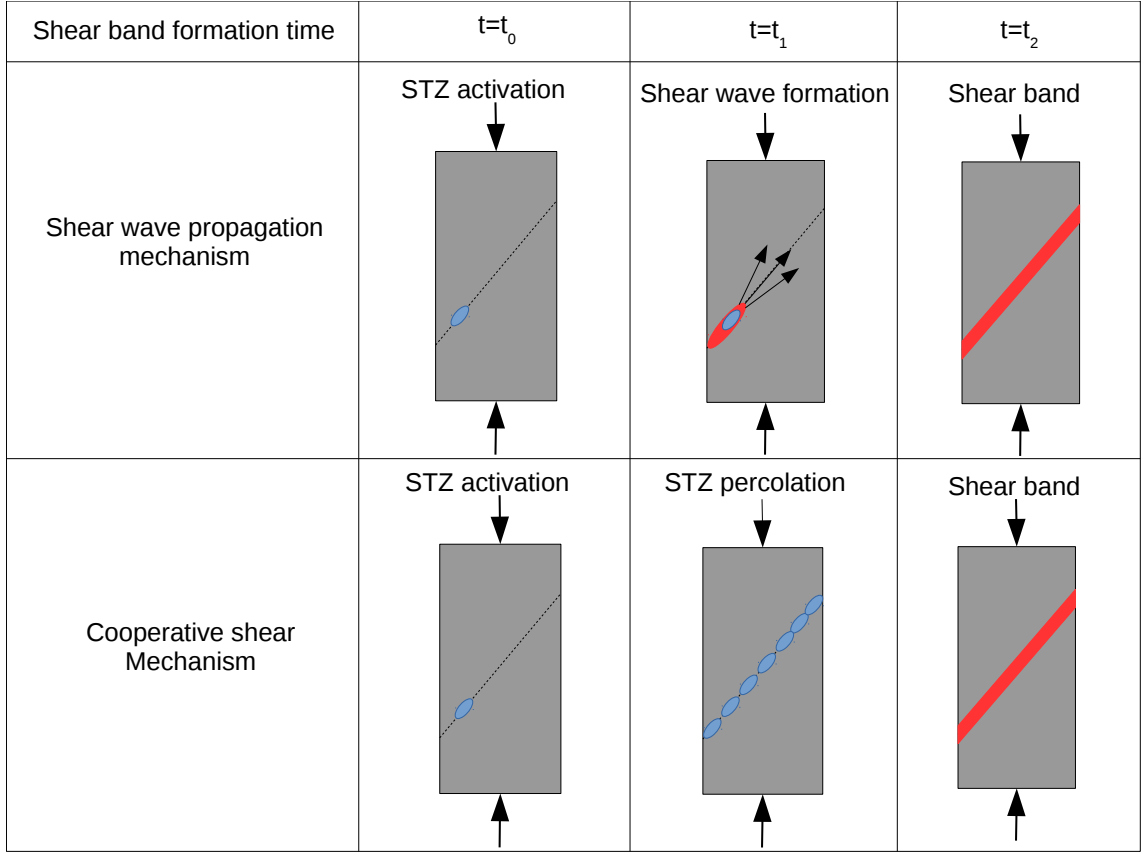


Figure 3.14: Schematic diagrams showing the 2 key shear band formation mechanisms for a BMG under compression from the activation of an STZ (blue ellipse) to the full shear band.

band propagation for a $Zr_{36}Cu_{64}$ BMG with 500,000 atoms. Their results also show bifurcation of strain rate of the material and produce shear bands that arrest due to thermal diffusion and material recovery during the process [136]. As none of these models have been completely verified experimentally as of yet, they do not give conclusive proof regarding propagation of shear banding. However they do impose limits on bulk shear banding behaviours which can be compared to some experimental results.

Beyond the statement that the process of strain localisation through accumulation of free volume forms shear bands, the process of shear banding itself is still a topic that is uncertain. Literature outlines 2 generic models, shown in Fig.(3.14), that could describe structural evolution and processes that occur during shear banding based on experimental and computational modelling simulations [136–141]:

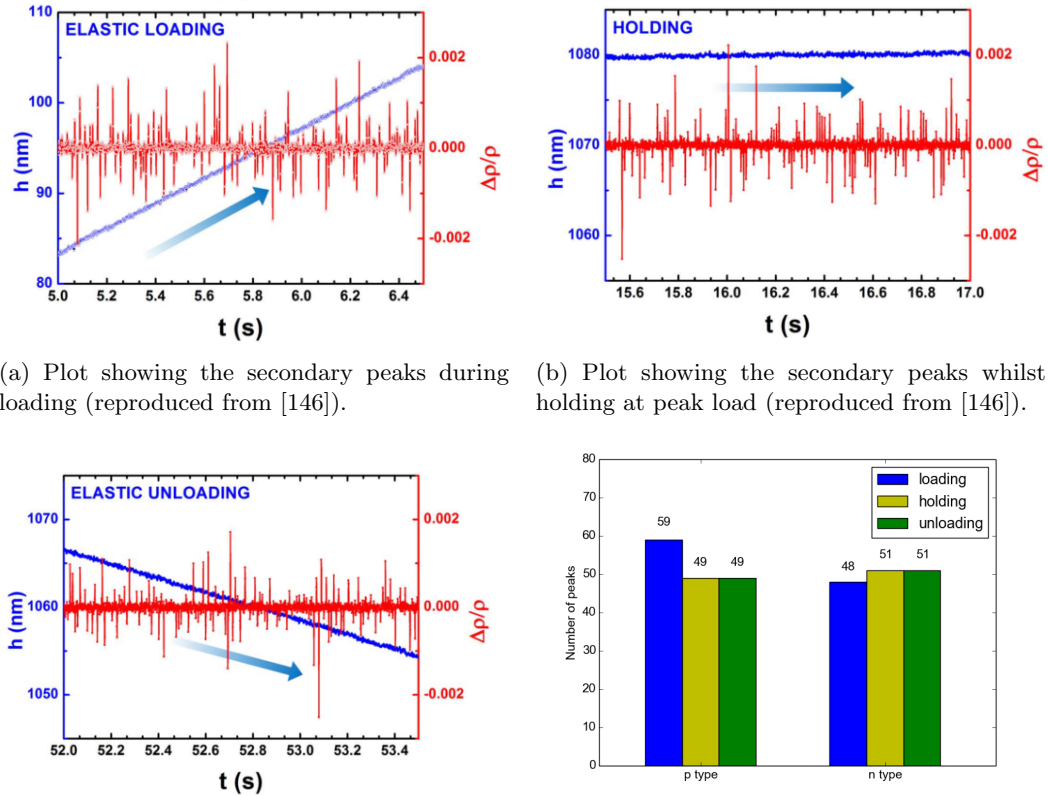
1. Multiple STZ activate along the plane of CRSS and coalesce to form a shear band.
2. A singular or cluster of STZs act as a nucleus from which a shear front is propagated throughout the material to produce a shear band.

Due to the time scales involved with shear band initiation and propagation, gaining data with sensitivity and temporal resolutions great enough to make informed conclusions is difficult. One of the first attempts at measuring the evolution of a shear band within a structure was made by Neuhäuser [127] through high speed cinematography. Their estimate for the velocity of shear band formation in metallic glass ribbons was $\approx 40\mu\text{ms}^{-1}$ based on the assumption that shear banding is an almost instantaneous process due to the percolation of individual STZs, however this estimate

is at the resolution of the experiments performed with some shear bands going from initiation to full propagation within two frames [127], far below the resolution requirement for accurate sampling [142]. Hampel and Neuhäuser then upgraded to an optoelectronic method whereby changes in photocell brightness were correlated with the formation of slip steps in ribbons of metallic glass due to shear banding (reference within [126]). Despite this, both of these methods only produce data relevant to the topology of the sample being tested, meaning that conclusions beyond that shear bands correspond with drops of load during plastic deformation of metallic glasses, and variation on the load drops are observed with respect to test time and sample composition cannot be made.

Further improvements to observations of shear bands were made through the introduction of infra red (IR) filming introduced by Bruck et al. [143]. Bruck's measurements involved high strain compression tests through Kolsky bar experiments of a $Zr_{41.25}Ti_{13.75}Cu_{12.5}Ni_{10}Be_{22.5}$ BMG coupled with a liquid nitrogen cooled HgCdTe IR detector. Their results showed that not only did significant heating occur during deformation, but that heating occurred post shear band formation thus providing further evidence that shear banding and strain localisation processes cause heating. Their work pre-dates that of Lewandowski and Greer's [84] and therefore assumes adiabatic heating occurs. Their work may have preceded Lewandowski and Greer to the claim of a non-adiabatic nature of shear banding, however their results were obtained with a single thermal detector such that the full thermal distribution of shear bands could not be recorded and interpreted [143]. Recent attempts at similar experiments have been performed by Qiao et al. [144], who compressed rods of $Zr_{64.13}Cu_{15.75}Ni_{10.12}Al_{10}$ BMG at strain rates of $2 \times 10^{-4} s^{-1}$ and filmed the compression with an IR camera with a frame rate of 33Hz. Measurements showed temperature rises greater than T_g , and measurements were used to correlate the drops in stress during shear band behaviour with temperature spikes. In addition, using a semi-analytical result published by Yang [145] which relates the amount of free volume generated during a test (providing the rate of free volume annihilation during the test is negligible [145]), Qiao related shear band propagation velocity to the free volume content of the material. As the free volume state of a BMG evolves with increasing levels of shear banding and STZ activation, Qiao stated that the volume may be used as a means to calculate the initial shear band formation and propagation rate, which in turn could be related to the intrinsic properties of a BMG such as Poisson's ratio [144].

One of the most recent new approaches at direct observation of shear band evolution was published in late 2014 by Yang et al. [146]. Their work involved probing shear band properties through measuring the effect of shear events ranging from STZs to shear bands themselves in a machined micro-pillar of $Zr_{55}Cu_{30}Ni_5Al_{10}$ BMG. The material was compressed under a flat indenter with a standard loading profile like that outlined in Fig.(4.5a) in Chap.(4), and changes in the potential difference across the sample were measured. Yang et al. claimed that shear bands manifested themselves as large sudden increases in the potential difference data, and STZ events are detected as smaller secondary spikes, supported by a presence of preferential positive or negative potential difference spikes depending on whether the material is being loaded or unloaded. The first point of interest regarding their work comes from the data sampling rate which has plagued all other attempts at experimentally probing shear band behaviours. Yang's work samples voltage data at every millisecond, meaning the strong signals (observed to last $\approx 10ms$) are sampled adequately. However the secondary signals are often only depicted by single data points; an unsatisfactory sampling rate which may mean that some secondary signals are not being sampled at all. A second point of concern regarding the data is the claim of a prevalence for secondary signal indicating a net difference in voltage spike direction in favour of voltage gain upon loading and vice versa. This can be tested; taking a sum of the peaks during loading, load hold and unloading, Fig.(3.15) tests



(a) Plot showing the secondary peaks during loading (reproduced from [146]).

(b) Plot showing the secondary peaks whilst holding at peak load (reproduced from [146]).

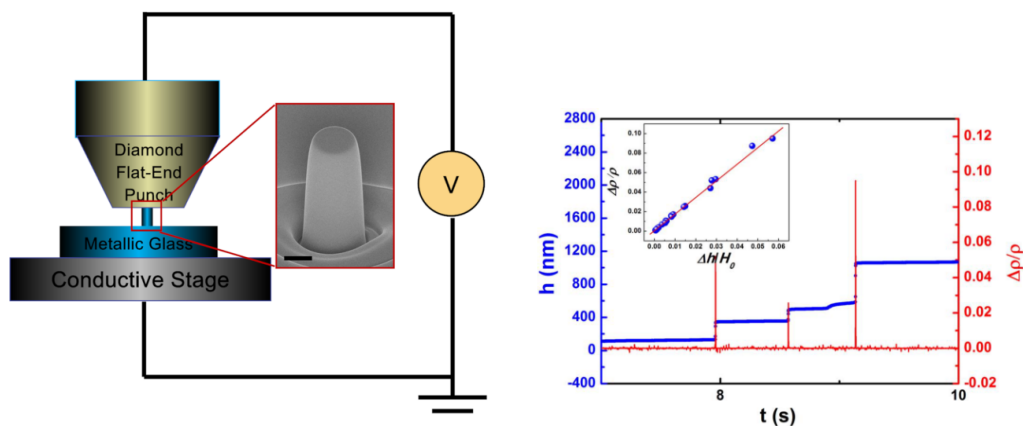
(c) Plot showing the secondary peaks during unloading (reproduced from [146]).

(d) Analysis of the number of positive (p type) and negative (n type) secondary peaks during each section of loading (this work).

Figure 3.15: An independent observation regarding the distribution of secondary peaks in Yang's experiments indicating that only p type peaks show any change during testing, which can be account for by a settling of the electronic contact during loading.

this claim, and finds that the difference between the voltage spike types is minimal at best. This, coupled with the poor data sampling rate, gives no foundation for such a claim. More worryingly, the frequency of the secondary peaks in Fig.(3.15) is $\approx 50\text{-}60\text{Hz}$, around the frequency of mains voltage of China, where the work was performed, indicating the potential for these signals to be due to electromagnetic pollution from surrounding mains connected equipment. No baseline voltage data was provided to determine if this indeed due to noise or a real material effect. Therefore, there is uncertainty if the source of secondary peaks is due to the activation of STZs or interference from the mains voltage. The final concern noted here with regard to his study is the experimental set-up, which has the electrical contact as the load bearing component. This means that any dynamic change in load will inevitably produce a small change in the measured potential difference. As such the dynamic load change brought about through shear banding of the BMG will likely affect the electrical contact of the material such that larger load drops produce larger sudden changes in potential difference that settle back down to a base value once the dynamic loading event has ceased. This is supported through the observation of ringing in the voltage data after the first primary signal, where contact between the indenter and the sample is likely to be at its weakest, and therefore will require the greatest amount of settling time of the 3 signals. As such the primary signals observed in Yang's study could be due to electrical contact considerations, thereby questioning the validity of any of the experimental results reported.

Due to the temporal and sensitivity issues of current experimental techniques, Molecular Dy-



(a) A schematic diagram of Yang's experimental set-up (reproduced from [146]).

(b) Observations of primary peaks attributed by Yang to shear bands (reproduced from [146]).

Figure 3.16: The correlation of peak sizes from Yang's experiment could be just as easily explained due to a change in the contact mechanics between the indenter tip and the sample as due to fundamental changes in on the voltage state of the material.

namics (MD) simulations have been the backbone to understanding shear banding behaviours through modelling processes, though the results of such approaches are open to interpretation and user bias, and therefore do not always agree. For example Ogata et al. performed a 3 dimensional MD simulation of $\text{Cu}_{57}\text{Zr}_{43}$ binary MG with a Lennard-Jones 4-8 potential under quasi-static loading [140] and found that the formation of shear bands occurs through the percolation of STZs to form a shear band with no shear wave propagation, as outlined in Fig.(3.17a).

Shi and Falk [137] developed an MD simulation for 2 systems, a 2D binary alloy and a 3 dimensional mono-component alloy using a Lennard-Jones 6-12 potential and a Dzugutov potential respectively for simulating indentation (2D) and uni-axial compression (3D). Both simulations report SRO breakdown in favour of percolation of regions of free volume to form shear bands. This finding could be explained through either of the shear band propagation processes.

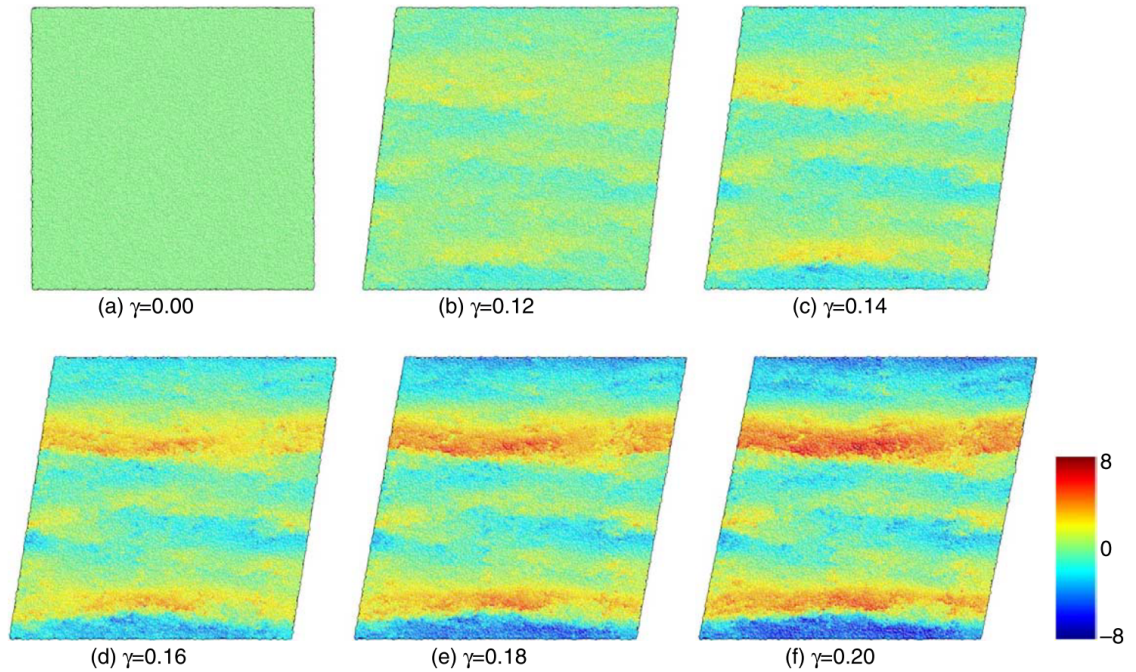
Cao et al's EAM approach, identified earlier, shows clear preference for the shear wave propagation argument for the initial formation of a shear band [136]. This model has been commonly supported and from recent advances in high speed photography has become the preferred (though not proven) method for shear band propagation, post initiation [125,144,147].

Initially, the adoption of meso-scale modelling helped to bridge this gap, through the use of course grains models that model course units of plasticity whose net effect describes deformation in a bulk BMG structure [141]. These units can be likened to STZs in a glass structure. Recent work from Homer et al. [141] examined the initial stages of shear localisation through such a meso-scale model and identified 5 key stages that occur during loading of a BMG under compression: linear elastic response, STZ clustering, growth following nucleation, relaxation thickening and flow thickening. The process is highlighted in Fig.(3.18).

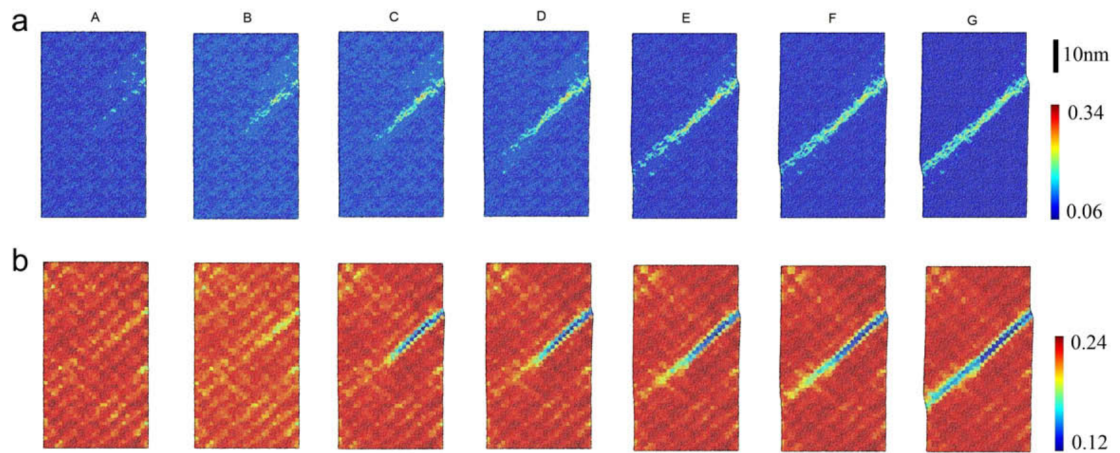
3.3.2 Shear band dependences

Processing history

There is a link between the structural state of metallic glasses and plasticity. Therefore changes to that structural state through thermomechanical processing will affect the yielding behaviour of a BMG. This was first observed through mechanical tests performed on cold rolled metallic



(a) MD simulation of a binary $\text{Cu}_{57}\text{Zr}_{43}$ alloy showing evidence for a shear band initiation and propagation mechanism through percolation of STZs (reproduced from [140]).



(b) MD simulation of a binary $\text{Cu}_{64}\text{Zr}_{36}$ alloy showing evidence for a shear band initiation and propagation mechanism through a shear wave nucleated from a cluster of STZs (reproduced from [136]).

Figure 3.17: MD simulations of similar MG structures showing different results regarding the propagation of a shear band from the point of initiation.

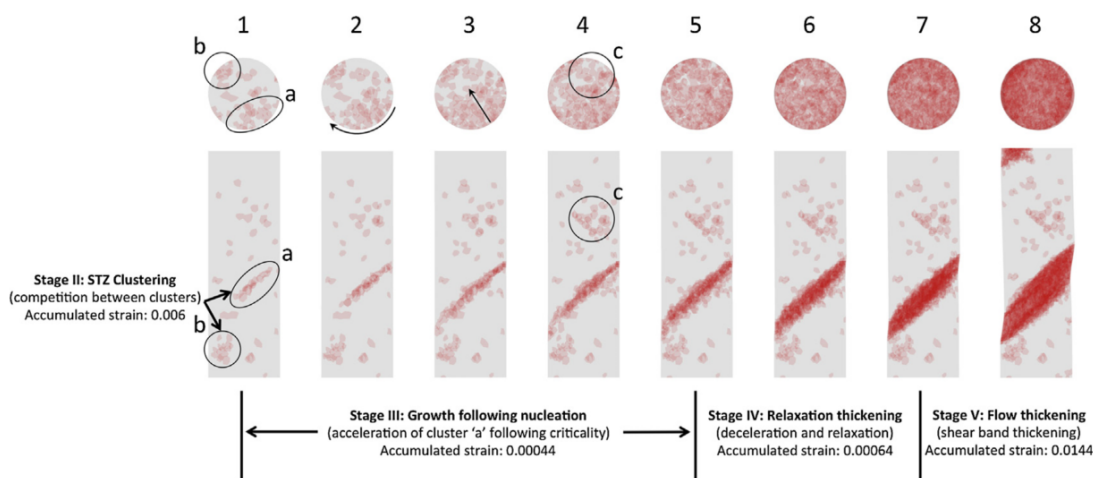


Figure 3.18: Model of the initial stages of shear band initiation (Reproduced from [141]).

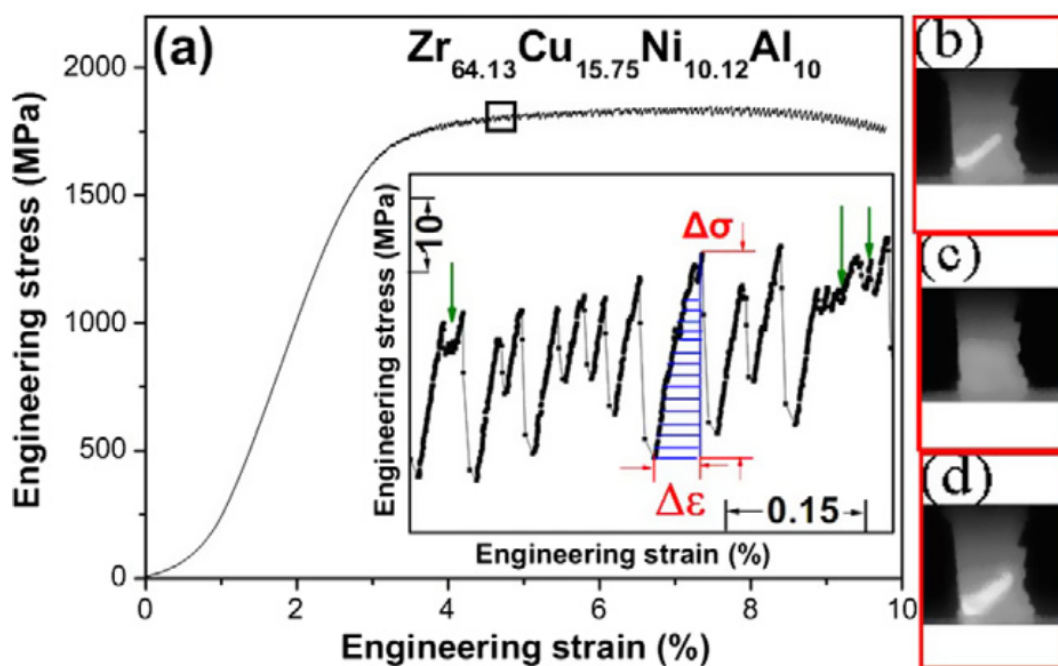
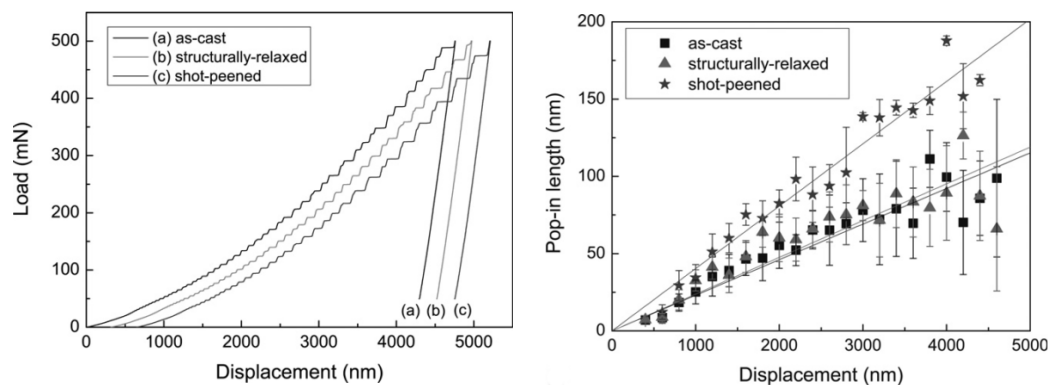


Figure 3.19: Serration behaviour of $\text{Zr}_{64.13}\text{Cu}_{15.75}\text{Ni}_{10.12}\text{Al}_{10}$ showing the elastic energy released during a serration. images b-d correlate to the green arrows on the serrated curve indicating that each serration induces an increase in temperature in excess of T_g (reproduced from [144]).

glasses, where significant plasticity was found. Work by Park et al. [148] and Yokoyama et al. [149] both found this for cold rolling of Zr BMGs. Yokoyama et al. observed multiple shear bands formed during the rolling process in the direction of maximum stress, but as rolling continued, the orientation of these shear bands rotated with the deformed material until new shear bands formed. New families of shear bands were noted to nucleate at rolling reductions of 10 %, 30 % and 60 %, with each set of new shear bands forming at 45° to the applied stress. This network of already initiated shear bands allowed for greater plasticity within the BMG, demonstrated through 3 point bend testing [149]. Work from Park et al. built on this, and found that cold rolling of a $\text{Zr}_{41.25}\text{Ti}_{13.75}\text{Cu}_{12.5}\text{Ni}_{10}\text{Be}_{22.5}$ BMG to reductions of 2 % to 18 % induced nanocrystallisation, and produced a material with both an increase in ductility and strength. The same multi-orientation shear banding was observed in this experiment, and it is thought that the nano-crystalline phase acts as nucleation sites for further shear banding. Furthermore the crystallisation introduced an interruption event in the propagation of the shear bands, as well as a level of work hardening within the material, thus increasing the strength of the BMG from 1.8 GPa to 1.95 GPa. However beyond 18% reduction, the strengthening of the material stopped and weakened, which coincided with the stopping of nanocrystallisation, however plasticity still increased due to multiple shear band nucleation events [148]. This work indicates that increases in material strength is therefore a product of nano-crystallisation rather than an intrinsic property of the material. To that end, Cao et al. performed rolling on a $\text{Cu}_{60}\text{Zr}_{20}\text{Ti}_{20}$ under room and 150K temperature conditions (RT and CT respectively), to evaluate structural changes [150]. Cao observed that shear bands form in both cases until reductions reach critical values. At these values, chemical segregation was observed in both cases, with CT rolling maintaining an amorphous structure, whilst RT rolling showed nanocrystallisation and phase separation, leading to instability in the glass structure as a whole [150].

A final key study into this effect, performed by Dubach et al., was carried out using thermomechanical processing techniques not focussed on rolling. Dubach took a $\text{Zr}_{41.25}\text{Ti}_{13.75}\text{Cu}_{12.5}\text{Ni}_{10}\text{Be}_{22.5}$ BMG in its as cast (AC), structurally relaxed (SR: achieved through a 12 hour heat treatment of the AC sample at 563K) and shot peened (SP: following the AMS-S-13165 standard [151]) states [97]. Each material state was then nano-indented with a standard quasi-static loading profile to determine the effect of the material treatments on ductility and strength of the material. Observations of serrated loading curves indicated high levels of SP state showing the toughest behaviour and the SR showing the most brittle behaviour. Such effects have recently been used to improve ductility of BMGs in the work of Fu et al. [152], whereby Laser Shot Peening (LSP) has been used to improve flexural plasticity in samples by inducing extra free volume at the material surface to form multiple shear band nucleation sites.

In addition to changes in ductility, hardness values were found to depend on the level of structural agitation, with the SP state returning the lowest hardness (14% less than the AC state), and the SR state giving the highest hardness (6% more than the AC state). As at least 2 of the 3 processing techniques could not form shear banding, this provides evidence that a change in yield strength is observed not as a result of nano-crystallisation as suggested by Park [148] and Yokoyama [149], but due to the intrinsic amorphous structural state. Dubach's work then went on to suggest that the pressure sensitivity of BMGs changes depending on the level of free volume present within the BMG matrix (with SP and SR states representing high and low levels of free volume respectively). It was found that the pressure sensitivity of the material to yield is minimal in the SP case, whilst the SR case was highly pressure sensitive, based on Tabor's hardness equation constant [153], whereby a low proportionality constant between yield strength and hardness is less pressure sensitive than a high proportionality constant [97]. In addition, observations of slip lines



(a) Plot showing the effect of structural state on serrated nano-indentation curves.

(b) Analysis of the serration morphology presented in Fig.(3.20a).

Figure 3.20: Results from Dubach's work indicating influence of free volume state affects the magnitude of shear bands, with deformed structures large pop-in lengths and vice versa (reproduced from [97]).

during indentation revealed that the pressure insensitive materials were found to fail through the Tresca or the Von-Mises criterion for yield (slip lines $\approx 90^\circ$), whilst the pressure sensitive materials fail through Mohr Coloumb yield (slip lines $<90^\circ$).

Atomic packing

Beyond the general consensus that Shear band formation is related to the level of free volume within a BMG structure, the details surrounding atomic packing effects of shear band behaviour are vague at best. Work from Lee et al. [98] attempted to rectify this issue by considering the evolution of SRO with MG deformation over a range of Zr-Cu compositions and found that both free volume and the nature of SRO packing should be taken into account, i.e. BMGs of the same free volume can have different SRO atomic packing cluster arrangements, which is observed to affect plasticity of MGs, with closely packed clusters being broken up with the evolution of plastic deformation within the material [98, 154].

Further work from Wakeda and Shibutani [155] investigated a molecular dynamics simulation of a binary Zr-Cu amorphous alloy containing 30,000 atoms and its effect on mechanical properties of the material. They found that through comparisons of a random network of atoms, amorphous materials are formed upon cooling through the formation of icosahedral clusters that are heavily interlinked, which provides a stiff structure, reflected by higher elastic moduli than material with lower fractions of interlinked icosahedra in the structure [155].

Material geometry

The mechanism for accommodating plastic strain requires the use of STZs, which are clusters of ≈ 100 atoms that are activated to accommodate shear strains. Therefore samples with dimensions smaller than this must behave differently. Jang and Greer demonstrated this with nano tension tests performed on $Zr_{35}Ti_{30}Co_{69}Be_{29}$ nano-pillars of different thickness machined through focused ion beam processing [156]. Fig.(3.21) shows that for samples of $z \approx 100$ nm in diameter, the material moves from a brittle failure mode to a ductile failure mode, with evidence of homogeneous plastic flow occurring during necking part prior to complete failure. It is noted that due to the complexity of such an experiment, tests appear to have not been repeated, which brings into question the validity of the yield values reported by such a study. However the images in Fig.(3.21b) clearly

show a necking phenomenon not typical of BMGs in tension. Therefore whilst repeatability of the experiment would aid in further validating the results reported in Jang's experiment, the validation of results with photographic data supports the finding of a size effect in BMGs on the scale of STZ operations. As such, the use of BMGs in small scale high strength applications such as micro electronic mechanical systems (MEMS) is popular [10].

Deformation conditions

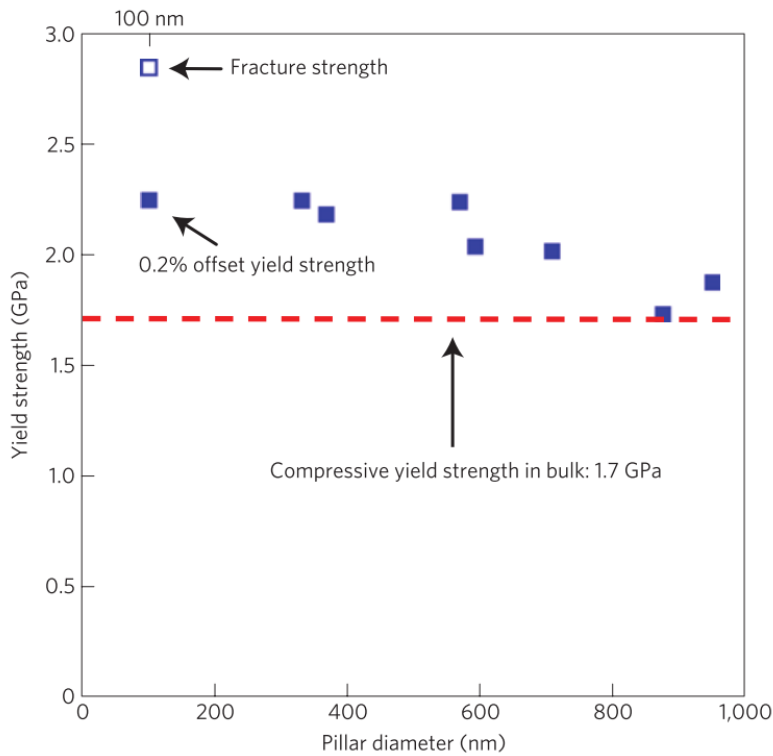
During low-room temperature deformation, BMGs are observed to have a minor negative strain rate sensitivity with regards to fracture stress, such that shear banding and fracture occur at lower stresses for loads applied at higher strain rates [6]. Bruck et al. were the first to observe such a feature [143], but passed the observation off as a dispersion effect in their data. Lu et al. [117] and Subhash et al. [157] also supported this observation. Gu et al. [158] also observed a similar effect reported by Bruck and corrected the data for the dispersion. However the negative strain rate dependence was still observed post correction leading Gu et al. to be the first to claim such an effect in BMGs explained as shear banding being approximately an adiabatic process, which in turn weakens the material causing failure at higher stresses. This claim has since been shown to be misleading, as shear banding occurs as a result of a weakening of the material through the generation of free volume rather than the generation of thermal energy [84, 134]. This being said, the observation of a negative strain rate effect on the fracture strength of MGs is generally accepted by the research community [159–163].

Strain rate sensitivity tests for high temperature conditions give clues regarding the deformation behaviour of a material. For example Lu et al. observed a stress overshoot in tests performed at high temperatures which became more prevalent for tests conducted at high strain rates and lower temperature. This is indicative of a plastic deformation model focused on the competition of generating and annihilating free volume whereby high strain rate tests generate free volume at rates higher than can be accommodated and vice versa [117], and marks the transition from ductile to brittle behaviour.

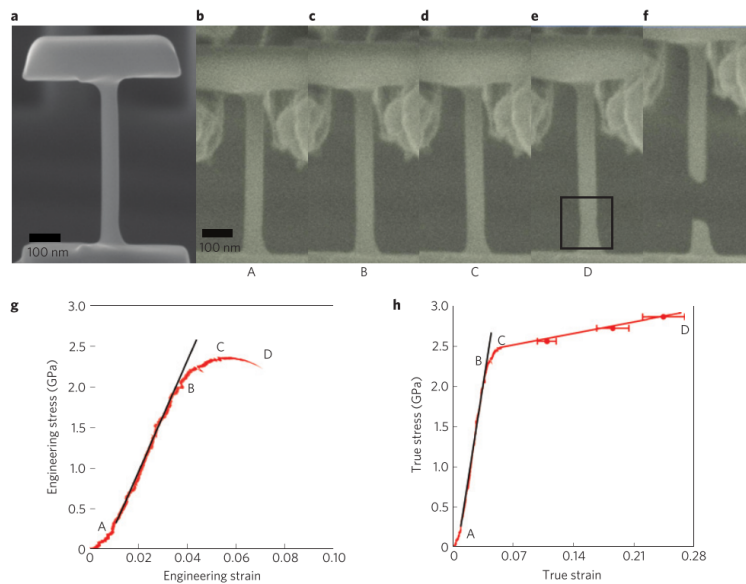
Complex stress states are also observed to affect shear banding behaviour of BMGs. Liu et al. performed axial compression experiments on a $\text{Zr}_{41.2}\text{Ti}_{13.8}\text{Cu}_{12.5}\text{Ni}_{10}\text{Be}_{22.5}$ BMG under different hydrostatic stress conditions enforced through the application of cemented carbide sleeves [139]. Results generally showed an increase in the strain to failure of the tested samples with increasing hydrostatic stress, which were further found to correlate with a branching process of shear bands, observed through SEM, which initiated at 680MPa. Similar to rolled samples the presence of branched shear bands is observed to improve ductility of BMGs. However Liu did not determine if crystallisation had occurred in the process as observed in the works of Yokoyama et al. [149], Park et al. [148] and Cao [150].

Elastic Properties

It is widely reported that shear and bulk moduli affect the ductility of crystalline materials [164], as these dictate the way in which stresses are accommodated within the crystalline matrix. For example, materials with large shear moduli relative to bulk moduli favour the generation of high stresses such that stresses are relieved through brittle cleavage, whilst the opposing case favours plastic deformation. Based on this, Pugh theorised that a ratio between the shear and bulk moduli (Pugh's ratio = G/B ; which is also directly related to ν) could be used to quantify the plasticity of a material [165], which was found to agree well with empirical observations [166]. Chen et al. was the first to report this effect in Pd rich BMGs through constrained load mode tests (indentation),



(a) A plot showing the difference in plasticity depending on the dimensions of a $Zr_{35}Ti_{30}Co_{69}Be_{29}$ metallic glass (machined from bulk)



(b) SEM observations of the nano tension test with the stress strain curves. Ductile plasticity is clearly observed with necking even occurring at point 'D' just prior to failure, indicating homogeneous plastic flow at the 100nm length scales.

Figure 3.21: Evidence of ductile plastic flow of a BMG composition at length scales of 100nm (Adapted from [156]).

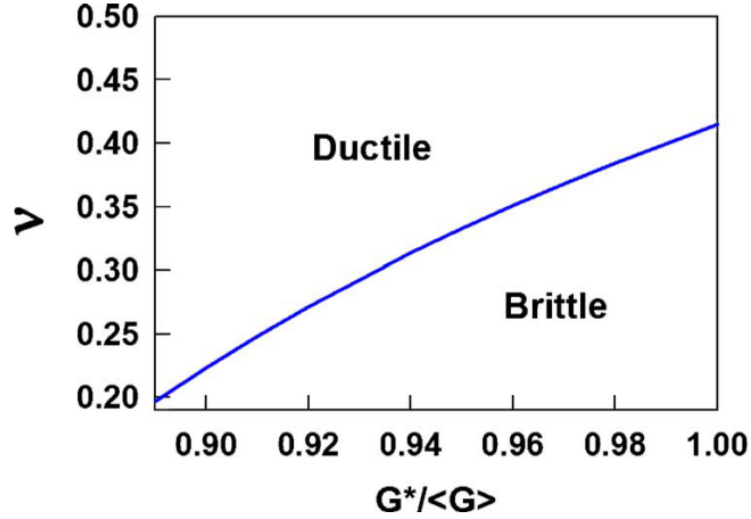


Figure 3.22: The critical value of ν separating ductile and brittle behaviours of BMGs based on local deviations of the shear modulus (G^*) compared to the bulk shear modulus ($\langle G \rangle$) (reproduced from [36]).

however the development of new BMG chemistries over time has found that this relationship applies across all BMG chemistries [36, 86, 87, 167]. For BMGs, high ν or low G/B values indicate the potential for ductile BMG behaviour due to low shear moduli allowing the dissipation of shear stresses through STZs with low activation energies (easy shear imposed by the low shear modulus in comparison to the required volume dilation imposed by the bulk modulus) [115]. Critical values of ν and G/B for all BMGs have been reported to be 0.32 and 0.4 [49], above which ductile inhomogeneous deformation can be induced (given the correct conditions), and vice versa.

Poon et al. [36] took the observation of the relationship between ductility and Pugh's/Poisson's ratio a step further by noting that plastic flow in BMGs differs from that of crystalline materials as plasticity is initiated with localised deformation units (STZs) rather than homogeneously throughout the structure (dislocations). Therefore localised variations in the concentration of flow units (characterised by the local variations in the shear modulus and consequently the Poisson's ratio) affect the deformation behaviour of a BMG, as it is only the stresses at localised stress concentrations that need to be relieved in order to initiate ductile behaviour [36]. Therefore, the bulk critical values of ν and G/B that would otherwise govern the ductility of BMGs can be adjusted if local deviations of shear modulus compared to the bulk are significant enough in regions of high stress concentrations; ductile behaviour can be observed in a BMG which is expected to show brittle behaviour, if localised deviations of the shear modulus are high enough, and vice versa. Therefore, STZs act as weak links in BMG matrix, which can initiate shear bands in macroscopic observation of ν would have been expected to appear brittle and vice versa, as outlined in Fig.(3.22).

Poon's work has significant implications regarding the relationship between structural evolution and plasticity. For example rapid quenching of a BMG with a naturally low ν would indicate a brittle glass in its rest state. However the effect of quenching introduces local volumes of material whose shear modulus will deviate greatly from the bulk, thereby providing sites for shear bands to initiate over brittle cleavage of the material [36]. Based on this, the effect of elastic properties on shear band behaviour is at the core of many of the factors we have previously considered to affect shear band propagation:

- Deformation conditions:

The temperature dependency of shear modulus is much stronger than the temperature dependency of bulk modulus [115]. Therefore deformation under high temperature environments favours plastic yield over brittle cleavage due to enhanced reductions of shear modulus over the bulk modulus. In addition, application of hydrostatic stresses to BMGs is believed to aid the generation free volume [139], giving rise to greater variations in the localised shear modulus compared to the bulk, thereby promoting plastic yield over brittle cleavage.

- Atomic packing:

Glasses that exhibit strong icosahedral packing (i.e. strong glasses) have both a high rest shear modulus and little localised variation in shear modulus, and thus exhibit brittle behaviour based on Poon's arguments [36]. However glasses that have more open structures (i.e. fragile glasses) will have more regions of localised shear modulus variations, and will therefore favour plasticity through the formation of multiple shear bands. This further affects how shear bands evolve and propagate, as the broken structure of a shear band will represent a localised reduction in the shear modulus [36], which is further aided by the high temperature aspect of a shear banding. However both of these processes also aid in the relaxation of the structure, thereby providing the means for stable shear band flow.

- Processing history:

Quenching BMGs from high temperature environments produces a more open agitated structure in accordance with the PEL. In addition, high strain rate inelastic deformation of BMGs has been noted to generate free volume [131]. As such, BMGs that have undergone a thermomechanical treatment that features either of the above are more likely to show ductile behaviour over BMGs that have not.

Other factors

Plasticity of BMGs can be influenced by the mode of deformation. Under tension, the majority of BMGs (with exceptions [21]) show no plasticity when deformed in the inhomogeneous deformation regime. However under compression or other constrained loading modes, plasticity can be achieved to relatively high levels. This is demonstrated in Fig.(3.23), where tests performed on $Zr_{57}Nb_5Al_{10}Cu_{15.4}Ni_{12.6}$ by Connor et al. [168], achieved $\approx 0.5\%$ plastic strain in compression, but no plastic strain in tension.

In addition to intrinsic factors, extrinsic factors must also be considered. It is widely observed that BMGs with good GFA and low fragility (strong glasses) tend to exhibit reduced plasticity. This has been argued through the PEL to be that the energy required to generate α transitions of strong glasses is greater than that of weaker ones. However Madge et al. [169] noted that glasses with good GFA often have high levels of zirconium or copper content, which are thought to improve GFA due to their ability to bind with excess oxygen in the melt to leave behind a high GFA melt. This binding produces zirconium and copper oxides, which can separate from the glass melt to form inclusions. These inclusions then act as stress concentrators such that when the material is deformed, brittle behaviour is observed macroscopically. However microscopic observations of the plane of deformation show high levels of plasticity in the vicinity of the inclusions. Therefore is the brittle nature of some BMGs due to extrinsic factors and not a true reflection of the materials fundamental behaviour? Whilst further work is required to determine if this is the case, the study acknowledges that plasticity behaviours of some other MG compositions cannot be attributed to extrinsic factors in this manner.

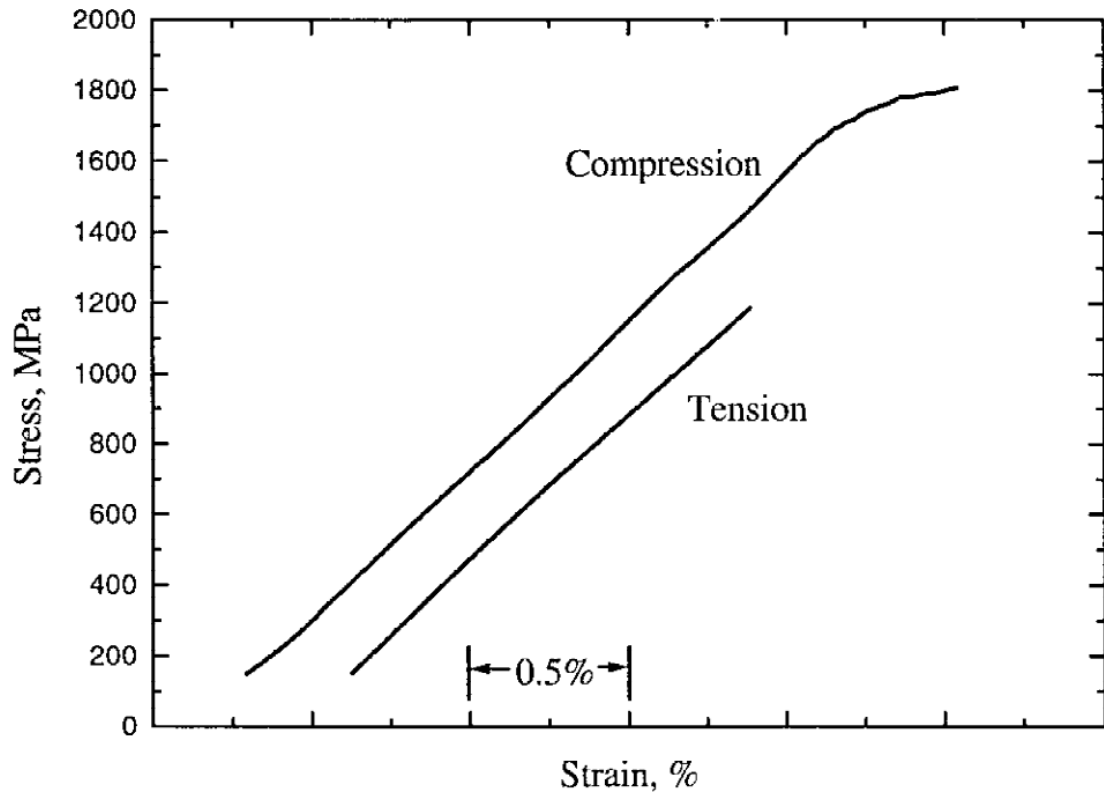


Figure 3.23: A plot showing the difference in plasticity in compression and tension for the $Zr_{57}Nb_5Al_{10}Cu_{15.4}Ni_{12.6}$ BMG (reproduced from [168]).

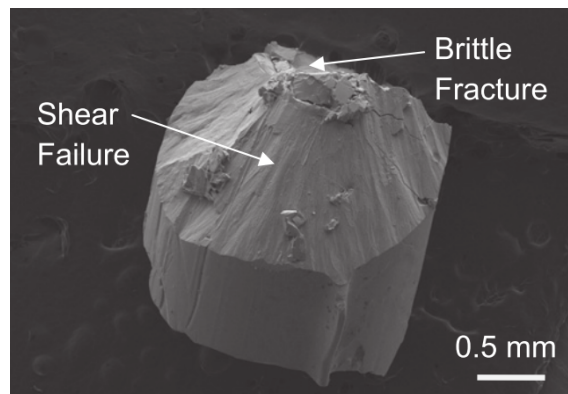


Figure 3.24: SEM image showing the brittle initiated fracture of a BMG under compression caused by an oxide inclusion, and the secondary plastic shear failure beyond the inclusion indicating significant plasticity (reproduced from [169]).

To summarise, there are many other dependencies of BMG yield, some of which will be explored later. Despite the range of behaviours that have been observed, plastic behaviour is an area of BMG behaviour that is still poorly understood, with linkages between microscopic processes and macroscopic observations still being unproven and disputed. From discussion of elastic behaviour, 2 atomic scale models were introduced, the free volume model and the STZ model. Investigations, suggest that STZs are the dominant model of deformation in BMGs as the non linearity of deformational resistance requires deformation units comprised of more than singular atoms [103]. However there is no experimental evidence suggesting that the free volume model is invalid and cannot occur alongside the STZ model. Therefore, by assuming that all plastic deformation in BMGs is the sum of local strains accommodated by STZs, the plasticity models concerning the activation of STZs under different conditions can be theorised to provide a basis from which macro-scale plasticity observations can be built.

3.4 Methods for assessing mechanical behaviours of BMG materials

In addition to understanding the mechanisms and mechanical behaviours of BMGs, measuring the physical mechanical properties of such materials is also difficult. Limitations to sample volumes means that manufacture of standard mechanical testing pieces, such as tensile dog-bone specimens, is often difficult or impossible for certain BMG compositions. To that end, small scale testing methods must be utilised to evaluate the mechanical properties of BMGs, for both elastic and plastic deformation. Some of the key testing techniques for evaluating these properties have been outlined below:

3.4.1 Ultrasonic testing

Ultrasonic tests can simply relate the velocity of a longitudinal and a transverse phonon modes to the shear and Young's modulus of a material based on relationship between the wave velocity and the stiffness of the inter-atomic bonds when subjected to deformation and distortion:

$$E = \rho v_l^2 \quad (3.21)$$

$$G = \rho v_t^2 \quad (3.22)$$

In the case of isotropic materials, ultrasonics can be used to calculate the C_{ij} elastic constants. As BMGs are amorphous it is a reasonable assumption that these materials are isotropic so long as anisotropy has not been induced through thermomechanical processing as outlined earlier. In addition, due to the level of tetrahedral packing in BMGs over SRO and high density, they can be treated as cubic materials in terms of transmission of phonons. Therefore the elastic constants can be reduced from the full 36 elements to 3:

$$E = \frac{(C_{11} - C_{12})(C_{11} + 2C_{12})}{(C_{11} + C_{12})} \quad (3.23)$$

$$\nu = \frac{C_{12}}{C_{11} + C_{12}} \quad (3.24)$$

$$G = C_{44} \equiv \frac{C_{11} - C_{12}}{2} \quad (3.25)$$

Elastic constants defined through this method can verify the level of anisotropy within a material. This method was utilised by Concustell et al. [114] to show that inelastic reversible loading can induce an anisotropy in the elastic response of a material. Plummer also used these equations to determine the effect of the Cauchy pressure criterion (defined earlier; the equivalence outlined in Eq.(3.25)), and defined a classification system based on the deviation of a BMG from this criterion [17].

The assumption of an isotropic solid can be extended to include the measurements of Debye temperatures (θ_d) and by extension heat capacity, so long as the BMG material can be considered as an elastic continuum, which is approximated due to the long phonon wavelengths in comparison with the inter-atomic spacing [92,110].

The use of ultrasonics has proven useful for identifying relationships between elastic moduli and other properties in BMGs. Wang used the technique on a range of BMGs and found measurements of the elastic moduli were in good agreement with values calculated from a rule of mixtures approach [40]. This work was then taken further to show the relationship between plasticity, GFA, T_g and fragility on elastic constants, as outlined in Fig.(3.8) [40].

3.4.2 Nano-indentation

Nano-indentation is an ideal testing method for BMGs as the test volume and sample requirements for such tests are both minimal. The following outlines the methods surrounding measurements of elastic moduli, hardness and creep. It is noted that indentation techniques have also been used to probe fracture toughness, where references [170–185] are recommended sources of information.

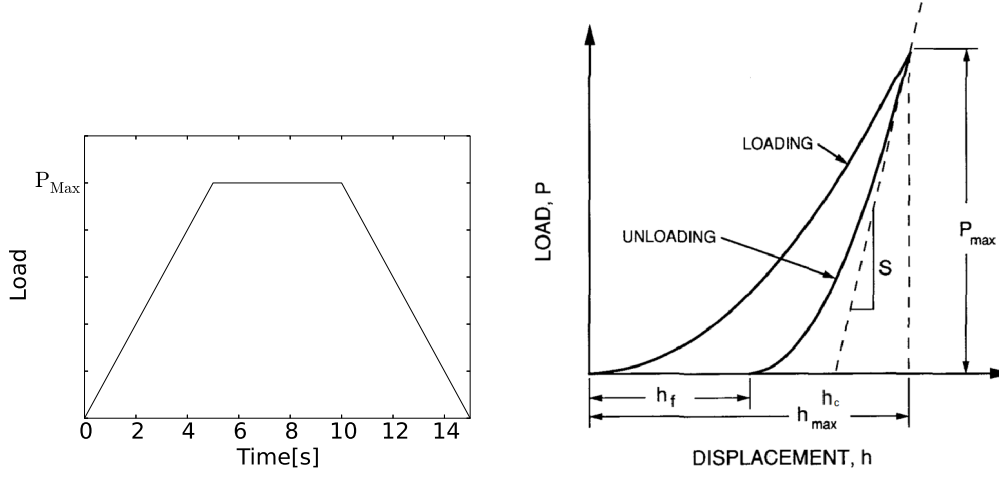
Modulus and hardness measurements

In recent years, indentation (particularly instrumented nano-indentation) has become a popular method for fast mechanical characterisation of metallic materials. Hardness measurements through nano-indentation are based on the same basic principles as hardness measurements through non-instrumented indenters. If a simple load profile like that outlined in Fig.(3.25a) is used to engage the indenter tip into a test material, the hardness is defined as the ratio between the force and contact area between the indenter tip and the material, effectively describing the contact pressure that can be sustained by the test material prior to plastic yield.

$$H = \frac{P_{max}}{A_c}. \quad (3.26)$$

P_{max} is defined by the peak load applied during the test and therefore requires no detailed interpretation at this stage. However values of A_c require some interpretation of the measurement data, as unlike P_{max} , A_c is not directly observable and must be extracted from P - h - t data. By assuming that the indenter tip is infinitely rigid in comparison to that of the material being tested, A_c can be related to the indenter contact depth (h_c) through a tip area function (TAF) by simple geometric arguments.

In the case of standard nano-indentation, Berkovich shaped tips are usually employed due to the accuracy to which these can be manufactured; it is significantly more difficult to grind a standard Vickers (4 sided pyramid) tip to an infinitely sharp point than a Berkovich tip [186]. Other tip geometries are available, but in the case of the commonly utilised Berkovich tip, knowledge of the tip geometry and its self similar nature allows a simple relationship to be formulated between the



(a) A typical constant load hold (CLH) loading profile commonly used to determine E_r and H through nanoindentation (b) A schematic load displacement curve adapted from [187].

Figure 3.25: Load profiles utilised in all testing regimes

indenter tip penetration depth and the area of the tip in contact with the material defined by

$$A(h_c) = 24.56h_c^2. \quad (3.27)$$

Whilst Eq.(3.27) describes the ideal Berkovich tip geometry, tip defects accumulate to shift the actual tip geometry away from this. To that end, accurate descriptions of the Berkovich tip geometry are defined by Eq.(3.28), where $C_0 \rightarrow C_8$ are determined by fitting the tip response to an indentation test in a mechanically stable material such as fused quartz. By choosing fitting constants such that subsequently derived the reduced modulus (discussed later) and hardness values over a range of material penetration depths match the expected values for fused quartz, a better representation of the tip area function can be derived.

$$A(h_c) = C_0h_c^2 + C_1h_c + C_2h_c^{1/2} + C_3h_c^{1/4} + C_4h_c^{1/8} + \dots + C_8h_c^{1/128} \quad (3.28)$$

Oliver and Pharr [187] introduced the current method for evaluating the Young's modulus of a metal using instrumented indentation. The value of h_c represents the contact depth of the indenter, qualitatively described as the penetration depth of the indenter tip accommodated through plastic deformation only. This value can therefore be calculated as the difference between the maximum penetration depth from the indenter tip and the amount of elastic recovery during unloading of the material.

$$h_c = h_{max} - \xi \frac{P_{max}}{S}, \quad (3.29)$$

$$S = \frac{dP}{dh}. \quad (3.30)$$

ξ is a geometric correction factor (≈ 0.75) and S is the stiffness response of the indenter-material system during unloading, when the mechanical response is assumed to be purely elastic. S is determined through a method defined by Oliver and Pharr [187], whereby the unloading curve of

the nano-indentation data is fitted to

$$P = B(h - h_f)^m. \quad (3.31)$$

This data can be applied to Sneddon's work, who produces a solution to the compliance of a material in contact with an axi-symmetric indenter (which a Berkovich tip can be approximated to [188]) in an elastically isotropic half space.

$$S = 2\beta\sqrt{\frac{A}{\pi}E_r} \quad (3.32)$$

A and β are fitting constants and E_r is the reduced modulus, which is a measure of the elastic compliance of both the indenter tip and the tested material. With knowledge of the indenter tip's elastic modulus and Poisson's ratio, and the Poisson's ratio of the test material, the actual elastic modulus of the material can be calculated through:

$$\frac{1}{E_r} = \frac{(1 - \nu^2)}{E} + \frac{(1 - \nu_i^2)}{E_i}. \quad (3.33)$$

Visco-elasticity

Models of BMG deformation have highlighted that the deformation behaviour of the material can be described as a combination of a spring and dash-pot response [79]. Indentation methodologies have been used as a means to separate these behaviours [79, 110, 189]. These mechanisms have then been linked to individual structural features in BMGs (namely through the core and soft shell model) such that information regarding MG deformation behaviours can be probed further through improvements to computational simulations with data from such measurements.

Indentation creep

Creep in metals is characterised through steady-state creep due to its longevity. Several deformation mechanisms contribute to creep, but analysis can be simplified by attributing deformation entirely to a single dominant mechanism defined by a specific stress and temperature condition [33]. The deformation behaviour of each mechanism is defined by Eq.(3.34), where ' n ' identifies the dominant deformation mechanism behind steady-state creep [33, 190–192]. The terms for Eq.(3.34) are outlined in Tab.(1).

$$\frac{d\varepsilon}{dt} = \frac{AGb}{k_bT} \left(\frac{b}{d_g}\right)^{p_g} \left(\frac{\sigma_i}{G}\right)^n D_i \exp\left(-\frac{Q_i}{k_bT}\right) = A\sigma^n \exp\left(-\frac{Q}{RT}\right). \quad (3.34)$$

Each creep mechanism is either diffusion, dislocation or viscosity controlled [193]; creep strain rate ($\dot{\varepsilon}$) is either controlled by the rate at which atoms diffuse to free otherwise locked dislocations, or the extent the dislocation velocity is restricted by obstacles in the metallic structure (precipitates, dislocation interaction and lattice resistance). The different steady-state creep mechanisms are fully described in literature [190, 192, 194, 195].

Conventional creep tests uni-axially load a test specimen of a specific geometry [196] under tension or compression (often at elevated temperatures in the case of metallic materials). Stress

and strain is simply measured using

$$\sigma = \frac{P}{A} \quad (3.35)$$

$$\varepsilon = \frac{\Delta L}{L_o}, \quad (3.36)$$

where P , A , ΔL and L are the applied load, the area which the load acts upon, the change in length along the direction of the applied stress, and the length of the specimen prior to any deformation respectively.

The strain rate ($\dot{\varepsilon} = \frac{d\varepsilon}{dt}$) during steady-state creep can be obtained from Eq.(3.36), which in conjunction with the data from Eq.(3.35) provides the necessary strain rate, stress and time ($\dot{\varepsilon}$ - σ - t) information required to calculate ‘ n ’, ‘ Q_i ’ and ‘ A ’; the three variables required to fully characterise the steady state deformation of a particular deformation mechanism. The stress exponent of the material can be found by taking the gradient of the plot of $\ln \dot{\varepsilon}$ vs. $\ln \sigma$ (see Eq.(3.34)) [191, 192];

$$n = \frac{\ln \dot{\varepsilon}}{\ln \sigma}. \quad (3.37)$$

A similar approach can be used to obtain the activation energy of a creep mechanism, whereby several tests at different temperatures are performed with stress and strain data being measured at a particular yet consistent value of displacement across all testing temperatures [191, 192]. The gradient of $\ln(\dot{\varepsilon})$ vs. the reciprocal of the temperature ($\frac{1}{T}$) allows the determination of the activation energy. Finally ‘ A ’ can be evaluated from the data using the intercepts of the log plots mentioned, or through independent microstructure analysis to evaluate all the terms that A is made up of [191, 192].

Conventional creep tests apply a uniform stress field to the test volume in the test specimen over time to produce a measurable strain rate. Indentation can be applied, where the indenter is loaded onto a material in a specific way, measuring the stress and strain rate through observations discussed later. Using indentation to provide an informationally comparative, yet quicker, testing method requires the consideration of an extra level of complexity. The stress applied in an indentation creep test is not uniform, as demonstrated in Fig.(3.26). The result of this non-uniformity is a complex transient deformation field, which produces a position-dependent and constantly changing strain rate as the indenter penetrates the sample. Therefore, unlike in conventional testing, the definition of stress and strain rate in an indented material is ambiguous. The only unambiguous observables generated from an indentation creep test are the applied load (P), the penetration/contact depth of the indenter tip (h_c) and time of the measurement (t) (P-h-t). In the literature, *representative* stress and strain rates are employed (Eq.(3.38) and (3.39) respectively) to convert P-h-t data into $\dot{\varepsilon}$ - σ - t data to characterise creep behaviour [191, 192];

$$\sigma \propto H = \frac{P}{A_c} = \frac{P}{\Psi h_c^2}, \quad (3.38)$$

$$\dot{\varepsilon} = \frac{1}{h} \frac{dh}{dt} = \frac{1}{\sqrt{A}} \left(\frac{d\sqrt{A}}{dt} \right) = \beta P^n. \quad (3.39)$$

In addition to the steady-state deformation approximation, other factors must also be considered when comparing uni-axial creep tests to indentation ones. For example, the effect of stress and strain rates have been reported to significantly affect mechanical property observations through indentation of some alloys. Wu et al. [197, 198] reports this for Cu-Zr based metallic glasses, which show underestimates of Young’s modulus values when tested at high strain rates. In addition the

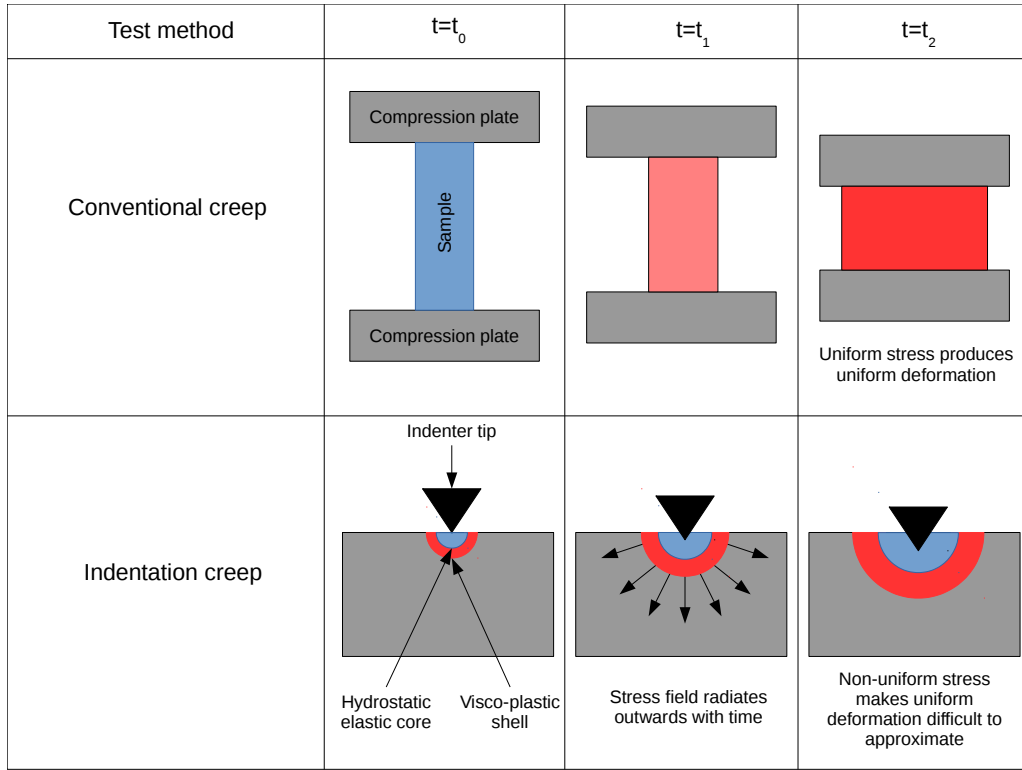


Figure 3.26: A schematic showing the evolution of stress fields in conventional and indentation creep tests.

depth of the indent is also thought to reduce both Young’s modulus values and hardness results. These effects are argued to be caused by the creation of free volume within the glass medium, which increases the potential for annihilation of free volume during deformation (the source of plastic deformation in MG) and increases atomic mobility to the disturbed packing during deformation (aids in deformation) [197, 198]. Other researchers have found that the stress exponent (determined through the method outlined in section (3.4.2)) is also dependent on the strain rate during indentation [199].

Whilst indentation size effect and strain rate dependencies of creep are of academic interest and can be studied with the aid of indentation, these factors make it difficult to replicate conventional creep test conditions, important for validating the use of indentation as a method to measure visco-elastic properties. In addition, the effects observed through indentation call into question whether the 3 factors that describe creep are enough in their scalar form to characterise viscoelastic properties, or is more information required to fully replicate the behaviour of creep under stress states comparable to that produced by indentation experiments.

The experimental method in which indentation creep tests are carried out has significant influence on how the data should be handled. Researchers tend to use the one of the following loading regimes in order to measure creep through indentation: Constant Load Hold (CLH) [191, 192], Constant Strain Rate (CSR) [190, 191, 200], Indentation Relaxation Loading (IRL) [192, 201] and Constant Rate of loading (CRL) [191, 192, 202]. Of these, the CLH is by far the most commonly used due to the simplicity of the experimental method [192]. A constant load is applied to the material by the indenter tip and displacement of the tip with respect to time is then recorded. As the indenter tip penetrates the material, the applied stress reduces due to the increase of the tip contact area (Eq.(3.35)). Eventually the applied stress drops just below the yield stress of the material, thus moving the deformation from time independent plastic deformation, to time

dependent visco-elastic deformation.

Many researchers use multiple pre-load cycles and sub-peak load hold to minimise primary creep and remove time independent plastic deformation, leaving only visco-elastic deformation (i.e steady-state creep) [195]. Load hold periods of 100s-1000s of seconds are utilised to achieve an approximate steady-state condition. Fig.(4.5b) outlines a potential creep loading cycle.

Despite the precautions taken to obtain steady state creep, the transient deformation field will always effect CLH results. This is supported by the poor CLH result's reproducibility (e.g. [190]). This is thought to be due to a variation in the depth at which an approximate steady-state regime is reached; different penetration depths result in different deformation fields (see Fig.(3.26)), which in turn will produce different strain rates. In addition, this method limits the accessible stress range, which may result in low stress mechanisms such as Nabarro Herring and Coble Creep convoluting pure power-law creep data [190].

There has been some suggestion in recent works regarding the practice of indentation creep tests to provide relevant comparative results to conventional creep tests. Su et al. [203] have shown that CLH, CLR and CSR tests are comparable to conventional uni-axial tests by correcting the indentation creep data with an elastic transient value,

$$h_{elastic} = \sqrt{\frac{\pi P}{2E^* \tan \theta_i}}. \quad (3.40)$$

Su et al. claim that as long as the depth of penetration is greater than $10 \times h_{elastic}$, then the data can be corrected and directly compared to conventional compression creep tests [203]; a correction which may remove indentation size effects from results [194, 195]. However their work was carried out on $n = 1$ materials, and needs further investigation [203], though this analysis may be suited to Bulk Metallic Glasses ($n_{(MG)} = 1$).

In addition to the difficulties surrounding the experimental aspect of indentation creep, there are other factors which need to be considered regarding the way the data is analysed. Researchers use a range of data handling methods to convert the indentation P-h-t data into σ - $\dot{\epsilon}$ -t data from their tests. These methods fall into two distinctive categories. The first method involves fitting the h-t data to an equation of some form, which allows the fitted data to be subjected to conventional analysis methods outlined in Sec.(3.4.2). These equations have their origin based in empirical or theoretical roots. For example $h(t) = h_0 + a(t - t_0)^m + kt$ is an equation first put forward by Li et al. [195] and is based purely on empirical observations. However Li et al. [204] and Wei et al. [199] use $h(t) = h_e + \sum_{i=1}^n h_i(1 - e^{-\frac{t}{\tau_i}})$, which is based on the Kelvin model of visco-elastic deformation, and attempts to characterise the viscous and elastic components of the deformation as a superposition of two equations in amorphous metals. Fitting equations effectively removes the influence of scatter in the measured experimental data on further analysis (but the scatter is still accounted for in the error of the fitting parameters). However the range of equations used in the literature may produce a wide range of behaviours, from factors such as anomalies introduced into the analysis from terms during differentiation for determining the representative strain rate (a particular issue for fitted equations whose origin is grounded in empirical roots).

The second method involves a manual analysis of the data, with the strain rate, stress exponent and activation energy evaluated through fitting a tangent to data over a small data window such that the surrounding data can be approximated to be linear. This approximation may be extended to larger data windows, whereby the surrounding tangential data is relatively symmetrical about a considered point during steady state creep deformation. The manual analysis method is subject to scatter in the measured data and is heavily influenced by sudden displacement events, such as pop-ins. These factors directly influence the tangent measured over a small data window, an

effect which is minimised by the fitting equations method because fitting an equation takes the into account the behaviour over the entire experiment. However, the manual analysis method is not subject to anomalies introduced by differentials of fitted displacement equations when attempting to evaluate the strain rate.

Chapter 4

Experimental Methods

4.1 Sample synthesis, preparation and confirmation

4.1.1 Arc melting and casting

Metallic glass materials were prepared through arc-melting bulk high purity elements, handled with clean latex gloves. The elements were prepared by cleaning with 4000 grit grinding paper (where possible) and thorough irrigation with isopropanol prior to sectioning for weighing. Masses of the required elements were calculated through atomic percentage calculations such that the constituent element mix came to no more than 5 g in total. Masses of each element were weighed to within 0.001 g of the target weight with the Precisa Series 320 XB mass balance. Elements were then ultrasonically cleaned in isopropanol for 5 minutes before being placed onto one of the outer crucibles of the copper melting hearth of the MAM1 Edmund Bühler arc melter (Fig.(4.1b)). Placement of the elements was done such that relatively large material pieces covered smaller material pieces to optimise the initial melting of the mixture. A CP titanium getter was placed in the center crucible position and the arc melter chamber was sealed and evacuated to 0.1 torr. The chamber was then backfilled with argon to 0.3 bar and evacuated again to 0.1 torr. This cycle was repeated a further 3 times, where upon the 3rd evacuation, the chamber was left to achieve an optimum vacuum of $\leq 6 \times 10^{-5}$ torr.

Once vacuum was achieved, the arc melter chamber was backfilled with argon to 0.7 bar and water cooling was applied to the copper hearth. The getter was then melted (to reduce residual oxygen content within the chamber) followed by the melting of the materials of a single BMG composition for no more than 10 seconds. This combined the elements into a single mass. Melts continued such that the getter was melted prior to every melt of a element mixture to ensure oxygen content of the chamber remained low. Once all melts were completed, the element mixture masses were flipped and remelted a further 4 times in the same manner to optimise mixing. This constitutes the creation of the master alloy ingots, which were removed from the chamber and weighed to ensure mass losses from the melting processes remained $\leq 0.1\%$. Samples with negligible mass loss were ground with 4000 grit paper and ultrasonically cleaned in isopropanol in preparation for casting.

For casting, individual master ingots were placed back into the arc melting chamber with the casting set-up, as shown in Fig.(4.1d), with a titanium getter and the appropriate casting mould, outlined in Tab.(4.1). The chamber underwent the same evacuation procedure as previous. During the final evacuation, prior to full evacuation to $\leq 6 \times 10^{-5}$ torr, the casting pressure was set, defined by the casting mould selected (as outlined in Tab.(4.1)). The chamber was then left to evacuate



(a) MAM1 arc melter in the melting only configuration.



(b) MAM1 arc melter in the melting only configuration.



(c) MAM1 arc melter in the melt and casting configuration.



(d) MAM1 arc melter in the melt and casting configuration.

Figure 4.1: MAM1 arc melter configurations for melting and casting.

| | | | | |
|--|---|---|--|---|
| Mould image |  |  |  |  |
| Mould Diameter [mm] | 3 | 2 | 1 | 3,2,1 |
| Cast pressure [$\times 10^{-1}$ torr] | 5.5 | 4 | 1.5 | 1.5 |

Table 4.1: Typical casting pressures utilised for casting BMG melts into different water cooled copper moulds (cast pressures for Pd based BMGs melts were set to $\leq 6 \times 10^{-5}$ torr for all moulds due its high melt viscosity).

again to $\leq 6 \times 10^{-5}$ torr.

Once vacuum was achieved, the water cooling system was switched on and left for a minimum of 2 minutes to ensure the coldest conditions for the best possible quench rate. The chamber was then backfilled with argon to 0.7 bar and the getter was melted to capture any remaining oxygen in the chamber. The master ingot was then fully melted and the casting chamber was opened to allow suction casting of the material into the water cooled copper mould. Once cooled, the cast was taken from the system and excess material from the casting was removed. The cast rods were placed in the Struers Minitom for sectioning with an aluminium oxide blade with rotation speeds limited to 300rpm. 2mm of material was removed from both the top and bottom of the casts to remove any material that may have crystallised due to ineffective cooling from the copper mould. The rest of the rod was then sectioned as appropriate for further study.

4.1.2 XRD structure verification

Two 4mm sections of the cast rods were taken from each end of the rod to verify the materials glassy state. Each sample was cold mounted in Struers Epofix cold mounting resin such that the curved rod surface aligned with the base of the mount. The rods were ground and polished with the Buehler Automet 250 Pro, such that half of the rods were removed, exposing a mirror finished cross section of the rods. Prior to testing, the prepared surfaces were observed under cross-polarised light of the Nikon Eclipse LV150 microscope to determine if any obvious crystalline structure was present. Materials showing signs of crystallisation, like that outlined in Fig.(4.2), were discarded, whilst materials showing no signs of crystallisation were broken from their mounts and observed through XRD analysis.

XRD analysis was performed on suspected glassy materials with the Siemens D5000 $\text{CuK}\alpha$ X-ray diffractometer over 15° to 75° with step sizes of 1°min^{-1} . The samples were continuously rotated during exposure to maximize the area of sample exposed to the x-rays. Results of the XRD trace were processed by comparing the results to a test performed for the sample holder only under the same test conditions. Peaks presented by the sample holder were removed from the data to give an XRD trace from the sample only. The presence of an amorphous phase was identified from XRD traces that show a broad diffraction peak spanning $\approx 20^\circ$ to 60° in range, centred roughly at $\approx 40^\circ$ as shown in the example Fig.(4.3). XRD traces for the successful detection of amorphous phase are outlined in Sec.(9.3) of the appendix.

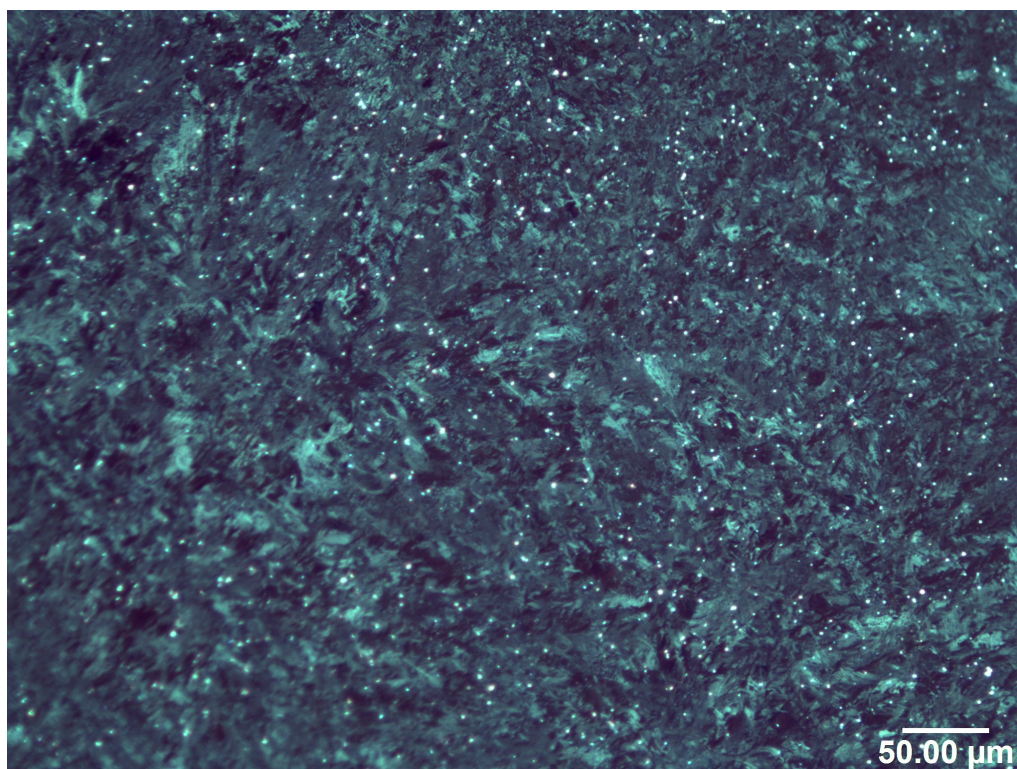


Figure 4.2: Polarised micrograph of Zr₅₄Cu₄₆ showing clear crystallisation and was therefore discounted from further analysis.

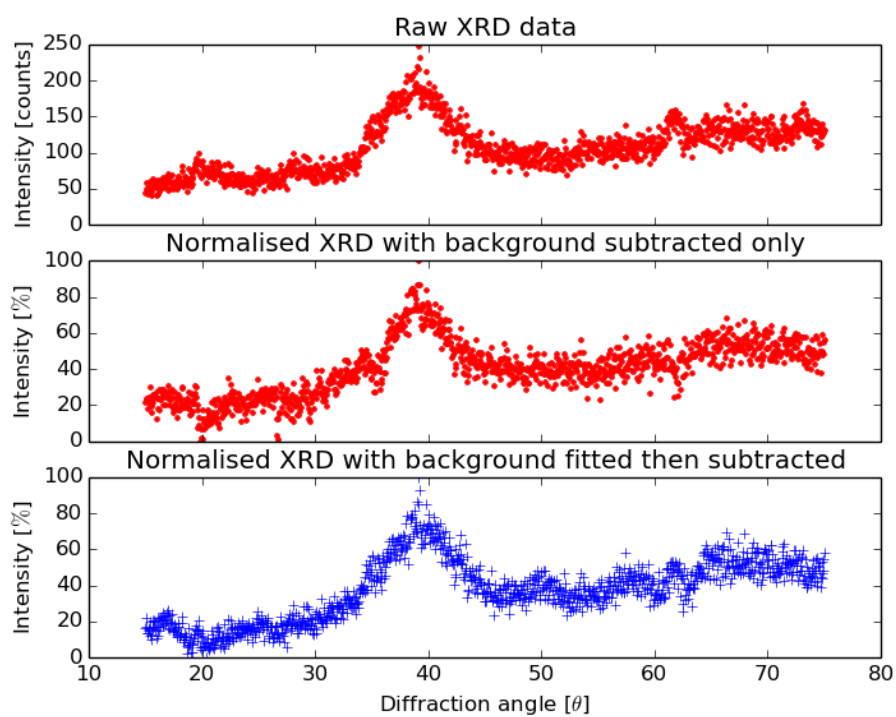
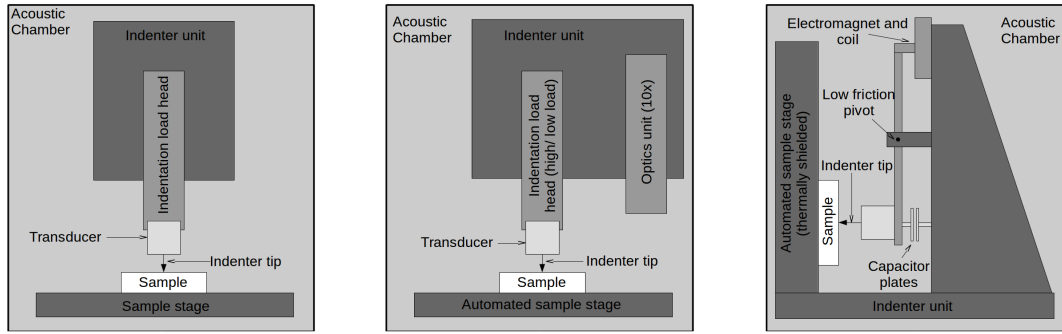


Figure 4.3: An example XRD trace confirming the presence of an amorphous structure in Zr₄₄Cu₄₄Al₆Ag₆.



(a) Schematic of the Hysitron Triboscope TS-70. (b) Schematic of the TI-Premier Nanomechanical testing instrument. (c) Schematic of the Micro Materials NanoTest nano-indenter.

Figure 4.4: Schematic layouts for all 3 nanoindentation systems.

4.2 Local mechanical testing

4.2.1 Nano-indentation tests

Nano-indentation tests were performed in a Hysitron Triboscope TS-70 nanomechanical test instrument attached to a Veeco Dimension 3100 atomic force microscope, a Hysitron TI-Premier Nano-mechanical testing instrument and a Micro Materials NanoTest nanoindenter as schematically detailed in Fig.(4.4). Henceforth these tests are referred to as Hysitron, TI-premier and Micro Materials platforms respectively. All test parameters are outlined in Tab.(4.2) and detailed the following sections.

Hysitron testing

Materials were mounted sectioned and polished to a $1\mu\text{m}$ finish no more than 24 hours prior to all indentation testing, with sample heights being kept to below 10mm due to limitations of sample loading in the Hysitron system. Creep, reduced modulus and hardness investigations were carried out on the Hysitron platform using the CLH method. Prior to testing, the nano-indenter's Berkovich tip area function (TAF) was calibrated to penetration depths of 20 nm to 600 nm by indenting fused quartz and fitting the indenter response at different loads to the expected load response (calculation performed by the triboscope software).

After cleaning with isopropanol and compressed air, samples were loaded into the indenter and fixed in place with the indenter vacuum holder. The system was then acoustically shielded from the surrounding environment with an acoustic hood and air table and left for 10 minutes to stabilise. The indenter tip was then brought into contact with the sample surface and allowed to scan a $50\mu\text{m}$ square of the sample. This was to ensure the sample surface was debris free and allow for further thermalisation of the sample and tip to reduce the effects of thermal drift.

The indentation load regime was then set for a grid of 3×3 indents spaced $10\mu\text{m}$ apart, centred in the middle of the $50\mu\text{m}$ scan area. For every indent, the system engaged the tip with the sample with $0.18\mu\text{g}$ of force and was held for 20 seconds whilst the drift of the indenter tip was evaluated. If the thermal drift rate was measured to be below 0.1 nms^{-1} , thermal drift was considered to be negligible in the context of the tests performed and the raw data was considered to be reliable. If the drift rate did not drop below this value over the 20 second window, the measured rates were taken every 5 seconds, averaged and subtracted from the actual test data to correct for thermal drift.

| Material | Hysitron tests | | Micro Materials tests | | Ti Premier tests | |
|---|------------------------------------|-----------------------------------|------------------------------------|-----------------------------------|------------------------------------|-----------------------------------|
| | P_{Max} [μN] | \dot{P} [μNs^{-1}] | P_{Max} [μN] | \dot{P} [μNs^{-1}] | P_{Max} [μN] | \dot{P} [μNs^{-1}] |
| Sn | 500 | 100 | 10000 | 1000 | 1000 | N/A |
| Al | 1000 | 200 | 2500 | 1000 | N/A | N/A |
| | 2500 | 500 | | | | |
| Mg | 2000 | 400 | N/A | 1000 | N/A | N/A |
| | 2500 | 500 | | | | |
| Pb | 500 | 100 | N/A | N/A | N/A | N/A |
| Ag | 1000 | 200 | N/A | N/A | N/A | N/A |
| W | 10000 | 2000 | 10000 | 1000 | N/A | N/A |
| Zr ₅₇ Cu ₂₀ Al ₁₀ Ni ₈ Ti ₅ | 10000 | 2000 | 10000 | 1000 | 10000 | 2000 |
| | 6000 | 1000 | | | 6000 | 1000 |
| | 2000 | 500 | | | 2000 | 500 |
| Zr ₄₄ Cu ₄₄ Al ₆ Ag ₆ | 10000 | 2000 | N/A | N/A | 10000 | 2000 |
| | 6000 | 1000 | | | 6000 | 1000 |
| | 2000 | 500 | | | 2000 | 500 |
| Cu _{57.5} Hf _{27.5} Ti ₁₅ | 10000 | 2000 | N/A | N/A | 10000 | 2000 |
| | 6000 | 1000 | | | 6000 | 1000 |
| | 2000 | 500 | | | 2000 | 500 |
| Ti ₄₀ Zr ₁₀ Pd ₁₄ Cu ₃₄ Sn ₂ | N/A | N/A | N/A | N/A | 10000 | 2000 |
| | | | | | 6000 | 1000 |
| | | | | | 2000 | 500 |
| Zr ₅₀ Cu ₄₀ Al ₁₀ | N/A | N/A | N/A | N/A | 10000 | 2000 |
| | | | | | 6000 | 1000 |
| | | | | | 2000 | 500 |
| Pd _{77.5} Si _{16.5} Cu ₆ | N/A | N/A | N/A | N/A | 10000 | 2000 |
| | | | | | 6000 | 1000 |
| | | | | | 2000 | 500 |
| Zr ₆₅ Cu ₁₅ Al ₁₀ Ni ₁₀ | N/A | N/A | N/A | N/A | 10000 | 2000 |
| | | | | | 6000 | 1000 |
| | | | | | 2000 | 500 |
| Ti ₃₃ Cu ₄₇ Zr ₉ Ni ₆ Sn ₂ Si ₁ Nb ₂ | N/A | N/A | N/A | N/A | 10000 | 2000 |
| | | | | | 6000 | 1000 |
| | | | | | 2000 | 500 |
| Cu ₅₀ Hf ₄₃ Al ₇ | N/A | N/A | N/A | N/A | 10000 | 2000 |
| | | | | | 6000 | 1000 |
| | | | | | 2000 | 500 |
| Ni ₄₀ Cu ₅ Ti _{16.5} Zr _{28.5} Al ₁₀ | N/A | N/A | N/A | N/A | 10000 | 2000 |
| | | | | | 6000 | 1000 |
| | | | | | 2000 | 500 |
| Zr _{57.5} Nb ₅ Cu _{15.4} Ni ₁₂ Al ₁₀ | N/A | N/A | N/A | N/A | 10000 | 2000 |
| | | | | | 6000 | 1000 |
| | | | | | 2000 | 500 |
| Ti ₃₄ Zr ₁₁ Cu ₄₇ Ni ₈ | N/A | N/A | N/A | N/A | 10000 | 2000 |
| | | | | | 6000 | 1000 |
| | | | | | 2000 | 500 |
| Cu ₄₃ Zr ₄₃ Ag ₇ Ti ₇ | N/A | N/A | N/A | N/A | 10000 | 2000 |
| | | | | | 6000 | 1000 |
| | | | | | 2000 | 500 |

Table 4.2: Materials tested for creep, moduli and hardness with each set of test parameters quantifying the peak load and loading rate used for measuring each of these properties. The single element materials represent the crystalline materials, whilst the alloys are the BMG materials.

During testing, the indenter tip loaded the material with one of the load profiles outlined in Fig.(4.5) (Fig.(4.5a) for modulus and hardness investigations, and Fig.(4.5b) for indentation creep investigations). Fig.(4.5a) is taken from Oliver and Pharr’s original reduced modulus measurements [187]. The pre-load cycles and pre-load hold in Fig.(4.5b) are inspired by Oliver and Pharr [187] and Li et.al. [195], which aims to remove much of the time dependent plasticity, reduce primary creep and to ensure good contact between the indenter and the sample, allowing for steady state creep to be approximated during the 5 minute peak load hold.

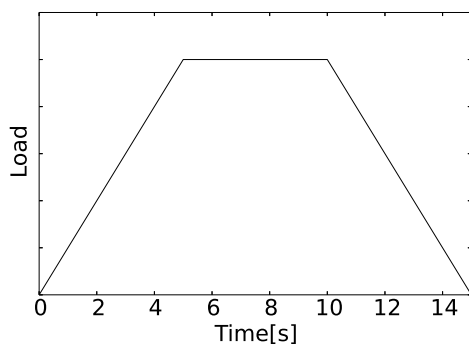
Loading rates for crystalline samples were defined by the peak load and a 5 second loading/unloading time, to give a range of strain rates over different samples, but provided a constant strain rate for multiple indents in a single sample. Investigations into creep of BMGs were performed at loads of 2000 μN , 6000 μN and 10 000 μN with loading rates of 500 μNs^{-1} , 1000 μNs^{-1} and 2000 μNs^{-1} to evaluate the effect peak load and loading rate has on indentation creep behaviour. Tests were performed at room temperature and peak loads were chosen such that the maximum displacement of the indenter did not exceed 600 nm.

Micro Materials test methodology

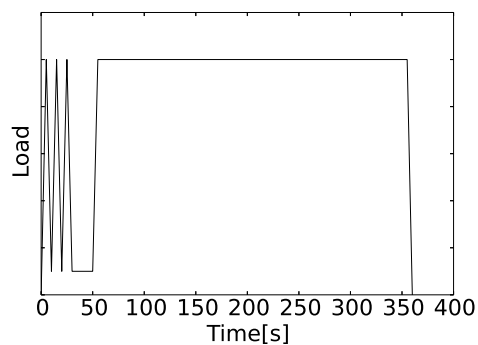
Micro Materials tests were performed at the materials science department of Imperial College London. In preparation for testing, the TAF was calibrated with fused quartz, and the electromagnet was calibrated for each sample tested. Materials were prepared in the same way as for Hysitron tests and indentation creep tests were performed using the loading regime outlined in Fig.(4.5c). The single pre load-hold-unload cycle prior to testing aims to reduce any transient deformation from the material. Following this, the material was unloaded to 10% of the peak load and held for 60 seconds prior to loading up again to start the test to evaluate and correct for thermal drift. The loading/unloading rates were set at 10mN/s⁻¹ with peak hold times of 500s. At least 4 indents were performed per testing condition, and a thermalisation time of 10 minutes was used between tests in order to reduce the effect of thermal drift. Due to time constraints, no modulus or hardness measurements were performed with this equipment.

TI-Premier Testing methodology

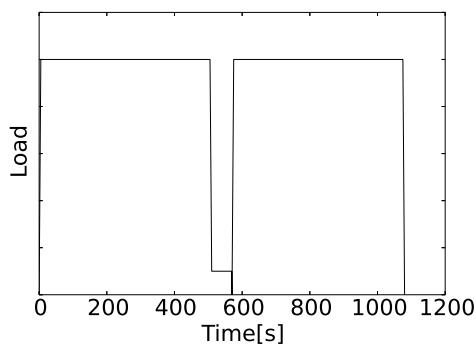
The indenter tip was calibrated prior to testing with fused quartz in the same manner as outlined for the Hysitron tests. In addition, the X-Y stage and optics also underwent calibration with a polycarbonate sample prior to each testing session. Multiple samples were loaded into the chamber at any given time and multiple indent test positions were set in 3 × 3 indent arrays with individual indent separations of 10 μm ; each array performing a different set of test conditions over different samples. An automated air indent calibration was set to be made prior to performing an array of indents to correct for drift in the transducer constants. Indents were set to perform modulus and hardness measurements on BMG materials only, using the load function outlined in Fig.(4.5a).



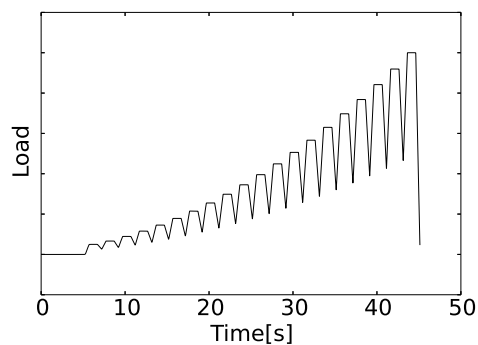
(a) Loading profile used for determining reduced modulus measurements in the Hysitron system.



(b) The loading profile used for Hysitron creep testing.



(c) Load profile used in Micro Materials investigations. The loading and unloading rates were kept constant at $10\mu\text{ms}^{-1}$.



(d) Loading profile used for the evaluation of the TAF over $500\mu\text{N}$ to $10\,000\mu\text{N}$.

Figure 4.5: Load profiles utilised in all testing regimes.

| Material | Crystalline (X) or amorphous (A) | Test load ([kg,N]) | Number of indents |
|---|--|--------------------|-------------------|
| Ag | C | 0.1 , 0.98 | 9 |
| Mg | C | 0.1 , 0.98 | 9 |
| Pb | C | 0.1 , 0.98 | 9 |
| Sn | C | 0.1 , 0.98 | 9 |
| Al | C | 0.1 , 0.98 | 9 |
| W | C | 0.1 , 0.98 | 9 |
| Ti ₄₀ Zr ₁₀ Pd ₁₄ Cu ₃₄ Sn ₂ | A | 0.5 , 4.90 | 15 |
| Zr ₄₄ Cu ₄₄ Al ₆ Ag ₆ | A | 0.5 , 4.90 | 15 |
| Zr ₅₇ Cu ₂₀ Al ₁₀ Ni ₈ Ti ₅ | A | 0.5 , 4.90 | 15 |
| Zr ₅₀ Cu ₄₀ Al ₁₀ | A | 0.5 , 4.90 | 15 |
| Pd _{77.5} Si _{16.5} Cu ₆ | A | 0.5 , 4.90 | 15 |
| Zr ₆₅ Cu ₁₅ Al ₁₀ Ni ₁₀ | A | 0.5 , 4.90 | 15 |
| Ti ₃₃ Cu ₄₇ Zr ₉ Ni ₆ Sn ₂ Si ₁ Nb ₂ | A | 0.5 , 4.90 | 15 |
| Cu ₅₀ Hf ₄₃ Al ₇ | A | 0.5 , 4.90 | 15 |
| Ni ₄₀ Cu ₅ Ti _{16.5} Zr _{28.5} Al ₁₀ | A | 0.5 , 4.90 | 15 |
| Zr _{57.5} Nb ₅ Cu _{15.4} Ni ₁₂ Al ₁₀ | A | 0.5 , 4.90 | 15 |
| Ti ₃₄ Zr ₁₁ Cu ₄₇ Ni ₈ | A | 0.5 , 4.90 | 15 |
| Cu ₄₃ Zr ₄₃ Ag ₇ Ti ₇ | A | 0.5 , 4.90 | 15 |
| Cu _{57.5} Hf _{27.5} Ti ₁₅ | A | 0.5 , 4.90 | 15 |

Table 4.3: Table showing indentation parameters used to investigate bulk mechanical behaviour of volume limited materials.

4.3 Bulk mechanical tests

4.3.1 Micro indentation tests

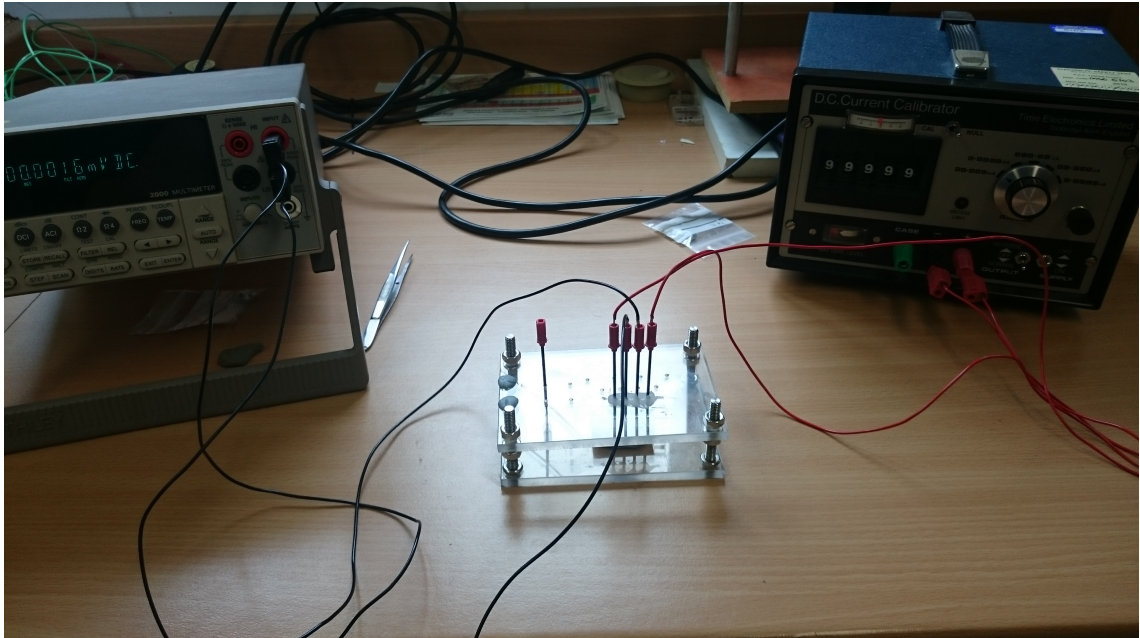
Bulk Vickers hardness values were evaluated through the Struers Durascan 70 automated indentation system. Samples were prepared in the same way outlined for nano-indentation and then placed the testing platform. Singular test indents were performed at loads between 0.05kg and 1kg (≈ 0.5 -10N) to gauge the average material response. Once completed, the test indent diagonals were used to identify test parameters from which an array of indents could be performed on samples such that a minimum of 9 indents were made whilst maintaining indent spacings of 3.5 times the indent diagonal length. Indents were performed on materials outlined in Tab.(4.3) with dwell times of 15s and loading speeds in accordance with ASTM standards [205]. Indents were measured through the systems software and hardness values were reported.

4.4 Resistivity Characterisation

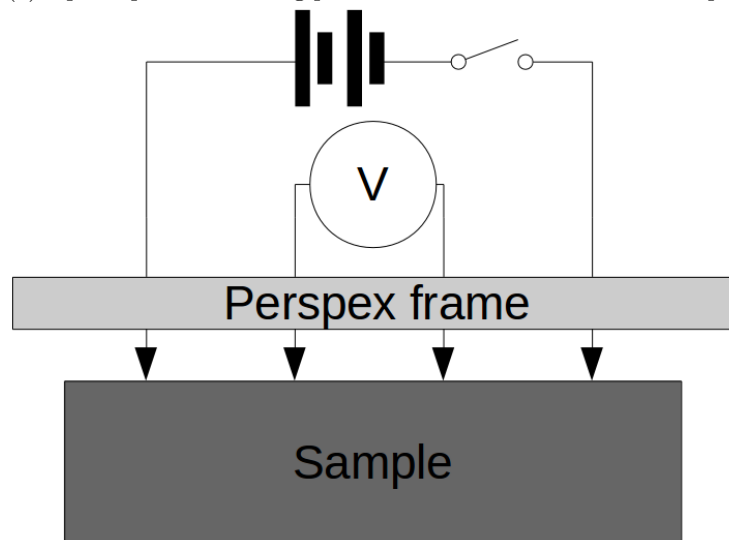
4.4.1 Static resistivity measurements

4 Point probe tests

A standard 4 point probe test, as shown in Fig.(4.6), was developed for testing all the 2mm diameter BMG casts. Four Hirschmann test and measurement MICRO-PRUEF MPS 2 0,64 FT spring loaded test probes were fixed into a perspex mount with a set spacings of 5.86 μm , 5.89 μm and 6.01 μm . Samples were fixed in place with a custom made sample holder beneath these probes, which were then subsequently lowered into contact with the sample in preparation for testing. A rest potential difference state was recorded from the sample through a Keithley 2000/E Digital



(a) 4 point probe test being performed on a 2mm BMG cast sample.



(b) Schematic of the 4 point probe testing rig.

Figure 4.6: Set-up for the 4 point probe experiment.

Multimeter in order to establish a baseline from which to measure a potential difference. A 100mA current was then applied across the sample with a Time Electronics Ltd. 1024 DC Current Calibrator unit. The potential difference due to the current was measured from the digital multimeter. The current was then disconnected and the voltage state post test was recorded again. This voltage was compared to the pre test voltage, and tests showing differences of over $0.5 \mu\text{V}$ between these values were rejected. The process was repeated 10 times per sample in order to obtain an average potential difference value between the rest and active current flow states. Resistivity values were then calculated from the average potential difference of the 10 tests through Ohm's law.

4.4.2 Dynamic resistivity measurements

Dynamic changes in resistance were measured through a prototype Shear Band Detection System (SBESD) developed and described in Chap.(7) of this thesis. Experiments that used this system are detailed as follows:

Resistivity-Compression tests

BMG casts of $\varnothing 2\text{mm}$ were sectioned into 8mm lengths and machined into miniature dog-bone shaped specimens with neck less than $\varnothing 1\text{mm}$ with a rotary drill and a titanium cutting blade, irrigated with $6\mu\text{m}$ diamond suspension polish. Necks were then polished to a $9\mu\text{m}$ finish to minimise surface cracks from which premature failure may occur. The ends of each sample were ground to the same $9\mu\text{m}$ finish to remove any lips that formed from the cutting process to give a sample with smooth parallel faces for compression.

Samples were placed into the Zwick Röel Z050 compression unit with the set-up outline in Fig.(4.7). Once the load bearing elements in Fig.(4.7) were aligned, the SBESD system was switched on and left to thermalise for 10 minutes. Adjustments to the SBESD system were constantly made to ensure the gate voltage in the amplified case ($1000\times$) remained $\approx 0\text{V}$. Once thermalised, the samples were compressed in the Zwick Röel Z050 compression unit at a rate of 0.5 mm/min until either the sample underwent catastrophic failure or a load of 25kN was achieved. SBESD data was recorded at the maximum sampling rate, and load and voltage data were synchronised post-testing using the sample fracture as a reference point.

Proof-of-concept: Enthalpic experiment

Metallic glass ribbons were coated with a thin layer of carbon through either powder deposition or an aerosolised spray. Ribbons were placed into the optical set-up, outlined in Fig.(7.14c) in Chap.(7), and ends of the ribbon were attached to the SBESD system to monitor resistance changes with laser exposor over different exposure times. The laser was then aligned with the sample as detailed in Chap.(7), and the laser power was measured pre test to ensure a power of 125mW was achieved for the 532nm laser wavelength. Once complete, the laser was pulsed onto the sample for different durations and resistance changes were recorded on the SBESD system for a total of 10 times per exposure time. Exposures times were tested in ascending order to minimise potential sample damage caused by the laser at longer exposure times for the shorter test times.

Proof-of-concept: Entropic experiment

A weak epoxy resin was made from the Struers epofix kit by mixing resin and hardener in a weight ratio 25:1 respectively (strong mix = 25:3). Once mixed thoroughly for 5 minutes, CP chromium powder was added until a relatively fluid slurry was formed. This mixture was then placed in

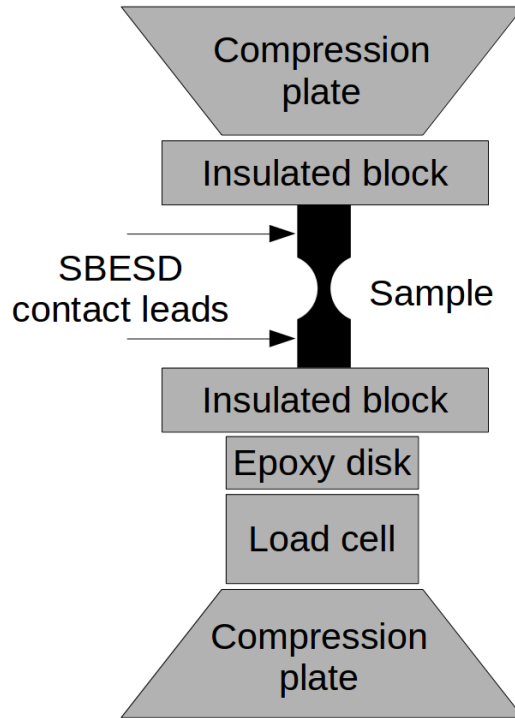


Figure 4.7: Schematic layout of the resistivity-compression experiments performed within the Zwick Röel Z050 compression unit.

Ø10mm compression dies and compressed until a steady value of 100bar was maintained, forcing the excess resin from the powder and out of the mould. Once compressed, the dies were placed in a Struers Citovac and evacuated for 3 episodes of 5 minutes to a pressure of 0.15bar remove excess air from the mixture. Samples were then left to cure for a minimum of 12 hours before being removed from their dies.

Once set, samples were removed from the die and the end faces of the cylinders were ground manually with 180, 400 and 1200 grit paper to remove any residual resin from the faces and produce parallel surfaces for compression. The samples were then electrically tested with a Tenma 72-7730A multimeter with points of contact made on the faces to ensure some level of conduction throughout the sample was possible. Samples that showed no sign of conduction were reground until conduction with the multimeter could be detected. Some samples were machined into dog-bone specimens with a rounded file and a rotary drill to resemble a scaled BMG sample outlined in the resistivity-compression tests.

Samples were placed into the resistivity compression test set-up, outlined previously. Electrodes were replaced with load bearing 1mm thick copper plates due to geometric limitations of the standard micro-probes.

Chapter 5

Local mechanical property assessments of BMGs through Nano-indentation

Nano-indentation is a popular method for determining mechanical properties of materials with limited test volumes and complex geometries. During testing, the applied load, indenter tip displacement and time ($P-h-t$) data are all recorded, from which hardness and elastic modulus data are extracted. Extracting more complex mechanical behaviours from nano-indentation, such as creep and fracture toughness, have been suggested to be possible. This chapter aims to explore the capability of nano-indentation for probing a full range of mechanical behaviours of materials whereby standardised tests are not practical (e.g. geometry requirements of standard test specimens and size limitations of novel alloys such as BMGs).

5.1 Measuring elastic modulus and hardness

Whilst nano-indentation is commonly employed in the literature to determine elastic moduli and hardness values of a range of materials, its use in characterising atypical materials needs to be treated with caution. For example, materials that have strong visco-elastic characteristics have been shown to influence the derived modulus and hardness values [206]. In addition, the length scales involved with nano-indentation deformation differ to that involved with bulk material deformation. Based on these potential issues, a full investigation has been performed in order to determine the validity of nano-indentation derived modulus and hardness values in both crystalline and BMG materials, and how these measurements compare to measurements on both micro and macro scales. Particular attention has been paid to features that exist within the raw test data, which in turn could provide information regarding further characterisation and understanding of the mechanical behaviours of BMGs.

The baseline performance of the nano-indentation technique was validated with simple crystalline materials outlined in Tab.(5.1), where elastic/reduced modulus values show good agreement with literature estimates. A detailed comparison of nano-indentation and literature reveals that hardness values show a greater deviation from the expected behaviour, consistently showing an overestimation for nano-indentation test results. One potential cause for this behaviour is scale dependent phenomena, such as dislocation starvation, which hinders the material's ability to facilitate deformation on localised scales [207]. Another cause of this behaviour could be due to sample

| Material | P_{max} [μN] | ν | E_r [GPa] | E [GPa] | E_{Lit} [GPa] | H [MPa] | H_{Lit} [MPa] | H_v [MPa] |
|----------|--------------------------------|-------|--------------|--------------|-----------------|----------------|----------------------|-------------------|
| Ag | 500 | 0.37 | 80 \pm 12 | 74 \pm 11 | 83 † | 1404 \pm 230 | 245-932 † | 436.5 \pm 29.9 |
| Mg | 2500 | 0.29 | 44 \pm 4 | 42 \pm 3 | 45 † | 568 \pm 57 | 294-441 † | 397.4 \pm 27.1 |
| Pb | 1500 | 0.44 | 24 \pm 2 | 20 \pm 1 | 16 † | 179 \pm 9 | 51.49* | 51.3 \pm 5.2 |
| Sn | 500 | 0.36 | 44 \pm 15 | 40 \pm 13 | 50 † | 176 \pm 18 | 39.2* | 56.7 \pm 3.1 |
| Al | 1000 | 0.28 | 63 \pm 14 | 62 \pm 14 | 70 † | 589 \pm 76 | 206-471 † | 152.7 \pm 12.5 |
| W | 10000 | 0.35 | 289 \pm 16 | 339 \pm 18 | 411 † | 7681 \pm 502 | 3531-4904 † | 4960.2 \pm 82.6 |

Table 5.1: Table showing the nano-indentation derived elastic modulus and hardness values compared to literature estimates of elastic modulus hardness data from † [209] and * [210].

preparation techniques, whereby deformation imparted on the samples during grinding and polishing effectively work hardens the material test surface. Work by Huang et al. has confirmed such an effect to also occur in BMGs [208]. To identify if either of these factors significantly affect nano-indentation results, larger length scale micro-indentation tests were performed in all the materials outlined in Tab.(5.1). These results show greater agreement with literature hardness estimates and return measurement errors that are significantly less than that observed in nano-indentation testing. This indicates that either size effects or sample preparation artefacts are causing a disconnect between nano and micro indentation results. This is not to say that the nano-indentation results are invalid, but that these results are not representative of the bulk mechanical behaviour of the materials being tested. This is an important distinction to make, as whilst bulk (micro-indentation) measurements represent the sample behaviour better for crystalline materials, BMG material deformation is governed by free volume distribution in the atomic structure (as outlined in Chap.(3)). Therefore, in these circumstances nano-indentation based mechanical assessments may be preferred.

To determine if the same measurement reliability holds for amorphous materials, a selection of BMGs (outlined in Tab.(5.2)) were tested with a range of test load and loading rates. Results outlined in Tab.(5.2) show that measured reduced modulus values approximate those reported in the literature, indicating that the methodology is satisfactory for determining elastic moduli of these materials. On closer inspection, measurements reveal that many of these results show a small unexpected overestimate of E_r , reminiscent of the $\approx 30\%$ difference commonly observed between BMGs and their crystalline counterparts [4]. A possible cause of this observation is the presence of crystalline phase within the material as, whilst XRD patterns of the majority of these compositions strongly confirm their glassy structure, some patterns do indicate the presence of crystalline phase. In addition, XRD results cannot state the absolute absence of crystalline phase in tested samples either due to the phase being a minor, and therefore weak, component of the diffraction spectra, or the assumption that a lack of crystalline phase on the test surface can be extrapolated to the bulk. In addition, observations by Kim et al. have reported the formation of crystalline phase in BMGs induced by nano-indentation [211], making any assumption regarding the amorphicity of the pre-indented material irrelevant. Taking these factors into consideration, it is understandable that some of the observed results produce elastic behaviours that are more characteristic of a crystalline sample than an amorphous one.

Hardness values for BMGs show a range of behaviours, with some predicting hardnesses close to that of literature values, and others predicting gross overestimates. This could again be a manifestation of small amounts of crystalline phase in the materials that form possible inter-metallics which are harder than the glassy phase. This is supported by some of the large errors

| Material | ν^{Lit} | E_r^{Meas} [GPa] | E_r^{Lit} [GPa] | H^{Meas} [MPa] | H^{Lit} [MPa] | H_v^{Meas} [MPa] |
|---|-------------|--------------------|-------------------|------------------|-----------------|--------------------|
| Ti ₄₀ Zr ₁₀ Pd ₁₄ Cu ₃₄ Sn ₂ | - | 133 ± 3 | 96.8 | 8700 ± 100 | - | 5500±60 |
| Zr ₄₄ Cu ₄₄ Al ₆ Ag ₆ | 0.32 | 107 ± 1 | 100.0 | 6800 ± 200 | 6270 | 4830± 60 |
| Zr ₅₇ Cu ₂₀ Al ₁₀ Ni ₈ Ti ₅ | 0.37 | 133 ± 1 | 81.8± 0.6 | 9200 ± 130 | 5460.0 | 4830±110 |
| Zr ₅₀ Cu ₄₀ Al ₁₀ | 0.37 | 117 ± 1 | - | 8100 ± 200 | 5580° | 5320±110 |
| Pd _{77.5} Si _{16.5} Cu ₆ | 0.41 | 128 ± 1 | 92±4 | 6930 ± 80 | 4918.9 | 4750±60 |
| Zr ₆₅ Cu ₁₅ Al ₁₀ Ni ₁₀ | 0.36 | 123 ± 1 | 84±5 | 8590 ± 90 | 4350† | 5000±100 |
| Ti ₃₃ Cu ₄₇ Zr ₉ Ni ₆ Sn ₂ Si ₁ Nb ₂ | - | 109 ± 8 | - | 7400 ± 700 | 6627† | 6000±120 |
| Cu ₅₀ Hf ₄₃ Al ₇ | 0.358 | 131.8±1.7 | 116.45 | 9300±200 | 6600† | 6000±100 |
| Ni ₄₀ Cu ₅ Ti _{16.5} Zr _{28.5} Al ₁₀ | 0.355 | 122±2 | 124.44 | 10000±300 | 7840° | 6850± 60 |
| Zr _{57.5} Nb ₅ Cu _{15.4} Ni ₁₂ Al ₁₀ | 0.379 | 104.5±1.6 | 93.62 | 7100±200 | 5400† | 4900±100 |
| Ti ₃₄ Zr ₁₁ Cu ₄₇ Ni ₈ | - | 130±10 | - | 9000±1300 | - | 5640±90 |
| Cu ₄₃ Zr ₄₃ Ag ₇ Ti ₇ | 0.373 | 110±2 | 94.83 | 7500±200 | - | 4800±110 |
| Cu _{57.5} Hf _{27.5} Ti ₁₅ | 0.356 | 123.5±1.7 | 106.95 | 8200±200 | 5820† | 5760±60 |

Table 5.2: Primary nano-indentation results for tests in BMG materials compared to values obtained from literature [7, 11, 17, 23, 40, 41, 85, 103, 110, 169, 212–216], † =hardness values estimated from yield, ◊= calculated from Vickers hardness.

associated with some of the harder materials, indicating a range of mechanical behaviours indicative of a multiphase system. As such, further investigations are required in order to determine if rules of practice can be identified in order to effectively measure mechanical properties of BMGs through nano-indentation. To that end, E_r and H values for measured BMGs were evaluated through tests utilising a small range of load and loading rates to evaluate their behaviours under a range of conditions.

Fig.(5.1) shows the results of tests across a range of loading rates and peak loads in a BMG whose hardness and modulus roughly reflect those of literature values. The plot identifies that reduced modulus measurements remain relatively consistent across all tests, indicating that elastic properties show little dependency on the test methodology over the parameter ranges utilised here. Hardness measurements show a far greater variation in the reported results, with no significant trend observed for peak load vs. hardness across any of the tested samples. A subtle trend is noted for load rate vs. hardness, with higher loading rates generally returning lower hardness values and vice versa. This behaviour has been reported in literature, whereby higher loading rates, and therefore greater strain rates, aid in a greater rate of generation of free volume in BMG structures [4]. If this rate outbalances the rate of free volume annihilation from natural BMG β relaxation processes, then the structure produced is one of lower viscosity, providing the recipe for the formation of shear bands in BMGs.

Beyond the general mechanical behaviours of modulus and hardness of BMGs, the raw indentation data was also scrutinised to identify features that would indicate the best test conditions for indenting BMGs. Fig.(5.2) shows some typical load-displacement indentation tests performed in a standard Zr₄₄Cu₄₄Al₆Ag₆ BMG with a range of testing conditions. It is observed within these plots that 2 features of interest occur. The first feature is characterised by minor pop-in/out signals that populate the loading, load-hold and unloading data. The frequency of these events is observed to be approximately the same during both loading and unloading, however during load hold tests, the frequency of is much higher. This difference may be due to observation bias, whereby the effect of the load change masks possible minor events. The second feature is characterised by larger pop-in signals only observed during the loading of materials and are more common in the higher load, higher loading rate tests.

Analysis of either of the signal types requires an understanding of their source. Due to the nature of the measurement, there are two potential causes of such a signal: an artefact associated with the measurement methodology, or a genuine mechanical response of the material. Observa-

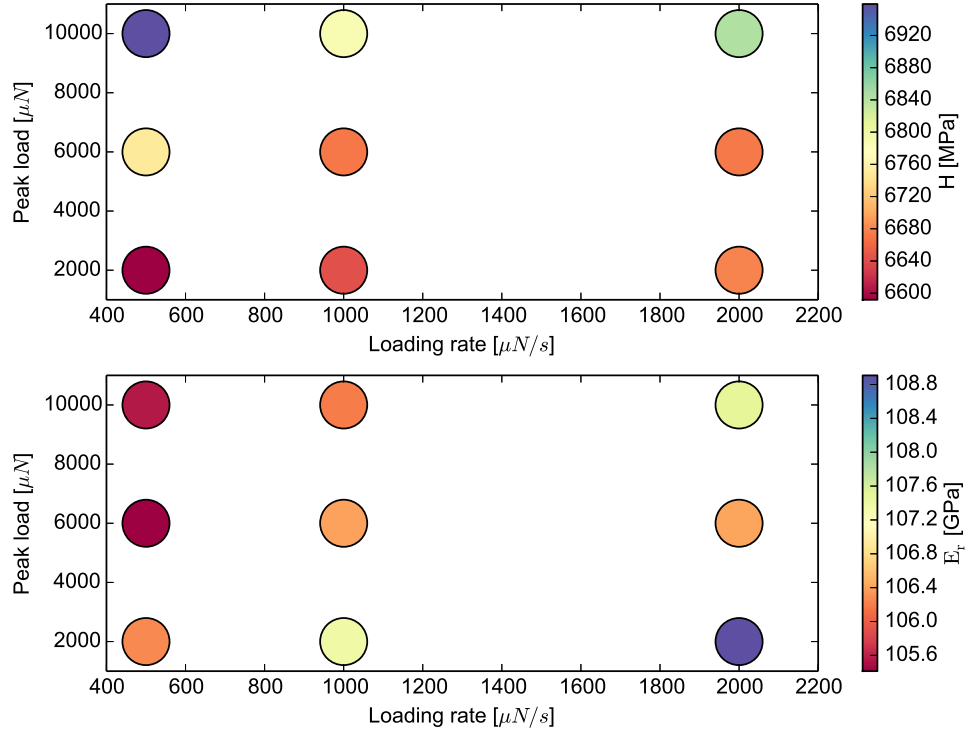
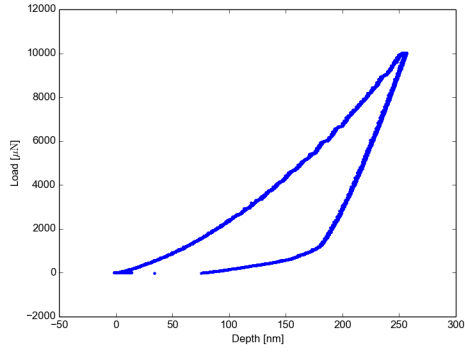


Figure 5.1: Plots showing how reduced modulus and hardness are affected by indentation tests performed with different peak loads and loading rates.

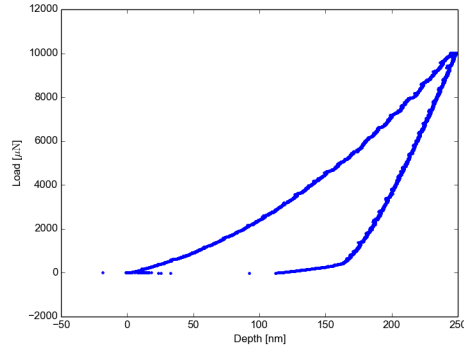
tions of both signal types are not always present across all tested materials, but are always present in certain materials tested with certain parameters. Therefore such an effect must be material-dependent and measurement artefacts can be dismissed.

The true source of the minor signals is difficult to determine through nano-indentation observations alone. During loading the signals can be characterised as a slowing of strain with increasing shear stress, followed by a sudden strain burst. Similarly during unloading, the reverse process is observed with signals showing a sudden strain burst, followed by a slower strain rate which then speeds up to continue the nominal unloading of the test material. It can be speculated that these events could be due to the activation of a single or a cluster of STZs, which is supported by the observation of a similar number of events of similar magnitude occurring during both loading and unloading, mimicking the reversible nature of STZs. The strain behaviour of these events also can be described through the process of STZ/STZ cluster activation, where an activation energy must be overcome. Therefore during loading, the strain burst could be the manifestation of an STZ/STZ cluster being activated from an applied stress, whilst during unloading the removal of an applied stress allows the back-stresses from the elastically strained BMG structure to activate previously activated STZs in reverse, resulting in a sudden displacement burst. Furthermore, events observed during load hold indicate a transient *reduction* in the penetration depth of a material (most clearly demonstrated in Fig.(5.3e)), which could correspond to the transient production of free volume required for the activation of an STZ/STZ cluster. Without independent in-situ observations to confirm if this is indeed the case, such a speculation cannot be proved, however this is an interesting prospect for further study.

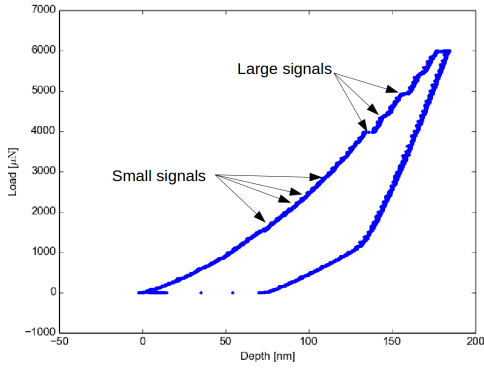
The stronger pop-in events are observed to only occur during the loading segments of the indentation tests. This, considering their strength relative to the minor pop events, is supportive of the idea that these events are due to shear band formation. Such events have been reported in



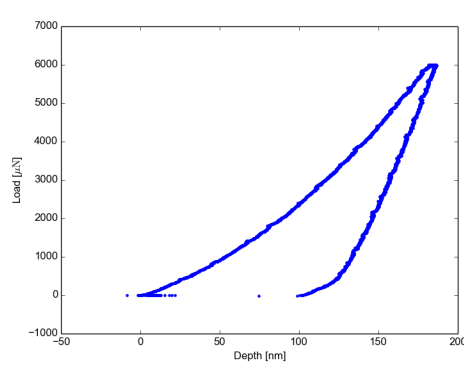
(a) Peak load of 10mN at a rate of 0.5mNs^{-1} .



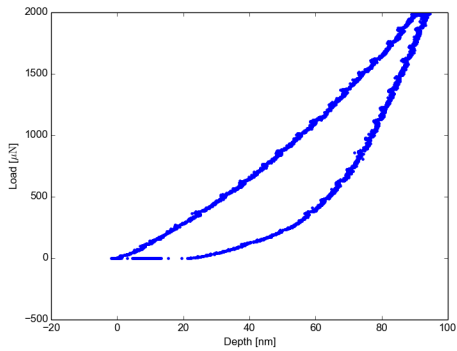
(b) Peak load of 10mN at a rate of 2mNs^{-1} .



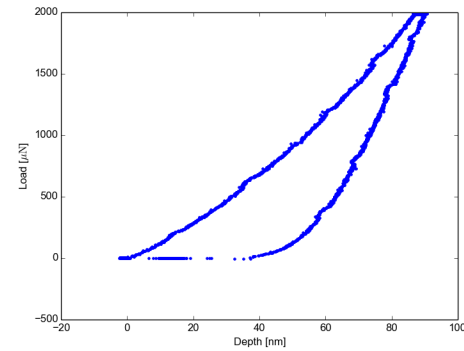
(c) Peak load of 6mN at a rate of 0.5mNs^{-1} .



(d) Peak load of 6mN at a rate of 2mNs^{-1} .

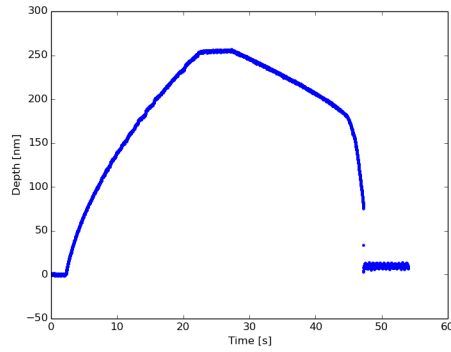


(e) Peak load of 2mN at a rate of 0.5mNs^{-1} .

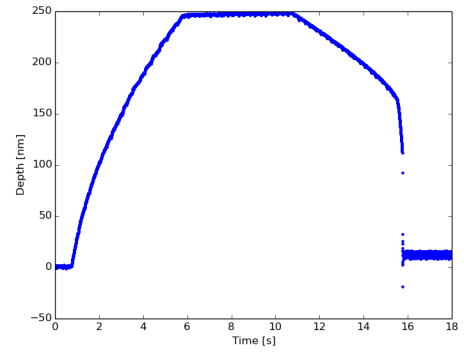


(f) Peak load of 2mN at a rate of 2mNs^{-1} .

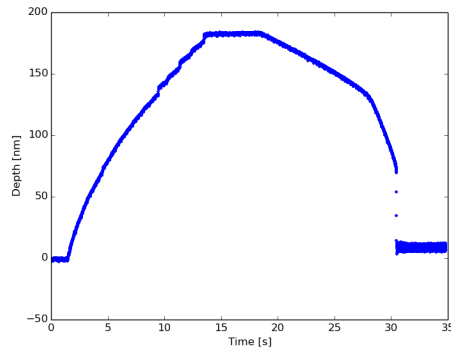
Figure 5.2: Load displacement data for a typical indentation tests performed in $\text{Zr}_{44}\text{Cu}_{44}\text{Al}_6\text{Ag}_6$ over a range of test conditions. Fig.(5.2c) shows the morphology of the different signal types.



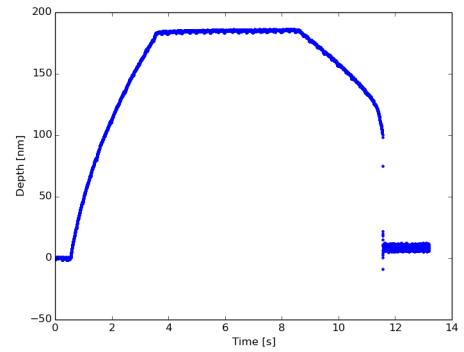
(a) Peak load of 10mN at a rate of 0.5mNs^{-1} .



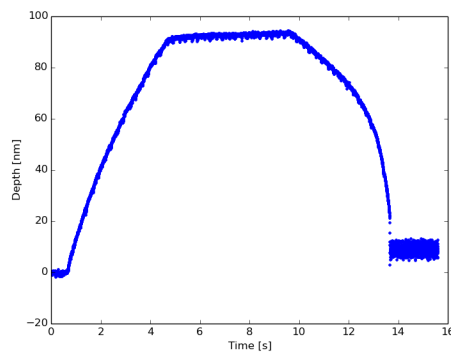
(b) Peak load of 10mN at a rate of 2mNs^{-1} .



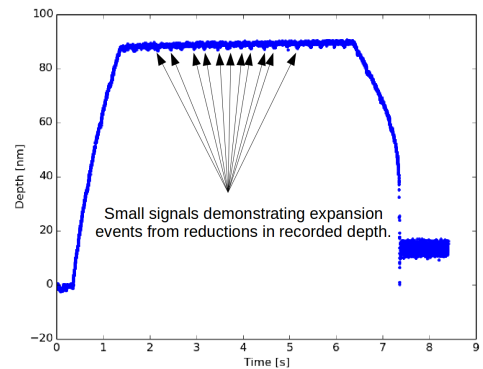
(c) Peak load of 6mN at a rate of 0.5mNs^{-1} .



(d) Peak load of 6mN at a rate of 2mNs^{-1} .



(e) Peak load of 2mN at a rate of 0.5mNs^{-1} .



(f) Peak load of 2mN at a rate of 2mNs^{-1} .

Figure 5.3: Displacement-time data for a typical indentation tests performed in $\text{Zr}_{44}\text{Cu}_{44}\text{Al}_6\text{Ag}_6$ over a range of test conditions. Fig.(5.3f) demonstrates clearly an expansion in the load hold minor signals, explicable from transient free volume generation of STZs.

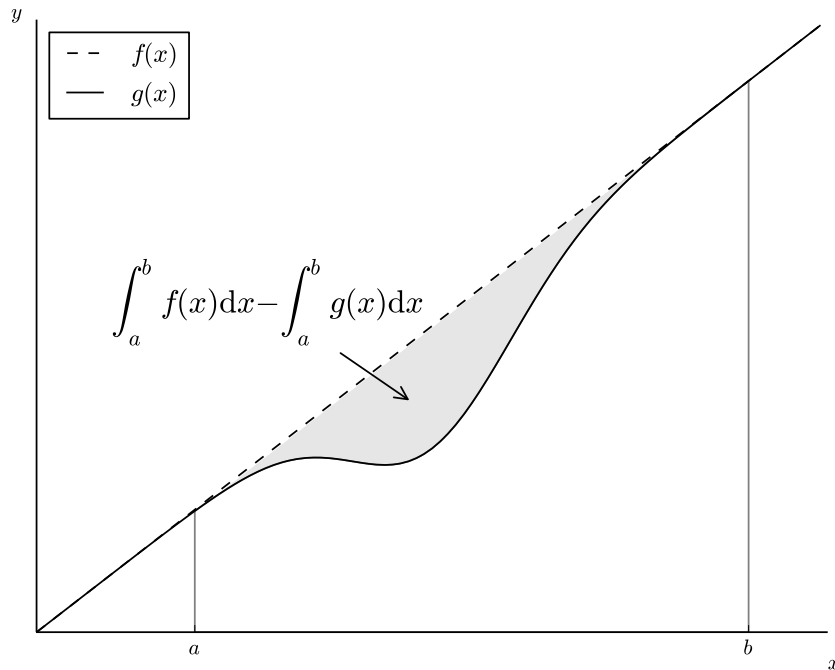


Figure 5.4: A schematic of a popin showing the general calculation required to determine the energy released from a pop-in event

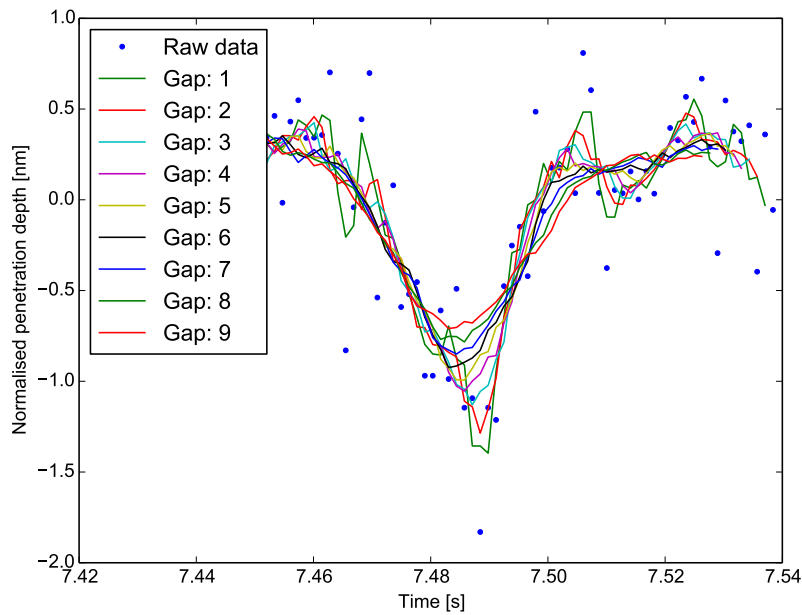
the literature to be associated with shear band formation in BMGs [4,217], which agrees with the observation of the trend of higher stronger pop-in densities for high load, high loading rate tests; conditions that produce greater fractions of free volume from which localised instabilities in BMG structures can nucleate and propagate a shear band.

Whilst proof of the signal sources described above is beyond the scope of the work presented here, analysis through a rudimentary calculation of the energy associated with the signals has been conducted, with the assumption that all the signals are due to mechanical processes occurring within a BMG structure as described above. The energy associated with these signals was calculated by approximating the energy released by the work done during a pop event, i.e. the sum of the products of the force and the displacements of the indenter tip with respect to test time. Whilst this is a simplistic approach, with no considerations given to energy losses from any other mechanism during indentation, the approach allows for a first approximation of the energies associated with the events, thereby potentially identifying their sources.

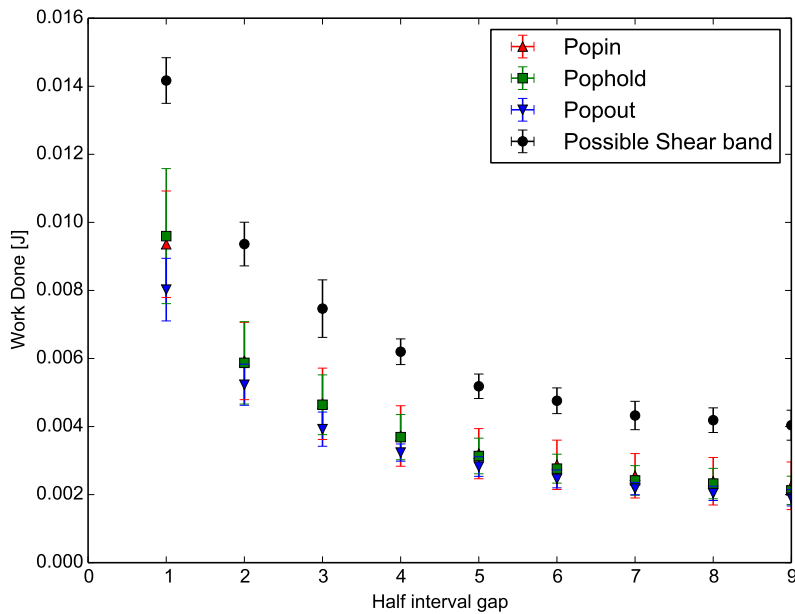
Extracting the energy from these signals requires some treatment to the data prior to analysis. Basing the calculation on work done during the event, the energy released is therefore the integral of the signal, normalised against the loading curve during that particular region of testing, as shown schematically in Fig.(5.4). An accurate analytical solution to this analysis would be possible if the data could be fitted to an equation, such as a Gaussian distribution. However Fig.(5.5a) shows an experimentally observed minor signal, and whilst its form looks similar to a Gaussian distribution of energy superimposed on the loading data, there is no reason for this to be a true representation of the data. Therefore, whilst the general form of the calculation identified in Fig.(5.4) remains the basis of this analysis, a numerical solution to the defined integrals must be found.

Numerical analysis of the signals uses some additional assumptions. The baseline data from

which the signal is extracted from is determined through a linear least squares fit of Oliver and Pharr's nano-indentation loading curve (Eq.(3.31)). The raw data is then subtracted from this fitted data to give a normalised pop-in event. Scatter within the raw nano-indentation data makes numerical integration difficult and introduces an unrealistic jagged energy distribution. Therefore, the corrected data was treated further through a moving average calculation, in an attempt to smooth the data. Determining the interval of data over which the moving average is calculated is open to interpretation as different intervals give different estimates of the energy released. Fig.(5.5b) highlights this, with increasingly larger intervals producing lower estimates of energy, which approaches relatively small values at high interval numbers. This inevitably results in an underestimation of the energy as the average energy calculated from larger data intervals tends to the of the average value of the baseline. Noise in the nano-indentation data makes this treatment necessary, and standard data smoothing requires that a minimum of 10 data points is required (equivalent to an interval gap of 5) to smooth data accurately, which corresponds to a significant underestimation of the pop event energy. Therefore for a rigorous treatment of these pop events, nano-indentation tests need to be performed with data being sampled at higher sampling rates. As no such capability is possible in the work presented here, energy values in presented in Fig.(5.5b) are calculated as result of the average energies of signals of individual types during loading, load-hold and unloading in $\text{Zr}_{44}\text{Cu}_{44}\text{Al}_6\text{Ag}_6$. As expected from observations of the raw data, the suspected shear band events have the greatest energy estimates. Suspected STZ events for the loading and load-hold observations are the next most energy intensive, followed by the pop events during unloading. This is in agreement with speculative theory identified earlier and literature, as STZs that have already been activated tend to have a greater fraction of free volume than their original rest state [4], thereby making the reversible process less energy intensive.



(a) An example of a pop event in $\text{Zr}_{44}\text{Cu}_{44}\text{Al}_6\text{Ag}_6$ indenter to 2mN at a rate of 1mNs^{-1} normalised to the loading data such that deformation due to the pop event only is shown.



(b) As the data interval used to evaluate your moving average increases, the profile of the pop-in becomes smoother, but the estimation of the overall energy decreases. This is true during loading, peak load and unloading.

Figure 5.5: Attempts at calculating energies associated with pop-in events in raw BMG nano-indentation data.

In summary, nano-indentation methods are a useful tool for characterising BMG materials whose sample volumes are limited. Hardness and reduced modulus are obtainable if careful sample preparation techniques are accommodated, and if indentation size effects are accounted for. Further more, the raw data of standard nano-indentations could hold vital information for the characterisation of the fundamental units of deformation in BMGs and shear band formation. Attempts of calculating the energies of such events have been made here, however it is recognised that improvements to the data sampling rate and accuracy is required in order to make any legitimate claims to the energy values associated with these observed events. This work has therefore provided the framework for future investigations regarding the observations and subsequent analysis of these features in the nano-indentation data.

5.2 Nano-indentation derived values and related properties

Standard usage of nano-indentation to measure elastic modulus in its absolute requires additional information regarding the elastic behaviour of the material, such as Poisson's ratio or the shear or bulk moduli, which can be linked to Poisson's ratio through

$$G = \frac{E}{2(1 + \nu)}, \quad (5.1)$$

$$B = \frac{E}{3(1 - 2\nu)}. \quad (5.2)$$

This is why in literature, many researchers tend to quote reduced modulus measurements for nano-indentation experiments, as this quantity is inherently linked to the elastic modulus of the material and does not require the input of elastic information that may not be known [8]. This is particularly troublesome for BMG mechanical property assessment, as the elastic behaviour of these materials is variable and the use of bulk measurements of properties such as Poisson's ratio to identify the values of localised elastic modulus cannot be satisfactory. To identify the full elastic and plastic response of a material undergoing nano-indentation, there is clearly a need to provide further localised elastic property information. A potential solution to this issue may come from the manipulation of hardness values gained through nano-indentation itself.

Several researchers have demonstrated a relationship between hardness and elastic properties of materials by examining the potential effect of inter-atomic bonding properties on yield [218–222]. However it has been demonstrated by work presented here and by other researchers [7] that hardness values of materials are dependent on a multitude of other factors, which make it difficult to state a standard hardness value for a given material. This is in stark contrast to elastic properties of materials, which only tend to be defined by the state of inter-atomic bonding of a material rather than its micro-structural state.

Initial attempts at relating elastic response to hardness came from Gilman [223] and Liu [224], who established a strong link between hardness and bulk modulus of materials. However further work led to the realisation that this relationship changed depending on the materials being considered, and it became apparent another influencing factor was at play. Observations from Teter [1] subsequently found that hardness values, particularly of hard and brittle materials, strongly correlated with shear modulus provided the basis for the empirical relationship

$$H_v = 0.151G, \quad (5.3)$$

with the odd exception of materials such as tungsten carbide [1, 7] which has an uncharacteristically

low modulus for the hardness value of the material. Chen et al. later provided a theory based derivation for Eq.(5.3) for perfectly elastic materials that demonstrate no plasticity [7]. Interestingly Chen et al. observed this relationship to work for a wide array of BMGs which, although appear to fail in a brittle manner on the macroscopic scale, are capable of immense levels of ductility in the regions of failure [7]. This could be considered as a manifestation of Johnson and Samwer's universal yielding criterion outlined in Eq.(3.13), which states that a given level of shear strain (≈ 0.027) can only be accommodated elastically before plastic shear is observed.

Accommodating plasticity into the models described up until now is difficult. However, the model can be simplified by considering the direction of deformation within an indent relative to the forces applied during indentation. From this simplistic treatment of the indent, it can be seen that the width of an indent is defined by the compression of material, which depends on Bulk modulus, and the depth of an indent depends on the shear deformation along the faces of the indent, which depends on shear modulus [7]. To that end, Hardness can be based on a ratio of bulk to shear modulus values in a material, i.e. Pugh's ratio [165], which leads to the formation of Eq.(5.4) (see [7] for details on the derivation);

$$H_v = 2 \left[\left(\frac{G}{B} \right)^2 G \right]^{0.585} - 3. \quad (5.4)$$

Chen et al. [7] showed that the application of Eq.(5.4) gave better correlations of derived hardness values to measured hardness values over all kinds of materials, thus providing a strong link between the elastic properties of materials and hardness values. Recent work by Zorzi and Perottoni [8] took the findings of Chen et al. and applied it to nano-indentation tests to determine the Poisson's ratio of materials through the substitution of Eq.(5.1) and Eq.(5.2) into Eq.(5.4);

$$H_v = 2 \left[\frac{9E (1 - 2\nu)^2}{8 (1 + \nu)^3} \right]^{0.585} - 3. \quad (5.5)$$

Their work showed that for a small number of materials tested, Eq.(5.5) could be solved numerically to produce relatively accurate Poisson's ratio estimates within the bounds of error of the defined hardness values [8]. Zorzi and Perottoni's publication acknowledges the clear limitations of deriving elastic properties from plastic behaviours. However many of their concerns originate from micro-structural considerations such as grain orientation effects, etc [8]. The lack of such features in BMG materials indicates that such an investigation may yield elastic property data previously unattainable through standard testing techniques.

5.2.1 H_v and ν in crystalline materials.

Zorzi and Perottoni's work tested their equation on a range of materials including Al_2O_3 , β - Si_3N_4 , Ni, BK7, B_4C and TiB_2 ; the only material tested that would behave as a metal (with metallic bonding) is Ni. In addition it was also noted that tests on Ni showed the greatest deviation from the behaviours dictated by Eq.(5.5) out of all the materials tested. There is therefore a need for a full investigation on the validity of Eq.(5.5) on standard metallic materials. To that end, hardness, elastic modulus and Poisson's ratio values for group I, II and all transition metal elements in the periodic table that are in a solid state under standard temperature and pressure have been collected from the literature. Hardness values from literature were then compared to hardness values calculated from literature elastic constants using Eq.(5.3), Eq.(5.4) and Eq.(5.5) in order to determine the validity using elastic properties to determine hardness values of elemental materials.

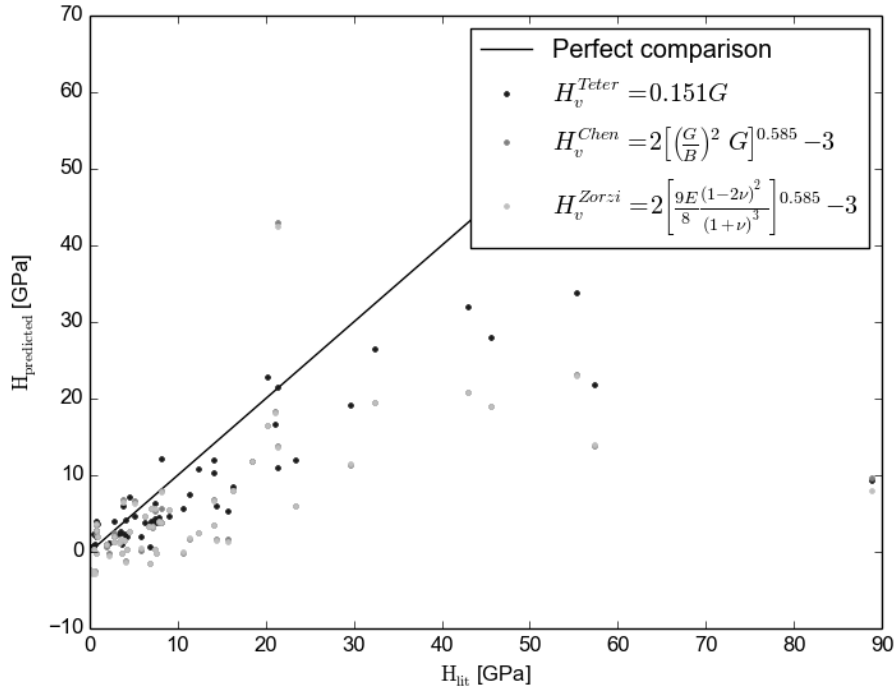


Figure 5.6: Hardness values for periodic table elements taken from literature [209, 210] compared to predicted hardness values from Eq.(5.5).

Fig.(5.6) shows that literature hardness values for elements produce a diffuse positive correlation with hardness inferred from elastic properties, indicating that Hardness values may indeed be linked to the elastic constants of the material through equations like that described above. The correlation is weak and deviates from the ideal 1:1 ratio in favour of predicting an underestimate of the hardness through elastic constants, which becomes more apparent for harder materials. Chen et al. briefly stated that these equations may not be very applicable to pure metallic materials due to their ability to work harden in localised regions from the accumulation of plastic deformation, an effect that has not been accounted for in the derivation of any of these equations [7]. This may account for the negative H values predicted for soft materials and the significant underestimate of hardness values for harder materials.

Comparison between hardness values predicted through Eq.(5.3), Eq.(5.4) and Eq.(5.5) surprisingly show Eq.(5.3) to produce the best correlations between reported and predicted hardness values for crystalline materials; the equation that assumes negligible plastic deformation during indentation. Values predicted by Eq.(5.4) and Eq.(5.5) both deviate from the nominal hardness behaviour, but predict very similar hardness values to each other due to their common origin. Differences in the predicted hardnesses from these two equations therefore only arise from measurement scatter in G , B and ν estimates.

To conclude, whilst a general positive trend has been observed between the measured and predicted hardness values, its strength and validity is questionable for elemental polycrystalline metals, and can therefore only be used as a comparative measure to determine significant differences in hardness. In order to utilise such a relationship universally, the effect of work hardening must be accounted for in the model equations.

5.2.2 H_v and ν in BMG materials.

Whilst hardness may provide a rough estimate of the elastic properties of a given material compared to another material, the dependences of hardness values on micro-structural effects, etc. makes this method a poor choice for a full nano-indentation evaluation of elastic behaviours in crystalline materials. However, these weaknesses may not be present for materials without a microstructure, i.e. BMGs. If shown to be the case, then this methodology would prove to be a powerful tool for providing data on previously uncharacterised BMG materials and aid in understanding the yield behaviour of BMGs.

To determine if elastic properties can be related to hardness values in BMGs effectively, a similar analysis to that performed for elemental crystalline materials was performed for a range of BMG materials using data obtained through literature (using measured hardness and hardness calculated through yield strength: $H \approx 3\sigma$.) The results shown in Fig.(5.7) show that hardness determined from Eq.(5.3) agrees relatively well with reported hardness values, indicating that hardness of BMG materials can be inferred from shear modulus values for a first approximation. However Eq.(5.5) fails to produce reliable estimates of hardness, in contradiction with observations made in Chen's work [7]. This may be due to the use of literature data from multiple sources to compare predicted and reported hardness values for this equation. Therefore subtle differences in the BMG composition, in the test methodology for evaluating properties, length scales used to evaluate properties and other experimental variations will all contribute to the predicted hardness and hinder the quality of the correlation between the measured and predicted hardness values. This will apply to Eq.(5.3) as well, and may be responsible for some of the scatter in the data. However Eq.(5.4) and Eq.(5.5) have an extra level of complexity associated with them which could strengthen the effect of these errors.

To evaluate if the errors highlighted above are indeed responsible for the poor correlation of hardness measurements to predictions through Eq.(5.4) and Eq.(5.5), another hardness comparison treatment was performed using data from tests performed through nano-indentation (outlined in Tab.(5.2)), thereby using elastic property information from a common source. It is important to note that whilst this analysis effectively screens out much of the scatter introduced from using literature property values, independent estimates of values (ν) must still be utilised in order to predict hardness values, as demonstrated by the calculation required to predict hardness directly from nanoindentation data based on Eq.(5.5):

$$H_v = 2 \left[\frac{9(1-2\nu)^2}{8(1+\nu)^3} \left(\frac{1-\nu^2}{\frac{1}{E_r} - \frac{1-\nu^2}{E_i}} \right) \right]^{0.585} - 3. \quad (5.6)$$

Fig.(5.8) shows the comparison of predicted and nano-indentation measured hardness values. Once again, hardness values derived from Teter's Eq.(5.3) (with G being substituted for Eq.(5.1) and E_r) shows a relatively good correlation with measured hardness values from nano-indentation, with only a slight systematic underestimation of hardness values to report. This indicates that measured values of E_r used in conjunction with literature values of ν are acceptable combination of values for this treatment of data. The systematic underestimate of hardness values may be a manifestation of the lack of consideration of bulk moduli during the indentation process, or a continuation of the problems surrounding using literature estimates of ν ; values which are usually evaluated on length scales far greater than that of nano-indentation testing. This highlights the need for a methodology that can evaluate elastic properties on the same local length scales as that

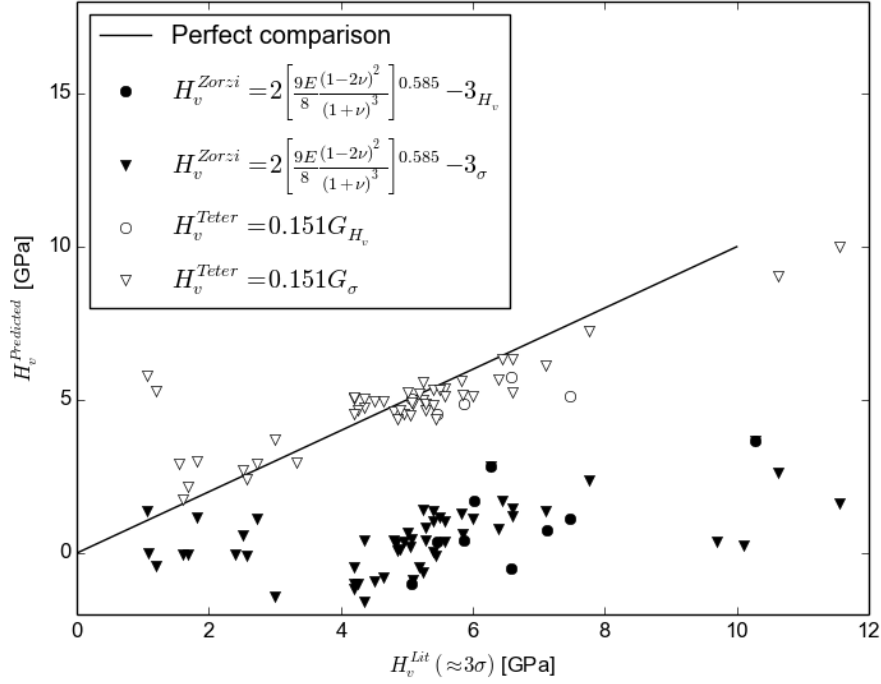


Figure 5.7: Plot showing measured and predicted hardness values for literature BMG values. The subscripts H_v and σ indicated whether the predicted hardnesses are compared directly to hardness measurements, or are compared to hardnesses derived from yield through Tabor's hardness equation, $H \approx 3\sigma$.

as the reduced modulus measurements.

Hardnesses predicted through Eq.(5.6) returns far less agreeable results compared to Teter's Eq.(5.3). Analysis was also performed using hardness values measured through a range of peak load and loading rate parameters, which clearly shows that the deviation of predicted hardnesses from measured hardnesses cannot be attributed to inappropriate testing parameters. Deviation between the two hardness evaluations may therefore be due the use of localised property information with bulk property information, providing misleading results. This is of particular concern for the determination of bulk and shear modulus of BMGs, where unlike crystalline materials, the variation of structural state must be considered. If areas of amorphous material are deformed such that a free volume rich or poor region is sampled compared to the nominal free volume distribution of the bulk material, then scattered results like that observed in Fig.(5.8) may be produced. In addition, effects such as the work hardening analogy identified by Chen et al. (where free volume sites for potential shear banding becomes depleted with deformation, making localised deformation more difficult [7]) may be present as Eq.(5.5) does not take into account the effect of localised instabilities in the material, assuming the test material behaves as a continuum [7]. This also means features such as shear bands are not accommodated by this model. In addition, potential presence of crystalline phase in samples outlined earlier may also be a factor to consider.

From the observations and analysis performed here, it is clear that Teter's Eq.(5.3) is the most accurate equation for estimating elastic properties from hardness measurements of materials which have limited elastic information available. Tab.(5.2) highlights the titanium rich BMG alloys; $\text{Ti}_{40}\text{Zr}_{10}\text{Pd}_{14}\text{Cu}_{34}\text{Sn}_2$, $\text{Ti}_{33}\text{Cu}_{47}\text{Zr}_9\text{Ni}_6\text{Sn}_2\text{Si}_1\text{Nb}_2$ and $\text{Ti}_{34}\text{Zr}_{11}\text{Cu}_{47}\text{Ni}_8$ to have no estimated ν in the literature. Therefore using nano-indentation hardness and modulus values and Eq.(5.3), ν of

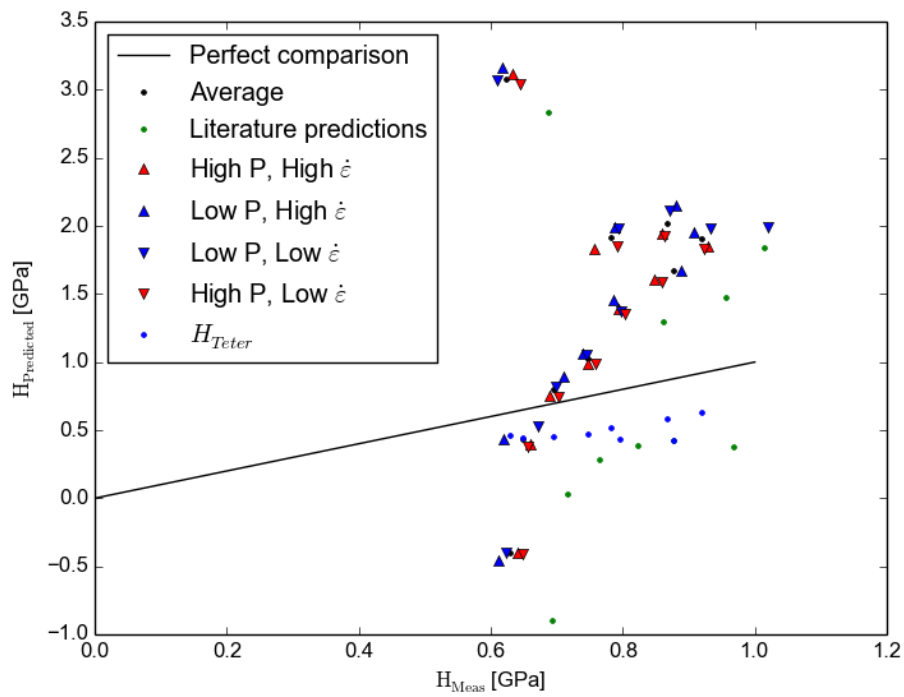


Figure 5.8: Plot demonstrating comparisons between predicted hardness from Eq.(5.6) and nano-indentation measured hardness, with values of ν being the only values that are drawn from literature. Effects of peak load (P) and strain rate ($\dot{\epsilon}$ inferred from loading rate) are also considered, and hardness values predicted from Teter's Eq.(5.3) have been included for completeness.

the 3 glasses are estimated as 0.23, 0.19 and 0.17 respectively, far lower than that considered for similar BMG compositions. Considering that this may once again be a size effect, use of micro-hardness data and bulk elastic modulus data for $\text{Ti}_{40}\text{Zr}_{10}\text{Pd}_{14}\text{Cu}_{34}\text{Sn}_2$ finds that the estimation of ν rises from 0.23 to 0.31, which whilst still lower than expected, is more in agreement with the general ν values of similar compositions, indicating a size dependence. In the case of nano-indentation, evidence of indenting over length scales of free volume sites is supported by the potential observation of the STZ/STZ cluster activation through nano-indentation detailed earlier. If this is the case, then the disconnect observed in predicted ν values in the nano and bulk scales may be due to the non-uniform nature of the deformation field produced during indentation, activating all the available STZ clusters in such a manner that STZ depletion model of Chen et al comes into effect [7]. To that end, nano-indentation with arguments made by Poon in Chap.(3) may provide a means to map free volume distributions in BMGs, and warrants further investigation.

5.3 Conclusions

Nano-indentation is a powerful tool for investigating mechanical behaviours in materials, particularly in materials with restricted geometries, or have variable mechanical behaviours over meso/micro length scales. To that end, nano-indentation has been performed in a range of materials with key findings of the results outlined as follows:

- Observations of E_r for tested materials are seen to correlate well with literature estimates, confirming the validity of the method used.
- The dependence of BMG hardness and reduced modulus on peak load and loading rate has been investigated, showing that hardness of BMGs decreases in tests performed at high loading rates, and very high loads (beyond the loading range of nano-indentation). There is therefore a need for the development of a standardised nano-indentation practice of BMG materials beyond the basic considerations of the production of a valid indent that is uninfluenced by surface roughness or stress fields of surrounding indents.
- Detailed observations of the raw nano-indentation data revealed features; weak signals, speculated to be associated with STZ processes, and strong signals, believed to be due to the initiation and propagation of shear bands. A rudimentary analysis of energies suggests that the energies of the observed signals corresponded with the mechanics of the processes used to identify them. Further investigations into these phenomena is therefore warranted.
- Predicted hardness values in elemental polycrystalline metals weakly agree with the semi-empirical equations put forward by Teter, Chen and Zorzi and Perottoni. The scatter, attributed to the lack of consideration of localised work hardening effects, makes the methodology unsuitable for the evaluation of elastic properties through hardness.
- Analysis of literature data of BMGs showed that Teter's Eq.(5.3) produces good hardness estimates for the most part, whilst Chen et al. and Zorzi and Perottoni's work still does not produce good hardness estimates. This is further validated through tests performed here, ruling out the potential for a nano-indentation based effect being the route cause of the discrepancy in the results.
- The good correlation of Teter's Eq.(5.3) allowed for the evaluation of elastic properties from measured hardness values of BMG alloys $\text{Ti}_{33}\text{Cu}_{47}\text{Zr}_9\text{Ni}_6\text{Sn}_2\text{Si}_1\text{Nb}_2$ and $\text{Ti}_{34}\text{Zr}_{11}\text{Cu}_{47}\text{Ni}_8$.

Estimates of these values have been assessed and quantified and interpreted, demonstrating the usefulness of nano-indentation to probe new materials.

- Reduced modulus measurements are shown to agree strongly with literature, however hardness values in both crystalline and glassy materials show a large scatter in the observed results that do not always correspond to the literature values. Variation of hardness values is expected due to the number of factors that can be linked to influencing hardness, from thermomechanical processing history to test methodology. As such, any elastic property estimated from hardness values must be treated with caution.

Chapter 6

Probing creep behaviour in crystalline and BMG materials.

Plastic deformation behaviour of BMGs, amongst other things, is governed by the conditions in which it is deformed, with high temperature-low strain rate conditions favouring homogeneous flow, and low temperature-high strain rate conditions leading to a runaway localised catastrophic deformation [4]. Understanding the factors that affect the progression of either of these mechanisms requires experimental approaches that are able to link micro-scale processes to macro-scale observations. This has been attempted by many authors with varying degrees of success through different approaches, from nano-pillar compression experiments [79] to computational simulation methodologies [66,136]. A fruitful investigatory tool in this effort (particularly for testing limited volumes) has arisen through the use of instrumented nano-indentation.

Chap.(5) evaluated the usefulness of nanoindentation to determine basic hardness and modulus measurements, with the additional insight of using the technique to probe nano-scale processes, such as STZ activation. Nano-indentation has been used to probe other more complex mechanical properties, such as fracture toughness [180,181] and creep [188,191,192,203,225,226]. Creep is of special interest with regards to deformation behaviour of BMGs, as creep deformation constitutes the low strain rate-high temperature deformation criteria for activating homogeneous deformation in metallic glasses.

Measuring creep through nano-indentation for both crystalline and BMG materials is not without its issues. Literature has identified many problems with the measurement validity, including a complex indentation stress field, poor definition of stress and strain during indentation, creep behaviour dependence on processing history, poor sensitivity of creep behaviour to load-displacement data, degeneracy during numerical analysis of creep behaviours, poor evidence for steady state creep being achievable through indentation and dependence of creep behaviour on sample preparation methodologies [191,194,195,206,208,227–235]. Despite these shortfalls, there are reports of good correlations between experimental results and expected creep behaviour in crystalline materials [190,203]. In addition Huang et al. have performed multiple indentation creep investigations into BMGs, and recognised that whilst indentation creep may not provide explicitly accurate creep parameters, it can provide a relative measure for creep behaviour in a material when subjected to a range of conditions [236–238].

The validity of the mechanics in indentation creep has been reviewed thoroughly by several authors [191,192]. However beyond the fundamental mechanics, the raw measurement must have known reproducibility and precision. Therefore, this chapter explores the use of indentation to

| Equation [$h(t) = \dots$] | Terms | Ref. | Justification of use |
|---|---|--|---|
| $h_o + a(t - t_o)^m + kt$ | $h_o, t_o, m, k =$ Fitting constants $t =$ Time | [195] [239] [236] [237] [240] [241] | Empirical fit |
| $a(1 - e^{-bt})$ | $a, b =$ fitting constants | [242] | An attempt at modelling a Kelvin-Voigt response |
| $h_e + \sum_{i=1}^n h_i(1 - e^{-\frac{t}{\tau_i}}) + \frac{t}{\mu_o}$ | $i =$ Deformation mode. $\tau_i =$ Retardation time of i h_i Penetration depth of i $h_e =$ Elastic displacement | [204] [199] | Uses a Kelvin model as a fitting equation. $\frac{t}{\mu_o}$ accounts for viscous flow. |
| $h_o + a + \ln(bt + 1)$ | $h_o =$ initial displacement $a, b =$ Fitting constants | [243] | No justification stated. |

Table 6.1: Literature examples of equations used to fit indentation creep data to in order to determine creep parameters algebraically.

assess creep from the point of view of uncertainties in the measurement, and most particularly the effect subsequent analysis can have on the results obtained. This will provide a limitation on the ability to use nano-indentation as a means to evaluate creep behaviour of materials and probe the mechanisms behind homogeneous flow of BMGs.

Analysis method considerations

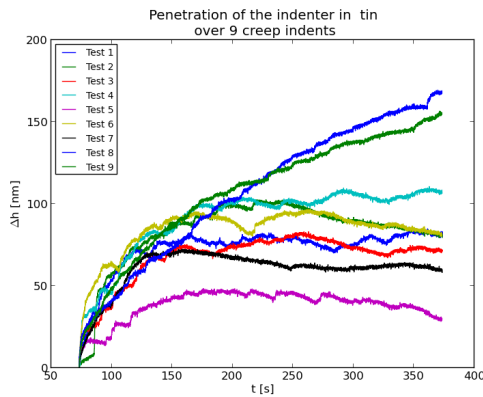
Researchers use a range of data handling methods to convert their indentation $P-h-t$ data into $\sigma-\dot{\epsilon}-t$ data. Broadly, the analytical methods used fall into two distinctive categories. The first category involves fitting an equation to the raw $h-t$ data, which is then used to extract creep parameters algebraically through Eq.(3.38) and Eq.(3.39). These fitting equations either have empirical or approximately theoretical roots, as outlined in Tab.(6.1). This analysis approach minimises the influence of scatter in the raw experimental data, whilst still accounting for measurement error in the uncertainty of the fitting parameters. As theories predict smooth changes, this approach is logical, although the range of equations used in the literature will produce different representative strain rates when the equations are extrapolated to beyond the test conditions.

The second method involves tangential analysis, where tangents are fitted to $P-h-t$ data over small intervals, such that the data can be approximated to be linear [191, 244]. These tangent values are then used to determine $\sigma-\dot{\epsilon}-t$ values through Eq.(3.38) and Eq.(3.39). Stress exponents and activation energies can then be evaluated through fitting further tangents to the $\sigma-\dot{\epsilon}-t$ data. The tangential analysis method is therefore subject to scatter in the measured data and heavily influenced by sudden displacement events, such as pop-ins, if not treated correctly. However this analysis method does not require an equation that fully captures strain rate behaviour during indentation creep, which makes it a more impartial analysis method provided the raw data is good.

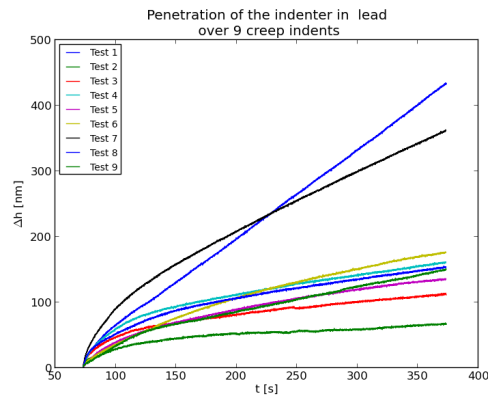
Nano-indentation creep investigations were performed on a range of crystalline and BMG materials, outlined in Tab.(4.2). Details surrounding the tests are outlined in Chap.(4), tests were

split into 2 approaches, Short Time Scale (STS) tests which focused on short (300s) but highly sensitive and highly sampled tests of materials, and Long Time Scale (LTS) tests, which focused on long (600s+) stable, high sensitivity with less sampling than that performed in the STS tests. Both raw and processed results were then critically analysed in order to determine the validity of indentation as a means to measure creep behaviour in both crystalline and amorphous materials, and the factors affecting such a test.

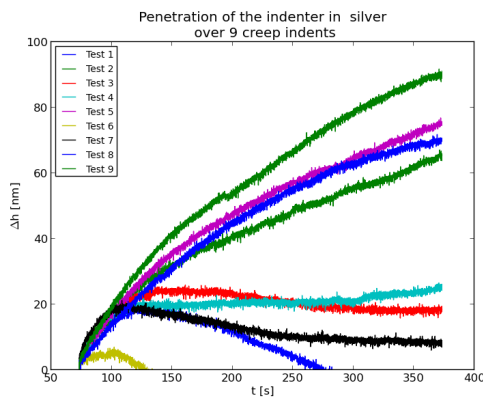
6.1 Observations of nano-indentation creep data



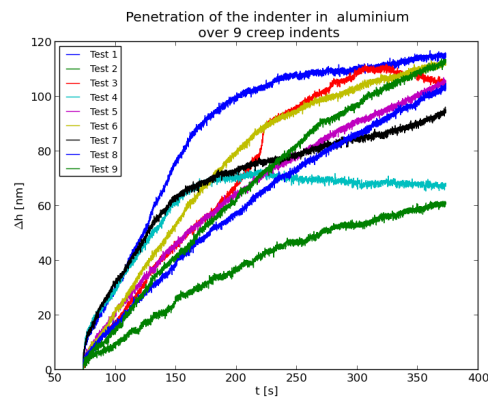
(a) Displacement-time data for tin.



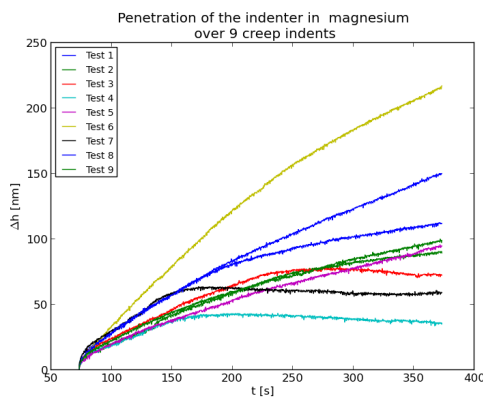
(b) Displacement-time data for lead.



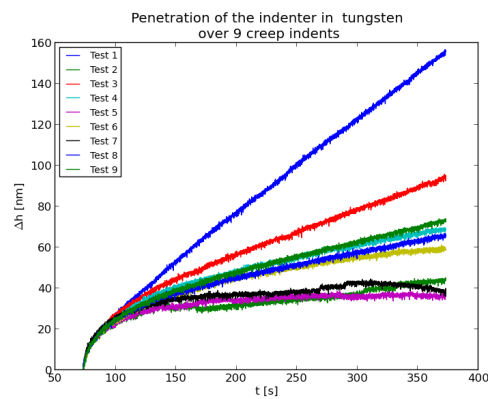
(c) Displacement-time data for silver.



(d) Displacement-time data for aluminium.

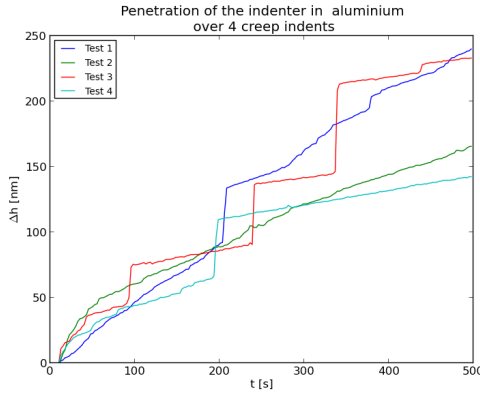


(e) Displacement-time data for magnesium.

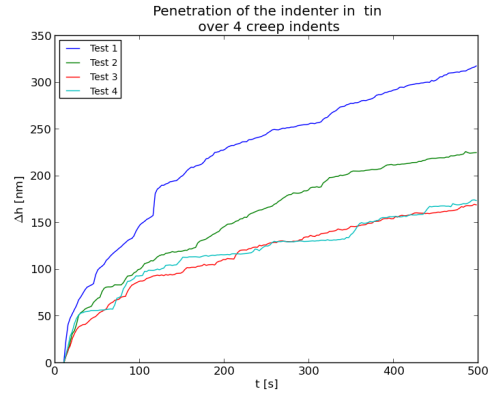


(f) Displacement-time data for tungsten.

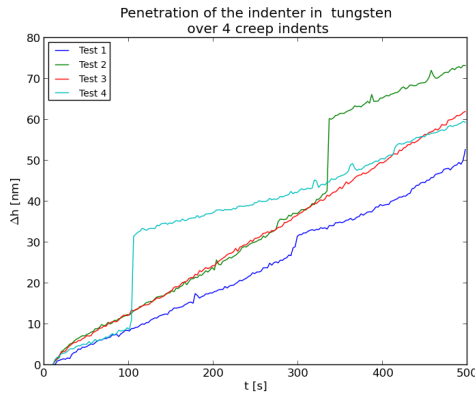
Figure 6.1: Displacement-time curves obtained from different materials using the STS testing regime. Note that all curves recorded for a particular material are shown, with no selection or discarding of potentially erroneous results.



(a) Raw data from a typical indentation creep test in aluminium using the LTS test regime.



(b) Raw data from a typical indentation creep test in tin using the LTS test regime.



(c) Raw data from a typical indentation creep test in tungsten using the LTS test regime.

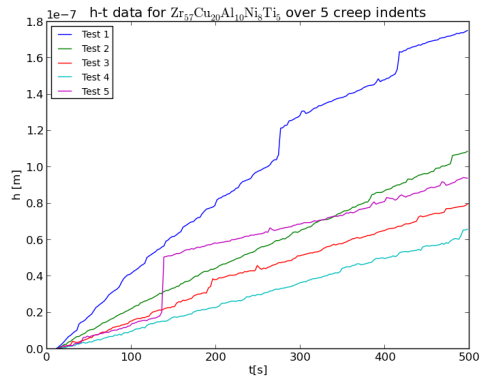
(d) Raw data from a typical indentation creep test in the $Zr_{57}Cu_{20}Al_{10}Ni_8Ti_5$ using the LTS test regime.

Figure 6.2: Displacement-time data for indentation creep tests in aluminium using the LTS test regime. Large displacement events were observed in many of the tests, making them unsuitable for creep analysis, even when the displacement events are removed from the data. This was observed for all materials tested with LTS tests.

Typical creep curves from STS tests are shown in Fig.(6.1). Tests mostly show a general profile of an initial high rate of deformation, sometimes described as being analogous to primary creep, followed by a region where the deformation either remains unchanging, or increases at a more constant rate. Tin has a less well-defined deformation behaviour compared to the other tested materials, with pop-in (sudden large deformation) like events occurring throughout all tests. Silver also produced a range of behaviours from characteristic indentation creep curves to curves which show an apparent expansion of material at long hold times. However, the silver samples contained some porosity, and measurement of thermal drift around sub surface pores could produce an over correction leading to this effect. Further investigations are required to determine if this is a cause of poor reproducibility in the silver creep curves.

Fig.(6.1f) shows results from indentation creep tests in tungsten. The deformation at the beginning of the load hold period shows good reproducibility across all 9 tests. However, the deformation rate near the end of the load hold period, whilst often linear, varies across all seemingly identical tests. Both tungsten and lead show the most linear steady state deformation regimes during testing out of all the tests performed, whilst aluminium, silver and magnesium all show significant variation in deformation behaviour after the transient deformation regime (with aluminium showing

the most linear deformation of the 3 materials, and tin showing the least).

Fig.(6.2) shows raw data for LTS tests. The general form of the raw indentation data between STS and LTS tests are comparable, however, greater stability in the overall behaviour is observed in the LTS tests. The longer pre-load hold periods utilised in the LTS tests may account for this. However the load profile outlined in Fig(4.5b) has been used successfully by other researchers with load hold times on a par or even less than that investigated here [195], indicating an extrinsic cause to the variability of the creep behaviour in the STS tests. Potential causes of this are explored in Sec.(6.1.2).

Variability between LTS tests are seen to occur during the first moments of the test, which then often settles to a common linear deformation rate for the rest of the test. The time at which this converges to a common deformation rate varies, indicating that steady state creep is approximated at different time values. This effect could be due the positions of the indents, which were spaced much further apart than in the STS tests and therefore will have been performed in different micro-structural environments.

In the case of tests performed in $Zr_{57}Cu_{20}Al_{10}Ni_8Ti_5$ where micro-structural variability is not expected, creep behaviour shows some variability. Three of the five tests settle into a common deformation rate quickly, despite the presence of pop-ins. Two tests show higher rates of deformation with less linearity than the remaining three, however it is observed that these two tests are the first tests to be performed in the material, and the first test shows the greatest deviation from the final three tests. This indicates an influence of thermal drift on and unachieved thermal equilibrium in the initial tests performed.

It is encouraging to note that despite this variability a common deformation rate is observed at longer test times for tests that are not the first tests performed in the materials and that show no significant pop-in events in the data. This indicates a particular deformation mechanism is consistent within the materials for these tests, though it is recognised that further tests are required to improve confidence of this statement.

6.1.1 Creep data analysis

Raw $h-t$ data (omitting any data with significant pop-in type events or poor creep curve forms) were taken and processed through the two analysis methods, described as follows:

Equation fitting vs. Tangential fitting

The equations below were fitted to the measured $h-t$ data:

$$h(t) = h_o + a \ln(t - t_o) + kt : (h_o, t_o, a, k = \text{Fitting parameters}) \quad (6.1)$$

$$h(t) = h_o + a(t - t_o)^m + kt : (h_o, t_o, m, k = \text{Fitting parameters}) \quad (6.2)$$

$$h(t) = h_e + \sum_{i=1}^n h_i \left(1 - \exp\left(-\frac{t}{\tau_i}\right) \right) : (\tau_i, h_i, h_e = \text{Fitting parameters}) \quad (6.3)$$

$$h(t) = a(1 - e^{-bt}) : (a, b = \text{Fitting parameters}) \quad (6.4)$$

$$h(t) = h_0 + h_1t + h_2t^2 + h_3t^3 + \dots + h_{10}t^{10} : (h_0 \dots h_{10} = \text{Fitting parameters}). \quad (6.5)$$

Eq.(6.2), Eq.(6.3) and Eq.(6.4) were taken from the literature as outlined in Tab.(6.1). Eq.(6.3) has the final term omitted from it, as the term accounts for viscous flow in crystalline materials (which is minimised during room temperature creep experiments [199]). Eq.(6.1) was here based on the potential for its form to fit indentation creep data. A similar form to this equation has

been used successfully in the literature previously (see Tab.(6.1)), but no justification for its use was given. Eq.(6.5) is a Taylor expansion equation (with all constant terms taken into the fitting constants). This is used in multiple data analysis techniques, such as wave analysis, where fitting an equation is necessary.

Fitting was achieved through a non-linear least squares fitting method implemented by a Python script written for this work, using the Kapteyn package developed by The University of Groningen [245]. Equations that produce a reasonable fit (fits which produce a reduced chi square statistic, χ_r^2 , ≈ 1) to the data were used to generate σ - $\dot{\epsilon}$ - t data through Eq.(3.38) and (3.39) (using differentiation of the fitting equations to determine \dot{h}). Eq.(6.5) was fitted to the data with an increasing number of terms (up to 10) to achieve a χ_r^2 value as close to one as possible.

Conventional indentation measurements of n were evaluated from the *fitted* data by considering gradients of the $\ln(\sigma)$ vs. $\ln(\dot{\epsilon})$ plots (Eq.(3.37)) taken from a range of data intervals, from 1 second of data at the end of the test, to the entirety of the fitted test data following the method outlined in Goodall et al. [191] and Choi et al. [192]. In addition, it was observed that the value of n is not constant. Therefore the time dependent stress exponent, $n(t)$, was evaluated by fitting a tangent between *adjacent* data points from $\ln(\dot{\epsilon})$ vs. $\ln(\sigma)$ plots. Generated data was sampled over the same time values as that of the experimentally measured data. Tab.(9.1) shows the fitting constants for all the crystalline materials over typical indentation tests.

Fig.(6.3a) and (6.3b) illustrates example fitting results for all the equations fitted to typical indentation creep tests in aluminium. The suitability of the fitting equations was scrutinised according to the two following criteria:

1. The quality of the fit achieved to the data.

Results indicate that Eq.(6.2), Eq.(6.3), Eq.(6.1) and Eq.(6.5) fit the crystalline h - t data well, with χ_r^2 values in the region of 1. STS results showed a tendency for the equations to be over-fitted ($\chi_r^2 < 1$), which leaves room for limited degeneracy in the fitting parameters. This is shown (below) to affect extrapolation of these equations. Conversely, fitting to the LTS results tend to indicate a slight under-fitting in the majority good fits ($\chi_r^2 \geq 1$), thus not completely representing (though still gives an excellent approximation to) the data.

Eq.(6.2) proved to be the most sensitive to the initial fitting parameters; a consequence of having a raised power fitting parameter. As such it shows a tendency to being under-fitted for the longer and less scattered data sets of the LTS results, although it fitted the majority of good creep curves in all tested materials in both the STS and LTS tests. Conversely, Eq.(6.1) was far less sensitive to the initial estimation parameters during the fitting process, and achieved similar fitting success to Eq.(6.2), thus making it the most suitable equation according to this criterion.

Eq.(6.3) is used in the literature to determine creep behaviours of BMGs. However results show no dependence to the fitting success of this equation to the amorphous or crystalline nature of the tested material.

Eq.(6.4) produces a poor fit over all tests, indicating either the equation is not suited to fitting indentation creep data, or the initial fitting parameters (despite substantial investigations) were not appropriate. Hackney et al. used Eq.(6.4) to successfully fit their nanoindentation creep data from tests on Sn-C nano-particles separated by a polymer binder (PVDF). The difference in mechanical behaviour between this material and the metals tested here may account for the poor fits produced in our investigations. As such no further creep investigations were performed using Eq.(6.4).

2. The extrapolation of the creep behaviour according to the fitted equation.

Extrapolation of the successfully fitted equations immediately identifies Eq.(6.5) to be unsuitable, producing an unphysical $\ln(\sigma)$ vs. $\ln(\dot{\epsilon})$ relationship even prior to extrapolation.

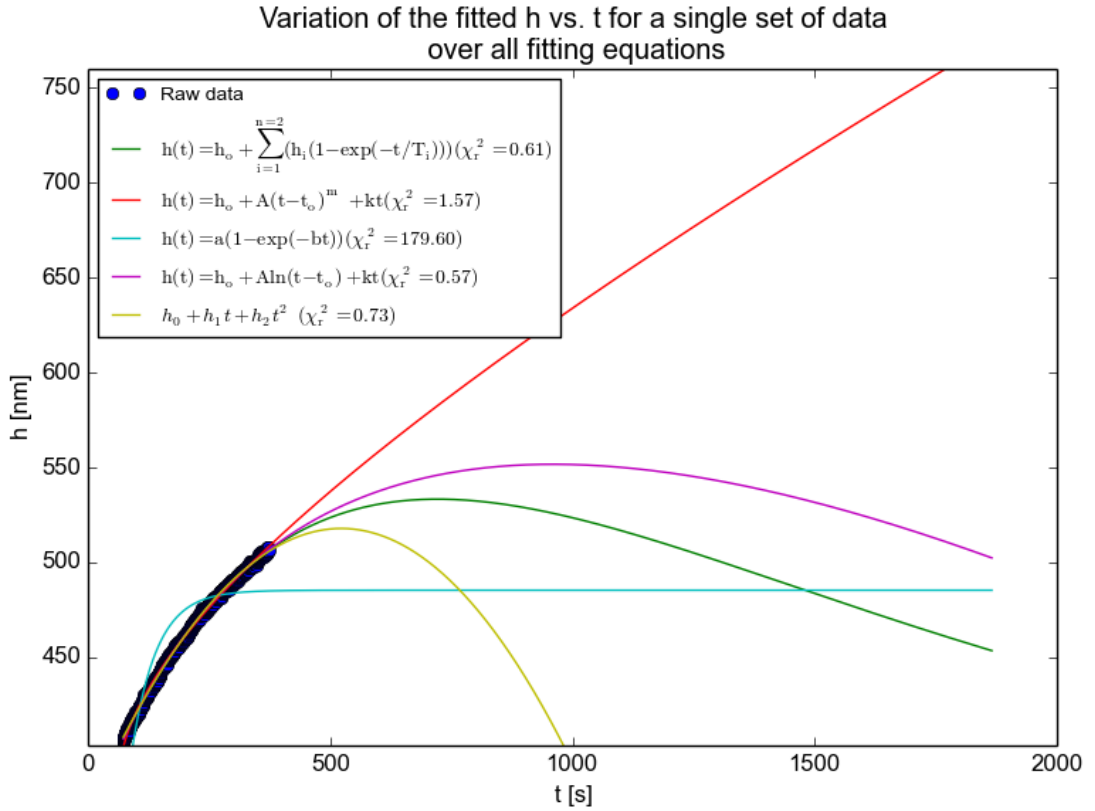
Fits to Eq.(6.1), Eq.(6.2) and Eq.(6.3) to LTS results show better extrapolation behaviours than the STS results, due to increased test times and reduced scatter. The same occurs for the other well fitting equations, which have extrapolated poorly. In these cases, $\ln(\dot{\epsilon})$ vs. $\ln(\sigma)$ show an inverted form, where the change in strain rate accelerates with test time whilst the applied stress reduces with test time. These plots are due to the differentiation of a fitting equation which has degenerate fitting parameters to give an expression that poorly describes the strain behaviour of an indenter during a creep test.

Good fits and extrapolation are found from Eq.(6.1) and Eq.(6.2). However no consideration is given to the physics implied by using a particular fitting equation. Therefore as mentioned earlier, each equation produces a different strain behaviour due to the differentiation of the different fitting equations. This makes it difficult to determine the best fit to estimate n from, as whilst forms of the plots may all look to be plausible, the values of n determined from the different plots can vary significantly (e.g. from 9.0 to 13.2 for aluminium).

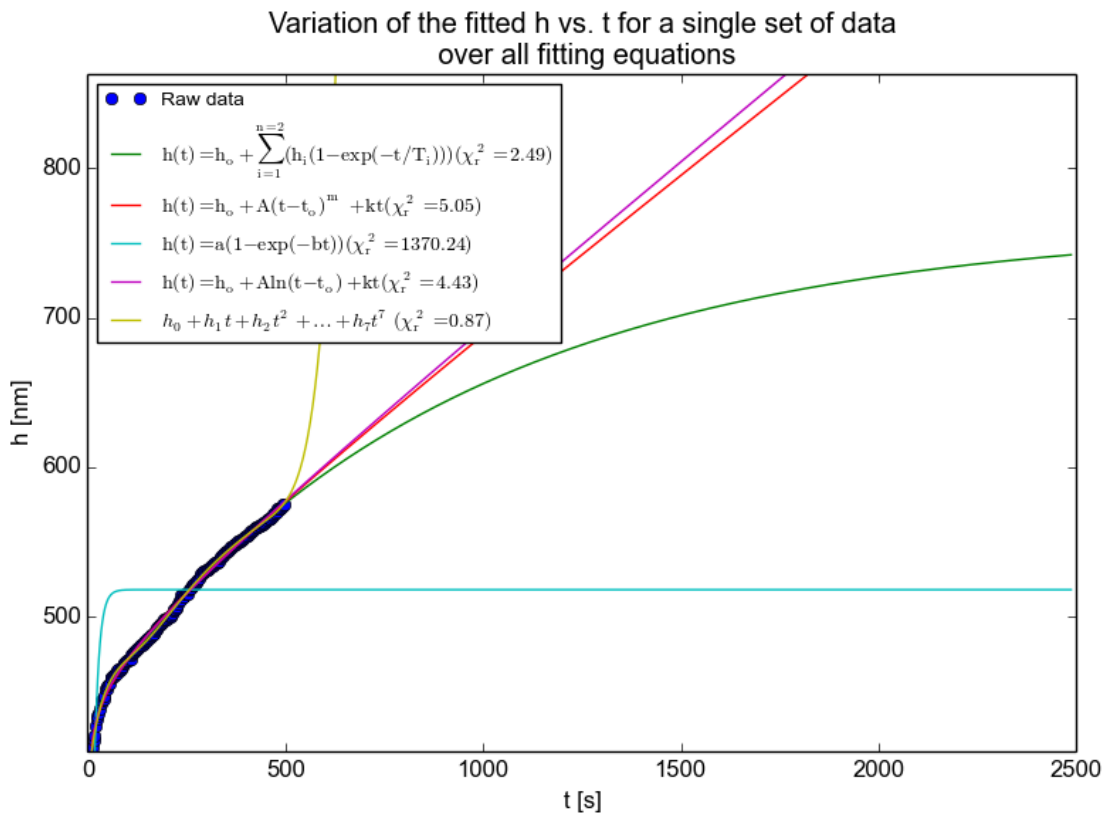
In contrast to the equation fitting analysis, the tangential fitting analysis makes no assumptions of the form of the indentation creep results, and therefore does not suffer from the issues surrounding poor descriptions of strain rate from a fitted equation.

For tangential analysis, tangents were taken to P - h - t data over time intervals of 5, 10, 25, 50 and 100 seconds to produce σ - $\dot{\epsilon}$ - t data such that the optimum time interval for further analysis can be determined; too short an interval will produce large variation in the σ - $\dot{\epsilon}$ - t data due to the influence of scatter over small data intervals, whilst too large an interval will cause the approximation of the linearity of the data from which the tangent value is estimated to no longer to apply. The time intervals were centralised about a particular measurement of interest from which the tangent was being measured, thus allowing tangents to be drawn for every measured data point within the bounds imposed by the time interval. The same process was repeated for the $\ln(\sigma)$ vs. $\ln(\dot{\epsilon})$ data over time intervals of 5,10,30 and 50 seconds, providing $n(t)$ data for each h - t tangential fit. Conventional indentation measurements of n were also evaluated from the *tangentially determined* data by taking the gradients of the $\ln(\sigma)$ vs. $\ln(\dot{\epsilon})$ plots derived previously, over the ranges of 1 second from the test end to the entire $\ln(\sigma)$ vs. $\ln(\dot{\epsilon})$ plot.

Fig.(6.6) shows the $\ln(\dot{\epsilon})$ vs. $\ln(\sigma)$ data from tangents taken from the measured data at time intervals outlined in the figure. The plot shows all the time intervals produce at least partial linear relationships, with plots produced from h - t data with time intervals below 50 seconds showing significant deviation from the nominal behaviour at both the beginning and the end of the experiment. This reinforces the point made by many authors, whereby indentation creep is usually treated such that primary creep is short lived and therefore can be ignored during analysis (a point which neglects to consider the evolving strain field during indentation which introduces more material to transient deformation with respect to test time [228]). Deviation from the nominal behaviour at the end of the test was not expected, as this region of the test is expected to be the most stable region; this deviation is believed to be due to changes in the strain rate becoming so small that it becomes lost in the scatter in the h - t data.

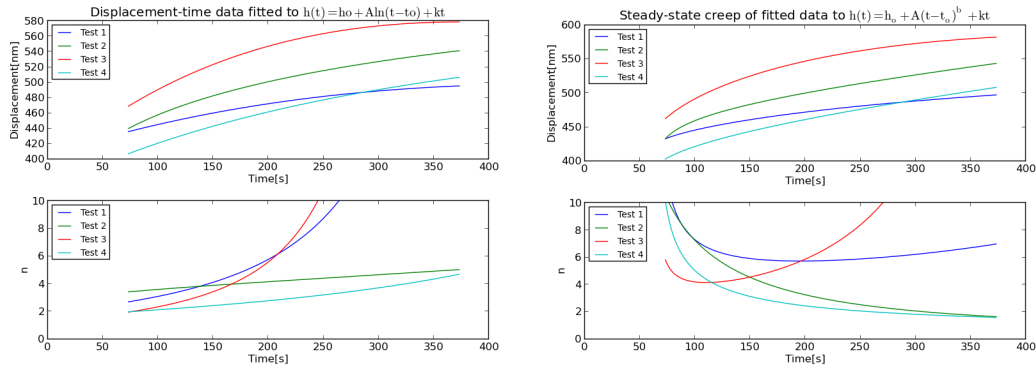


(a) A plot showing the success of all the evaluated fitting equations for STS tests in aluminium.

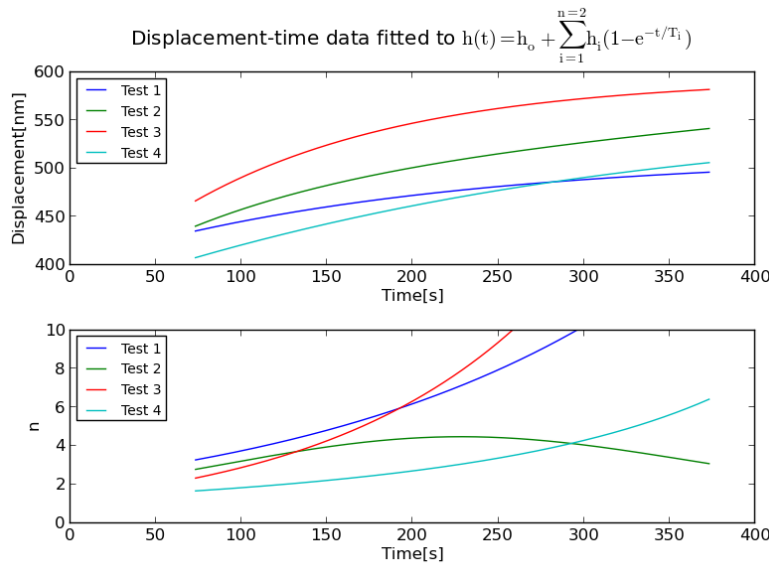


(b) A plot showing the success of all the evaluated fitting equations for LTS tests in aluminium.

Figure 6.3: Plots showing the success of the fitting equations method for Eq.(6.2)-(6.5), and the effect small variations in the data has on the subsequent extrapolation of creep behaviour.

Measuring the time dependent stress exponent: $n(t)$


(a) Fitted Eq.(6.1) data from STS indentation creep tests. (b) Fitted Eq.(6.2) data from Hysitron indentation creep tests



(c) Fitted Eq.(6.3) data from STS indentation creep tests.

Figure 6.4: The fitting results for the most reproducible indentation creep curves. Evolution of $n(t)$ throughout the test evaluated from each equation is also shown.

As n defines a steady state stress exponent value, then it is expected that n values evaluated throughout indentation creep would tend towards a steady value near the end of a test. Therefore $n(t)$ behaviour could identify whether the equation fitting or the tangential analysis method is the most suitable option, and if the test conditions used are suitable.

Fig.(6.4) shows $n(t)$ behaviour evaluated algebraically from the *fitting equation* analysis for the most reproducible tests in aluminium over all suitable fitting equations (Eq.(6.1), Eq.(6.2) and Eq.(6.3)). Each suitable equation shows evidence for approaching a steady n value at long hold times. However it is observed that even for equations that produce similar fits, the analysis produces widely varying stress exponent behaviours with respect to test time. The sensitivity of $n(t)$ to small differences in the measured data and the poor reproducibility of tests in a single material makes it difficult to determine which (if any), is the most valid fitting equation, and therefore the most valid $n(t)$ behaviour which a material conforms to. For a successful analysis, steps must be taken to improve the reproducibility of raw measurements, even if the measurements

appear to reflect good indentation creep curves.

Tangential analysis cannot be applied to adjacent data points (as achieved with the fitting equation method) due to the presence of scatter in the data. Therefore the best interval depends on the raw data obtained. For study of $n(t)$ behaviour, the smallest data range possible must be considered to carry the full range of measured data through to $n(t)$ values, but small evaluation intervals are the most sensitive to scatter in the data. There is foreseeably a condition whereby data point resolution and stability of the tangent values can be optimised. This condition would depend on the quality of the raw measurements and therefore would certainly vary from test to test. As previously stated, the scatter in the stress and strain rate data obtained here only show typical indentation $\ln(\sigma)$ vs. $\ln(\dot{\epsilon})$ behaviours when tangentially fitted to over 50 seconds worth of data. This heavily dilutes the time resolution of the considered data points, which would be further diluted by the need for further tangent fits to determine n values. It is therefore not recommended to use this method to accurately evaluate $n(t)$, unless the data obtained has exceptionally low scatter and is sampled rapidly.

Measuring the time independent stress exponent: n

It is noted that data collected at the start of any indentation creep test is likely to contain significant additional contributions to deformation other than creep, despite the pre-loading profile. Therefore it is expected that not all the data will be suitable for a conventional analysis of n .

Fig.(6.5a) shows conventionally measured stress exponent values (that is n evaluated from the gradient of $\ln(\dot{\epsilon})$ vs. $\ln(\sigma)$ data) from data from fitting equations Eq.(6.1)-(6.3) over time intervals of 1 second from the test end to the entire data range in typical tests in aluminium. The value of n remains relatively constant at time intervals close to the end of the tests (≈ 1 s from the end of the test) for individually considered fitting equations. Interestingly, the values of n from all equations converge in both STS and LTS tests to a value that is representative of literature data for aluminium (see Tab.(9.3)) when evaluated over all the data. However Fig.(6.5b) shows the tangents responsible for n for the entirety of the data set and the data just prior to the test finishing. This clearly identifies the converging values of n to expected values to be due to poor fitting and is therefore mathematical coincidence.

Evaluation of conventional n values from tangentially evaluated data is possible due to the large data intervals being evaluated. Fig.(6.6) shows that fitting the $h-t$ data to larger data ranges removes the extraneous features of the shorter data range evaluations and provides a more conventional $\ln(\dot{\epsilon})$ vs. $\ln(\sigma)$ plot from which to evaluate n . Plots of 100 second evaluated $\ln(\dot{\epsilon})$ vs. $\ln(\sigma)$ data in both STS and LTS tests show the most stable behaviour, which translates to a more stable conventional n value. However, this smoother profile from the longer evaluation times may not be indicative of a better approximation to the n , as the data analysed to achieve n may not be representative. Reducing the noise in the raw $h-t$ data allows tangential fitting to be achieved over smaller time intervals, with no loss of accuracy in determining the $\ln(\dot{\epsilon})$ vs. $\ln(\sigma)$ plot.

Scatter and deviations at the start and end of the plots change with each $\ln(\dot{\epsilon})$ vs. $\ln(\sigma)$ data set, with greater variation and scatter being more prevalent for smaller time interval evaluated stress-strain rate data. However, there are three key sections common to all the $\ln(\dot{\epsilon})$ vs. $\ln(\sigma)$ plots produced this way (See Fig.(6.6)):

- Section 1 (right side): This data represents data not consistent with the steady state creep approximation and should be avoided when evaluating n .
- Section 2 (Linear section): This gives data for the most stable estimation of n . The length and stability of this section varies with the time interval used to evaluate $\ln(\dot{\epsilon})$ vs. $\ln(\sigma)$

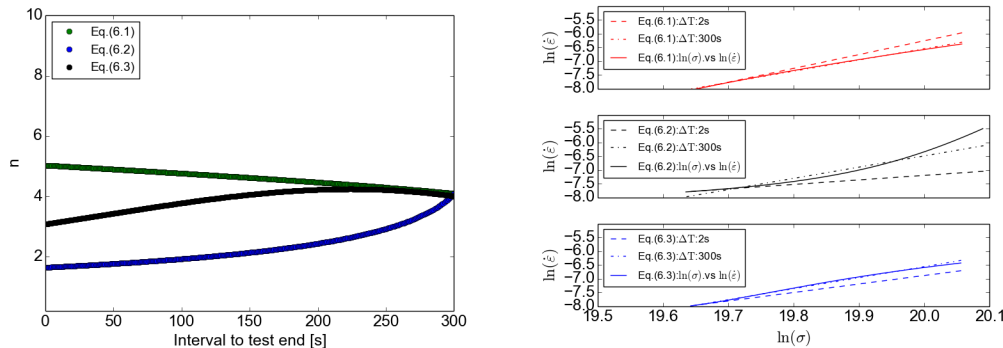
data.

- Section 3 (left side): This section is caused by tangents fitted to the data being heavily influenced by scatter. The time at which this occurs defines the minimum limit where n can be evaluated.

Understanding the cause of the different sections of these plots will allow users to make the most valid estimate of n . It is immediately apparent that sections 1 and 3 produce poor estimations of n due to the contribution of primary creep and scattered data respectively, so estimation of n must be taken from section 2. However identifying where within section 2 is safe to sample to evaluate n is subjective. Using the criterion whereby n is taken when the maximum amount of data is utilised such that the data remains linear (i.e. from the section 1-2 border to the end of the test data) gives the most valid estimation of n from the point of view of the data. However, steady state creep can only be approximated after long hold times, with primary creep convoluting early measurements the most. Therefore this approach will introduce a systematic error in favour of overestimating the value of n values.

Measuring n from data on the border of section 2-3 whilst the tangential fitting still produces a $\chi^2 \approx 1$ will sample less primary creep. However this method is reliant on levels of scatter in the $\ln(\dot{\epsilon})$ vs. $\ln(\sigma)$ data, thus will introduce more random error associated with n than the section 1-2 case. Therefore measurement of n depends on the quality of the raw data and the length of the data being considered, with short and scattered data requiring analysis from the section 1-2 border and vice versa.

There is little consensus in the literature for a set time or defined conditions beyond being approximately linear over which n should be evaluated for both analysis methods. This presents a problem for achieving estimates of n that conforms to other works. To that end, in addition to fitting tangents to the data points defined by the section borders in Fig.(6.6), n values were measured using the χ_r^2 technique to fit a straight line from the end of the $\ln(\dot{\epsilon})$ vs. $\ln(\sigma)$ data to a point such that the maximum amount of data from the test end is considered whilst χ_r^2 remains ≈ 1 . Tab.(9.4) and Tab.(9.5) shows the values of n derived through these three approaches for all materials tested in all test conditions. The results show little evidence that any of the approaches here indicate an n which conforms with literature with any confidence.



(a) A typical indentation creep test in aluminium using the STS test regime.

(b) The $\ln(\sigma)$ vs. $\ln(\dot{\epsilon})$ plots for each fitting equation from data in Fig.(6.5a).

Figure 6.5: Plots showing how conventional measurements of n vary as different amounts of data is considered for the evaluation of n .

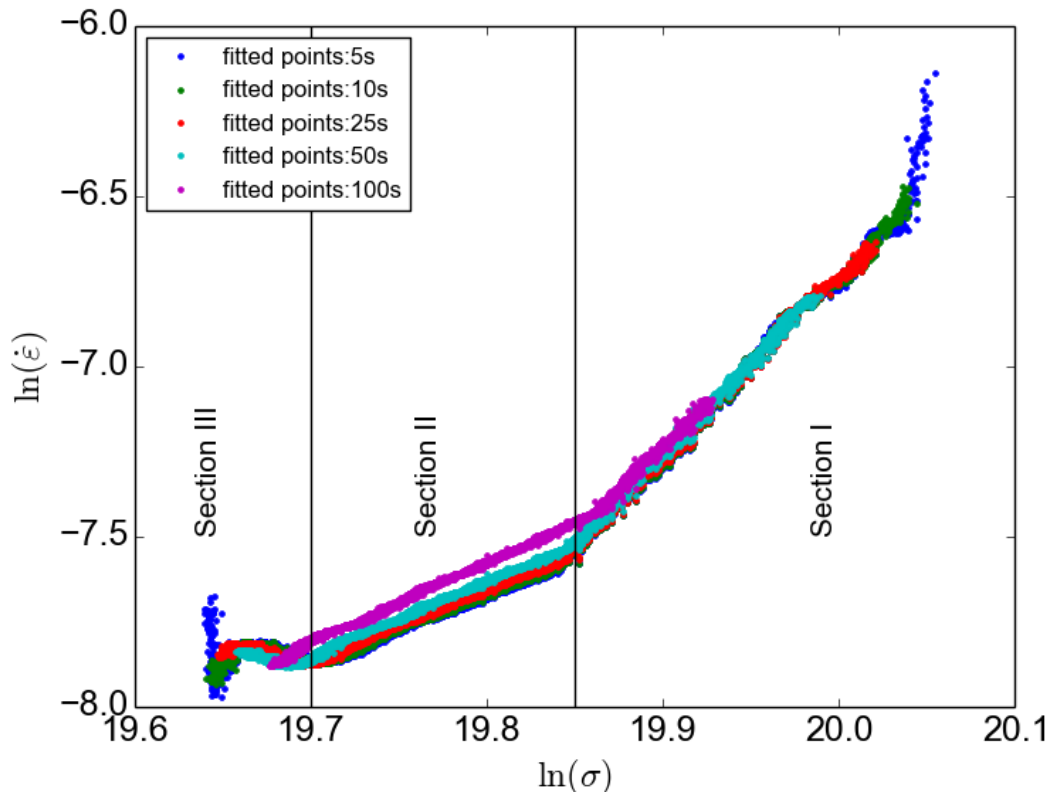


Figure 6.6: The derived $\ln(\sigma)$ vs. $\ln(\dot{\epsilon})$ data from STS investigations through fitting tangents to the data over time intervals indicated by the figure.

6.1.2 Other factors for consideration

Microstructure

It should be noted that microstructure was not quantified in any of the materials prior to testing, so variability may arise due to mechanical anisotropy over differently orientated grains in crystalline samples. However, tin samples had microstructure large enough to be visible by eye after sample preparation (as shown in Fig.(9.14) in the appendix), such that all indentation creep tests performed on tin were purposefully confined to a single grain. The poor test reproducibility in tin as well as the other samples indicates that there is more affecting the results than just grain orientation. This is supported from the tests performed in BMGs where, whilst local mechanical variability is expected, the lack of crystal structure does not diminish the variability of the indentation creep results. It is recognised that the characterisation of a single microstructure in one sample is not enough to absolve grain orientation as a potential factor which may affect test reproducibility, especially considering how mechanically different tin is compared to the other tested materials, so the effect of grain orientation on indentation creep tests requires further investigation (as it has been noted to play a considerable role in the reproducibility of indentation results [230]).

Thermal Drift

STS tests show varied reproducibility of general creep trends, which deteriorates with the experiments progression compared to that of the LTS testing regime. If this variation is due to thermal drift, then this indicates the initial correction made for thermal drift for STS tests is not applicable for the entirety of the test. Therefore *transient* drift is a problem for indentation creep,

which becomes dominant with longer test times. This is supported with STS testing, where the drift stability of the system did not allow the load hold time to extend beyond 5 minutes. In addition, STS tests in tungsten (shown in Fig.(6.1f)) show that initial stages of deformation are all reproducible, but subsequent deformation shows little compatibility across any of the tests. This implies that the drift rate deviates from its original correction after ≈ 30 seconds at peak load, ≈ 80 seconds after the drift correction is estimated. This effect is not strongly observed in the LTS tests of tungsten, which was tested to the same peak load in both systems, and so that further tests are required to quantify this effect.

Peak load and loading rate effect

The loading methodology has been shown to have a clear impact on the reliability of indentation creep tests. Fig.(6.1) shows the reproducibility of the creep data mostly improves with a combination of higher loads and greater penetration depths for crystalline materials. This reduces the potential influence of indentation size effects on the results (e.g. dislocation starvation, contact area differences, elastic transient effects and residual stresses) and increases the accuracy of the equipment by minimising the effect of percentage error in measurements.

To explore this further, indentation creep in metallic glasses has been explored (details outlined in Chap.(4) and Tab.(4.2)) in order to evaluate the effect of different loads and loading rates. BMGs have a simple flow based creep mechanism due to their lack of crystalline structure. Therefore whilst activation energies of this creep mechanism may differ across different BMGs, the stress exponent is not expected to vary significantly. It is recognised deviations in creep behaviour may occur due to the relatively random nature of atomic packing within metallic glass structures and the local nature of the tests, but these deviations are expected to be small.

Observations of the $h-t$ data of the BMG tests confirm the findings of higher peak load experiments producing more plausible indentation creep behaviour than the lower load experiments regardless of loading rates. As with the crystalline samples, apparent expansion is observed in some of the lower load tests. Whilst this previously could be attributed to thermal drift, the metastable nature of BMGs has led to reports of nanocrystallisation during indentation, allowing for another explanation for the phenomena [211]. On a bulk scale, this would result in an overall densification of the material due to differences in packing efficiencies. However on a local scale, the reverse is true where efficient packing of short range atomic clusters in BMG structures can be accommodated [5]. Nevertheless the scale of the poor reproducibility in these tests is similar to that observed in the crystalline materials and nano-crystallisation is therefore unlikely to be the primary cause of these poor indentation creep results at lower loads, even if the effect does occur.

Pop-in features are seen to occur in both the high and low load cases in BMGs. Fig.(6.7) shows that pop-in events produce substantial displacement events in the $Zr_{44}Cu_{44}Al_6Ag_6$ BMG at $2mNs^{-1}$ loading rates. This is reduced in population and size for loading rates of $1mNs^{-1}$, however it is observed that at $0.5mNs^{-1}$, smaller pop-ins are numerous, whilst large pop-in events are absent. Schuh et al. [246] reported the increase in density of pop-in events during loading of BMGs with increasing loading rate to the point where the pop-in events saturate the loading curve, and are not observed discretely. There is potential for a similar effect to be occurring here. Therefore low loading rates and high peak loads are recommended for evaluating indentation creep behaviour. Conversely, the findings of Dean et al. suggest higher loading rates produce approximate steady state creep more rapidly in crystalline materials [228]. Regardless of the nature of the creep at different loading rates, sudden large deformation events are unfavourable.

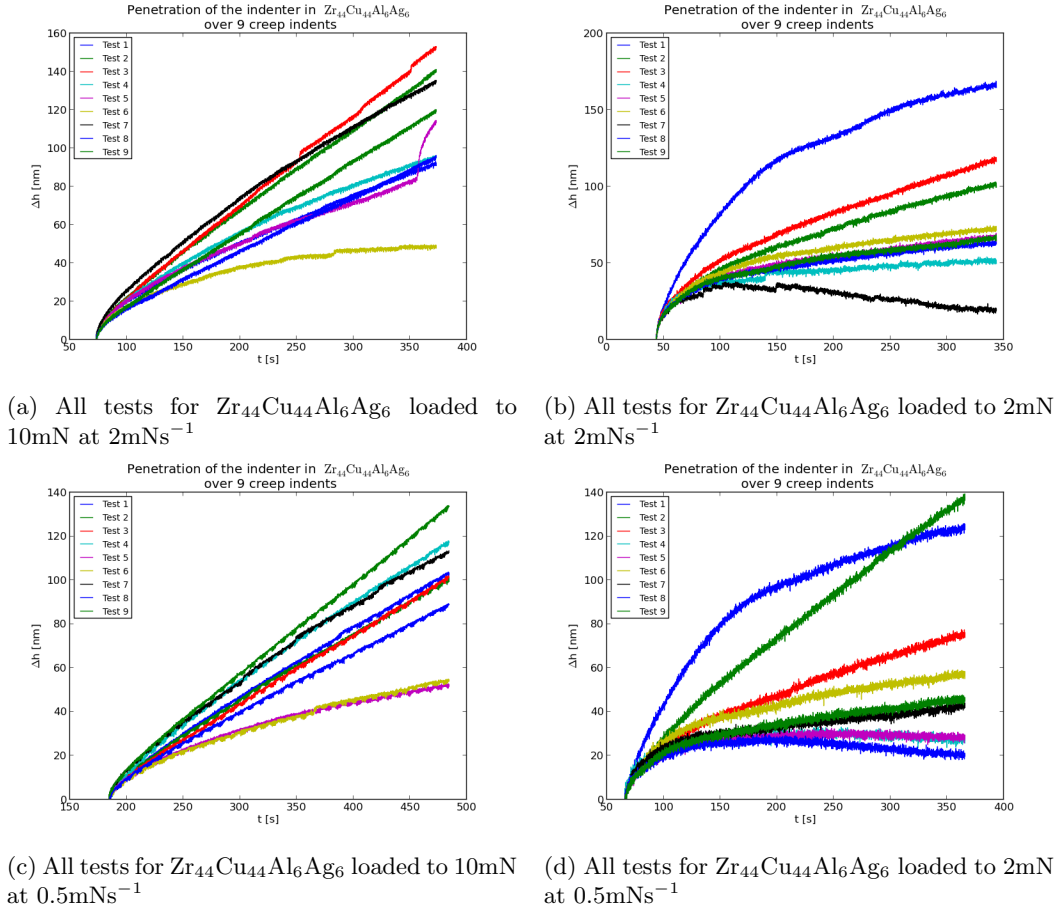


Figure 6.7: Displacement-time data for indentation creep tests in $Zr_{44}Cu_{44}Al_6Ag_6$ at different peak loads and loading rates.

6.1.3 Optimal method and limitations

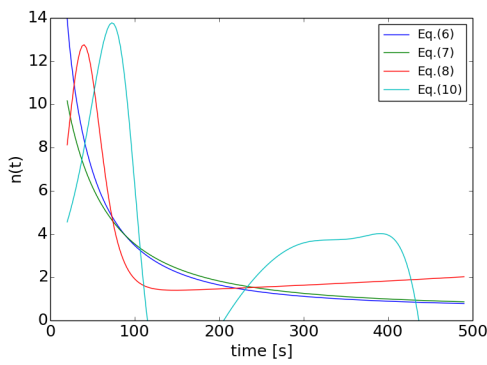
The two data analysis methods described so far have had mainly mutually exclusive weaknesses, with the tangential method being dependent on measurement scatter, and the fitting method introducing error from poor fitting and an incomplete description of strain rates from the fitting equations. As such it is possible to combine the methods whereby:

- Measured data is fitted to an equation to produce continuous data from the fit (measurement scatter remains accounted for in the error of the fitting parameters of the equation).
- Stress, strain rate and stress exponent behaviour are extracted from the continuous data through a tangential analysis approach. This forces strain rate behaviour to be dependent only on the quality of the fit, and not on the incomplete mathematical description of the strain rate that the fitting equation portrays. High resolution $n(t)$ results can then be produced, as the scatter in the results no longer directly affects the tangent measurements.

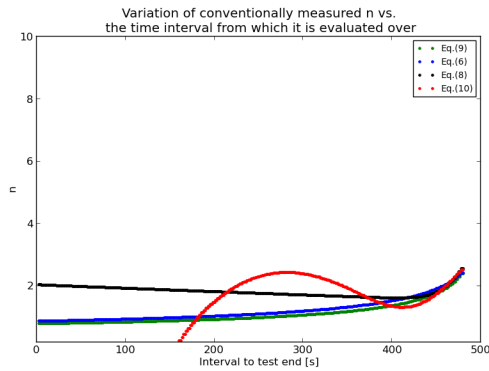
Indentation results for aluminium for both STS and LTS tests are given as an example to demonstrate the combined analysis method; the method was performed on all indentation creep tests, with results reported in Tab.(9.4) and Tab.(9.3). Fig.(6.8a) and Fig.(6.8b) shows the successful use of the method in LTS data. All equations, except Eq.(6.5) (for reasons outlined in Sec.(6.1.1)), predict individually consistent $n(t)$ values at long hold times; the expected typical case for CLH indentation creep tests. However, Fig.(6.8b) shows significant differences in the measured values of n to that reported in literature. This discrepancy of n can not be explained through

the fitting equations themselves (see Sec(6.1.1)). Therefore the discrepancy must be either be due to the reproducibility of steady state creep during indentation or inaccuracies in the theory.

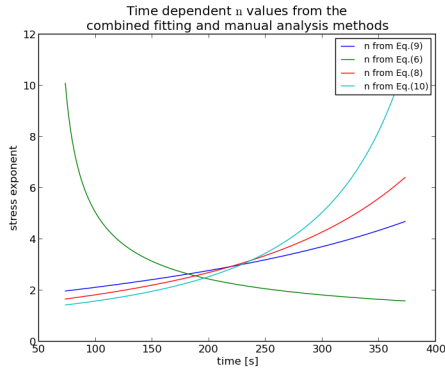
Though the combined method aims to reduce the weaknesses of either of the two analysis methods, analysis of STS test shows it is still heavily dependent on the quality of the input data. Fig.(6.8c) highlights this, whereby all the equations fit the data adequately, with a slight over-fitting noted for Eq.(6.1), Eq.(6.3) and Eq.(6.5). However analysis from Eq.(6.1) and Eq.(6.3) produces an unphysical creep behaviour reminiscent of the pure fitting equations methodology. These equations have poor extrapolation behaviour, although that is not important as the method uses an equation purely based on its ability to fit the data. Therefore the failure of this method in the STS case must be due to the definition of a good fit utilised, i.e if the fit produces a $\chi^2 \approx 1$. This could occur with data that may have been slightly over-fitted, or to poor fitting conditions in local regions near the start and end of tests. More scatter and shorter test times in the STS results allow for both of these effects to be present.



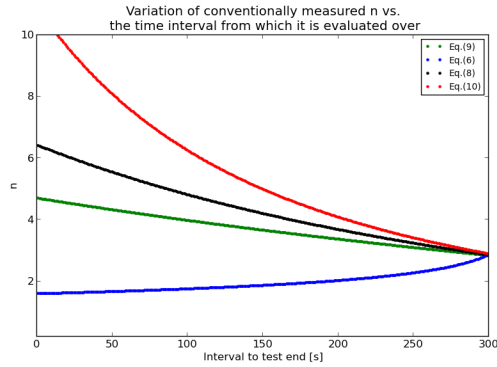
(a) Time dependent n from LTS fitted data, converted to stress and strain rate data through the tangential analysis.



(b) Conventionally measured n from LTS fitted data, converted to stress and strain rate data through the tangential analysis.



(c) Time dependent n from STS fitted data, converted to stress and strain rate data through the tangential analysis.



(d) Conventionally measured n from STS fitted data, converted to stress and strain rate data through the tangential analysis.

Figure 6.8: Results for the creep analysis combining the fitting and tangential methods.

6.2 Conclusions

The methodology for the use of nano-indentation to probe homogeneous flow in BMGs or creep in crystalline materials appears to be sensitive to multiple extrinsic factors, making it a difficult test to perform accurately and reproducibly. Based on these observations, use of nanoindentation

to probe the absolute nature of homogeneous flow in BMGs cannot be recommended. However the use of the technique to determine relative changes in flow behaviour with changes in affecting factors such as test temperature, chemical composition or thermomechanical processing history may still yield useful insights to BMG deformation behaviour results.

Work presented here has shown that even small changes to the way a test is performed can have a large effect on the measured values. Beyond optimised sample preparation and minimisation of environmental sources of noise, the following points could help improve reliability, accuracy and validity of indentation creep tests:

- Higher loads during testing.
- Low loading rates in BMGs and higher loading rates in crystalline materials.
- Characterisation of the stability of the thermal drift assessment.
- Long thermalisation times.
- A load profile featuring a pre-load hold cycle.

Analysis of the raw data has highlighted that low noise and long test times are paramount for accurate and reliable analysis of CLH indentation creep data. In addition, results have a strong dependence on the use of a tangential or fitting equations approach to analyse the data. Whilst the understanding of stress and strain fields below indenters remains poor, the use of any method to evaluate absolute indentation creep parameters is not advised. However the method may be used to judge the general creep behaviour within a material.

It should be noted that the work reported here has restricted itself to the stress dependency of creep. Related analysis techniques have been proposed and used for indentation creep data gathered making use of the increasingly widespread capability to perform indentation tests at elevated temperature to make an assessment of the activation energies. While these types of experiments have not been used here, it is clear that many of the issues associated with determining an accurate value for a representative strain rate at a particular point in the test will also affect these measurements.

Chapter 7

Probing inhomogeneous yield behaviour in BMGs

Chap.(3) discussed the main mechanical failure modes in BMGs under a range of different stress-strain rate conditions defined by the deformation map in Fig.(3.9). Failure in high strain rate and low temperature (but not cryogenic [247]) environments leads to the most catastrophic failure mechanism of BMGs, preventing the use of BMGs in applications which would greatly benefit from the other properties BMGs have to offer, (outlined in Tab.(3.1)). Whilst certain features regarding the shear band failure mechanism are widely accepted, such as a critical elastic shear strain of $0.0027\gamma_c$ prior to the onset of plasticity [41], the specifics, especially during its early stages of shear banding, have yet to be fully understood [4, 6, 98].

Literature has highlighted two main mechanisms through which shear bands form; shear transformations, propagation of a shear front from a nucleation site comprised of a cluster of STZs [99] and through the percolation of STZs along the plane of critically resolved shear stress [140]. Schuh suggested that the true nature of shear banding may lie somewhere between the two methods [4], but experimental proof regarding these mechanisms has yet to be reported. Chap.(3) outlines the significant progress made in understanding the mechanisms and factors affecting the catastrophic failure of these materials.

Whilst improvements in theories as well as experimental and analytical investigations have improved the understanding of shear band processes, a fundamental understanding of the true mechanism behind shear banding still eludes researchers. To that end, novel testing methodologies are clearly required. This chapter provides the framework for the development of a new probing technique, capable of indirectly measuring structural changes during shear band events.

7.1 Use of cross property characterisation of inhomogeneous yield

Indirect testing methodologies involve the measurement of one material property to provide information regarding another material property. For example, the work performed by Plummer outlined in Chap.(2) used measurements of Poisson's ratio to infer information about BMG structures [17]. This chapter aims to utilise a similar philosophy to probe shear band behaviours through measuring properties that play no direct part in the shear band process, but are affected by the formation of shear bands. Observations of electrical properties are the most obvious indirect property to investigate, as the charge carriers responsible for electrical conduction of BMGs are also

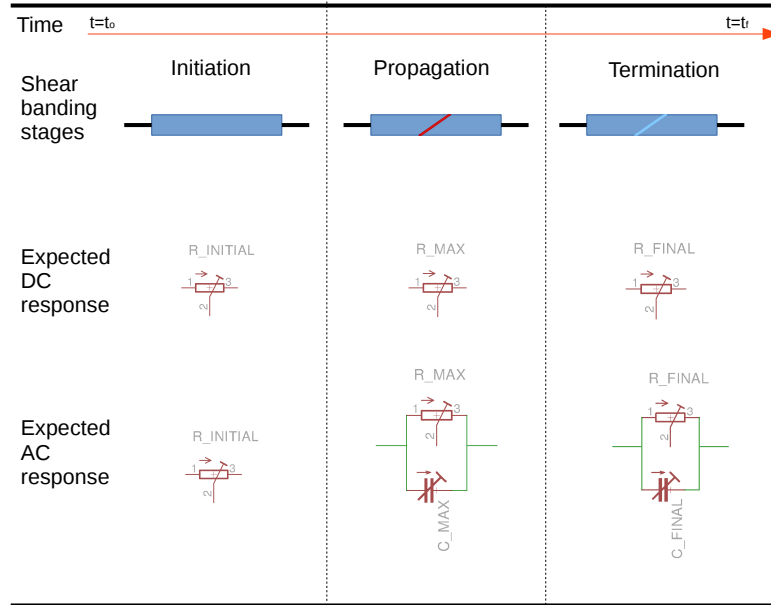


Figure 7.1: A schematic of a shear band from initiation to rest with the expected electrical responses associated with each stage depending on the electrical current source used.

responsible for the bond strengths between atoms in a BMG structure, from which mechanical behaviours arise. However, whilst complex correlations between electrical and mechanical parameters are reported in the literature [48], these parameters are based on what will now be termed as static properties, where correlations are explored with no consideration given to how these properties may change with time. For all theories behind catastrophic failure in BMGs, it would be assumed that the shear banding process is highly dynamic. Therefore similarly dynamic correlations and measurements of electrical and mechanical parameters are needed to understand the shear banding process further through this philosophy.

7.1.1 Using an electrical response to probe shear banding behaviour

Fig.(7.1) shows a typical schematic of a shear band event in a BMG under compression. The details surrounding exactly how a shear band form are still unclear, however there are certain facts known to be true during the formation of a shear band:

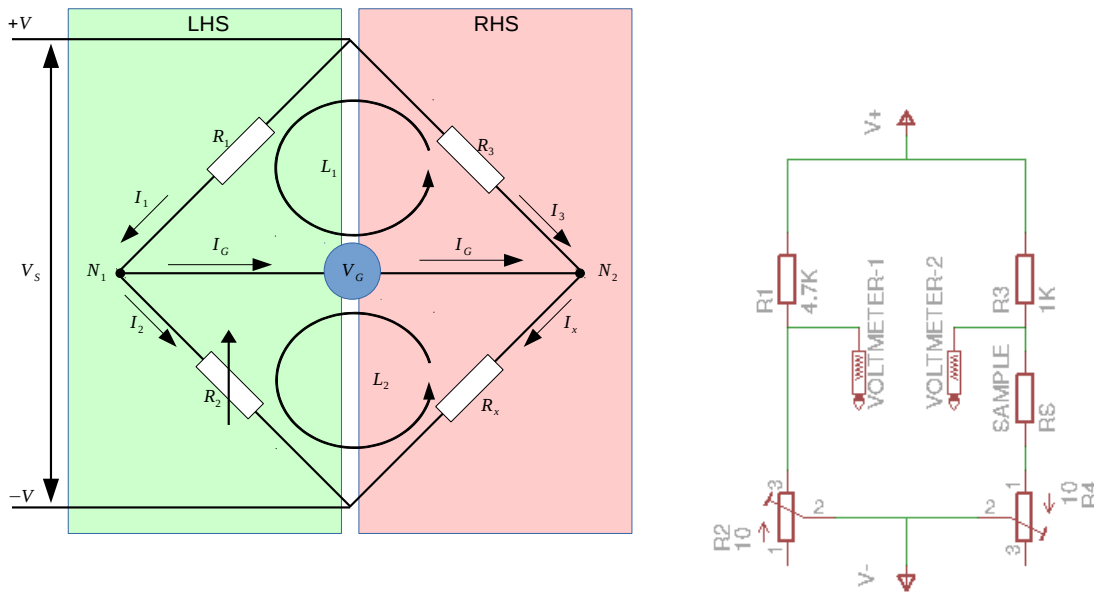
1. Shear band initiation and propagation is very quick [141].
2. Thermal energy is produced during shear banding [84, 129].
3. Structural changes occur during shear banding [57, 98, 141].

Thermal and structural changes in any material are known to affect the electrical resistance (and impedance) of that material [89, 90]. As shear bands are known to produce both thermal and structural changes, it follows that the shear band process will also affect the electrical resistance of the material. Based on this assumption, Fig.(7.1) schematically identifies the electrical response expected from shear band behaviour if monitored with an AC and a DC current. This provides a basis upon which shear band behaviours can be measured through electrical properties.

The first step is designing an experiment capable of correlating shear band behaviour with resistance change. This highlights the key aim of this section: the design, manufacture and testing of an experiment capable of linking shear band behaviours to dynamic changes in resistivity.

7.1.2 Wheatstone bridge calculations and expected signals

The Wheatstone bridge shown in Fig.(7.2a) is a fundamental piece of equipment, first created by Samuel Hunter Christie in 1833 and improved on by Sir Charles Wheatstone a decade later [248]. Fig.(7.2b) shows the circuit diagram for the Wheatstone bridge utilised for shear band detection; this is almost identical to the classic version, save for the extra variable resistor at R_4 in Fig.(7.2b) to give extra sensing flexibility.



(a) Schematic of the classic wheatstone bridge.

(b) Wheatstone bridge set-up utilised in the development the proposed experiment.

Figure 7.2: Circuit diagrams of the classic set-up of the Wheatstone bridges and the slightly modified Wheatstone bridge proposed for experimental investigations into the effect shear banding behaviour have on resistance measurements

The Wheatstone bridge uses a comparative measure between the current flow through two sides of the circuit, labelled LHS and RHS in Fig.(7.2a). LHS of the circuit has a known electrical resistance determined through the sum of R_1 and R_2 , whilst the RHS of the circuit has an unknown electrical resistance due to the unknown resistance value of the material being tested (labelled R_x). A Wheatstone bridge set-up can accurately measure values of R_x based on the measurement of the gate voltage (V_G) through

$$V_G = \left(\frac{R_2}{R_1 + R_2} - \frac{R_x}{R_x + R_3} \right) V_s. \quad (7.1)$$

From the gate voltage to shear band resistance measurements

The Wheatstone bridge is suitable for detecting static values of resistance but has potential difficulties when applied to detecting highly dynamic, unpredictable and tiny changes in resistance,

such as those expected for shear banding. For example, at the high sensitivity end of the Wheatstone bridge's capabilities, the requirement of setting the gate voltage to exactly zero is a practical impossibility due to surrounding electromagnetic noise and thermal drift. In addition, measuring the resistance values of R_2 and R_4 to the required accuracies such that an absolute resistance values of R_x can be determined at any given point is also every difficult. As such a revised use of this aspect of the experimental equipment is required.

The Wheatstone bridge is based on comparative measures of a known and unknown state of the system. By taking this philosophy further, it can be stated that changes in gate voltage measurements over a time interval of Δt must be due to changes in the resistance behaviour of the material if the circuit is kept in a static state (i.e. all values of R apart from R_x in Fig.(7.2) remain fixed). Therefore if experimental noise remains relatively static over short time intervals, then any change in the value of V_g over these time intervals must be due to changes the resistance at R_x ; i.e. resistance changes due to a shear band event. This is described mathematically as follows:

$$\frac{V_G(t) - V_G(t_0)}{V_s} = \left| \frac{\Delta V_G(t)}{V_s} \right| = \left| \left(\frac{R_x(t)}{R_x(t) + R_3} - \frac{R_x(t_0)}{R_x(t_0) + R_3} \right) \right| \quad (7.2)$$

Taking $V_G(t_0)$ and $R_x(t_0)$ to be the voltage state of the circuit and the resistance state of the material just prior to a resistance change event, then Eq.(7.2) allows the measurement of relative voltages to infer relative changes in resistance state of a material. Further to this, careful selection of the fixed resistance value R_3 such that $R_3 \gg R_x(t_0)$, even when R_4 (the extra variable resistor added to the classic bridge circuit which is captured by $R_x(t_0)$) is in the most resistive state, then the contribution of the $\frac{R_x(t_0)}{R_x(t_0)+R_3}$ term to $\Delta V_G(t)/V_s$ can be neglected:

$$\begin{aligned} R_x(t_0) &\ll R_3 \therefore \\ \frac{\Delta V_G(t)}{V_s} &\approx \frac{R_x(t)}{R_x(t) + R_3} \\ R_x(t) = R_{par} + R_x(t_0) + R_4 + R_{SB}(t) &= \frac{\frac{\Delta V_G(t)}{V_s} R_3}{1 - \frac{\Delta V_G(t)}{V_s}} \end{aligned} \quad (7.3)$$

Eq.(7.3) shows that $R_x(t)$ can be measured based on the difference in the gate voltage prior to a shear banding event, and knowledge of R_3 , which is fixed at a known high value for the experiments performed here. The value of R_x is made up resistance contributions due to shear banding, the resistance of the material pre shear band event ($R_x(t_0)$) and parasitic resistances from wiring and other resistance sources native to the circuitry (R_{par}). Therefore measuring resistance change in a BMG due to shear banding requires the separation of R_{SB} from all contributors to $R_x(t_0)$. Values for these contributors cannot be measured in their absolute, however the comparative philosophy of the measurement aids in eliminating these contributors by stating that they are either static throughout a shear band event or have negligible contribution to the resistance compared to the resistance contributions afforded by a shear band event. Therefore any changes in the $\frac{\frac{\Delta V_G(t)}{V_s} R_3}{1 - \frac{\Delta V_G(t)}{V_s}}$ term must be due to a change in R_{SB} :

$$R_{SB}(t) = \frac{\frac{\Delta V_G(t)}{V_s} R_3}{1 - \frac{\Delta V_G(t)}{V_s}}. \quad (7.4)$$

In conclusion, Eq.(7.4) shows that the resistance state of a shear band can theoretically be measured through a Wheatstone bridge based set-up through a comparative measurement approach.

Such a set-up is here described as a Shear Band Electronic Signal Detection (SBESD) system. The following sections describe the design, development and testing of the SBESD system, and its use for developing a first approximation regarding the relationship between shear band behaviours and resistance responses.

7.2 Shear band detection limits through the Shear Band Electronic Detection System (SBESD)

Detection of shear band events through a SBESD system requires a system capable of detecting changes in resistance that are small and fast enough to represent a shear band. As such, we discuss the theoretical detection capabilities of a SBESD system.

7.2.1 Shear band lifetime

The lifetime of a shear band depends on the definition used to define shear band activity. If an active shear band is defined as an event capable of actively accommodating plastic deformation, then the lifetime of the shear band is defined by the time taken to accommodate said deformation. However if the active lifetime of a shear band is defined by time over which the state of the shear band material *could* accommodate deformation, then the shear band lifetime is defined by the time taken for shear-banded material to return to a metastable rest state. The first instance describing shear band lifetimes is purely dependent on mechanical response, however the second instance is dependent on the state variables of the material. We recall that the SBESD system relates the indirectly linked resistivity values to the shear banding behaviour; both of which are dependent on the material's state variables. To that end, the latter definition of shear band lifetimes must be considered in order to fully characterise shear band behaviour through changes in resistance.

The uncertainty behind the exact mechanism by which shear bands initiate makes it difficult to determine a specific minimum time in which a shear band can form. The first approximation that can be made to this value is that defined by the Debye frequency (i.e. the natural frequency of atomic vibrations within the structure). This defines time scales in which individual atoms can undergo a spatial transformation with the BMG structure. As such, no plastic process can occur quicker than this, thereby providing an absolute lower limit to lifetime of a shear band, whilst recognising it as a significant underestimate of the true lifetime value.

The next approximation to the lower limit of shear band lifetimes is the time taken for a sonic pulse to traverse the material. The validity of this condition depends on the mechanism through which shear bands are formed. If shear bands are formed through the nucleation of a shear wave from a single or cluster of shear transformation zones, then this lower limit to shear band lifetimes is likely to be accurate. However if shear bands form due to the coalescence of STZs along the plane of critically resolved shear stress, then lifetimes could be either quicker or slower than this estimate. As mentioned in Chap.(3), current estimates of shear band formation theory state that shear bands are initiated through the 'shear wave' approach, but are maintained through the coalescence of STZs [136], making sound velocity a good lower limit estimate of shear band lifetimes.

The upper limit to a shear band life span, based on the life span definition outlined earlier, depends on the length of time a shear band can maintain a material state whereby the viscosity remains low enough to allow for Arrhenius flow behaviour. Work by Qiao et al. on shear banding behaviour under cryogenic conditions showed that the required viscosities for localised flow are achievable if temperatures of shear banded material of $\geq 0.8T_g$ are achieved and maintained [247].

Therefore the time over which shear banded material can maintain a $T = 0.8T_g$ defines the upper time limit of a shear band's life span. It is worth reiterating that temperature increases due to shear banding behaviour are a consequence of the shear banding process rather than a cause. This is why temperature considerations are only used in estimating the upper limitation of shear band life spans. Lower lifespan limits are focused around the initiation of a shear band, a process shown to be reliant on viscosity reduction through free volume generation, not thermal energy generation.

Literature has noted significant releases of thermal energy during shear band formation, capable of local melting of tin coatings [84] and has been reported to reach temperatures ranging from 3400 K to 8600 K in the initial stages of shear band formation. By substituting these temperature conditions and thermal conductivity terms into Eq.(7.7) (described later), the time required for the material to reach a thermal state whereby $T \leq 0.8T_g$, an upper limit to shear band lifespans can be found. For most BMGs, lifespans are limited to ≤ 1 ms from reported literature values [141] and observations of the time required to dissipate a compressively loaded material (see Fig.(7.9)).

7.2.2 Shear band energy and its effect on resistance

The effect of shear banding on measured resistance is complex. Chap.(3) describes the some of the mechanisms and factors affecting current flow in BMGs, which are difficult, convoluted and only work well in very specific simplified amorphous alloys. Therefore application of these mechanisms to the case of a shear banding BMG to define the magnitude of the resistance response of the material undergoing the process is beyond the scope of this work. However, there are still certain limits that can be imposed on the ability for a shear band to affect the resistance response of a material, which can aid in defining the specifics of the proposed SBESD system. Based on the Drude and Ziman models of resistance in amorphous alloys, 2 key factors are likely to affect the resistance behaviour, resistance dependence on the material's thermal state, and the resistance dependence on the material's structural state. Defining the limits of the effect on resistance of either of these factors will narrow down the detection limits in where shear band events will be observed to be active.

In the case of the thermal influence, Chap.(3) alluded to several cases whereby thermal resistance ranges from weak to non existent in contrast to the positive strong values of crystalline metals. Shear band behaviour may therefore show no dependence on thermal state of the material, meaning no high end sensitivity limits can be set for the detection limits to which the thermal state could potentially affect resistance. With regards to structural effects, the biggest change in resistivity behaviour is one afforded by the rest glass state changing to a crystalline state through the act of nanocrystallisation. BMGs have resistivity values that are 5-100 times that of the crystalline phase [83]. However when considering the volume of a shear band, these small volumes of material are expected to make a very small difference in the resistance behaviour observed, indicating that the design of the SBESD system must be as sensitive as possible to be able to detect any changes in material resistance due to shear band processes. Based on these considerations, Fig.(7.3) shows an attempt to quantify the potential limits these changes, calculated for a $Zr_{50}Cu_{40}Al_{10}$ BMG alloy, to which a SBESD system can be designed towards.

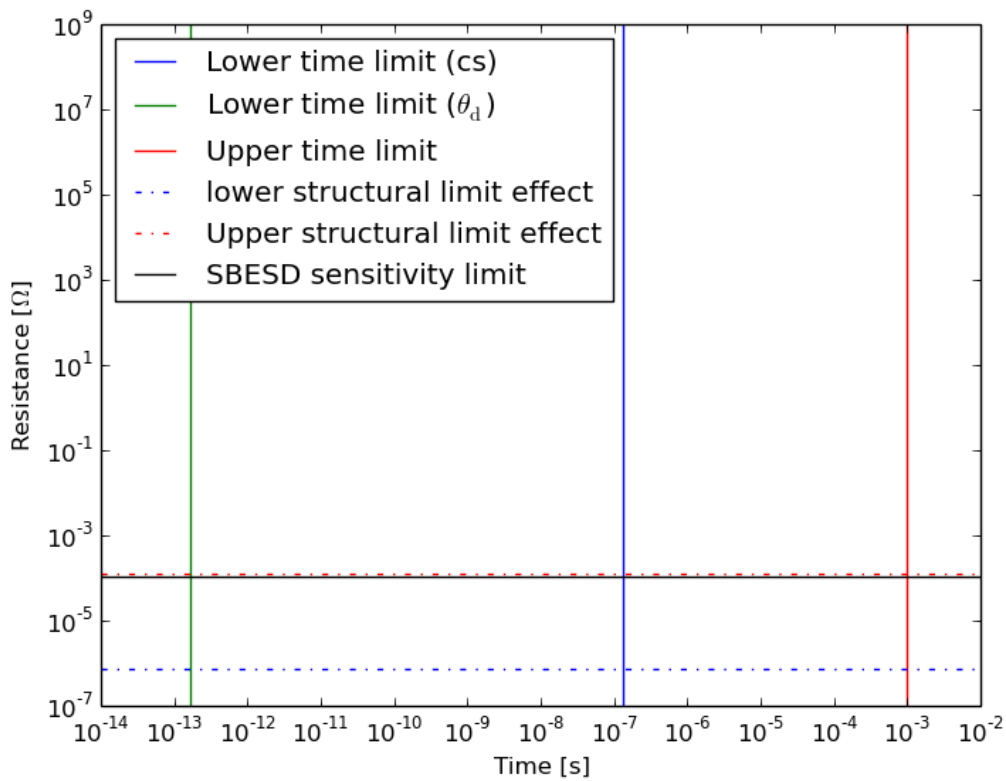


Figure 7.3: Plot showing the theoretical sensitivity limits of the effect shear bands can have on resistivity based on structure (thermal arguments omitted due to uncertainties of α_θ) and the detection capability of the SBESD system in operation.

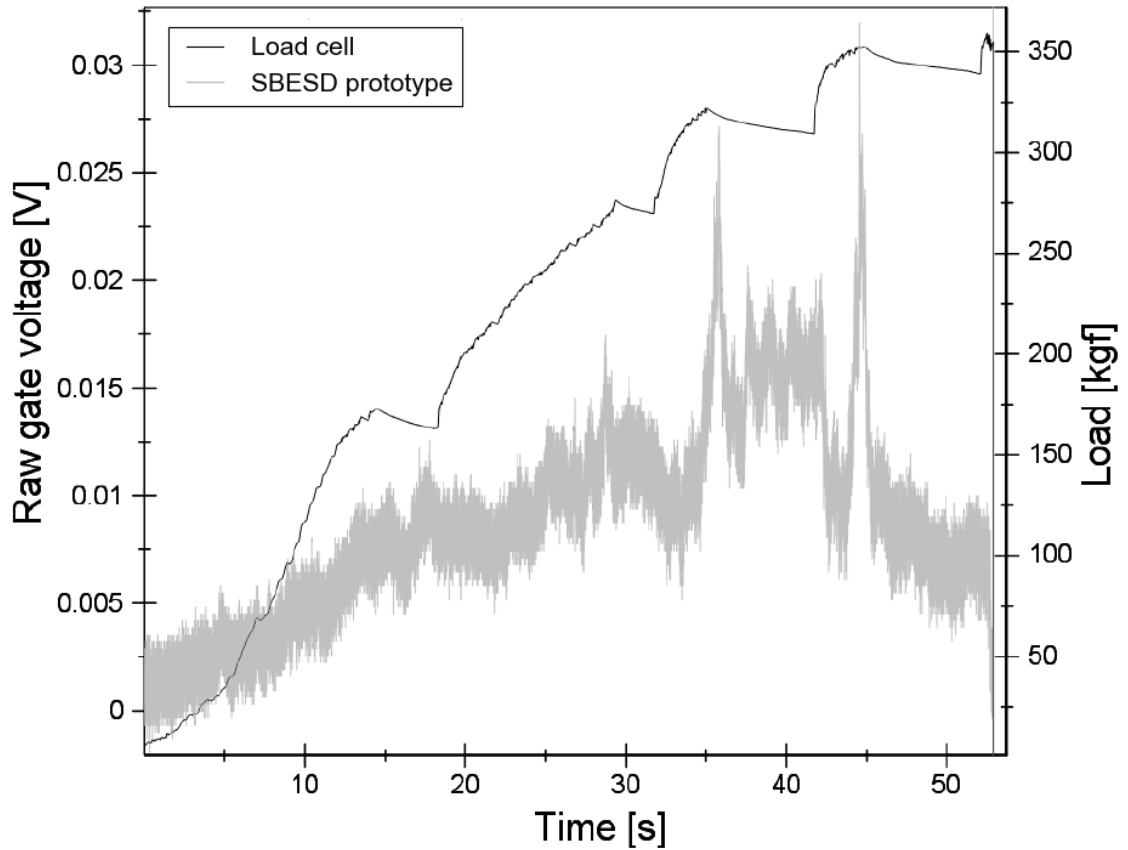


Figure 7.4: Data obtained from the desktop compression prototype demonstrating the concept of the experiment and the areas required form improvement.

7.3 Prototype and development of the SBESD system

Based on the criteria defined in Sec.(7.2), a prototype SBESD system was constructed and tested, with details of the circuit outlined in Fig.(7.2b). The system was initially supplied with a 5V Thurlby Thandar PL330 DC source, and gate voltage measurements were taken at the fastest possible sampling rate though the National Instruments 9223 Data Acquisition System (DAQ) with a LabView programme written for this work (outlined in the appendix).

Initial tests of the were performed through a table top manual compression unit constructed for this work. The compression unit was designed to accommodate a $\varnothing 35\text{mm}$ CCM compression load cell capable of measuring load at 100Hz for loads up to 2500kg; sufficient enough to determine the event of a load drop due to a shear banding event from reported nano-indentation experiments [141]. The compression unit was electrically insulated with black insulation tape.

The first tests for the SBESD prototype were performed on (\varnothing) 2mm \times (height) 4mm cylindrical samples sandwiched between 2 flat copper electrodes, outlined in Fig.(7.8f). The SBESD system was then tuned such that the gate voltage read approximately 0V prior to compression. The samples were then compressed manually with the most constant strain rate possible until catastrophic failure was achieved. Results were recorded and synchronised based on the point of material failure, defined by the most dramatic voltage and load changes.

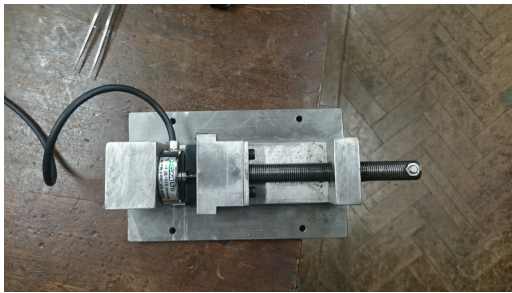
Example results for the prototype SBESD system are shown in Fig.(7.4). The results were poor from the point of view of isolating a single shear band event, due to the poor linearity of the applied strain rate. However the concept of the experiment was shown to be valid, with loading to failure achieved and with electrical resistance changes monitored throughout. The following issues

that needed to be addressed were identified.

Loading regime

The lack of accurate control over the loading parameters with the manual unit made it difficult to identify which load variations were due to poor loading application, and which were due to potential shear band events. Therefore the manual compression unit was replaced with the Zwick Röel Z050 compression system.

In addition, changes were made regarding the compression components. In the manual compression set-up, samples were delicately balanced between the load-cell, a buffer material to protect the load cell and the loading block. The shape of the load cell caused alignment issues during compression, resulting in materials either springing loose from the set-up, or undergoing catastrophic fracture-like failure rather than a controlled failure through shear banding. To solve this issue, an epoxy disk was crafted for the load cell to provide an electrically insulating flat surface upon which a sample could be placed. A SS-316 stainless steel plate of 1cm thickness was placed on top of the epoxy disk such that the sample did not fracture or indent the disk. The combination of these adjustments allowed for the sample to be loaded in a controlled measured manner with good alignment between the sample and the compression plates.



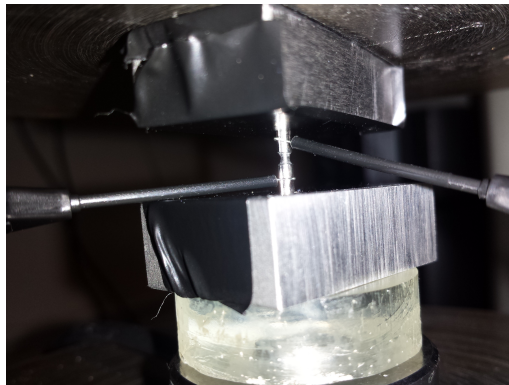
(a) An overview of the manual compression set-up



(b) Custom made epoxy disk for the load cell ($\varnothing 32\text{mm}$)



(c) Epoxy disk installed into the load cell, showing the load cell button being the only element in contact with the load cell



(d) Final SBESD iteration load cell set-up showing a level compression platform for tested samples

Figure 7.5: Improvements made to the load bearing components of the SBESD system.

The introduction of the extra components to aid in the controlled loading of samples could introduce errors. Although the different compliance of rig components should only affect apparent strain (which was not measured), a sudden yield event in any of the load bearing components may be mistaken for a shear band event. Therefore, a validation run of the compression system

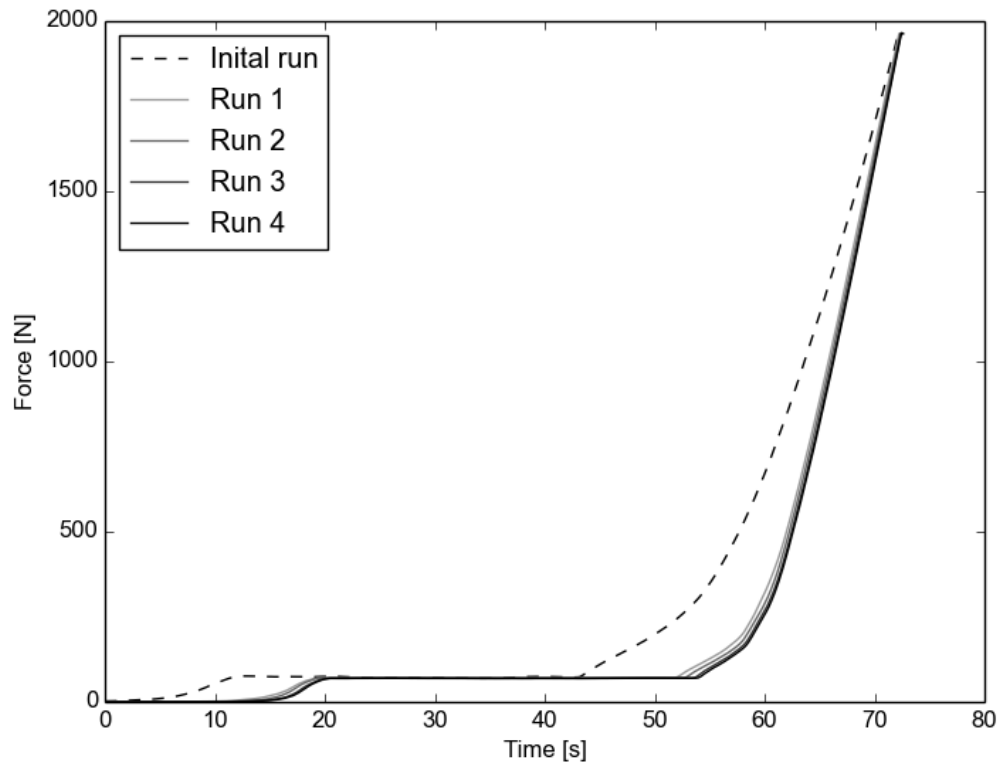


Figure 7.6: Load-displacement data for the Zwick Röel Z050 system for compression experiments with absent samples. Each compression shows the initial low load feature that occurs at low strains, which then becomes overtaken by the typical load-displacement behaviours expected for a fixed strain rate compression test.

without a sample was performed, results of which are shown in Fig.(7.6), showing no sudden changes in the loading profile, indicating there are no features that could be mistaken for a shear band event. This being said, a clear non-linear loading region is observed at the beginning of the test, seen to be common across all non-validation tests. This was found to be associated with the deformation of insulation tape and the establishment of a good mechanical contact at low strains. Attempts at replacing the insulation tape with a less compliant insulating material (Boron-Nitride spray) introduced significant electronic noise in the SBESD data. However, the initial transient in loading feature occurs far below the loads at which shear bands are observed, and could there for be removed from the data during subsequent analysis.

Electrical contact issues

The prototype experiment had copper electrical contacts as a load bearing component in the system due to the limited space afforded by the samples tested. However there was significant plastic strain of the copper electrode, and the altered contact mechanics between the sample and the electrodes affected the SBESD data, resulting in large variations in gate voltage that could mask any relevant signals in the data.

Electrical contacts were replaced with micro-probes outlined in Chap.(4). Whilst the mechanical contact to the electronics through the flexible wiring may still influence the detection signal (as is observed to be the case in many of the optimised experiments) the effect is observed as a messy signal with no preferred signal shape or magnitude, lasting longer than that any event expected

from a shear band. The distinctiveness of such a signal therefore allowed for data demonstrating these features to not be considered as a potential shear band candidate.

Sample geometry

A sample geometry of 2mm diameter 4mm length was initially selected due to the optimised 2:1 aspect ratio defined in ASTM standards for sample compression [249]. However this set-up made compression of the sample with electrical contacts defined above impossible due to spatial constraints. Therefore longer samples of 7 mm to 8 mm were used. Whilst these samples could accommodate the electrical contacts, spatial constraints further prevented samples from being fitted with a strain gauge for strain measurements to be extracted. Therefore any strain information required had to be approximated from the displacement of the Zwick Röel Z050 cross-head, with accurate measurements of strain being left as a future improvement for the SBESD system.

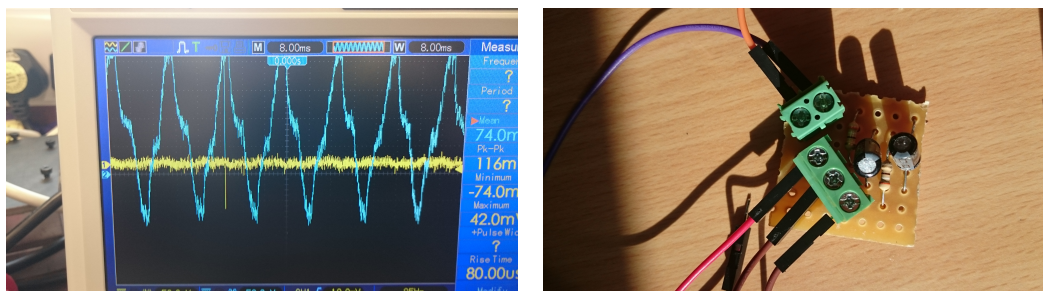
Tested cylindrical samples showed no preference regarding the position for the formation of shear bands, often resulting in potential shear bands forming outside the region encapsulated by the electrodes. As such, necks were machined into the samples in order to concentrate the stress and localise any shear banding to within the electronically encapsulated region. Machining was carried out by placing samples into a rotary drill and wearing material away with a titanium cutting blade irrigated with 6 μ m diamond suspension polishing fluid until the necks were approximately \varnothing 1mm. The necks were then finished with grit paper irrigated with 6 μ m diamond suspension to a 9 μ m finish under a rotary drill, to reduce the presence of scratches that may act as surface cracks for initiation of fracture, or cause premature catastrophic shear band based failure.

SBESD signal quality

The raw SBESD signal from the Wheatstone bridge outlined in Fig.(7.2b) has a limited sensitivity to resistance changes. The DAQ system used to measure the gate voltage has a measurement accuracy of 2mV, therefore according to Eq.(7.4), a significant detectable signal ($\geq 3\sigma$) requires, resistance changes of at least 333m Ω (calculated with $V_s = 18V$; the maximum possible supply voltage). To achieve this in the bulk would require a change in resistivity of the shear band material of over 262 times. This is greater than expected during the shear band process, and so steps were taken to improve the SBESD sensitivity. One method to do this was through the addition of an amplification circuit to the gate voltage terminals, outlined in Fig.(7.8d). Introduction of this stage led to the discovery of significant electronic noise within the SBESD output, particularly in high frequency noise within the data that could disguise any potential SBESD events. Therefore steps were taken to reduce the level of noise in the data.

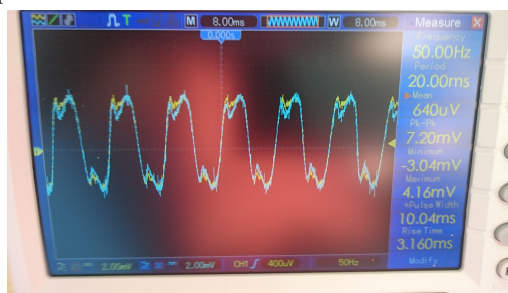
The first step considered was to reduce the noise produced by the DC source, which upon testing with an oscilloscope in Fig.(7.7a) showed significant variation in the DC voltage over a range of 400mV. A passive low pass filter as shown in Fig.(7.7b) was employed at the DC source output to screen any high frequency noise being passed into the bridge. However, whilst the noise was reduced to 8mV in range, this was still beyond the sensitivity of the DAQ system and still occurred at frequencies that could mask potential SBESD signals. As such, the DC unit was replaced with batteries. Whilst over time these cells will degrade from their initial voltage, high frequency noise was eliminated leaving only low frequency noise, which is not thought to mask potential SBESD events.

Another noise reduction step involved electronic shielding of the SBESD system. All SBESD electronics were placed in an earthed aluminium box with access holes drilled in. This resulted in a reduction of high frequency noise and an increase in the baseline stability of the data.



(a) The unfiltered DC source passed through the SBESD system showing the amplified (blue) and unamplified (yellow) response.

(b) The low pass filter designed to remove the high frequency noise from the DC source.



(c) The filtered DC source passed through the SBESD system showing the amplified (blue) and unamplified (yellow) response.

Figure 7.7: Images showing the attempts made to improve the DC source.

The final noise reduction step involved the general performance of the experiment. Supply voltages were kept as high as possible (18V) to achieve maximum sensitivity of the bridge circuit without component burnouts. In addition steps were taken to ensure wiring was kept as isolated as possible and all SBESD components were isolated from components that directly carried mains current. This step was found to be essential to provide reasonable SBESD data from which shear band analysis could be performed.

Sampling rate

The maximum possible sampling rate is fixed at 1MHz due to the capability of the DAQ system. However, the addition of the amplification stage led to a delay time in the circuit response due to the rise and fall times of the operational amplifier. The use of an improved LM6171BIN operational amplifier with a slew rate of 100MHz was required such that the DAQ was the only limiting factor in the sampling rate.

High volume data analysis

Due to high data sampling rates, substantial volumes of data were accumulated for single tests, making data analysis impossible in some cases. Therefore restrictions on the experimental parameters were needed to be able to store, access and analyse the data post test. A minimum strain rate during compression was set at 0.5 mm/min to limit the amount of data recorded whilst maintaining deformation parameters for multiple shear band formations. The National Instruments DIAdem software was utilised to synchronise the load cell data with the voltage data, and split the data obtained into sections which may contain a shear band event.

Final SBESD system

From the issues identified in the above sections, several iterations of the SBESD system were generated to produce an optimised SBESD system. The final result is shown in Fig.(7.8).

7.3.1 Sensitivity analysis and noise reduction of the SBESD system

The final SBESD system outlined in Fig.(7.8) represents the optimal SBESD system given the resources available. Whilst this final system is a marked improvement on the initial version, there still limitations for shear band detection. These limitations, and the methods used to deal with them are outlined as follows:

Signal sampling rates

It has already been mentioned that the sampling rate of this experiment is defined by the maximum sampling rate of the DAQ system, (1MHz). However this value is not the same as the time interval over which shear bands can be potentially measured. Standard signal processing practice states that any analysis of a measurement from raw data requires approximately 10 data points to confirm that the measurement is real and not due to random error [142]. Based on this, the rate at which the effect shear banding influences resistance behaviour can be sampled is reduced to 100kHz. Due to the mismatch between the nanosecond time intervals of shear band processes and the 10 μ s intervals defined above, flexibility must be found in this condition to improve the potential of probing shear band behaviour. To that end, all signals are treated with a moving average in addition to observations being made on the raw data.

When a signal is sampled appropriately, a moving average treatment has been observed to significantly reduce high frequency electronic noise in the data. However the method relies on the fact that the sampling rate is high enough such that the data surrounding the point of interest shows differences only due to random noise. When the signal life time approaches that of the sampling time, then the analysis can suppress the magnitude of the signal and skew signals that are asymmetrical in the raw data. This is demonstrated in Fig.(7.9).

Sensitivity limits of the SBESD measurements

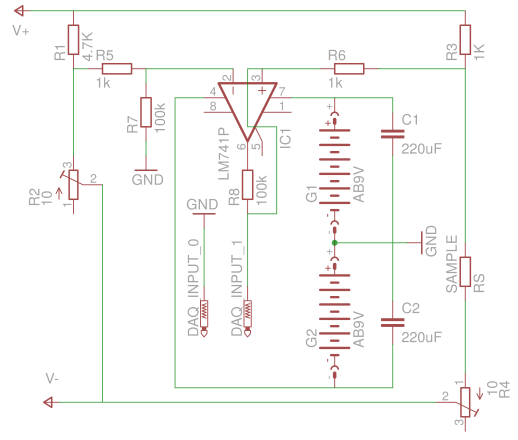
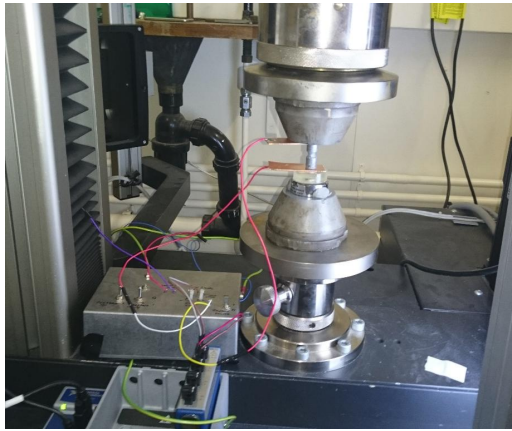
The theoretical limits to changes in resistance due to the shear banding phenomena have been covered in Sec.(7.2). While efforts have been made to match the practical limits of the SBESD system to these, electronic noise in SBESD data naturally prevents this from being fully realised.

In consideration of the upper limits to detectable change, the maximum change in resistance is defined by the un-amplified bridge set-up. During testing the unamplified gate voltage is ≈ 0 V and the maximum change in resistance detectable is defined as:

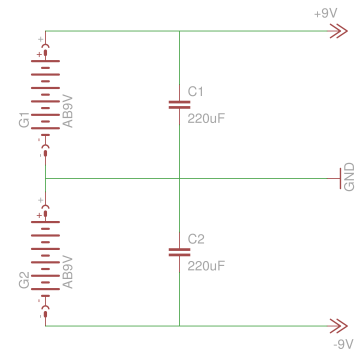
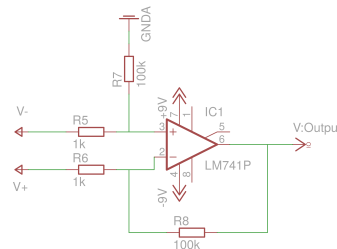
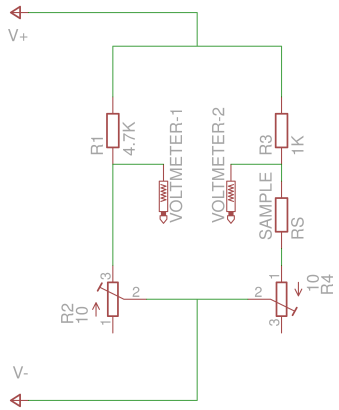
$$R_{SB} = \frac{\pm V_s R_3}{1 - \frac{\pm V_s}{V_s}} = \frac{R_3}{0} = \infty \text{ or } \frac{-R_3}{2}. \quad (7.5)$$

The negative upper limit to resistance change is an unphysical result and it is seen that there is no upper limit to the measurable resistance change, providing the change in gate voltage can be measured accurately enough. R_{SB} values approaching ∞ would effectively require complete fracture in the material.

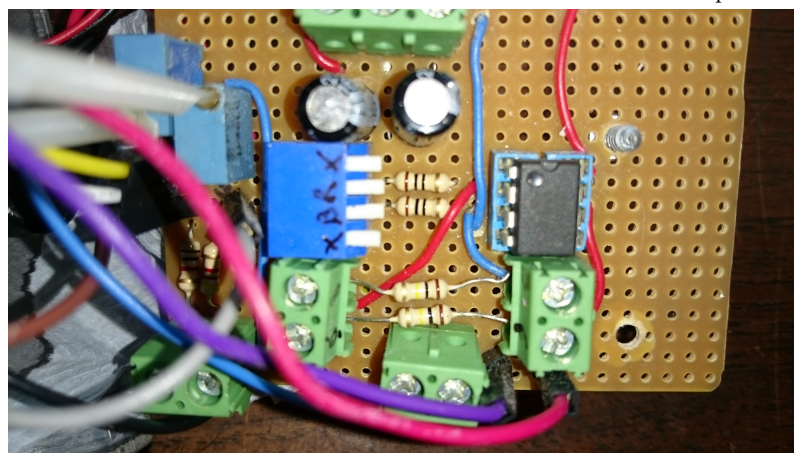
In consideration of the lower limits to detectable change, the minimum change in resistance is defined by the amplified bridge set-up. These limits vary depending on the test. Taking a strong set of SBESD data from Sec.(7.4), where potential shear band resistance signals were observed, an



(a) The final iteration of the SBESD system (featuring the entropy proof-of-concept experiment discussed in Sec.(7.5.2)). (b) Circuit diagram showing the entirety of the detection electronics.

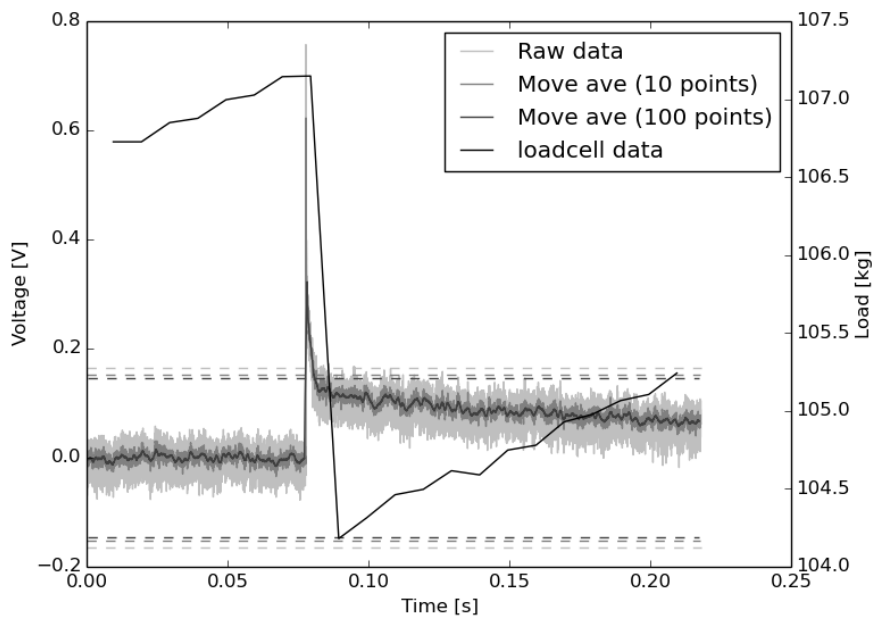


(c) The Wheatstone bridge module. (d) The amplification module. (e) The stable current module for the amplification module.

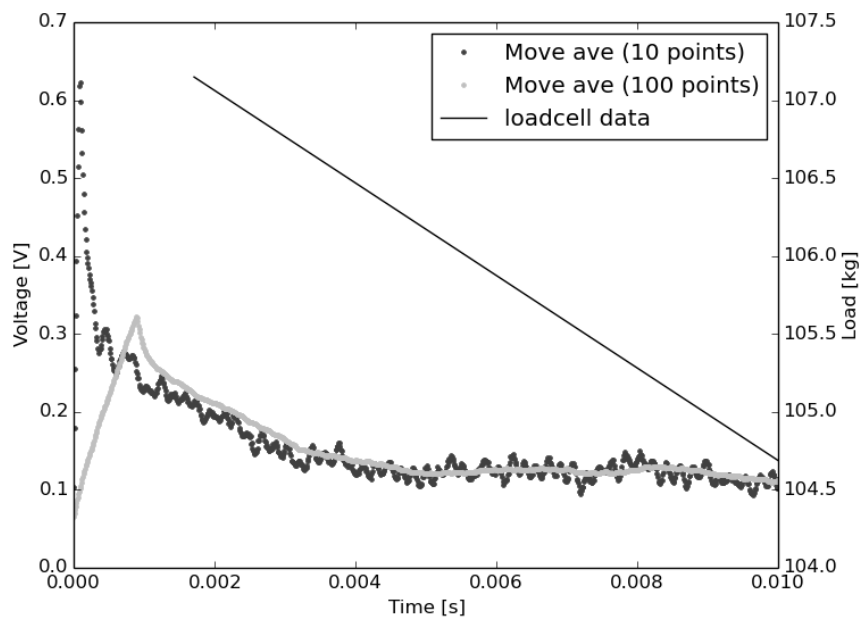


(f) Circuitry for the final iteration of the SBESD system.

Figure 7.8: Schematic overview of the detection electronics. Resistor values are outlined in the schematics, but may change depending on the circuits use.



(a) A SBESD signal detected in $Zr_{50}Cu_{40}Al_{10}$ alloy treated with different moving averages. The solid lines indicated the voltage data whilst the dashed lines indicate the 3σ signal limit.



(b) Zooming in on the data above the 3σ limit outlined above, this shows the price paid for using the moving average method for ever increasing data intervals, with signals becoming skewed and reduced in magnitude the more aggressive the treatment being used.

Figure 7.9: The affects of using a moving average treatment on a strong SBESD event.

estimate to this limit can be derived. For this test, the amplification of the gate voltage was set to 1000 and the bridge supply was set to 18V, meaning the detection resolution (in the absence of electronic noise) is set by the DAQ system to be $2\mu\text{V}$ ($= 1000 \times 2\mu\text{V}$). Through Eq.(7.4), this corresponds to a resistance change of $\approx 100\mu\Omega$. This value is of the order of the resistance values observed in BMGs in the rest state, indicating that the SBESD system developed is capable of detecting minor changes in the resistance of BMGs.

This limit description is an absolute limit for a particular configuration of the SBESD system. However in reality, the presence of electromagnetic noise increases this limit significantly. For high frequency noise in the case described above, voltage variations 0.1 V (in the amplified voltage) are observed, despite noise reduction precautions. In its unprocessed form, this variation is considered high and only permits detection of significant SBESD events. Recalling the signal processing treatments outlined earlier, this noise limitation is diminished if a moving average treatment is used at the sacrifice of time resolution. As such the level of moving average treatment that can be applied to a potential signal is dependent on the duration of the signal that has been observed in the raw data.

Treatment of low frequency noise can also be performed; however the time scales of the effect are so large that low frequency noise can be considered to be absent for shear band analysis. However, low frequency noise plays a significant role in the overall performance of the SBESD system. The magnitude of low frequency noise is far greater than that for the high frequency noise, with values of $\approx 1\text{V}$ being observed for the data above. It is for this reason that the maximum amplification is $1000\times$; greater than this value will result in the gate voltage measurements drifting between $\pm 9\text{V}$, the limit over which the amplification circuit can operate. This imposes a new upper limit range of resistance changes that can be detected. Using the example defined above once again for the case of $1000\times$ amplification SBESD system with a bridge supply voltage of 18V:

$$R_{SB} = \frac{\frac{\pm 9/1000}{V_s} R_3}{1 - \frac{\pm 9/1000}{V_s}} \approx \pm 0.5\Omega \quad (7.6)$$

In summary, the SBESD system in its most sensitive form is capable of detecting changes in resistance of up to 0.5Ω down to $\leq 100\mu\Omega$ over time-scales of minutes to microseconds. Fig.(7.3) shows a detection window defined by these limits. These improvements to these limits would require further specialised electronically-isolated environments with an improved DAQ sampling rate. However this detection set-up has been shown to be good enough for the evaluation of the shear effect of shear banding behaviour in BMGs as outlined in the following sections.

| Composition | V_s [V] | Amplification | R_3 [Ω] | Resistivity [Ω cm] |
|--|-----------|---------------|--------------------|----------------------------|
| Zr ₄₄ Cu ₄₄ Al ₆ Ag ₆ | 18 | 1000 | 1000 | 1.74×10^{-6} |
| Zr ₅₀ Cu ₄₀ Al ₁₀ | 9,18 | 1000 | 1000 | 1.73×10^{-6} |
| Cu _{57.5} Hf _{27.5} Ti ₁₅ | 9,18 | 1000 | 1000 | 1.82×10^{-6} |
| Ti ₄₀ Zr ₁₀ Pd ₁₄ Cu ₃₄ | 9,18 | 1000 | 1000 | 1.89×10^{-6} |
| Zr ₆₅ Cu ₁₅ Al ₁₀ Ni ₁₀ | 9 | 1000 | 1000 | 1.66×10^{-6} |
| Zr ₅₇ Cu ₂₀ Al ₁₀ Ni ₈ Ti ₅ | 9 | 1000 | 1000 | 1.72×10^{-6} |
| Ti ₃₃ Zr ₉ Ni ₂ Cu ₄₇ | 9 | 1000 | 1000 | 1.86×10^{-6} |
| Ti _{33.85} Zr _{11.4} Ni _{8.4} Cu _{46.34} | 9 | 1000 | 1000 | 1.81×10^{-6} |
| Cu ₅₀ Hf ₄₃ Al ₇ | 9 | 1000 | 1000 | 1.83×10^{-6} |

Table 7.1: Overview of all the test conditions leading to the positive detection of SBESD events.

7.4 SBESD results and critical analysis

Compression SBESD experiments were performed on a range of different metallic glasses in different test configurations. A small selection of tests showed a sudden change in resistance behaviour during compression which coincided with a sudden decrease in the applied load from the compression unit. These events, termed SBESD events, match the characteristics expected of shear band events. Tab.(7.1) depicts the test conditions for which these signals were detected.

Due to the sensitive nature of the experiment and uncertainty surrounding how resistance behaviour couples to shear band behaviour, it is recognised that a proportion of the detected SBESD events may not be due to the intrinsic processes associated with shear banding. Without information available to certainly identify which signals could be due to shear banding, all the observed events are treated under the assumption they are caused by shear band processes. Conclusions drawn from such an inference are then used to identify which signals (if any) are compatible with shear banding, and what the signals say about the shear banding phenomena with regards to a resistivity response.

7.4.1 Positive detection events

SBESD events followed 2 distinct behaviours based on their duration and strength. These are defined as weak (W) signals and strong (S) signals.

Weak (W) signals

Weak signals are categorised as significant drops in the load data that correspond to sudden observable changes in resistance with a signal to noise ratio that is no stronger than $\geq 3\sigma$. Examples of these observed signals are outlined in Fig.(7.10).

W signals usually present as a small but definite and permanent change in the gate voltage, which infers a small but definite permanent change in the electrical resistance of the system. Step changes both for increasing and reducing resistance are observed with magnitudes ranging from barely detectable to just below the 3σ signal to noise ratio limit.

Despite the lack of signal strength of W signals, the signals are relatively well sampled. Therefore a moving average treatment can be applied to these signals to remove much of the random high frequency electronic noise; a useful step considering the signal weakness. Fig.(7.10a) and Fig.(7.10b) shows the effect such a treatment. The moving average treatment with 10 data points improves the observed signal by cutting the random error by approximately a third. Further im-

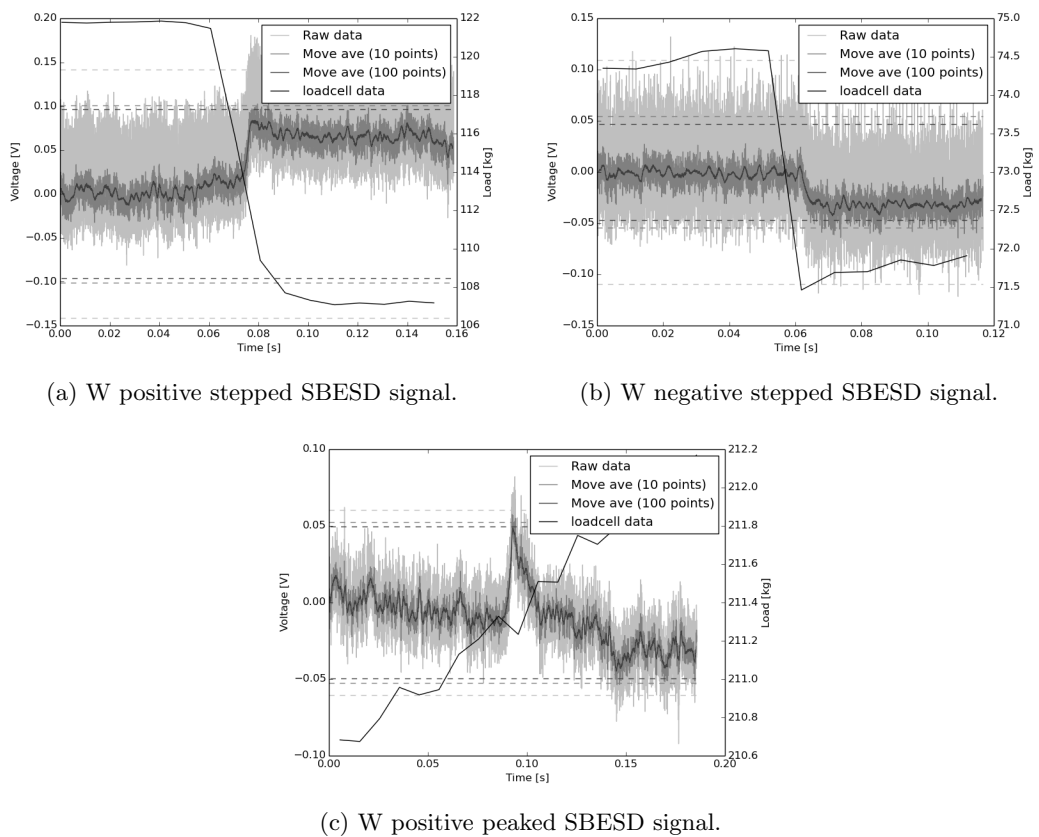


Figure 7.10: An array of W type SBESD signals demonstrating a range of detected resistance behaviours during shear banding.

improvements are observed when considering moving averages involving 100 data points. However use of more points than this for the W signals then introduces systematic error into the results, as the data interval considered for 100 points is 0.1 ms, approximately a 10th of the order of the duration of the signal itself, and so are not representative of the measurement in question.

Despite the moving average treatments, W stepped signals show little evidence of the expected dynamic behaviour outlined in Fig.(7.1), with SBESD data indicating that the material only moves from resistive state to another (i.e. the shear band propagation stage in Fig.(7.1) is not detected). This does not mean that SBESD signal transience is not present during the shear banding process, only that the feature is not detectable through the experimental set-up outlined here. Therefore, further work in improving the SBESD system's sensitivity and sampling rate may reveal transience in the signals and shift some of what would have otherwise been classified W stepped signals to S signals (described later).

W signal frequency varies from test to test, with some tests only demonstrating a single signal, whilst other tests demonstrate multiple signals. Fig.(7.11) shows results for a SBESD compression test in the alloy Cu₅₀Hf₄₃Al₇, where 4 W SBESD signals are observed. Each signal is observed with relative clarity allowing an effective moving average treatment to be performed on each signal. It is encouraging to note that all 4 signals show the same general change in resistance behaviour, indicating a small permanent increase in the systems resistive state with each step. In addition, the magnitude of each of the signals is also similar, indicating that the factor responsible for these signals comes from a common source. Furthermore, it is noted that the magnitude and duration of the load drops that coincide with these signals are also similar, indicating that the process causing the drop in load is also the source of the SBESD events. These load drops also all tend to initiate around the same loading value, indicative of shear band behaviour, as BMGs tend to re-activate previously active shear bands to accommodate deformation due to their already weakened structure compared to the surrounding glassy matrix [109]. All of these factors add up to make relatively convincing evidence that W signals (especially in the case of multiply observed similar W signals) are caused by a shear banding process, the nature of which is discussed further in Sec.(7.5), and may reveal further information through testing with a SBESD system with greater sensitivity and sampling rates.

In addition to the 'stepped' signals, it is worth mentioning the observation of 'peaked' W signals, as demonstrated in Fig.(7.10c). The morphology of these signals indicates a transient change in the resistance state of the system. As shear bands are also transient, this signal initially looked promising, but the introduction of electronic shielding, better circuit layout and the use of the amplification module saw observations of such signals diminish significantly. This indicates that these signals are due to experimental noise, and are therefore not considered in any further analysis.

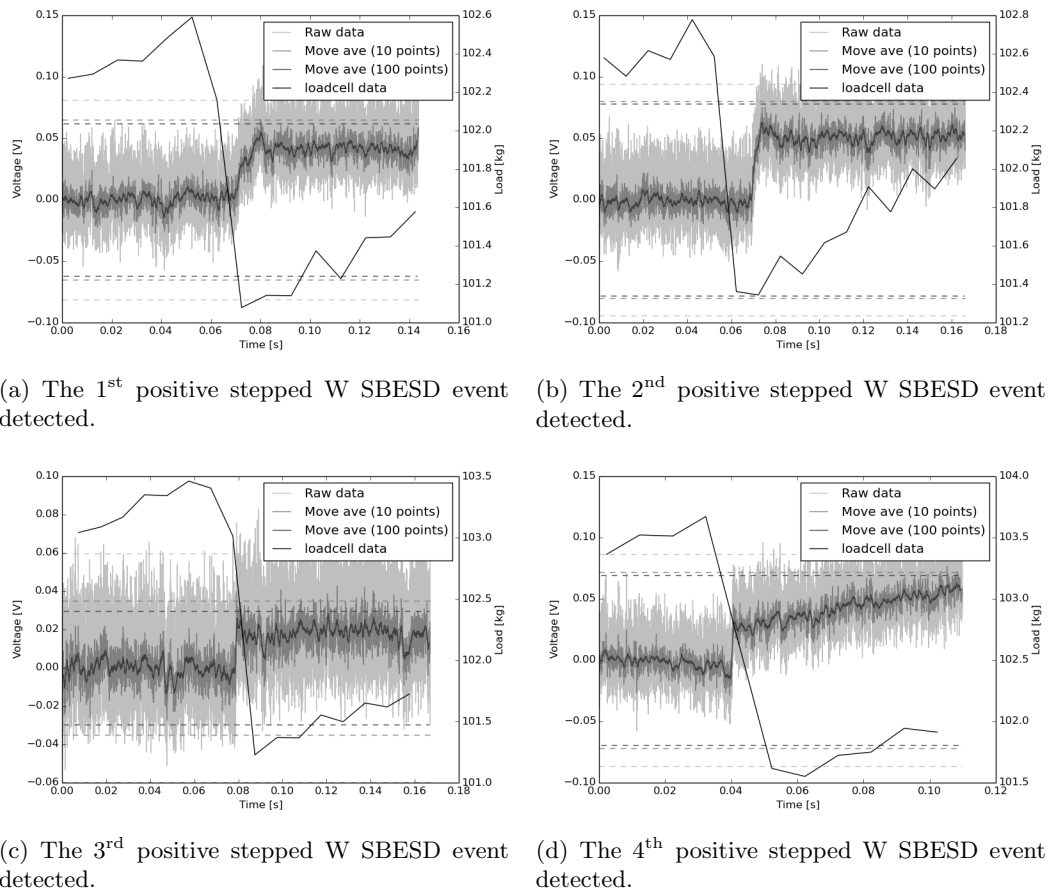


Figure 7.11: Multiple positively stepped W SBESD signals observed in an in-situ SBESD compression test with the final iteration of the SBESD system.

Strong (S) signals

S SBESD events are defined as well sampled events that show significant drops in load that coincide with significant changes in the gate voltage with signal to noise ratios $\geq 3\sigma$. These signals cannot be explained by electronic noise, so are likely to be due to shear banding events or significant experimental artefacts. Fig.(7.12) show the 2 strongest examples of S SBESD signals, detected in $Zr_{50}Cu_{40}Al_{10}$ and $Zr_{44}Cu_{44}Al_6Ag_6$ alloys.

Observations of S SBESD events are rare, with tests in $Zr_{50}Cu_{40}Al_{10}$ alloy being the only tests to show any level of reproducibility of these signals. Individual occurrences of these signals have been observed in other materials, such as the $Zr_{44}Cu_{44}Al_6Ag_6$ alloy. If these signals are due to shear banding, strong evidence is required from analysis of the signals in support of their origin, which this case comes from the enhanced level of detail afforded by the signal magnitude.

The initial stages of S signals are similar W signals; typically being initiated within no more than 2 or 3 data points, indicating the peak resistance change requires $\lesssim 3\mu s$ to be achieved. Poor sampling of the initialisation of both S and W signals means that probing shear band initiation is beyond the reach of the SBESD system in its current form. Despite this, the sampling rate is good enough to depict other enlightening features of the S signal. After the initial rise of the signal, a steady gate voltage is observed sampled with ≥ 10 data points. This is then followed by a 2 stage decay process. The first is a rapid decay in the resistance change, recovering much of the original resistance. The duration of this decay appears to be approximately 1ms, the approximate time observed for a drop in load in the case of signals observed in the $Zr_{50}Cu_{40}Al_{10}$ alloy. The second decay is gentler, lasting around 100 ms to 200 ms depending on the magnitude of the signal, and in the case of a clean S SBESD signal, continues beyond any observations of further reductions of load. Based on these observations, a convincing argument can be built for the case that these signals are a direct result from the shear banding and not a consequence of experimental artefacts affecting the results.

The first observation in favour of S signals being caused by shear banding is that all the observed signals indicate a sudden, transient increase in resistance. In the case of W signals, no significant transience was detected, and both increases and decreases in resistance were observed, causing doubt in validity of the source of some of the SBESD signals. The observation of a uniform behaviour across all the observed S SBESD signals reduces the concern of random experimental error being the source of these signals. Whilst it could be argued that the low number of observations of these signals means that the absence of signals with negative resistance change cannot be concluded, the number of observations of positive S SBESD signals means the conclusion holds for the work presented here, though further tests are recommended to confirm this.

The second observation in favour of S signals being caused by shear band processes is based on the decay features observed within the signals, and how they correlate to the loading response of the tested material. The initial rise and first decay feature of the S signals for tests in $Zr_{50}Cu_{40}Al_{10}$ alloy all occur within the duration over which a load drop is observed. Assuming that the load drop is due to the formation of a shear band within the material, then it follows that the initial rise and first decay is a direct consequence of the active processes of a shear band. This was not observed in W signals due to the noise considerations, but by definition, S signals are signals that surpass the background electronic noise of the experiment, thus this transient argument stands for S signals.

The secondary decay feature further strengthens this second observation in favour of being caused shear banding processes. It is known that shear bands produce significant increases in temperature during formation. This thermal energy must dissipate throughout the material, resulting

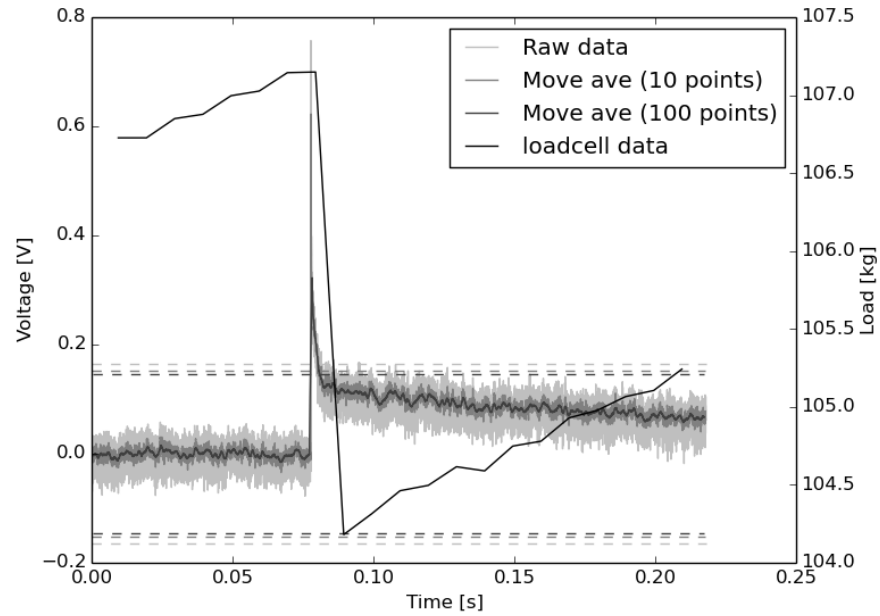
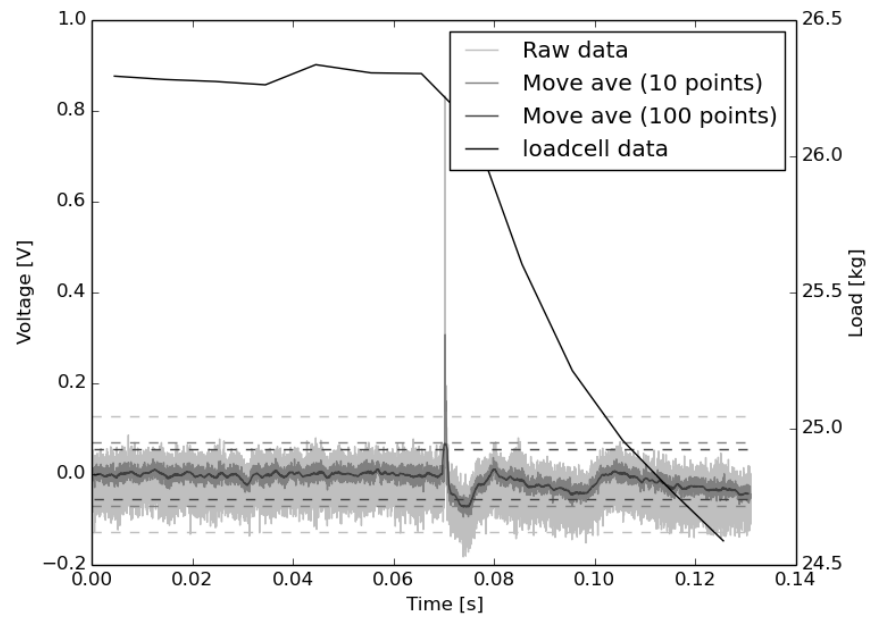
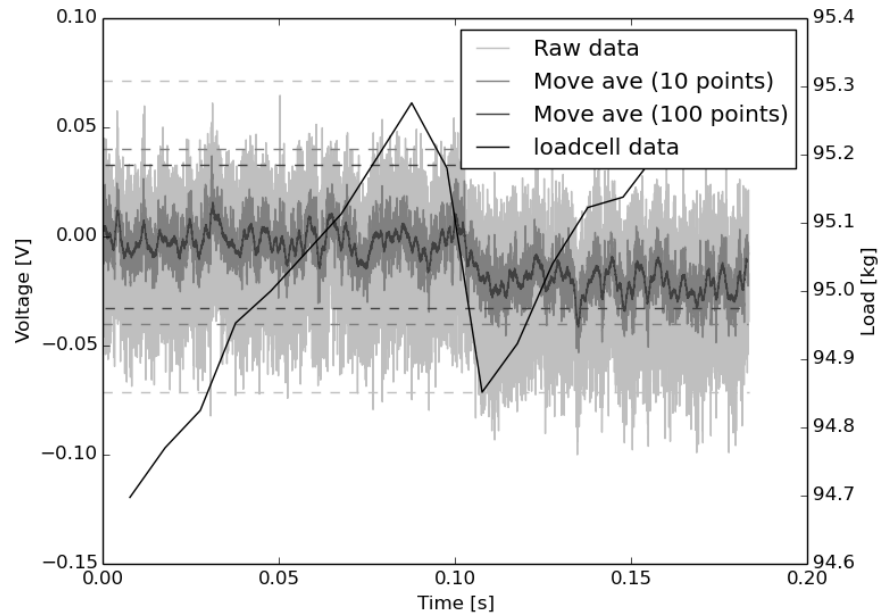
(a) S SBESD signal detected in $Zr_{50}Cu_{40}Al_{10}$.(b) S SBESD signal detected in $Zr_{44}Cu_{44}Al_6Ag_6$.

Figure 7.12: Examples of rarely detected S SBESD signals.

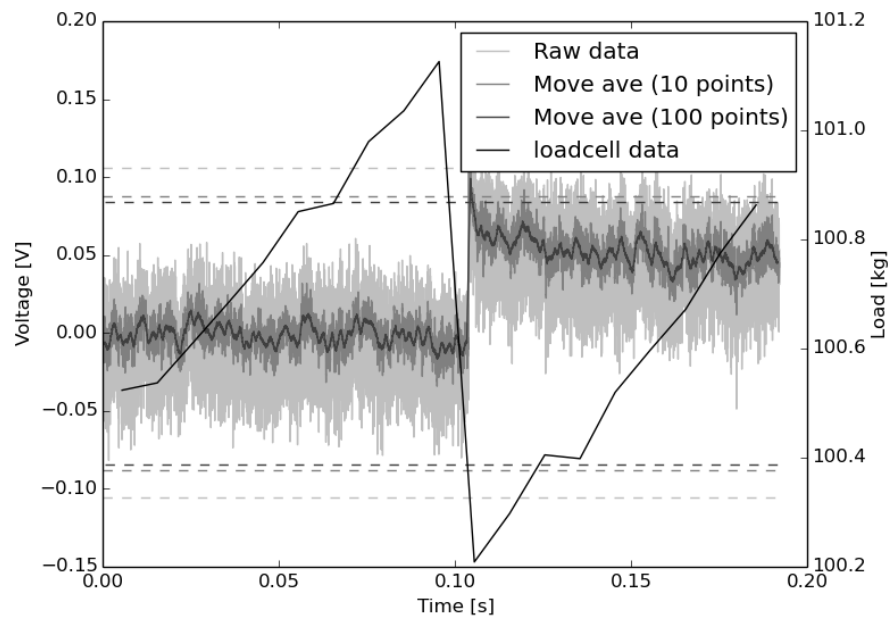
in a decay in the temperature of the material in the vicinity of the shear band with respect to time. Thus the explanation could be given that the initial rise and decay in the signal is due to the active shear band process, whilst the secondary decay feature is due to the dissipation of thermal energy generated by the shear band.

Another observation in favour of S signals being caused by shear band processes comes from the ability to explain differences across similar S signals in the light of current understanding of shear bands in metallic glasses. Fig.(7.12a) shows an S result for a SBESD compression test in $Zr_{50}Cu_{40}Al_{10}$, which has been used as model data for the observations given thus far. The test responsible for producing this signal also produced a further 2 signals prior to this, shown in Fig.(7.13). The first signal is extremely weak, and therefore categorised as an W SBESD signal. The form of the signal depends on the treatment of the data, with the raw data indicating a weak stepped signal morphology, but a 10 point average shows hints of transient peak behaviour within the signal. The drop in load required for this signal is approximately 2N, in comparison to the 30N drop in load observed in the signal in Fig.(7.12a). The second signal (stronger than the first signal, but weaker than the third) observed in during the aforementioned test only just qualifies as an S signal. In addition, the signal corresponds to a drop in load of ≈ 10 N, a value that sits between the load drops of the first and final signals. This signal also shows the same rise and decay features as described in Fig.(7.12a), with the notable reductions in durations of each these features. The comparison of these 3 signals leads to the conclusion that features within these signals are dependent on the stress dissipated during the events. Larger drops in load for a fixed strain rate compression experiment indicate an increased level of work done during a shear band event. Therefore the amplitude of SBESD signals with large load drops are likely to be greater than the amplitude of the SBESD events with lower load drops, as observed. In addition the thermal energy generation for SBESD events associated with a larger load drop is likely to be greater than that with lower load drops. This is also reflected in the secondary decay feature of the intermediate and larger observed SBESD signals. These observations once again provide further evidence that S SBESD signals are not only due to shear banding, but provide valid descriptions regarding the shear banding processes at work.

The final observation in support of these signals being due to shear bands comes from the ability to use previous observations to explain non-typical S SBESD events. For example, the signal associated with the $Zr_{44}Cu_{44}Al_6Ag_6$ alloy appears to be more complex than the signals detected in $Zr_{50}Cu_{40}Al_{10}$, with multiple secondary decay features being present after the signals initial transient feature and an extended complex reduction in load compared to other signals. To understand this complex event from the inferences made thus far, attention is initially drawn to the load response of the signal, indicating that the active shear banding period for accommodating deformation is far greater for the $Zr_{44}Cu_{44}Al_6Ag_6$ alloy in comparison to signals observed in the $Zr_{50}Cu_{40}Al_{10}$ alloy. Therefore, the S SBESD response of the $Zr_{44}Cu_{44}Al_6Ag_6$ can be justified in terms of a compound SBESD event, constructed from a single S event and two subsequent S signal secondary decays in quick succession. This supports the observation of the load values at the onset of the event in the material, which from simple approximations to shear band dimensions (see Sec.(7.5) for details) show stress values of $\approx 2.7\times$ less than that observed for S SBESD events in the $Zr_{50}Cu_{40}Al_{10}$ alloy. Whilst variations in yield strength in chemically similar BMGs are expected, a difference in yield of this magnitude is difficult to justify in this way, especially when there are no potential micro-structural processes that could be behind it. This indicates another factor affecting the yield, such as an unknown stress concentrator or an inclusion, like that suggested by Madge et al. [169]. Such a factor would explain the atypical yield behaviour and therefore subsequent SBESD observations.



(a) A weak W SBESD event showing a minor reduction in the resistivity state of the material. This was the first signal to be detected for a test of the $Zr_{50}Cu_{40}Al_{10}$ alloy which was later populated with S SBESD events.



(b) The first weak S SBESD event observed to occur in $Zr_{50}Cu_{40}Al_{10}$ prior to the formation of a much stronger S SBESD event.

Figure 7.13: Further SBESD events observed in the $Zr_{50}Cu_{40}Al_{10}$ alloy, which precede the dominant S SBESD event highlighted in Fig.(7.12a).

To end this discussion regarding the validity of the S signal source, comparisons between S and W are made. Whilst the SBESD data appears to show very different behaviours for the 2 cases, it is noteworthy that the load drops, both in terms of magnitude and duration are similar across both cases. This is an encouraging observation, as the load drops signify the mechanical behaviour of shear bands, which appear to be common across all materials that demonstrate a SBESD signal response. As such, the presence of the 2 distinguished signal types indicate another possible indirect factor that affects resistivity behaviour during shear banding. Hypothetically, one such factor could be the effect of nano-crystallization during shear banding; commonly observed in the literature [148, 150]. If this were to occur, the following would be observed:

- The formation of a nano-crystalline phase as a consequence of a shear band event would introduce a work hardening component into the load response, as crystalline material cannot undergo shear banding so further shear banding would occur at higher applied loads. The magnitude of load drops as well as the initial values from which they drop are likely to increase with respect to the number of shear bands formed within the material.
- The formation of crystalline phase within the material will influence the temperature-resistivity relationship within the vicinity of shear bands. There will be an increased magnitude of resistance change during the shear band event, and a strong thermal decay feature after the active period of the shear band.

Both of these factors are observed in the S SBESD results; indicating the potential for nano-crystallisation causing the observation of S SBESD events. The implications of such an affect are discussed further in Sec.(7.5).

7.5 Signal analysis and enthalpy/entropy implications

So far, relative changes in resistance of BMGs have been measured using the SBESD system, which shows that resistance of a BMG can undergo both transient and permanent changes due to shear banding. Based on these findings, the actual change in resistance of shear banded material has been extrapolated to link to factors and processes in the material using simple but reasonable assumptions about the properties of a shear band (outlined schematically later in Fig.(7.18)):

- Shear bands form an approximately elliptical plane at 45° to the direction of applied stress with a semi-minor axis defined by the radius of the neck of the sample.
- The thickness of the shear band is 10nm and it is assumed that the shear band is fully adiabatic for the work presented here.

Using only a change in resistance to describe the intimate details surrounding the mechanics of shear banding is difficult. These factors are dependent on a number of variables, and a number of factors contribute to the resistance behaviour of a BMG material. As such, extracting information from SBESD event data requires the simplification of the factors affecting shear band behaviour into terms that can be extracted. To that end, it is noted that many of the factors that influence both electrical resistance and shear band behaviour are dependent on 2 parameters; a BMG's structural state and internal energy. The reduction of variables to these 2 key terms allows SBESD events to be interpreted with respect to each, from which useful information regarding shear band mechanics can be extracted. It should be noted that some parameters cannot be easily described through these 2 key variables; sample geometry changes being one of them. However for the purposes of this work, it is assumed that these factors either remain effectively constant, or have a negligible

contribution to the change in BMG resistance during shear banding event. As such, interpretation of the SBESD signals has been performed in terms of internal energy changes (Enthalpic changes) and structural changes (Entropic changes).

It is important to note that analysis of the SBESD events from separate enthalpic and entropic points of view does not mean that the 2 terms are independent of each other. For example Dubach et al. have shown the structural state of a BMG is dependant on the thermal processing history [97]. Therefore thermal energy generated during a shear band event is likely to affect the structure within the vicinity of a shear band, which in turn will affect the resistance of the material. Equally, thermal conductivity of a BMG is proportional to the material density (see Eq.(7.7)), leading to any thermal effects to also be dependent on the structure of the material.

Despite the interdependencies of the two key terms, characterisation of SBESD events with respect to each of these terms is important, as each of these terms yields information regarding different processes. The enthalpic approach focuses on how the temperature state of the material interacts with current flow through ‘elastic’ atomic vibrations within the material, whilst the entropic approach deals with how structural change interferes with current flow within the material.

In this section, analysis of the SBESD events has been performed with the assumption that the processes affecting resistance behaviour are a combination of separate enthalpic (internal energy changes) and entropic (structural changes) effects. The following outlines investigations of how these two effects are likely to influence electrical resistivity of a BMG undergoing shear banding, and the implications surrounding the use of the effects to extract parameters from SBESD event data from which certain shear band behaviours can be inferred.

7.5.1 SBESD events and enthalpic processes

The enthalpic contribution to SBESD events neglects the effect of structure change and seeks to describe how significant the contribution of the thermal energy-resistance coupling is in producing the observed SBESD results. This knowledge determines if just temperature information is required to recreate SBESD events, and consequently if SBESD events only yield information that refers to the thermal state of BMG shear bands.

To understand these questions, knowledge of the expected temperature behaviour during the shear band process is required as well as how this temperature profile is expected to affect resistance of the BMG. Once this has been identified, the thermal state of shear bands can be extrapolated from observed SBESD events.

Description of temperature behaviour: Enthalpic process

Many researchers have noted thermal energy release during shear banding and this is significant, with estimations of material temperatures reaching 3400 K to 8600 K during the shear band process [84]. The manner in which energy is released has been likened to that of an adiabatic [130] or near adiabatic [84] process, and the way in which this energy is dissipated has been shown to play a part in the difference between the ductile and brittle behaviour of a BMG [247].

The temperature profile (and by extension the resistance changes) from the enthalpic process of a BMG undergoing approximate adiabatic shear banding can be dictated by Eq.(7.7), derived for the laser flash method for determining heat capacity, thermal diffusivity and thermal conductivity of materials [250].

$$\Delta T = \left(\frac{H}{2\rho C_p \sqrt{\pi \alpha_\theta}} \right) \frac{1}{\sqrt{t}} \exp\left(\frac{-x^2}{4\alpha_\theta t} \right). \quad (7.7)$$

Eq.(7.7) is valid for a material that has been heated uniformly and adiabatically, valid for the case where heat dissipation only propagates in a single direction. In the case of a perfect shear band, these assumptions are valid as shear banding propagates throughout the entire length of the BMG due to the shear softening effect, providing a fast uniform increase in temperature across the entire cross-section of the material, whose thermal dissipation is then accommodated by the dissipation of heat away from the shear band. Therefore, whilst the description of shear band initiation cannot be accommodated by this model, the rest of the process is thought to be described well by Eq.(7.7).

Chap.(3) describes how the thermal coefficient of resistance (α_Ω) is usually (but not always) negative and relatively weak for BMGs. In addition, α_Ω is barely dependent on the test temperature for temperature ranges $16\text{K} \leq T \leq T_g$ [90]. BMGs annealed at temperatures beyond T_g begin to manifest a positive α_Ω until it reflects that of the relevant crystalline material [90].

This description of resistance-temperature dependency applies to BMGs in their static bulk form. However several factors required to describe the above resistance-temperature dependency are not valid for the dynamic nature of a shear band. For example the sign of α_Ω is defined by the structure factor-fermi wave vector ratio: $\frac{2k_f}{K_p}$. In the case of a shear band, this ratio is likely to change, as the structure factor must evolve to accommodate the free volume generated during shear formation. In addition, the temperature criteria outlined for the observation of a negative α_Ω is not obeyed during shear banding, with temperatures reported to reach over $10T_g$ in some cases [84]. Finally, nano-crystallisation has been observed to occur on a multitude of BMGs at shear banding sites [141]. Therefore any simplistic bulk resistance vs. temperature dependence cannot be utilised to probe thermal behaviour of shear bands, and a more complex dependence capable of describing an amorphous material undergoing both melting and nano-crystallisation and severe localised flow, whilst reaching temperature values potentially in excess of the vaporisation temperatures of all the constituent components (molybdenum being the highest of the BMG compositions considered here at 4885K [251]) over nanosecond time-scales.

It is clear that there are significant difficulties surrounding the definition of a theoretical relationship between the resistance and thermal energy state of a shear banding BMG. Based on this, a simple proof-of-concept experiment was envisaged to determine if the enthalpic effect is observable through the SBESD system, and, regardless of the details surrounding the actual relationship between thermal energy and resistance in a BMG undergoing shear banding, what limits can be put on shear band behaviour from the SBESD results.

Proof of concept: Enthalpic process.

To validate if the effect of a sudden input of thermal energy into a material would produce a detectable change in resistance through the SBESD system, a simple laser pulse experiment was devised to simulate a 2 dimensional representation of the thermal energy distribution expected from shear band formation without the structural changes caused by shear banding. Due to equipment limitations, the energy densities and thermal heating times of these experiments were lower and longer than that expected from actual shear banding behaviour. However the experiment aims to answer whether resistance changes due to temperature variations are detectable in amorphous materials, therefore the experiment does not require the exact temperature conditions of a shear

| Composition | λ_L [nm] | Power [mW] | Exposure times | Amplification | Carbon coating |
|--|------------------|------------|----------------|---------------|-------------------|
| Fe ₇₈ Si ₉ B ₁₃ | 532 | 125 | 10ms,1ms | 120 | Powder deposition |
| Fe ₈₀ Si ₁₀ B ₁₀ | 532 | 125 | 10ms,1ms | 120 | Powder deposition |
| Al ₈₇ Ni ₇ Nd ₆ | 532 | 125 | 10ms,1ms | 120 | Powder deposition |
| Fe ₈₀ Si _{7.5} B _{12.5} | 532 | 125 | 10ms,1ms | 120 | Powder deposition |
| NiSiB | 532 | 125 | 1s,10ms,1ms | 1000 | Aerosol spray |
| Ni ₆₂ B ₃₈ | 532 | 125 | 1s,10ms,1ms | 1000 | Aerosol spray |
| (Fe ₄₀ Ni ₆₀) ₈₃ B ₁₇ | 532 | 125 | 1s,1ms | 1000 | Aerosol spray |
| (Fe ₅₀ Ni ₅₀) ₈₃ B ₁₇ | 532 | 125 | 1s,1ms | 1000 | Aerosol spray |
| (Fe ₆₀ Ni ₄₀) ₈₃ B ₁₇ | 532 | 125 | 1s,1ms | 1000 | Aerosol spray |
| (Fe ₉₀ Ni ₁₀) ₈₃ B ₁₇ | 532 | 125 | 1s,1ms | 1000 | Aerosol spray |
| (Fe ₈₀ Ni ₂₀) ₈₂ B ₁₈ | 532 | 125 | 1s,1ms | 1000 | Aerosol spray |
| (Fe ₉₀ Ni ₁₀) ₈₀ B ₂₀ | 532 | 125 | 1s,1ms | 1000 | Aerosol spray |

Table 7.2: Samples tested and test conditions for amorphous ribbons in the laser heating experiment

band to be replicated.

Amorphous ribbons made through a melt spinning process were supplied by the University of Torino (research team of Prof Livio Battezzati) and the University of Sheffield (Andrew Cunliffe). The ribbons were cleaned with isopropyl alcohol and marked with a thin band of carbon applied through either an aerosol spray or powder deposition, Tab.(7.2). Ribbons were then placed in the optical set-up shown in Fig.(7.14) and were attached to the SBESD system for testing.

A tricolour PULSELAS[®]-P-355-300 20kHz laser with a pulse width of ≤ 1 ns was shone through a prism to isolate the 523nm wavelength light, which was then subsequently aligned with the exposure shutter to be pulsed onto the carbon band on the ribbons. The carbon bands on the samples were exposed to the laser light by the opening the shutter for durations of 1 ms, 10 ms and 1000 ms for preferential heating of each ribbon over the carbon band area. The effect of thermal energy input and dissipation on resistance of these bands was monitored through the SBESD system sampling at 1MHz.

Fig.(7.15) shows examples of results obtained on amorphous ribbons for 1ms exposure times. This exposure time represents the closest possible conditions for replicating adiabatic heating behaviour of a shear band given the equipment available. For the ideal case, it was expected that the resistance change during laser exposure would be minimal, with only a small decrease in resistance observed for amorphous ribbons, and a small increase in resistance observed in ribbons which hold a small amount of crystallinity with respect to test time during light exposure. What is actually observed is a double peak signal common to all tests over all tested materials. The signals were highly repeatable and show only slight differences in the signal amplitude across different samples. By running the experiment with the laser aperture closed so no light reached the sample, it was found that significant electromagnetic interference from the opening and closing action of the exposure shutter was responsible for these peaks. No other features could be observed in the data, indicating that resistance changes due to enthalpy over the energy levels utilised here are not detectable through the SBESD system under these conditions.

Experiments performed with longer exposure times of 10 ms and 1000 ms are further from the criteria of adiabatic heating of the ribbons required for Eq.(7.7) to be valid. However, as shown in Fig.(7.17), these resistance changes show (in addition to the doublet peak) an overall increase in resistance during light exposure followed by a decay in the resistance post light exposure. This observation indicates that a higher level of thermal energy is required to observe a significant

| Exposure time [s] | Beam radius [mm] | Laser power [mW] | Maximum energy [Jm^{-2}] |
|-------------------|------------------|------------------|-------------------------------------|
| 1 | 1 | 125 | 39800.0 |
| 0.01 | 1 | 125 | 398.0 |
| 0.001 | 1 | 125 | 39.8 |

Table 7.3: Calculation of thermal energies imparted into the test ribbons assuming an adiabatic heating condition and 100% absorption efficiency over different exposure times.

change in resistance behaviour than that afforded by the 1ms exposure times.

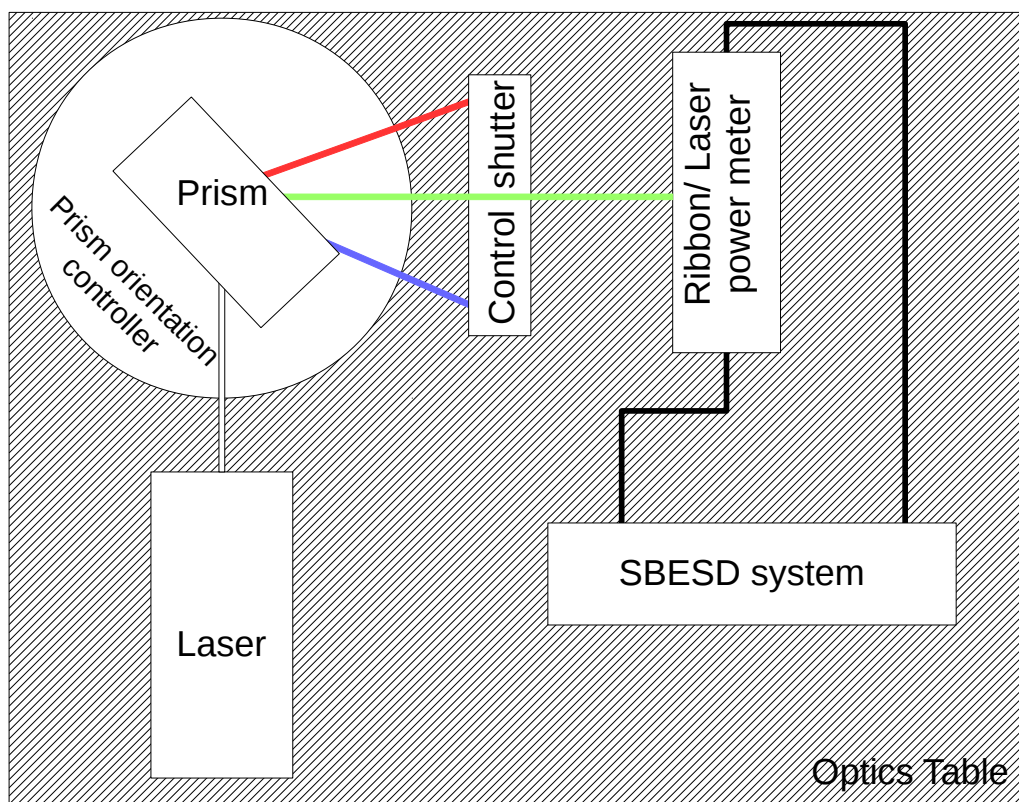
In order to show this experiment acts as a valid proof of concept experiment for the SBESD compression tests, there needs to be an understanding of how the thermal energies generated here compare to that of a shear band formed in a BMG under compression. Work by Qiao et al. has shown that minimum energy produced during shear band formation is 1.4 Jm^{-2} to 61.2 Jm^{-2} , the energy required to maintain the sample temperature of $0.8T_g$ long enough to dissipate any shear stress [247]. This is in agreement with other energy estimates found by other researchers of a range of BMGs [84]. In the case of the laser experiments performed here, we assume that the heating for all 3 exposure times occurs adiabatically, and that the heating for each ribbon is 100% effective over the area or the applied carbon coating and 0% effective everywhere else. Based on these assumptions, the difference in the thermal power distribution between the shear band and laser flash experiments (outlined in Fig.(7.16)), are calculated in Tab.(7.3) for different exposure times. It can be seen that energy values generated with the given assumptions under the 1ms exposure times are comparable to the values stated by Qiao et al. However the electromagnetic interference from the control shutter means one cannot state whether detectable signals are present in the SBESD data over time periods which reflect the energy inputs according to the assumptions outlined above, and a revised optical table layout is recommended for future work. This being said, the performed experiments are not likely to approach the 100% absorption efficiency or have an adiabatic condition during heating. Therefore detection of any resistivity change in the SBESD data over any exposure time period indicates that the SBESD system is capable of detecting resistivity changes due to enthalpy changes, though the sensitivity to this change cannot be accurately determined through the results reported here.



(a) Tricolor laser being split into the constituent laser wavelengths prior to passing through the control shutter.

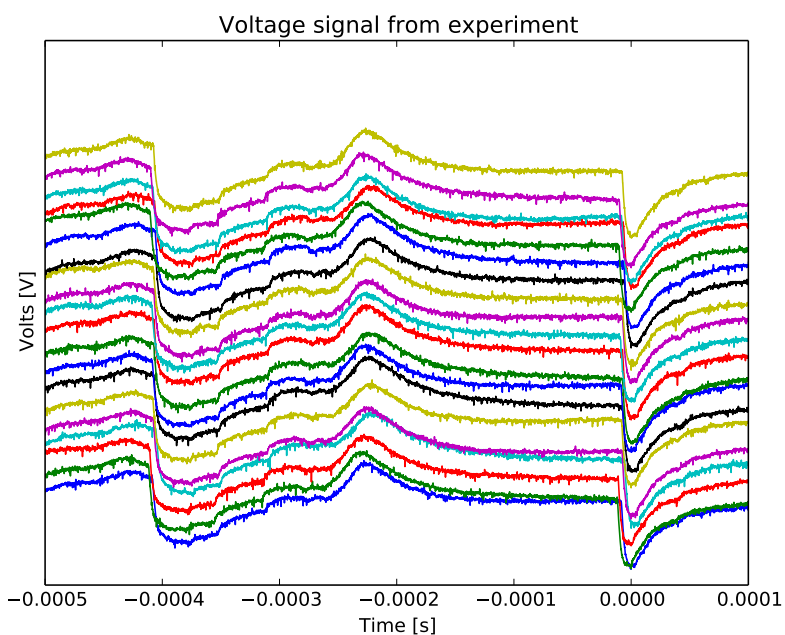


(b) Optical setup showing the path of the laser light to the sample.

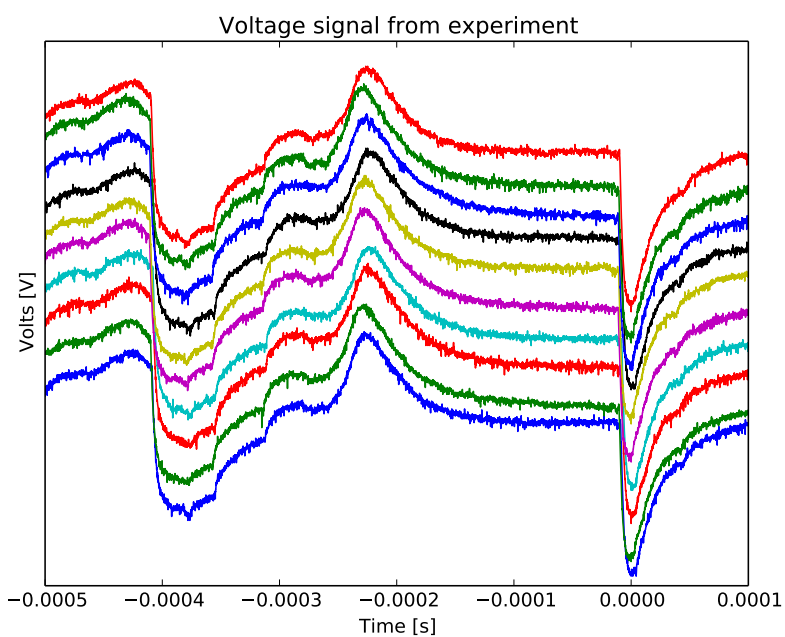


(c) Schematic of the optical table and experimental layout.

Figure 7.14: Layout of the proof-of-concept experiment to determine if enthalpic changes could be detected with the SBESD system.



(a) The result of ten 1ms duration pulsed from a 532nm laser on the carbon coated $\text{Fe}_{78}\text{Si}_9\text{B}_{13}$ ribbon.



(b) The result of ten 1ms duration pulsed from a 532nm laser on the carbon coated $\text{Fe}_{80}\text{Si}_{7.5}\text{B}_{12.5}$ ribbon.

Figure 7.15: Resistance response of 2 different amorphous ribbons when lit for 1ms with the 532nm wavelength of the tricolour PULSELAS[®]-P-355-300 20kHz laser with a pulse width of $\leq 1\text{ns}$.

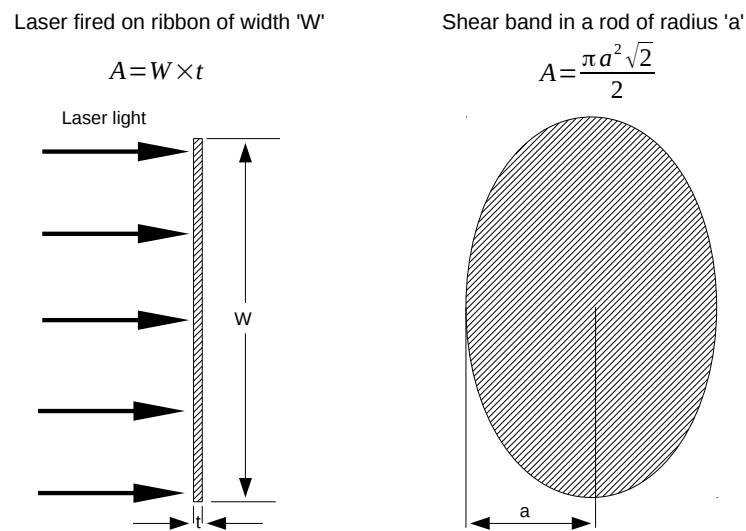


Figure 7.16: Schematic showing the areas over which thermal energy is absorbed during the laser flash proof-of-concept experiment and shear banding. The difference in power densities has prompted the calculation of the expected energy absorbed during the proof-of-concept experiment (Tab.(7.3)) to determine if similar energies are absorbed into the test material, albeit over different time periods.

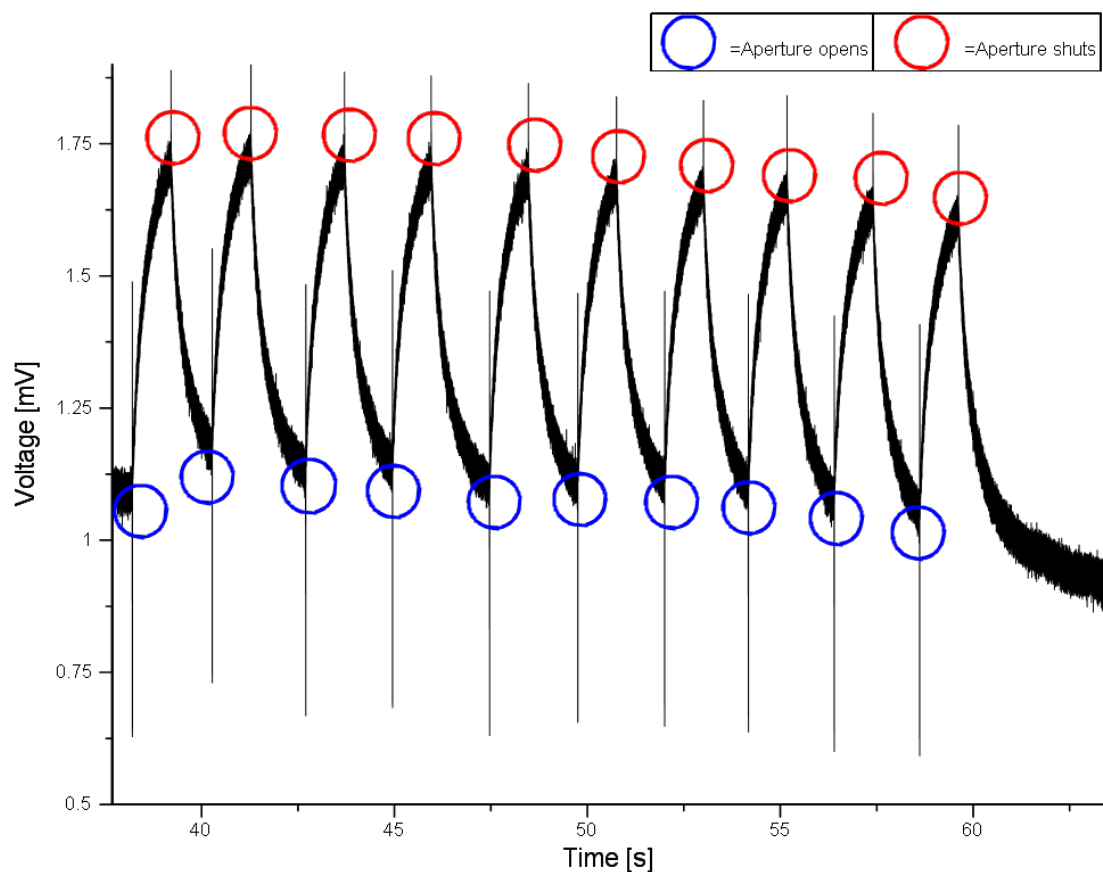


Figure 7.17: SBESD voltage response for tests performed on the NiSiB ribbon with for 10 exposures with 1 second exposure times showing an increase followed by a decrease in resistance behaviour of the material indicating a positive thermal resistance coupling. Peaks highlighted by blue and red circles indicate the signals observed in Fig.(7.15a) and Fig.(7.15b).

SBESD signals and the Enthalpic process

Based on the findings of the proof-of-concept experiment, detected SBESD signals have been analysed solely with respect to thermal processes. Some of the behaviours will be explicable through known or expected shear band characteristics, whilst others will require further factors to be considered. This can therefore be used to further the assessment of the validity of these signals through thermal arguments only.

Linking thermal events to resistance change

$$R = R_o(1 + \alpha_\Omega \Delta T) \quad (7.8)$$

$$\Delta R = R_o(1 + \alpha_\Omega \Delta T_2) - R_o(1 + \alpha_\Omega \Delta T_1) = \alpha_\Omega \Delta T \quad (7.9)$$

The absolute resistivity state of a simplistic conducting material can be described broadly through Eq.(7.8), which describes the effect of elastic phonon scattering interactions within a conductor have on the flow behaviour of electrons. For crystalline conductors, α_Ω is a positive value, whilst semiconductors show a negative α_Ω value. This value has been observed to be negative and weak for BMGs, and relatively independent of temperature for temperatures between tens of kelvin to $\approx T_g$. The details surrounding the factors governing the sign and magnitude of α_Ω for BMGs have been covered in Chap.(3), and will be referred to throughout the analysis performed here. Due to the comparative nature of the SBESD system, Eq.(7.8) cannot be used in its current form and a modified version of the equation (Eq.(7.9)) must be used in order to evaluate temperature changes in terms of thermal resistance change.

Characterising thermal shear band responses through resistivity change requires certain assumptions to be made surrounding the shear banding process. Firstly, the assumption that the active shear band process is adiabatic is key. This assumption states that all the thermal energy generated during the process remains within the volume of the shear band itself, thus allowing accurate determinations of thermal energy without the need to accommodate uncharacterisable thermal diffusion processes during shear banding. There is strong evidence suggesting that this assumption is not true [84]. However, the act of approximating a near-adiabatic process to an actual adiabatic process has allowed researchers to successfully validate their first approximations into shear band investigations [130]. To that end, this assumption is used here with the potential for work on accommodating a non-adiabatic model in the future.

The second required assumption regarding the thermal processes in shear banding (an extension of the first assumption) is that the volume of a shear band remains constant during the active period of shear band operation. This volume is described in the literature as bands of widths of $\approx 10\text{nm}$ that propagate throughout the entirety of the cylindrical sample at angles of $\approx 45^\circ$ to the direction of applied stress. Therefore, for a cylindrical rod of radius a_r like that shown in Fig.(7.18), a shear band will have a volume approximated by

$$V_{SB} = \pi a_r^2 d_{SB} \sqrt{2}. \quad (7.10)$$

Whilst this is valid for uniform rods, SBESD compression experiments involve the use of necked rods. The difference in geometry requires Eq.(7.10) to be modified accordingly, using the term a_n instead of a_r to give a good estimation of the modified shear band volume. This can only be considered an estimate, as the geometry of the neck means the potential of forming a perfect elliptical shear band centred at the centre of the sample is limited, as demonstrated in Fig.(7.18).

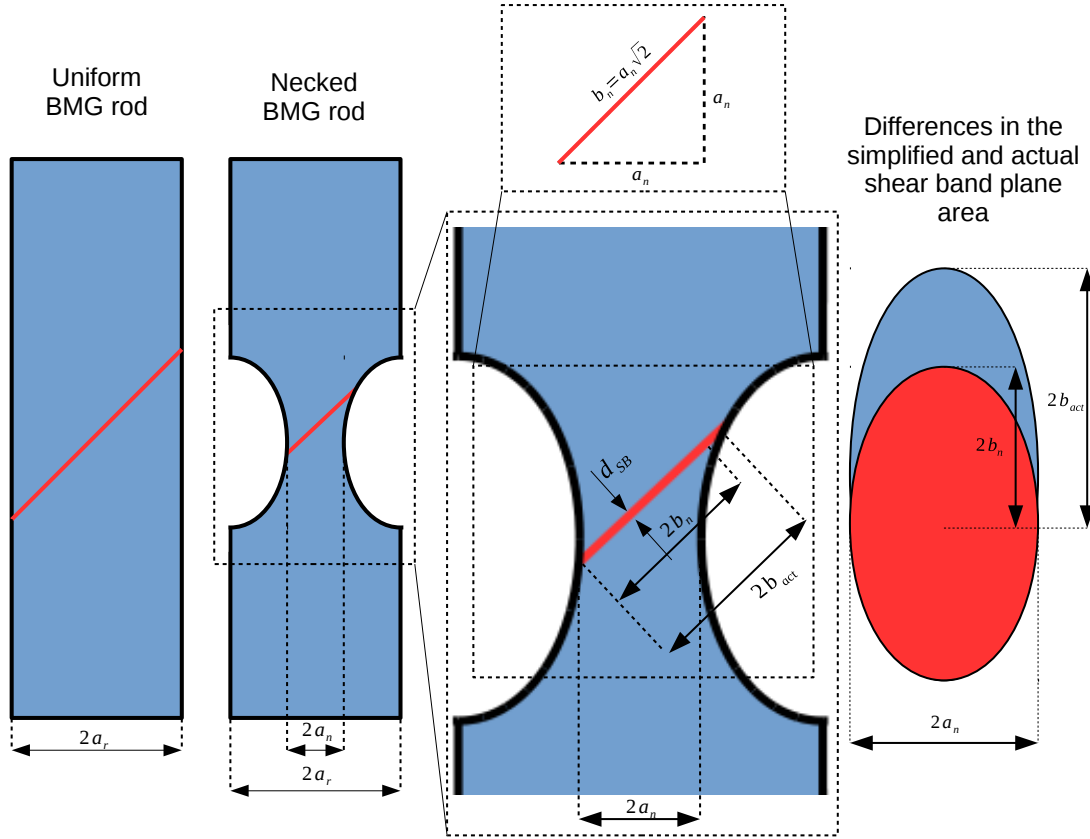


Figure 7.18: A schematic showing the source of the mismatch in shear band volumes used in the enthalpic SBESD calculations and the volumes expected to be generated during a SBESD compression test.

In addition, whilst it is expected that shear bands will likely initiate in the middle of the neck (the point at which stresses are concentrated), this cannot be confirmed as absolute. The manual preparation process and the potential for nano-crystallisation from previous shear band events may force shear bands to form a short distance away from the neck centre. Based on these considerations, shear band volumes are calculated using Eq.(7.11) and are noted only to be an approximation to the true shear band volume.

$$V_{SB} = \pi a_n^2 d_{SB} \sqrt{2} \quad (7.11)$$

Tab.(7.4) outlines the estimated shear band material rest resistances based on a_n measurements from optical micrographs (see Fig.(7.19)), the assumption that shear bands form according to the schematic given in Fig.(7.18) and values of ρ_Ω , taken both from literature, estimated through a rule of mixtures approach and measured in the as cast BMG rods through a 4 point probe measuring rig designed for this work (outlined in Chap.(4)).

The other term to estimate in Eq.(7.8) is α_Ω . BMGs tend to show a weak and negative α_Ω , however the observation that S signals show exclusively positive changes in resistance requires a positive α_Ω value to explain any part of the S signals in terms of the model constructed here. As strong and positive values of α_Ω are present in metal alloys in their crystalline state, use of the crystalline α_Ω values provide a lower limit to the thermal response of the material undergoing shear banding. As literature values of α_Ω for BMG compositions tend to focus on values valid for

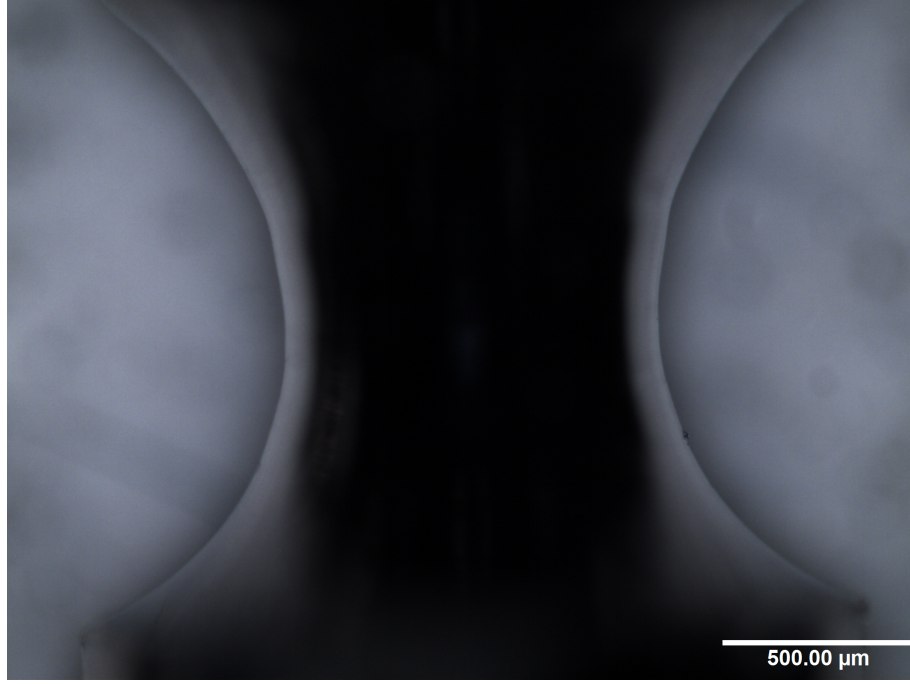


Figure 7.19: An example micrograph of a $Zr_{50}Cu_{40}Al_{10}$ necked sample prior to testing. These images were used to measure all neck diameters of tested samples for use in further analysis.

the glassy state, attempts were made to measure α_{Ω} for crystallised samples made here through the SBESD system. Details surrounding the experiment used for this measurement are given in Chap.(4). However the results demonstrated in Fig.(7.20) show that the induction furnace introduces too much electronic noise in the SBESD data to be able to extract α_{Ω} values. As such, an approximation to α_{Ω} values was made through a rule of mixtures approach from the constituent elemental values of α_{Ω} for all tested BMG compositions. Improvements to these values are suggested for further work.

The final required assumption is one regarding the validity of Eq.(7.9) for describing the relationship between thermal energy and change in the resistance state during the shear band process. The equation describes systems that are in an equilibrium state, i.e. not undergoing significant

| Sample | Neck diameter [μm] | SB facial area [m^2] | R_o [Ω] |
|---|---------------------------------|---------------------------------|-----------------------|
| $Zr_{44}Cu_{44}Al_6Ag_6$ | 799 | 7.09×10^{-7} | 7.71×10^{-8} |
| $Zr_{50}Cu_{40}Al_{10}$ | 988 | 1.08×10^{-6} | 5.01×10^{-8} |
| $Zr_{57}Cu_{20}Al_{10}Ni_8Ti_5$ | 865 | 8.31×10^{-7} | 6.50×10^{-8} |
| $Zr_{65}Cu_{15}Al_{10}Ni_{10}$ | 1008 | 1.13×10^{-6} | 4.62×10^{-8} |
| $Ti_{33.85}Cu_{46.35}Ni_{8.4}Zr_{11.4}$ | 1022 | 1.16×10^{-6} | 4.90×10^{-8} |
| $Ti_{40}Zr_{10}Pd_{14}Cu_{34}Sn_2$ | 1036 | 1.19×10^{-6} | 4.98×10^{-8} |
| $Pd_{77.5}Si_{16.5}Cu_6$ | 846 | 7.95×10^{-7} | 2.34×10^{-8} |
| $Cu_{57.5}Hf_{27.5}Ti_{15}$ | 796 | 7.04×10^{-7} | 8.12×10^{-8} |
| $Zr_{57.5}Nb_5Cu_{15.4}Ni_{12}Al_{10}$ | 830 | 7.65×10^{-7} | 6.86×10^{-8} |
| $Cu_{43}Zr_{43}Ag_7Ti_7$ | 829 | 7.63×10^{-7} | 7.28×10^{-8} |
| $Cu_{50}Hf_{43}Al_7$ | 998 | 1.11×10^{-6} | 5.20×10^{-8} |
| $Ti_{33}Cu_{47}Zr_9Ni_6Sn_2Si_1Nb_2$ | 939 | 9.79×10^{-7} | 5.97×10^{-8} |

Table 7.4: Data for the necked samples and the calculated values of resistance of samples prior to undergoing a shear band process.

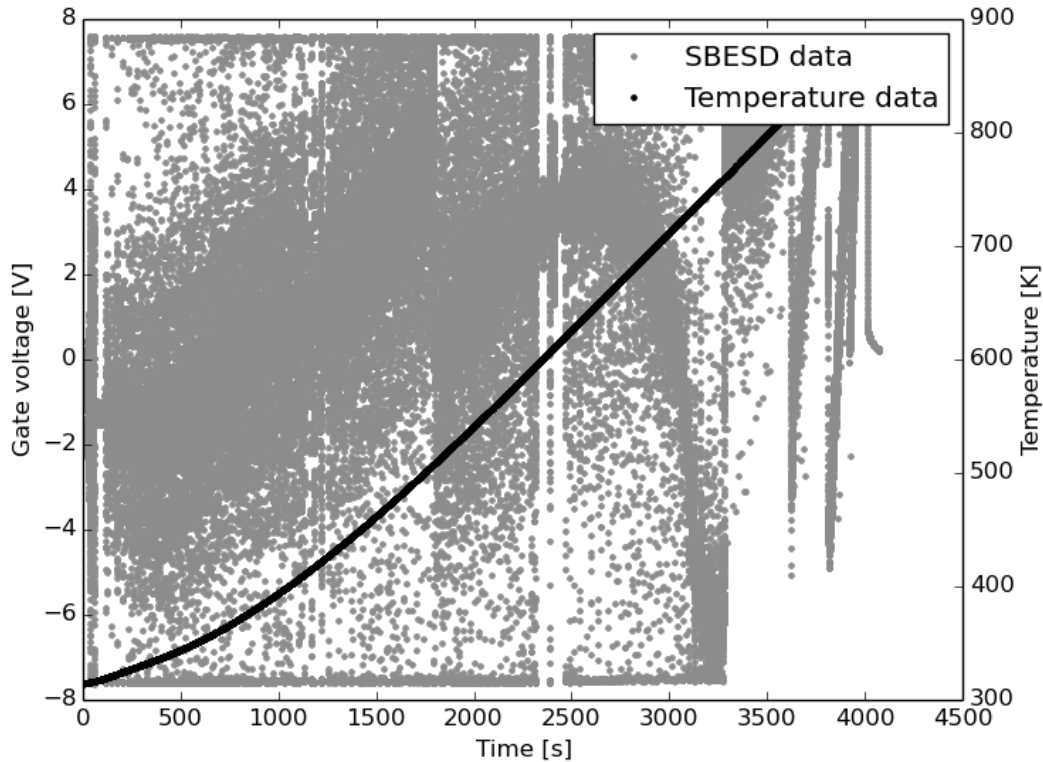


Figure 7.20: Results showing the typical resistivity response with respect to temperature for $\text{Zr}_{44}\text{Cu}_{44}\text{Al}_6\text{Ag}_6$. The noise within the data is too great to make any significant estimate on α_Ω . The large sudden changes in the SBESD data are due to the need for continual corrections in the balance of the bridge such that the gate voltage remained within the voltage range defined by the amplification unit.

structural changes. This does not apply in the case of a shear band, potentially resulting in a non constant value of α_Ω . It is therefore the hope that splitting the thermal and structural contributions to resistance will isolate sections of the detected signals where this equation is valid for a first approximation to the thermal shear band behaviour.

The combination of all three of these assumptions stated above provides the framework for the analysis of the enthalpic approach. Specific details surround how the detected signals are analysed are outlined below:

Analysis of W signals with respect to thermal arguments

W SBESD signals are generally observed as permanent step changes in the resistivity behaviour of the material. Based on Eq.(7.9), such a behaviour would indicate a permanent change in thermal energy within the material due to a single input of energy from a shear band. This is a clear violation of the 2nd law of thermodynamics, therefore the W signals cannot be analysed with respect to the purely to changes in thermal state.

The absence of a thermal feature in W signals does not necessarily mean that these signals are invalid descriptions of how shear banding affects resistance behaviour of the material. It is well known that the temperature dependence of BMG materials on resistivity is weak and generally negative. Therefore absence of a thermal response may be a reflection of the insufficient sensitivity

| Composition | signal type | ΔT_{\max} [K] |
|---|-------------|-----------------------|
| Zr ₅₀ Cu ₄₀ Al ₁₀ | S | 505 000 000 |
| Zr ₅₀ Cu ₄₀ Al ₁₀ | S | 112 000 000 |
| Zr ₄₄ Cu ₄₄ Al ₆ Ag ₆ | S | 248 000 000 |

Table 7.5: Results for determining ΔT_{\max} for clear S type signals from section I of the data.

and sampling rates of the SBESD system. It may also be an indication of a lack of certain processes occurring within these materials that separate the behaviour between W and S signals. For example, it was briefly hypothesised in the description of S signals that nanocrystallisation could explain some of the features. A lack of nanocrystallisation would equally explain the change in resistance states observed in W signals, as the strong resistance-temperature dependency of crystalline materials is not observed. Only permanent resistance changes are observed during the shear-banding process, possibly due to a permanent structural change from the shear band itself.

Based on the arguments given above, no quantitative analysis of the thermal response of W signals have been performed here. However it is suggested for further work that thermal observations in W signals should be explored with an improved SBESD system capable of probing higher sensitivities and sampling rates.

Analysis of S signals with respect to thermal arguments

S signals appear to be comprised of 2 distinct sections; an initial fast transient increase and decrease in resistance (section I) and a final slow resistance decay (section II). Data from section I coincides with the active region of the shear band defined by the duration of a significant drop in load, whilst data from section II appears to be associated with a recovery process within the material. Both sections could potentially be associated with a thermal process, with section I being due to the sudden generation and release of thermal energy, and section II being due to the dissipation of thermal energy from a shear band event. By treating each of the signal sections separately, an assessment can be made as to whether any part of the measured S signals can be treated solely due to the thermal response from shear banding.

Starting with data from section I, an estimate of the maximum temperature change is calculated based on the maximum observed resistance change in the raw, amplified and untreated (i.e. no moving average) SBESD data, and the rearranged Eq.(7.9). Tab.(7.5) shows the inferred increase in temperature for all observed S SBESD results is far beyond that of any conceivable temperature change reported for the shear band process. This indicates that either estimations of α_{Ω} in Eq.(7.9) are wrong, or that S SBESD signals cannot be represented purely through thermal energy considerations. As the values of α_{Ω} utilised are already generous, it is difficult to justify an adjustment to this value to reduce the observed ΔT , which stands at 10,000-50,000 \times greater than the temperature rises reported in literature [84]. Therefore it is concluded that other contributors need to be considered in order to produce section I of the S signals observed.

For data from section II, an estimate of maximum temperature rise during shear banding can be inferred through an extrapolation of the section II data to a point in time where a shear band initiates. Extrapolation requires the fitting of section II data to an equation that could be used to describe the resistance (and therefore temperature) evolution of shear band material. Therefore a modified heat flow equation was utilised for fitting, whose derivation and justification is outlined

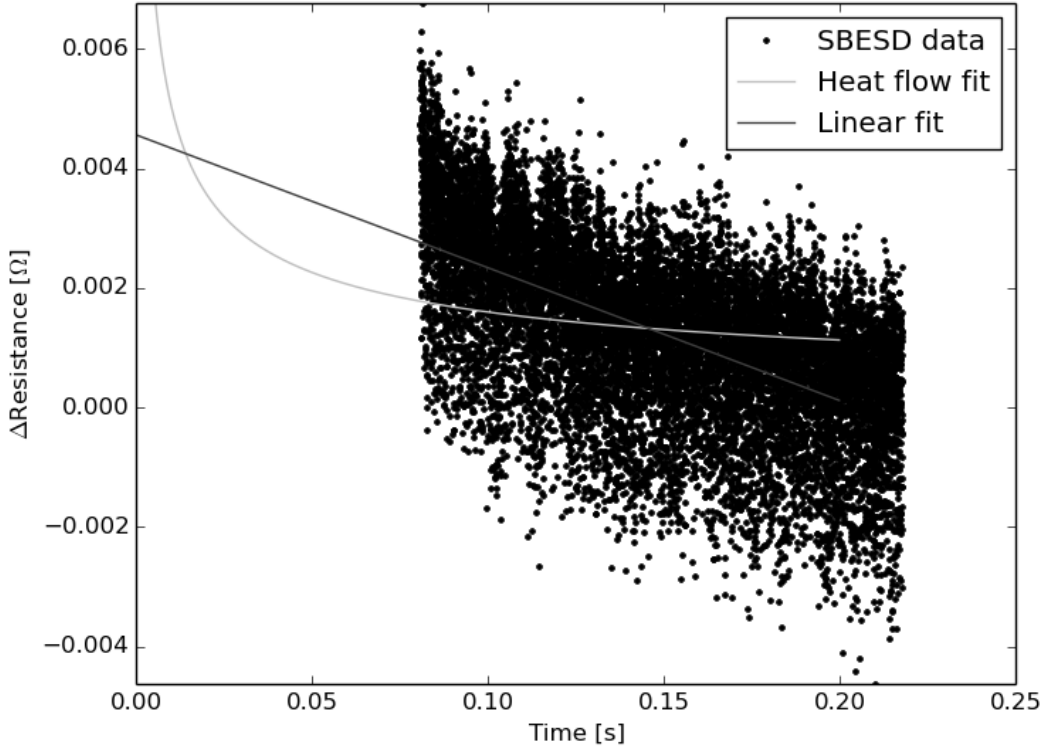


Figure 7.21: Secondary decay signal in S SBESD data treated with a 100 point moving average to reduce the level of noise for a successful fit.

in Sec.(9.5):

$$\Delta R(t) = A\sqrt{\pi B} \times \operatorname{erf} \left[\frac{x}{\sqrt{Bt}} \right], \quad (7.12)$$

Fig.(7.21) shows an attempt to analyse section II data from the strongest observed signal in $\text{Zr}_{50}\text{Cu}_{40}\text{Al}_{10}$. It is immediately obvious that the fit has not been successful due to the level of scatter within the data (despite a 100 point moving average treatment). Therefore the extrapolation produces temperature estimates that are once again too large. To compensate for the poor fitting of Eq.(7.12), a linear equation was fitted to the data to determine a lower limit for the temperature change. These estimates, provide a good lower estimate to the temperature rise of shear bands, given the generous values of α_{Ω} utilised. Results are highlighted in Tab.(7.6). It is noted that the moving average treatment affects the estimate of ΔT_{max} , with more aggressive treatments affecting weaker signals more, and vice versa. As such, both fitting approaches require a reduction in the scatter of the data in order to provide a more accurate estimation and limits to ΔT_{max} through enthalpic considerations.

To summarise, purely enthalpic contributions cannot completely account for the source of S SBESD signals, with the dominant peak change in resistance requiring contributions beyond that which can be offered from thermal processes. However the secondary decay features in S signals may be due to a purely thermal processes. Noise in the data prevents accurate extrapolation of these features to the point of shear band initiation, which would allow for detailed temperature information to be extracted. However linear fits to these features have provided a sensible lower limit to the minimum temperature rise due to shear banding the signals observed, so long as the

| Composition | Signal type | ΔT_{max} [K] | |
|---|-------------|----------------------|-------------------|
| | | 10 Point average | 100 Point average |
| Zr ₅₀ Cu ₄₀ Al ₁₀ | S | 78.551 | 75.254 |
| Zr ₄₄ Cu ₄₄ Al ₆ Ag ₆ | S | 32.187 | 47.2294 |
| Zr ₅₀ Cu ₄₀ Al ₁₀ | S | 32.187 | 7.208 |

Table 7.6: ΔT_{max} estimates for S signals in descending signal strength order from extrapolation of secondary decay data in S signals.

moving average data treatment is applied with caution.

7.5.2 SBESD events and entropic processes

Purely enthalpic processes cannot explain W signals or S signals in their entirety. Therefore the contribution of structural evolution to SBESD signals needs to be considered. It has been shown that electrical resistance is structure dependent, with early literature clearly identifying a strong change in resistivity as a material undergoes a drastic phase change, such as a solid to a liquid [83]. Literature has shown that the structure of shear bands in BMGs are different compared to the rest of the matrix, with Pampillo [128] showing preferential etching at shear banding sites and multiple authors noting preferential deformation in material already populated with shear bands [131, 139, 252]. Based on this, it is reasonable to assume that the structural state of a shear band will have different resistivity properties to that of the rest of a glassy matrix, however the difference is expected to be small due to the similarity of shear banded and non shear banded structures. As previously highlighted, conduction of an electrical current in an amorphous structure is a highly complex problem, especially when the conducting medium is undergoing highly localised flow, producing severe changes in temperature and structure over the nanosecond time-scales.

A full quantum mechanical treatment of this process is suggested as a topic for further work. For current purposes, a basic model of how structural changes influence resistivity behaviour must be constructed in order to explore the contribution of structural changes to a SBESD signal.

Proof of concept of modelling the effect of entropy change on resistance.

It has been shown that during a shear banding event, free volume is generated and relatively densely packed structures within the glassy matrix are broken into more open and less stable structures [5, 98]. These reduced density structures are expected to be less effective in the conduction of an electrical current. From a quantum mechanics point of view, the energy band gap of electron shells of atomic pairs is decreased when the inter-atomic distance is small, and vice versa and in the case of the densely packed cluster structure of a BMG, more electrons can be shared between atoms, thus facilitating a greater potential for electron conduction, Conversely in the case of an open cluster structure like that observed in shear bands conduction will be limited.

From the point of view of classical mechanics, the valence electrons, which are responsible for conduction, can pass from atom to atom if the atoms are packed more closely together. Therefore higher fractions of free volume reduce the fraction of atoms that are packed closely together and therefore reduces the number of low energy paths through which a valence electron can travel in accordance with the ‘nearly free electron’ model [83], increasing the resistivity of a BMG. Therefore it is expected that structures associated with shear banding (both during and post process) are likely to have higher resistivity values than that of a relaxed BMG structure. Based on these observations, a pseudo-SBESD proof-of-concept compression experiment was devised, based on the

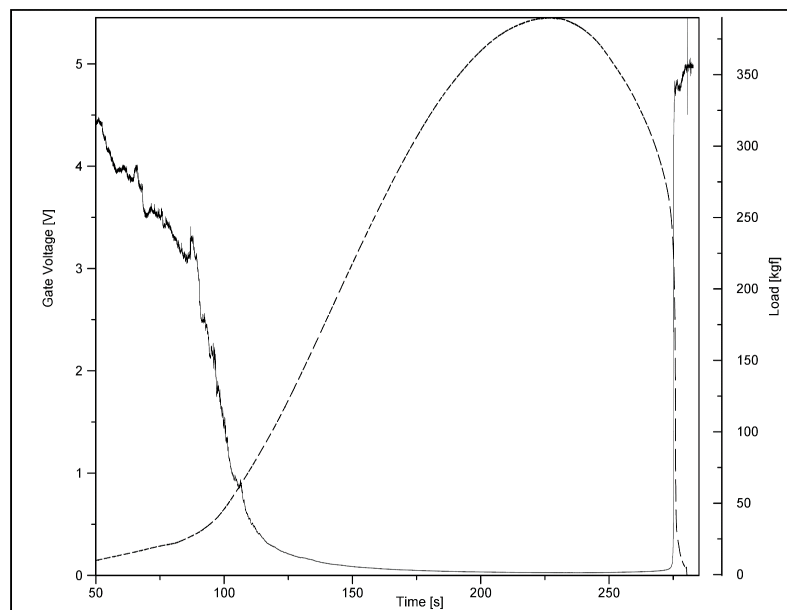
philosophy of Argon's 'bubble raft' experiment [101], to produce similar signals to those expected in SBESD based solely on the given entropic considerations.

Samples were constructed from a chromium powder and weak epoxy mix and prepared as outlined in Chap.(4). These samples were created in order to mimic the structural process of shear banding and how this affects resistance behaviour of the material. Chromium particles represent the atoms or clusters of atoms within the BMG structure, and the contact between the chromium particles represents the current flow ability of the material. The weak epoxy resin serves as the inter-atomic potentials within the structure holding the material together. Samples were then compressed in the SBESD compression manner as outlined in Chap.(4). As the structure deforms, areas of free volume between the chromium particles are expected to form. This effectively increases the resistivity of the material during deformation as would be expected during shear banding. The expected signal response would therefore be as follows:

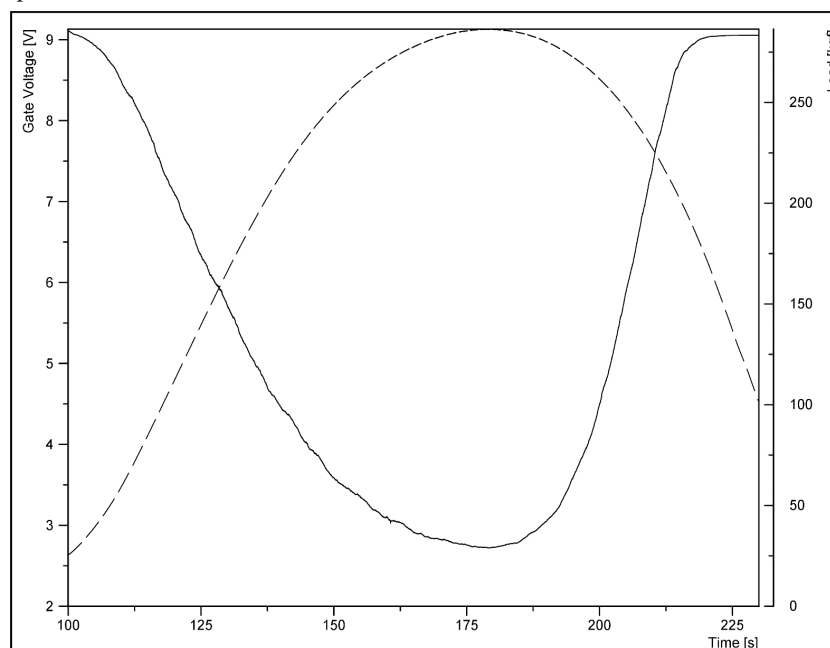
1. The resistivity would increase, at an increasing rate at the start of the shear band formation as free volume develops.
2. The rate of resistivity change will then slow and a single, steady-state resistivity value will be established as the effect of extra generation of extra free volume is countered by the annihilation of previously generated free volume .
3. Once the shear band has arrested, some free volume is lost as the structure recovers elastically. A band of less densely packed material with higher resistance remains, which is analogous to a shear band.

Steps 1 and 2 above are expected to be produced in the proposed experiment, though the 3rd step may not.

Fig(7.23) shows the results for the two trials of the proof of concept experiment. Fig.(7.22a) shows the results for a uniform rod. This gave good load response and a general SBESD signal as outlined by the points defined above. However, the slip band formed near the contact between the electrode and the sample. Therefore steps were taken to modify the tested samples. A neck was machined out of the sample in a similar fashion to that for the samples for the actual SBESD compression experiments, through the use of a round file and a rotary drill. The neck successfully concentrated the stress such that failure occurred along the necked region at an angle near the 45° plane of CRSS, as shown in Fig.(7.23b). The improvement in the experiment is demonstrated in SBESD data in Fig.(7.22b), whereby the gate voltage response shows a much smoother profile to that of Fig.(7.22a) afforded by a constant and consistent sample-electrode contact, providing the expected resistivity response due to shear band structural change.

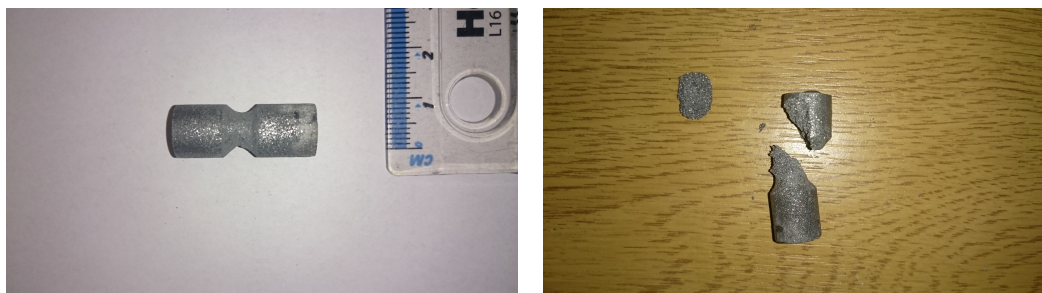


(a) The load and SBESD response for the uniform chromium-epoxy sample under compression.



(b) The load and SBESD response for the necked chromium-epoxy sample under compression.

Figure 7.22: The results of the initial and improved proof-of-concept experiments for showing the potential effect structural change can have on the resistance behaviour of a BMG undergoing shear banding. The dashed lines represent the load cell data, whilst the solid lines represent the SBESD data. It is worth noting that the reduction in gate voltage in these cases are a consequence of the experimental set-up and signify an increase in resistance during compression, not the opposite.



(a) The necked compressed chromium-epoxy sample prior to SBESD compression.

(b) The necked compressed chromium-epoxy sample post SBESD compression showing the $\approx 45^\circ$ shear plane formed as a consequence of the necked preparation.

Figure 7.23: The improve chromium-epoxy sample showing the success of the failure mode when tested under the SBESD compression regime.

The experiment replicated the key expected behaviours during shear banding: an initial increase in resistance due to free volume generation and dense cluster structure breakdown, a plateau of resistance during the balance of free volume generation and annihilation as steady state flow within the shear band is achieved, and partial resistance recovery from the relaxation of the material post shear band propagation. The form of the signal generated here predicts similar observations to that predicted for purely enthalpic processes, with only the steady state and partial recovery features differing from the enthalpic signal. Given the lifetime of a shear band, and the similarity of shear band structure post formation to that of the structure of the glassy matrix, both of these features may not be observable in a given SBESD event, making it difficult to distinguish the enthalpic and entropic processes responsible for resistivity change in a BMG during deformation. This supports the approach of treating all SBESD results as being exclusively caused by either entropic or enthalpic processes. Inferences from each of these treatments provides valuable information regarding the shear band process, even if the relative contribution of both these effects cannot be separated.

Analysis of SBESD results: Introduction to entropic modelling approaches

Based on the success of the proof-of-concept model, and the basic descriptions of how resistivity behaviour of BMGs relates to changes in BMG structure, steps can be taken to relate observed SBESD events to structural changes with BMGs. To that end, the following modelling approach is proposed to give a first approximation regarding how structural changes can be extracted from SBESD signals.

Modelling how resistance change depends on structural change requires a description of how a structure interacts with a current to produce resistance, and how that interaction changes with structure. To accommodate this, the modelling performed here utilises a simple first principles model whereby the charge distribution of atoms from an amorphous structure is used to produce an electrostatic potential energy landscape defined by the interactions between modified Lennard-Jones potentials from each atom. This is then related to resistance values based on the following hypothesis:

- *Resistivity of a material is directly proportional to the amount of work required to pass a charge carrier (electron) through a unit volume of material.*

In essence, this statement defines resistance as the work required to pass electrons from one valence shell to another across the whole material. More advanced descriptions of electron transport

in amorphous materials are available [83]. However their validity is limited to a simplistic and static metallic glass structures. Therefore incorporating these models into a dynamically changing amorphous structure to explain resistance changes is a subject for further work, and has not been considered here. As such, the model presented here defines the barrier to electron transport to be due to potential energy barriers produced by the interaction of inter-atomic potentials within the material, over which electrons must pass in order to allow current flow. Therefore evaluation of how these potential energy barriers evolve with different structural states during shear band formation will give a first approximation to how structure changes relate to resistance changes in SBESD events.

To construct a valid resistivity vs. structure model based around the evolution of inter-atomic potentials for the description of shear banding behaviour, certain assumptions have been made about structural changes that occur within the shear bands themselves. The first assumption is that structural homogeneity of the material within the shear band is retained at all times. In this case the entire shear band can be described to be in a single structural state at any given time during the shear banding process. If there is a level of segregation in the shear band structure, multiple models may have to be used. The assumption of uniformity is justified due to the 10nm thickness of shear band being an insignificant distance over which a structure would be able to homogenise. The sampling of the SBESD system is also likely to be insufficient to capture any inhomogeneity, further strengthening the justification for this assumption.

A second assumption concerns material in the vicinity surrounding a shear band. This assumes that only material within the shear band evolves during shear banding and subsequently affects current flow from a structural change point of view. In reality, the energies reported to be released from shear banding events with the applied stresses may also change the surrounding material structure both during and post shear banding. Modelling of this effect could explain any potential SBESD events, which in the framework of the entropy require shear band structures that are infeasible to explain the observed signals. However given this is a first approximation, with which other unknown factors need to be addressed, this is once again suggested as a topic for further work.

Now a framework has been defined for structural changes due to shear banding details surrounding the model construction can be discussed. For a first approximation, a 2 dimensional atomic box model and a pseudo-one dimensional thermal expansion model have been used to relate SBESD events to structural change. Both of these models relate structural changes to resistance results through the evaluation of how inter-atomic potentials effect the work required to pass charge electrons through a metallic structure. To avoid confusion, the details surrounding the individual models set-ups are covered in separate sections below, with results from both models being compared and discussed later.

Analysis of SBESD results: Modelling through atomic box simulations

The atomic box model is a pseudo-Monte-Carlo based model. An general algorithm defining the model's logic path is defined in Fig.(7.24) for clarity.

The atomic box model is constructed from 20 2 dimensional square atomic boxes with areas of 1nm^2 . Each box is populated with atoms through a Monte Carlo approach, whereby an atom is selected at random based on the composition of the BMG being considered and a weighted statistical selection module written for this work. This means for the composition of $\text{Zr}_{50}\text{Cu}_{40}\text{Al}_{10}$ every 10 atoms chosen to populate a box will have on average 5 zirconium atoms, 4 copper atoms and 1 aluminium atom. For each atom chosen, a position is randomly assigned and checked against

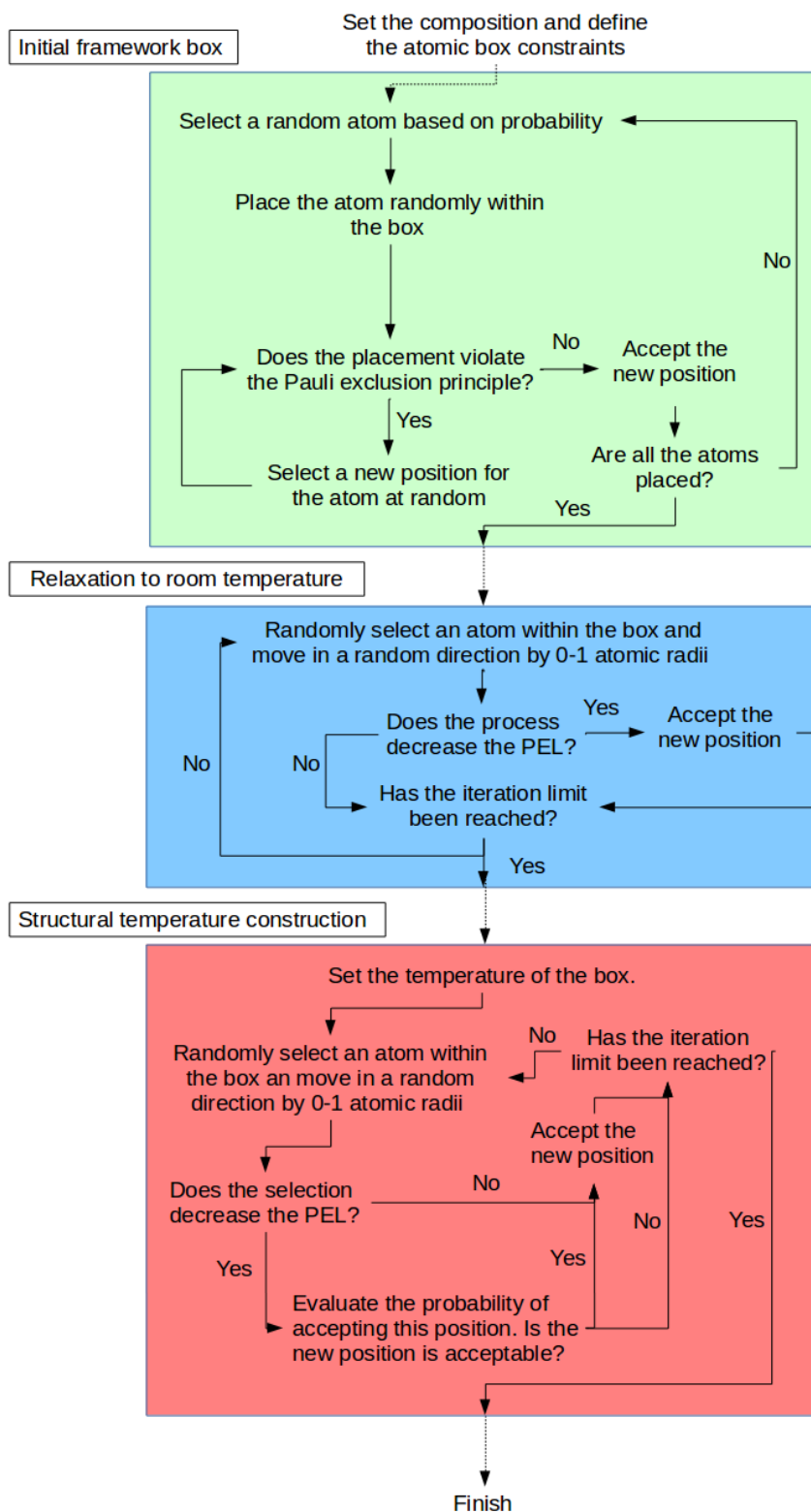


Figure 7.24: Schematic identifying the general algorithm used to produce atomic box with a given structural state.

positions of other atoms within the box such that no significant overlap of atoms occurs in the initial box set-up. The criteria for this overlap splits this model into a further 2 sub-model approaches, defined as the hard sphere (HS) model and a soft-hard sphere (SHS) model:

- The HS model ensures that no 2 atoms ever lie within a distance of less than the sum of the radii of the atoms ($\sum \sigma_r$) (σ_r is defined by the distance from the atoms center whereby the atomic potential is 0).
- The SHS model allows for the distance between the centre of atoms to be such that the inter atomic distance is always greater than the largest atom radius of any given inter-atomic pair.

These separation criteria ensures no atoms are placed at separations where the Pauli exclusion principle would be violated. Atoms found to violate the criteria were reassigned new positions and re-evaluated until the criteria were met. Each atom is placed sequentially in each box for both models until 40 atoms populate the boxes of the SHS model, and 20 atoms populate the boxes of the HS model. These are termed the initial framework boxes.

The initial framework boxes undergo a relaxation process for both HS and SHS models to reduce the agitated state of the atoms present from their random initial distribution, and form the atomic boxes from which potential shear band structures can be generated. The relaxation is performed based on the change in the potential energy state of the box when an atom is moved from one position to another. Calculation of this value requires knowledge of the potential energy distribution of all the atoms within the box.

The potential energy produced by each atom in the box is calculated through a modified Lennard-Jones 6-12 potential (LJ 6-12). Whilst the Lennard-Jones potential is only exact for describing the Van der Waals inter atomic forces in inert gas crystals at 0K and 0Pa [92], a modified LJ 6-12 potential is considered suitable for use in the models presented here [64, 253]. This potential is outlined in Fig.(7.25a) and described by Eq.(7.13). The main features of the potential defined and justified for use in the presented models as follows:

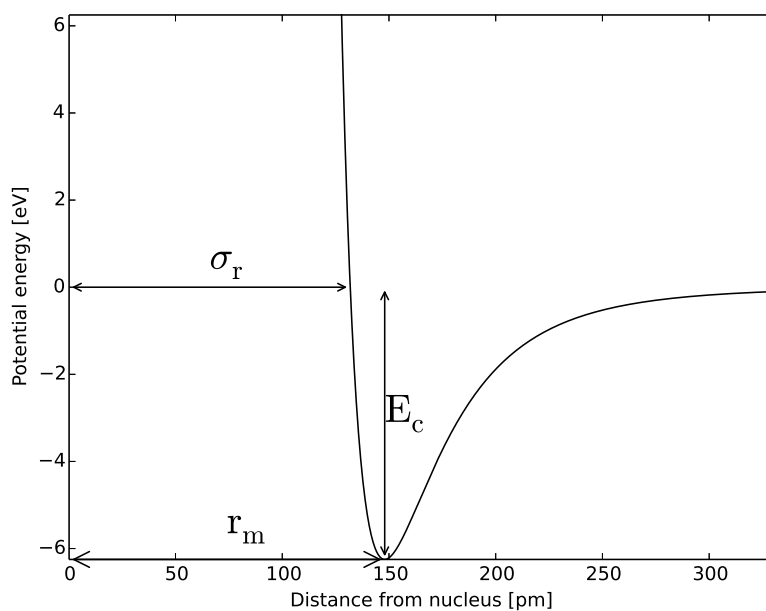
$$V(r) = \begin{cases} E_c \left(\left[\frac{r_m}{r} \right]^{12} - \left[\frac{r_m}{r} \right]^6 \right) & \text{while } r > \sigma_r \\ \infty, & \text{otherwise} \end{cases} \quad (7.13)$$

- Maximum depth of the potential well: E_c

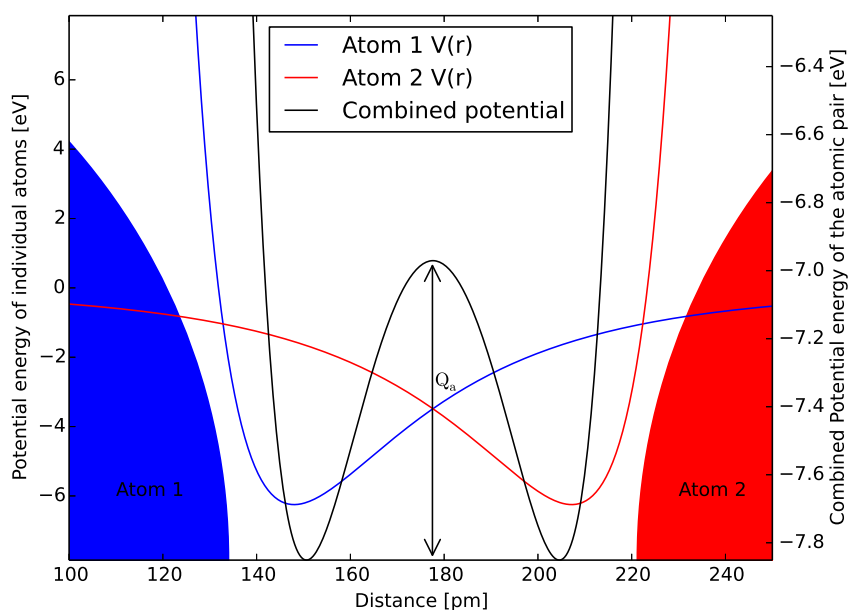
This value is defined as the energy difference between the atom in a gaseous and *crystalline* state, but the bond itself is of the same metallic nature as in a glass so the strengths are comparable. Between the glass and crystalline states, the local bond distances are different; crystalline structures show poorer packing efficiencies compared to the glassy structure over the scale of tens of atoms [5]. Therefore binding energies of glassy materials over local volumes are actually higher than those for the crystalline state. This being said, the local glass binding energies must be similar and proportional to E_c . Considering that the model employed here uses relative changes in structure rather than absolute ones any errors from an underestimation of E_c are likely to be minimal.

- Radius of the atom: σ_r

The definition of atomic radius used in this model is one based on the potential itself. At this distance, the potential energy is defined as zero, with distances below σ_r reflecting a violent increase in the potential energy according to Pauli's exclusion principle.



(a) The modified LJ 6-12 potential for an atom of zirconium where $E_c = 6.25\text{eV}$ and $r_m = 148\text{pm}$.



(b) The interaction of 2 modified LJ 6-12 potentials zirconium for atoms potential producing a potential energy barrier over which a chard move overcome in order to flow.

Figure 7.25: Schematic of the modified LJ 6-12 utilised in the models presented here, and the energy barriers that they form to resist the flow of electrical current.

- Position of the potential minima: r_m

The covalent radius of an atom is used as a first approximation in the described models to define the radial distance of an atom's potential minima. In reality, this distance will vary depending on the chemical environment and packing efficiency of the material. However this work observes that the difference between r_m calculated through the summation of covalent radii, and the value r_m observed through the PDF for a relaxed $Zr_{50}Cu_{40}Al_{10}$ BMG [254] are in good agreement (see Tab.(7.7)). This implies that the covalent radii are satisfactory for use as values for r_m in the models employed here.

Based on the above description of the modified LJ 6-12 potential, it is believed to be satisfactory for use in a first approximation to how structure affects resistance. It is worth noting other potentials are available, such as the Hard sphere, Morse or Dzugotov potentials [5] which may improve on this approximation, but these are not addressed here.

Now the potentials for the atoms within the box have been defined, the relaxation module can be described. In this process, an atom from the initial framework box is chosen at random and removed from the box entirely. The energy required to then take the removed atom from infinity and place it back in its original position is then evaluated as the sum of all the potentials of all the atoms remaining within the box acting on the removed atom's old position; calculated through Eq.(7.14). A new atomic position is then assigned by defining a position at random that is within one atomic diameter of the former position. The validity of this position is evaluated through the same algorithm defined for the formation of the initial framework box. Once a valid atomic jump has been identified, the energy required to bring an atom from infinity to the new position is evaluated as the sum of the potentials of all the atoms remaining within the box acting on the new position, defined by Eq.(7.15). The difference between these 2 energy values (ΔV) defines the favourability and driving force for this relaxation event to occur. The entire process is shown schematically in Fig.(7.26).

$$V_{old} = \sum_{n=1}^{N^{of\ atoms}} V(r) \quad (7.14)$$

$$V_{new} = \sum_{n=1}^{N^{of\ atoms}} V(r) \quad (7.15)$$

$$\Delta V = V_{old} - V_{new} \quad (7.16)$$

If ΔV is negative, then the atomic jump is energetically favourable, and is therefore accepted. If a positive ΔV is observed, then the relaxation event would serve to increase the potential energy of the all the atoms within the box, making it an unfavourable relaxation event. Whether this relaxation event state is accommodated by the system therefore depends on the energy of the environment in which the atoms lie. If the energy of environment is high enough compared to the increase in the energy of the box, then the position will be accepted based on a statistical approach. This is calculated based on random number generation and statistical weighting of the box condition defined as follows:

$$\text{if } P > \exp\left[\frac{-\Delta V}{(K_b T)}\right] \text{ where } P = 0 \dots 1 \quad (7.17)$$

If the value of P is greater than the value determined by the Boltzmann energy distribution

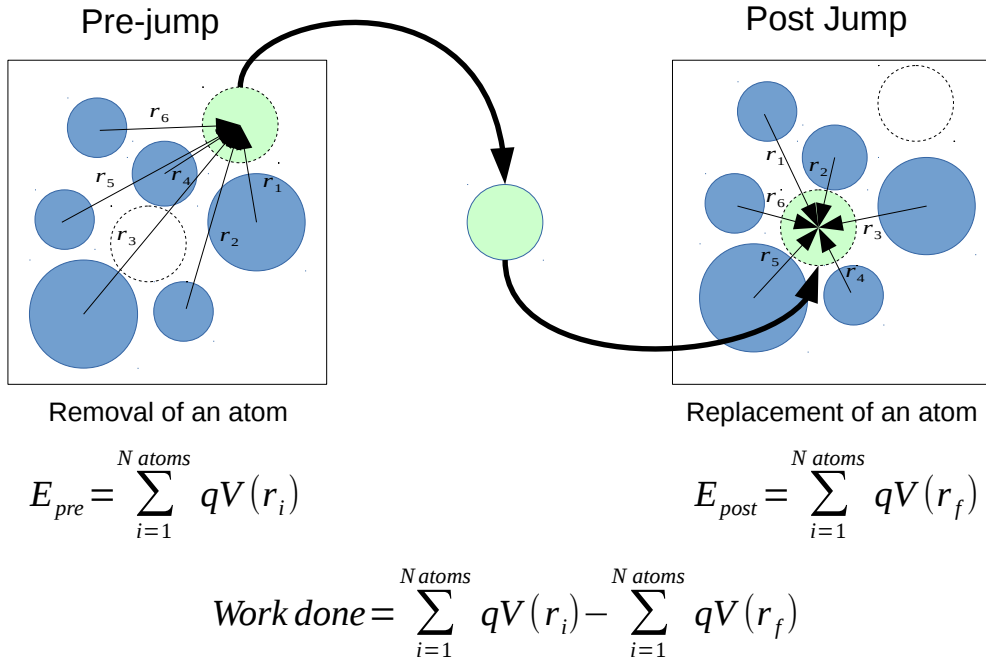


Figure 7.26: Schematic depiction of a relaxation event within the atomic box model and how the energy difference between the pre and post relaxation state is calculated.

term defined above, then the new position of the atom will be accepted, and vice versa. The consequence of this is if the energy (represented by temperature) of the system is too low, or ΔV is too high, $\exp\left[\frac{-\Delta V}{(K_b T)}\right] \rightarrow 0$, an acceptable value of P will not be obtained. In the opposing case, $\exp\left[\frac{-\Delta V}{(K_b T)}\right] \rightarrow 1$, therefore at high temperatures the accommodation of unfavourable relaxation events is more likely.

The relaxation process described above is iterated over 10,000 times per box for both HS and SHS models at room temperature (298K) to give relaxed structures from which shear band-like structures can be made. Fig.(7.24) shows a flow diagram for this process for clarity.

Once the relaxed structures are calculated, different structural states for BMGs can be produced by relaxing the atomic box structure through the algorithm defined above to any given temperature value. In addition to the relaxation algorithm, the atomic box dimensions were also adjusted to the test temperature being considered. Room temperature relaxations had box side lengths fixed to $L_{box} = 1\text{nm}$, whilst box dimensions for relaxation procedures to other temperatures defined through the thermal expansion equation:

$$L_{box} = 1\text{nm} \times (1 + \alpha_x(T - 298)) \quad (7.18)$$

Adjustment of the box dimensions provides a rudimentary mechanism for accommodating free volume within the BMG structure for more open structures. Simulations performed without this condition found that at low temperatures, atoms were observed to cluster together (as expected), but at higher temperatures the constraints of the atomic box meant that atomic structures could not evolve past a certain temperature value, which depended on the number of atoms per box,

initial box dimensions and whether the HS or SHS model was employed.

Structures were generated for both HS and SHS models from 298K to 50,000K at intervals of 100K with 10,000 iterations per relaxation condition per box. An upper temperature limit of 50,000K, whilst an overestimate to the potential temperature that could be generated through shear banding, provides a full range of structural states with which to relate observed SBESD signals to. Each temperature value considered the structural state of the box generated from the previous temperature condition in order to make full relaxation most probable. Results demonstrate that the system reaches full relaxation conditions prior to performing any significant analysis.

Once structures for a given temperature over all 20 atomic boxes have been generated, pair potentials across every single possible pair of atoms within each box were calculated by summing the potential functions of pairs of atoms. Calculated pair potentials were then listed in order of atomic separation for every single atom in the box for every single central atom-neighbouring atom pair combination. This ranking defines pair potentials for every possible nearest, second nearest, third nearest, . . . n^{th} nearest atom pairing for all atoms within the box. This ordering will be termed as ‘separation ordering’, and is required to identify the work required to pass an electron through the pair potentials to facilitate current flow within across the atomic box in terms of the model presented here.

Calculations of the resistance to current flow come from considerations of the pair potentials of the atoms within the box. Fig.(7.25b) shows a schematic of 2 atoms separated by a distance greater than the sum of the respective covalent radii. It is observed that for these cases, the pair potentials produce a potential energy peak between the atoms, which increases in height to a maximum value of E_c with respect to atomic separation. This peak acts as a potential energy barrier to electron transfer between that atoms. From the definition of resistance utilised in this model, changes in this peak height ($= Q_a$) are taken as the source of the resistance change in SBESD events. It is noted that for atoms spaced over distances less than the covalent radii, no peak is produced. This describes the case whereby charge carriers to flow from one atom to another through a single common, uninterrupted potential well, thereby contributing nothing to the change in material resistance based on the definitions utilised here. To that end, pairs found to obey this behaviour were neglected from further analysis.

Potential energy barrier heights of pair potentials, Q_a , were calculated by the average difference in the potential barrier peak energy to the energies at the foot of the peak, as outlined in Fig.(7.25b). Q_a values were calculated for every separation order for all atoms over all boxes and were averaged with respect to separation order and temperature state to give an average Q_a value for nearest, second nearest, etc. atoms across for every structural state considered. This is the basis behind which SBESD events are linked to structural changes in a BMG during deformation.

Analysis of SBESD results: Modelling through atomic Thermal expansion coefficient

Another approach used here to model structure changes in BMGs was to consider only pairs of nearest neighbour atoms independently from the surrounding amorphous structure. The potential, and therefore the potential energy barrier to current flow, is still evaluated as outlined in the atomic box simulations, however the inter-atomic distances are for nearest neighbour atoms through the use of the thermal expansion equation:

$$L = L_o(1 + \alpha_x \Delta T) \quad (7.19)$$

The use of this equation requires a detailed knowledge of nearest neighbour distances of atoms of a BMG in the relaxed state. This information can be taken from a radial distribution function

| Atomic Pairs | Sum of covalent radii [\AA] | Pair separations [\AA] | % difference |
|--------------|--|-----------------------------------|--------------|
| Zr-Zr | 2.96 | 3.23 | 8.36 % |
| Cu-Cu | 2.76 | 2.65 | -4.15 % |
| Al-Al | 2.36 | 2.86 | 17.48 % |
| Zr-Cu | 2.86 | 2.86 | 0.00 % |
| Cu-Al | 2.56 | 2.69 | 4.83 % |
| Zr-Al | 2.66 | 3.05 | 12.79 % |

Table 7.7: The comparison of inter-atomic distances determined through the sum of the covalent radii and through measurement of a radial distribution function (data from [254]).

(RDF) for a given metallic glass in its relaxed state. This information is not required in the atomic box modelling, as these inter-atomic distances were determined as a consequence of the relaxation algorithm in the model.

High power XRD or neutron scattering experiments are required to measure the RDF of a given BMG. This has not been performed as part of the work conducted here, however Matsubara et al. has published an RDF for the $\text{Zr}_{50}\text{Cu}_{40}\text{Al}_{10}$ BMG alloy [254], the alloy which returned the strongest and most repeatable SBESD events during testing. These results were used as a basis for defining the initial state of this alloy (equivalent to the L_o term for atomic pairs in Eq.(7.19)). Evaluation of other alloy signals through this method ideally requires RDFs of that alloy in its relaxed state, which are not always available in quantitative form. However Tab.(7.7) shows that the sum of the covalent radii provides a good approximation for atomic pairs in $\text{Zr}_{50}\text{Cu}_{40}\text{Al}_{10}$, thereby allowing use of the sum of covalent radii as a substitute for the RDF if the RDF is not available. This work only reports the findings of the $\text{Zr}_{50}\text{Cu}_{40}\text{Al}_{10}$ alloy through this method with the relaxed state based on the published RDF by Matsubara et al. [254]. However the application of the above methodology is suggested for further work.

The thermal expansion model utilised 100 atomic pairs per structure evaluation, whose atom identities were defined through the statistical weighting defined by the composition of the material. Structural states were explored with the same temperature range defined for the atomic box model; from 298K to 50,000K over 100K intervals. The inter-atomic separations are defined through the RDF published by Matsubara et al. [254] and Eq.(7.19) for each temperature condition investigated.

The interaction between the inter-atomic potentials, and subsequently the potential energy barrier heights were evaluated through the same methodology defined for the atomic box model (see the potential calculations in the atomic box model for further details) for each atomic pair at each temperature condition. The potential energy barrier heights and inter-atomic separations were then averaged over the 100 atomic pairs for every temperature condition to give an average bulk response of the potential energy barrier height and inter-atomic separation change with respect to the structure change.

It is important to note that this model is realistically only accurate for describing structures for temperature ranges below T_g , because the model is based on changes in inter-atomic spacing from thermal expansion arguments and cannot describe a permanent structural change. This being said, the model does produce a range of inter-atomic distance values, over which different potentials and different potential barrier energies can be described. Therefore using the model to categorise the structural change rather than measure absolute temperatures of the structure may provide a means to relate structural changes to changes in resistance values.

Analysis of SBESD results: Results analysis through Entropic process

Regardless of the model utilised in evaluating the entropic approach, all of the results are related to the SBESD event data through the same general approach, defined by the potential energy barrier heights calculated for each model and the resistance statement upon which these models are based.

The SBESD set-up has been designed to measure relative changes in resistance. Therefore all interpretations of the structural change require a similar treatment; relating relative changes in structural state to relative changes in measured resistance. This relationship can be expressed as:

$$\frac{R(T)}{R(T_{=298K})} = K_Q = \frac{Q(T)}{Q(T_{=298K})}. \quad (7.20)$$

This is valid for all the modelling approaches described. The value of resistance in the relaxed state ($R(T_{=298K})$) is the first measurement prior to the signal being observed. For some signals, such as the S signals, this is a clearly definable value, set to the SBESD resistance value prior to the signal breaching the 3σ value defining the experimental noise. Other signals, such as the W signals require a more subtle approach to evaluate $R(T_{=298K})$. In these cases the value of $R(T_{=298K})$ is evaluated as the average SBESD value of $R(T_{=298K})$ for a small interval of data prior to the SBESD event. This is important, as the base line resistance value of W signals varies significantly compared to the SBESD signal itself. Therefore the normalising $R(T_{=298K})$ value for W signals incorporates further uncertainty into the already weak signal. As such analysis of these signals needs to be treated with care.

For the atomic box case, the evaluation of the potential energy barrier to current flow (Q_a) in the relaxed state ($Q(T_{=298K})$) and the state at any other temperature depends on the number of atoms considered to be involved with the conduction process. It is at this point we make an important distinction between the nearest neighbour atoms and nearest atom neighbours. Nearest neighbour atoms are atoms that are considered to be in direct contact with a given central atom, whilst a nearest atom neighbour is simply a neighbouring atom which is nearest to the atom in question. Fig.(7.27) clarifies the difference between these two cases.

In the case of the atomic box model, the 2 dimensional nature of the model means that the nearest atom neighbour approach is the best way to evaluate neighbouring-atom based behaviours. Using the nearest neighbour atom approach introduces misleading inter-atomic separation values, as the box models place atoms a single plane, which neglects a degree of freedom required for accurate descriptions of amorphous structures. This effect could be corrected for though manipulation of the inter-atomic potential strengths, such that the atomic box models are constructed with inter-atomic potentials from atoms outside the plane of consideration permeating into the plane of the model. However, the nearest atom neighbours approach circumvents the issues surrounding the 2 dimensionality of this model.

Using the nearest atom neighbour treatment, resistance changes due to structural change can be categorised as difference in Q_a between the relaxed and agitated box states ($= \Delta Q_a$). Individual Q_a values for the two box models are evaluated through the average of the Q_a values calculated between only the nearest atom neighbours for all possible nearest atom neighbours over all atomic boxes for a given structural state.

In the case of the thermal expansion model, the 3 dimensional structure is accounted for through the RDF, meaning the nearest neighbouring atom approach is naturally described by the inter-atomic spacing predicted by Eq.(7.19). However, as described earlier, it is recognised that

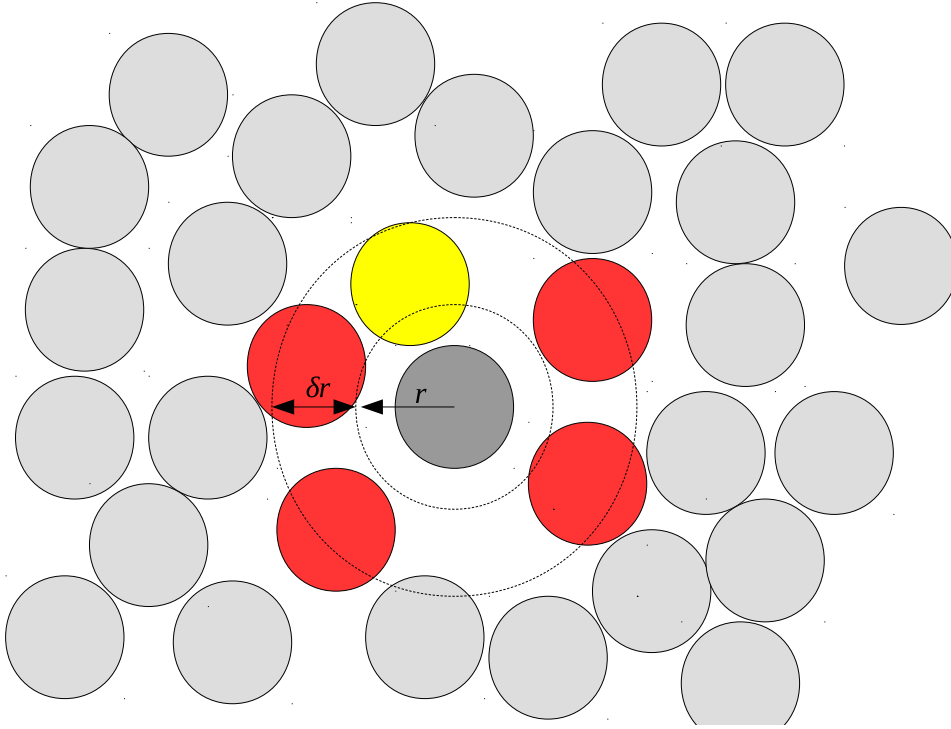


Figure 7.27: A 2 dimensional schematic highlighting the nearest atom neighbour (yellow) and the nearest neighbouring atoms (red and yellow) to a given central atom.

changes in the RDF brought about by this model will not reflect true structural changes for a given temperature during a shear banding process. It is therefore once again stressed that use of this model for evaluating structure change is limited only to the categorisation and comparison of structural change and how this relates to observed SBESD events.

It is interesting to note that both atomic box and thermal expansion models have limitations to the maximum resistivity as the maximum potential barrier height is limited to the value E_c , at which point the interaction between the atomic potentials becomes insignificant, such that charge carriers have to overcome the entire potential well depth of a single atom in order facilitate current flow. This distance is commonly referred to as the cut-off distance [255], and is defined numerically as

$$\sigma_c = 2.5\sigma = \frac{2.5r_m}{2^{1/6}}. \quad (7.21)$$

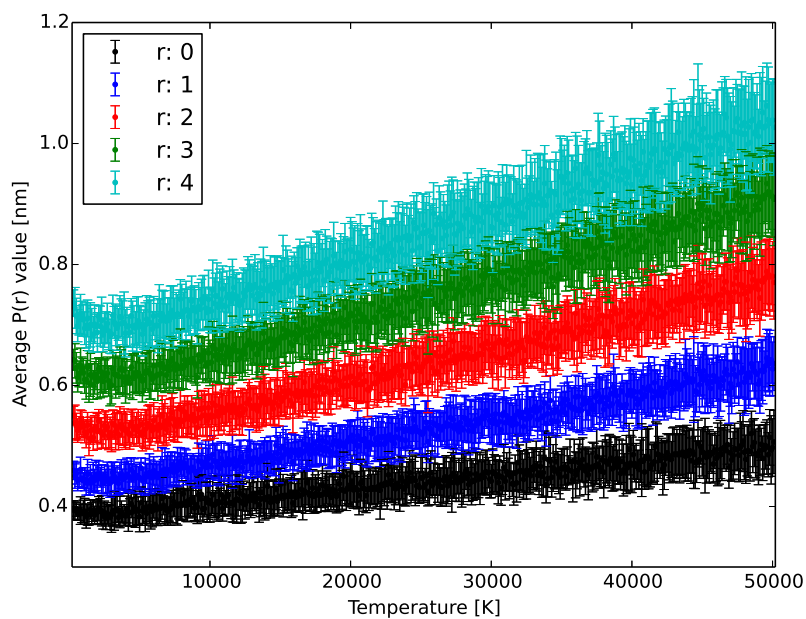
Therefore, based on the modelling approaches outlined thus far, the maximum change in resistance explicable by the models is limited to

$$\frac{R(T)}{R(T=298K)} = K_Q = \frac{E_c}{Q(T=298K)}. \quad (7.22)$$

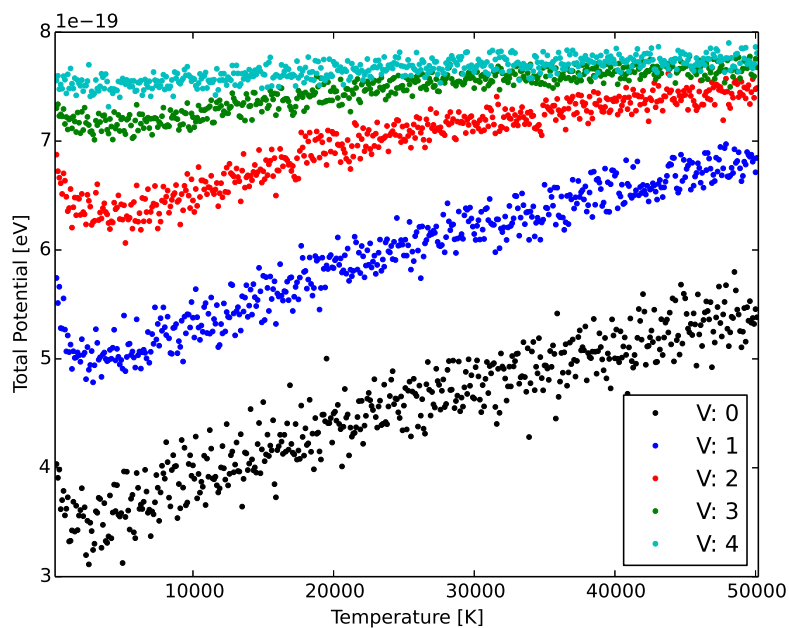
This provides a mathematical limitation to resistance change values explicable through these models, albeit one that, with barely interacting potentials, is a poor description of any BMG structure.

SBESD results evaluated through Entropic considerations

Analysis of SBESD events through the methodology highlighted in Sec.(7.5.2) requires modelling of structures such that $\frac{R(T)}{R(298K)}$ measurements can be related to a $\frac{Q_a(T)}{Q_a(298K)}$ estimations, and subsequently structural temperatures of the material during a shear band process. To that end, Fig.(7.28), Fig.(7.29) and Fig.(7.30) show the correlation between $\frac{Q_a(T)}{Q_a(298K)}$ and inter-atomic distances with respect to structural temperature states derived from the HS and SHS and thermal expansion models respectively for the $Zr_{50}Cu_{40}Al_{10}$ alloy. These relationships have been determined for all alloys that have demonstrated SBESD events, however $Zr_{50}Cu_{40}Al_{10}$ has been chosen for demonstration purposes in this section due to the reproducibility of S SBESD events observed in this alloy.



(a) Inter-atomic separation with respect to structural temperature evaluated by the HS model for several nearest atom neighbour considerations.



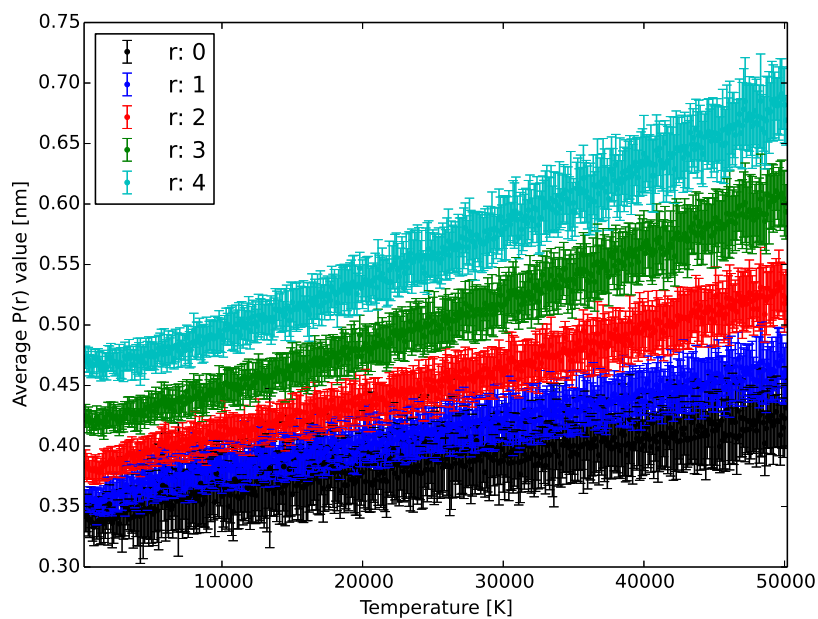
(b) Potential energy barrier heights with respect to structural temperature evaluated by the HS model for several nearest atom neighbour considerations.

Figure 7.28: Potential energy barrier and inter-atomic distance relationships with respect to temperature for the hard atomic box model.

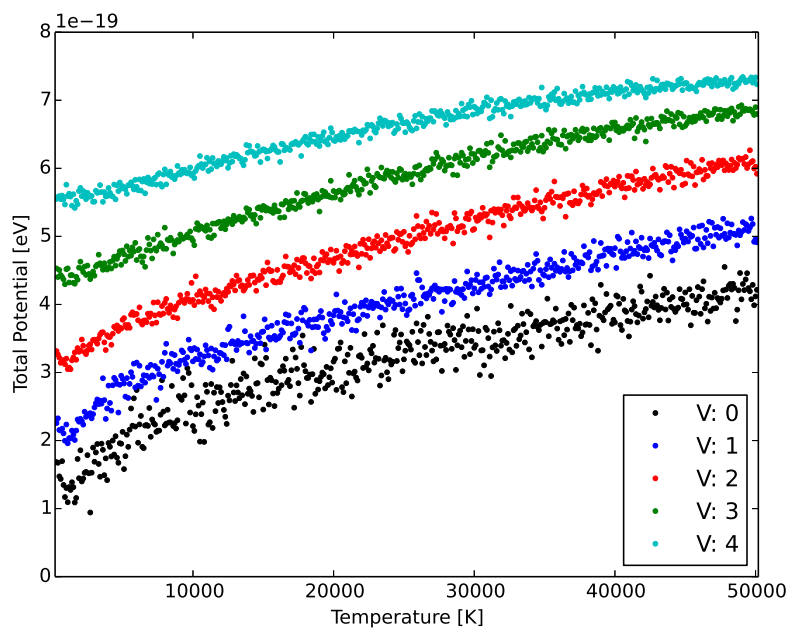
Fig.(7.28), Fig.(7.29) and Fig.(7.30) show the general trends expected for all 3 models, demonstrating an increase in inter-atomic spacing and potential energy barrier heights with respect to temperature. However differences in the relationship strengths and across the different models have significant implications regarding the predicted behaviour of shear bands in BMGs.

HS and SHS models show similar generic trends as they are based on the same calculations. However resistance changes are observed to be systematically lower for the SHS model than the HS model, because the SHS accommodates closer packing of atoms than the HS model, and therefore a more tightly bound structure which requires higher energies to break down. The Q_a values reflect this, with the SHS models producing lower Q_a values than the HS model across all evaluated temperatures. The difference in these predicted behaviours has a significant affect on the evaluation of SBESD events. Recalling there are limits on the maximum achievable Q_a values set when the distance between nearest atoms approaches σ_c , then it can be seen that the SHS model with a more densely packed structure at the rest state is capable of describing a greater range of resistance changes for a given structural temperature range than the HS model. This observation identifies a weakness in the models used, being that the relationship between potential and resistance utilised is dependent on an incomplete description of electron transport theory, and recommended for further work.

Another interesting feature common to HS and SHS models appears in the low temperature condition. Both models appear to undergo relaxation steps beyond that performed for the initial room temperature relaxed box state. One explanation for such an observation could be that the boxes have not been fully relaxed from the initial framework boxes. To determine if this is the case, the relaxation behaviour of the atomic boxes whilst treated with the relaxation module were monitored for every single atomic relaxation event considered. Fig.(7.31) shows these observations, plotting for a given number of relaxation events, the number of successful energetically favourable atomic jumps, and the number successful energetically unfavourable atomic jumps accommodated due to the structural temperature condition of the box. For the initial framework box being relaxed to a room temperature state, Fig.(7.31) clearly shows that the iterations required to reach an equilibrium structural state (i.e. when the number of favourable and unfavourable jumps are approximately equal) are below 1000 iterations; far below the number of iterations performed for a given box at any temperature state. This, coupled with the fact that the calculation of each structure uses the temperature condition previous to the one being considered as a seed structure, indicates that the relaxation module performs more than enough iterations per structural condition to generate a fully relaxed state. Therefore the low temperature feature must be caused by a phenomenon in the model, and not by poor parameter selection.



(a) Inter-atomic separation with respect to structural temperature evaluated by the SHS model for several nearest atom neighbour considerations.



(b) Potential energy barrier heights with respect to structural temperature evaluated by the SHS model for several nearest atom neighbour considerations.

Figure 7.29: Potential energy barrier and inter-atomic distance relationships with respect to temperature for the soft hard atomic box model.

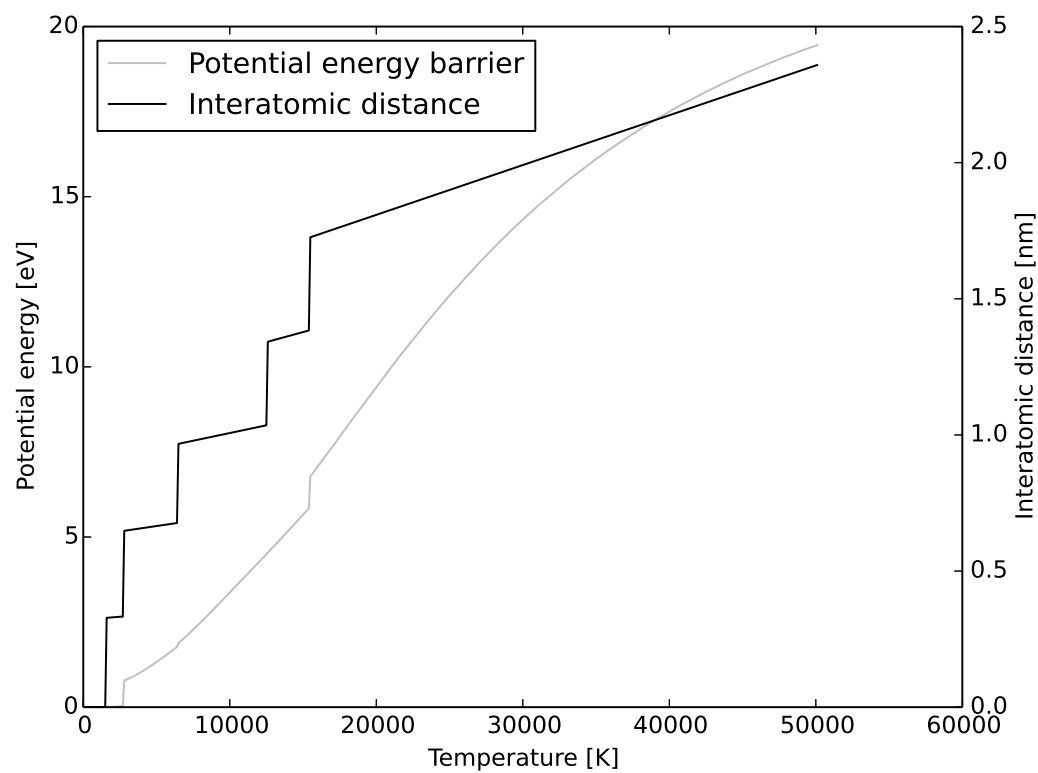


Figure 7.30: Potential energy barrier heights and inter-atomic separation changes with respect to structural temperatures evaluated by the thermal expansion model.

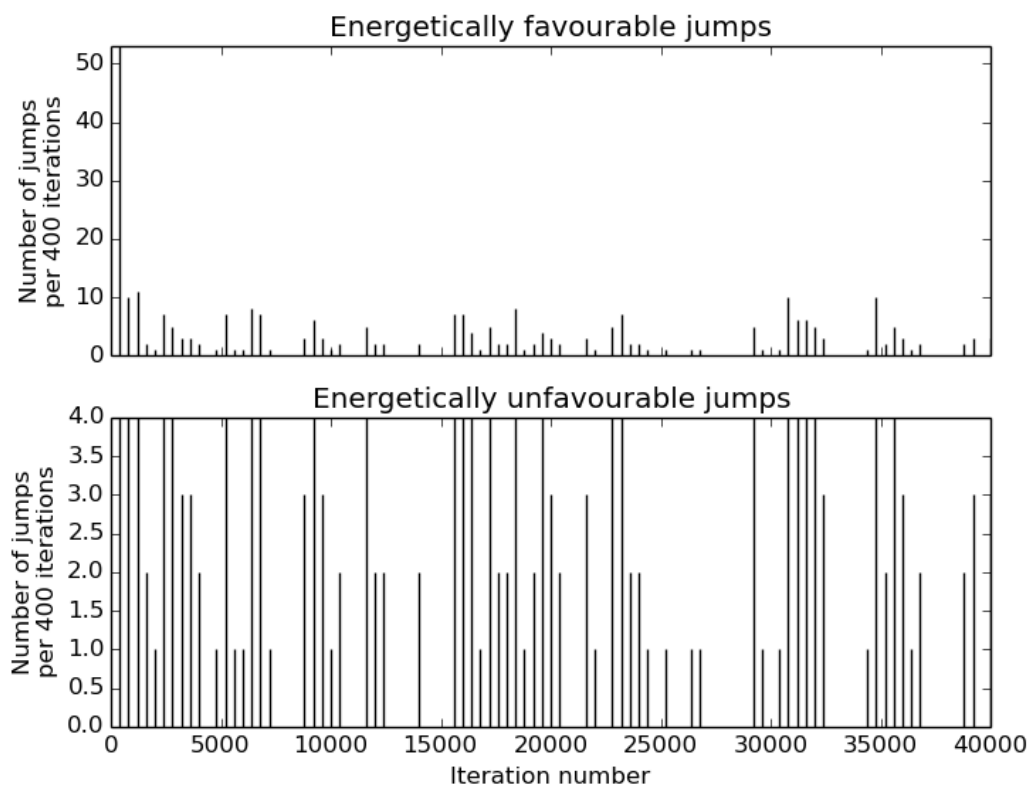


Figure 7.31: Favourable and unfavourable relaxation events for SHS the atomic box model form the initial framework box to the room temperature relaxed state.

An interesting explanation for the relaxation feature at low temperatures is relatable to a real quenching effect which may have arisen from the algorithm used for calculating the relaxed structures. In relaxing the atomic boxes from the initial framework box state to the room temperature states, the relaxation module only considers the room temperature condition. This is the equivalent of taking a high energy structural state, such as a melt, and instantaneously quenching it to room temperature conditions. If this were to occur in reality, the amorphous structure formed by such a process will be in an agitated state, rather than a relaxed one, thus giving the potential for further relaxation to occur upon heating. This may be the process being simulated here.

If this is case, then the relaxation algorithm is responsible for the feature. The relaxation module has both energetic and kinetic processes inherently built into the algorithm. Energetic processes are accommodated by the evaluation of energy changes during individual atomic jumps, whilst kinetic process are accommodated by each atomic jump per relaxation event to distances of no more that one atomic diameter. Based on these facts, a situation described by Fig.(7.32) and the following can be envisaged:

- The room temperature atomic box structure is formed though relaxing the structure from the initial framework box to a room temperature state.
- During the relaxation process, a few atoms find a stable configuration with respect to each other. These atoms surround a further atom which is in a high energy state. On the other side of the stable atoms exists a site of low energy with which the high energy atom is energetically driven to move towards. However the distance the atom has to jump is greater

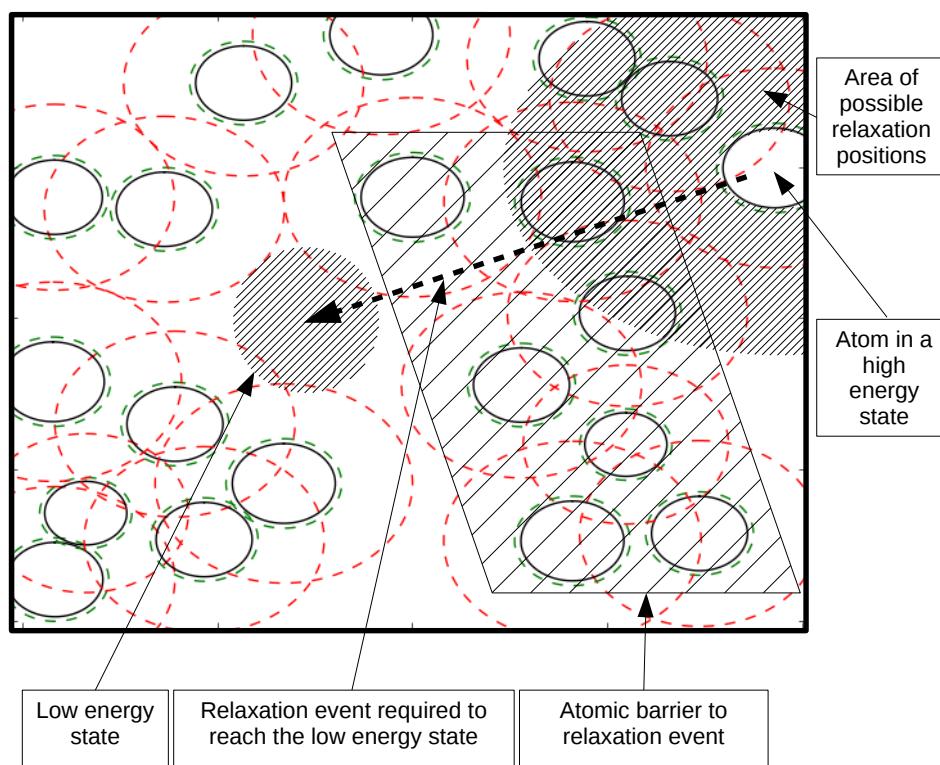


Figure 7.32: Potential explanation for the presence of the low temperature relaxation features in Fig.(7.28) and Fig.(7.29).

than 1 atomic diameter. No significantly lower energy jump sites exist between the unstable high energy atom and the cluster of stable low energy atoms. The structure is therefore considered ‘relaxed’ with high energy state atoms trapped in the atomic box.

- The temperature of the box is increased and relaxed to produce a new structural state. The temperature considerations increase further and further until there is enough energy to break up stable atomic cluster, thereby freeing the high energy atom to relax to the low energy state.
- The result is a structure that appears to lower in its overall energy state with temperature until high energy atoms have been released to low energy sites. After this all atoms tend to move on average from low energy sites to higher energy sites during each temperature consideration.

It is interesting to note that this quench and relaxation process ceases to occur at around 500K for both box models, approximately $0.8T_g$ of the alloy demonstrated. This is the condition commonly required for homogeneous plastic flow to occur within a BMG and has also been defined as the minimum temperature state for the flow behaviour required for shear band propagation (not initiation) [247]. Whilst this is not conclusive proof that the atomic box models correctly predict the structures formed during quenching as well as relaxation, the observation of the effect is good evidence that the model is satisfactory.

In addition to the atomic box model, the thermal expansion model provides further tool to consider in the analysis of SBESD events. Fig.(7.30) shows the result of the thermal expansion coefficient response for $Zr_{50}Cu_{40}Al_{10}$. Changes in inter-atomic distance, and subsequently the change in the inter-atomic potential, reflect a more (though not completely) linear dependence on temperature than that predicted by the atomic box model due to the linear dependence of inter-atomic distance with temperature from Eq.(7.19). However it is clear that there are multiple disconnects in the linear relationship throughout the temperature range considered. The source of the fractured behaviour is due to the conditional analysis of the pair potentials and the absolute values of inter-atomic distances derived from Eq.(7.19). For a given temperature condition, the thermal expansion model assumes that all atomic pairs of a given chemistry have exactly the same potentials and inter-atomic separation values. Recalling from the description of the source of resistance changes utilised for these models, only atom pairs separated by distances of more than the sum of the covalent radii are considered to contribute a change in the measured resistance. Therefore, when a temperature condition is considered such that a set of atomic pairs that were previously neglected can now contribute to resistance, an influx of new resistance contributors are suddenly available. This creates the disconnects observed in Fig.(7.30), which are clearly a manifestation of a weakness in the model, not a real observable effect.

Despite the issues surrounding the validity of the model highlighted earlier (relating an elastic effect to a plastic process), and the disconnect issues described above, the thermal expansion model provides a means of relating SBESD signals to a greater range of structural states with reduced error compared to the atomic box model approaches. This is due to the quasi-continuous nature with which potential energy barrier heights of a given alloy are described by a single temperature variable, (due to a lack of spread in the described inter-atomic potentials for a given temperature), and the use of the RDF to describe the inter-atomic separation values in the rest state (values which are lower than that predicted by both atomic box models) allowing sampling of a greater range of potential energy barrier heights. Derived structural states are determined by the temperature variable in Eq.(7.19), which does not reflect the actual physical temperature state required to

produce a BMG structure. This temperature variable serves to describe a particular structural state with a given Q_a and should be considered to be more of a structural index rather than a temperature value. This being said, the structural description afforded by this model is poor compared to the atomic box model, with no consideration given to the environment immediately beyond the atomic pair under scrutiny. As such, factors that rely on the immediate structural environment, such as free volume, cannot be realised through this model in its current form.

To summarise, whilst all the models qualitatively produce behaviours that represent the expected structural dependences of inter-atomic potentials, there are significant differences between the quantitative descriptions in these behaviours depending on the modelling approach considered, and how the model is conducted. Improvements to these models requires absolute details surrounding how inter-atomic potentials of the derived structures affects the current carrying capability of the material. In addition, independent verification regarding the structural states predicted by each modelling approach would also serve to improve the predictions made by the models presented here. Therefore, whilst treatment of the SBESD results with these models requires caution, the models presented here are believed to be capable of providing a first approximation to how shear band processes affect resistance behaviour from a structural change point of view.

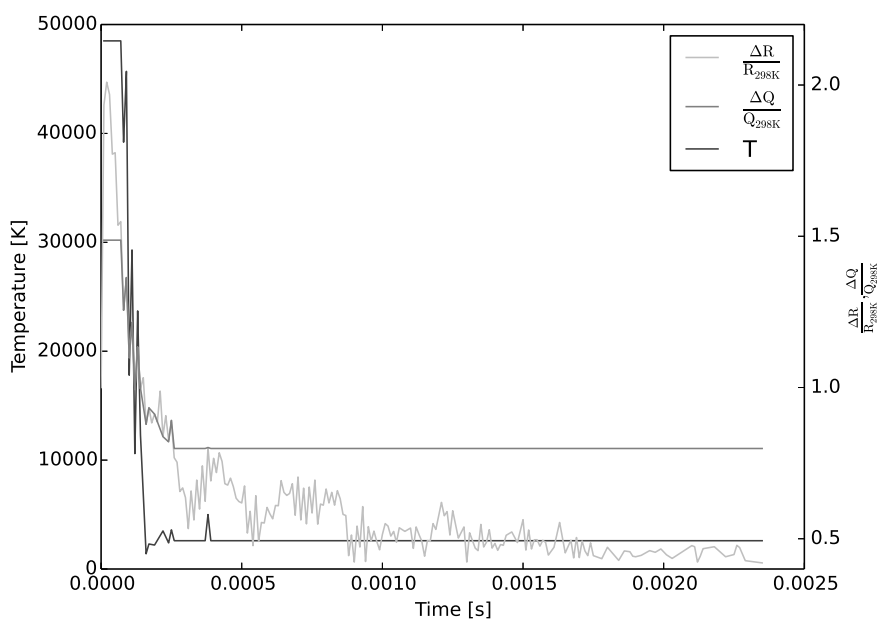
7.5.3 Application of entropic models on observed SBESD events.

The models outlined in Sec.(7.5.2) describe how simplified BMG structures are assumed to evolve with temperature, and how the derived structures have been assumed to influence resistance behaviour. To that end, the results from all modelling approaches have been applied to measured SBESD signals in order to obtain structural change information during a SBESD compression event. It is stressed that findings from these models are a first approximation and warrant further study. Taking the uncertainties into consideration, the following outlines a full analysis of the different SBESD signals detected in terms of structural evolution only, neglecting the effect purely thermal processes have on resistance of BMG structures. Based on these findings, conclusions can be drawn about the most valid description of shear band behaviour in terms of structural evolution, and how these processes are believed to affect the resistance behaviour of that material. This provides the framework for describing how SBESD analysis can be used to analyse structural evolution within a shear banding BMG.

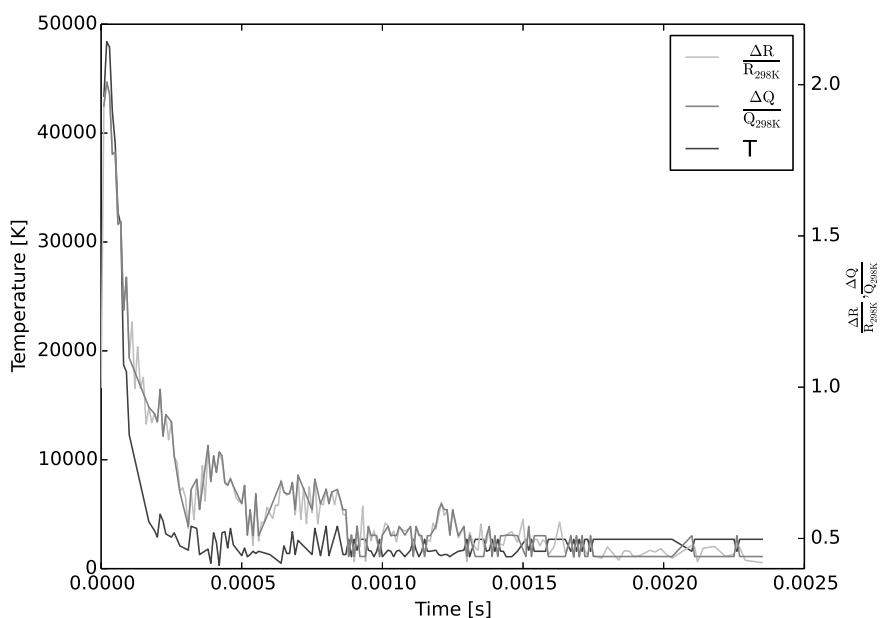
Assessment of model validity in describing observed SBESD results

S SBESD signals provide the most promising evidence for shear band based processes affecting the resistance behaviour of a material, with signals being well sampled, above the 3σ noise threshold, and even showing evidence of thermal decay behaviour. To that end, a case study using the strongest SBESD result observed in $Zr_{50}Cu_{40}Al_{10}$ is used to evaluate the validity of the different modelling approaches employed here, starting with the atomic box model approach.

Fig.(7.33a) shows the application of the HS model to the defined S SBESD signal. The dominant change in resistance behaviour reflects a structural state far in excess of structures calculated to reflect the 50,000K limit structure, resulting in a clipping of the temperature data derived through this model. In addition, the temperature predicted by the system returning to a rest state is in excess of over 10,000K, which in itself is greater than the upper limit to temperatures generated by shear banding. This indicates that the structures generated by the HS model are either not reflected by the temperature conditions from which they are formed, the resistance structure coupling utilised here is a poor approximation of the resistance-structure relationship, or a further contributor to the resistance change behaviour must be considered. To determine which



(a) Temperature and structure data inferred from the structural state of a shear band calculated through the HS model.



(b) Temperature and structure data inferred from the structural state of a shear band calculated through the SHS model.

Figure 7.33: Plots showing the SBESD data and the corresponding change in structure and temperature from both the HS and SHS models.

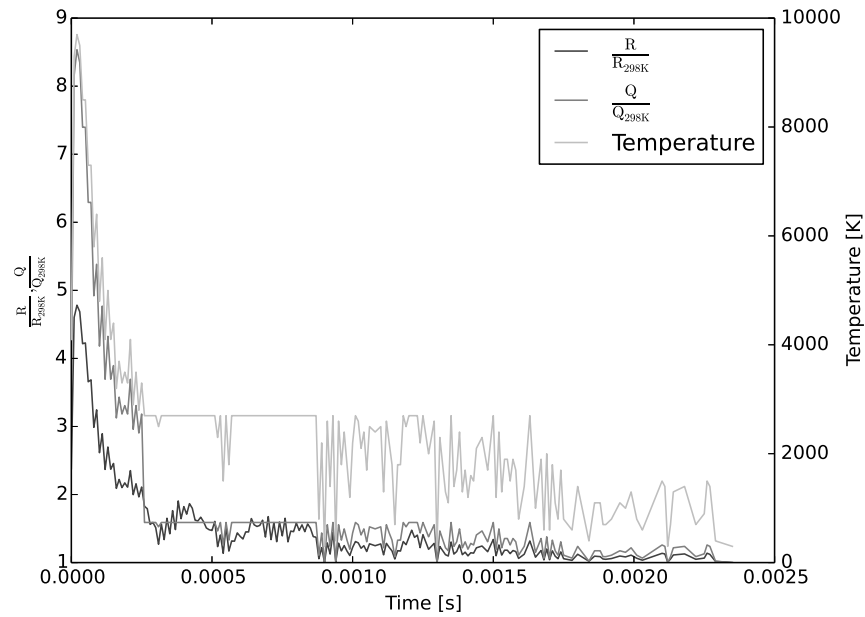


Figure 7.34: SBESD data and the corresponding change in shear band structure and temperature from the thermal expansion model.

is the case, results for the SHS model are considered.

Fig.(7.33b) shows the results of relating the observed SBESD result to the SHS model. Unlike the HS model, the SHS model captures temperature data for the entirety of the SBESD signal, however once again the peak change in resistance reflects an unreasonable temperature change of 50,000K. This being said, the temperature data in this case approaches a near room temperature structural state condition relative to the HS model (with an offset provided by the initial low temperature relaxation feature in Fig.(7.29b)) as the SBESD signal returns to a rest state, indicating an improved structure-temperature-resistivity relationship than that predicted through the HS model. This indicates that further improvements to the SHS model (such as the utilisation of a 3 dimensional model, an even more densified structure and a more realistic description of inter-atomic potentials) could align the SHS model with experimental findings of temperature evolution during shear banding.

Finally results from the thermal expansion model are considered. Maximum temperatures inferred by this model are more in line with the temperatures predicated for shear banding in the literature; approaching a structure generated by 10,000K for the maximum change in SBESD derived resistance. However it is noted that recovery of the SBESD signal indicates significant temperature fluctuations that become increasingly dramatic with lower values of resistivity change considered. This is due to the fractured temperature-resistivity behaviour outlined in Fig.(7.30), where a large disconnect in the relationship influences violent variations in the inferred temperature data at resistance values described by the structures that surround the disconnect. As such improvements to this model can be made through the introduction of a normalisation factor that can eliminate these disconnects.

Based on the SBESD observations and the entropic models, it is conceivable that the dominant change in resistance behaviour in SBESD signals could, in contrast to thermal considerations, be attributed to changes in entropy. The models presented here are a first approximation of how the

coupling between structure evolution during shear banding can relate to the resistivity behaviour of a BMG, with models favouring more densified rest structures producing behaviours that are more representative of behaviours expected in the literature. Further work is required to refine the proposed models such that more realistic structural information can be extracted from SBESD data, and estimations of peak resistance are more in line with that determined through independent means. However the modelling framework has successfully shown that with the right equipment, resistivity changes during shear banding can be used to probe both structure and temperature evolution during all stages of of the shear band process, thereby providing a means to solve the currently unanswered questions surrounding shear banding mechanics.

7.5.4 False result analysis

As mentioned previously, there is of course the potential that the signals detected are not due to shear banding events. Potential other causes need to be understood and if possible removed from either the measured data, or from detection in the first place.

Contact mechanics

The first, and most likely source of signal misinterpretation is due to the shear event itself. Shear banding involves rapid deformation of material, to which the electrical contacts are connected. The shock waves or the sudden movement of the material could affect the electrical contacts, and therefore the measured resistance. The effect would be similar to that expected by a shear band, with a sudden increase of resistance.

Whilst this signal may be indistinguishable from a genuine shear band signal, there are a few markers that would be commonly (but not necessarily) associated with it:

- Oscillations on the voltage:

A sudden load to the electrical contact may also cause the probe to vibrate or oscillate for a short period of time, which would be reflected in the voltage data. Such events have been witnessed in tests and were discounted from further analysis.

- Lower resistance post event:

A lower resistance after shear banding cannot occur, as the sheared material has reduced (negligibly) the cross sectional area in which current must flow, thus producing a more resistive component (the sheared material also has a more disrupted structure, which must increase resistance).

Electromagnetic interference

Another factor affecting signals could be EMF interference. The SBESD design relies inputs at the gate voltage to be in phase. In reality this is not the case, as the paths in which the current passed is different on both sides of the bridge. As such a small oscillation on the current on entering the bridge circuit can be split and amplified considerably by the time the data has been recorded. This is believed to be the cause of the majority of the noise in the SBESD system. However any random surges from the power supply, environment, etc. above that of the random noise may look like a potential shear band signal. This is highlighted in the laser work where initial investigations showed doublet peaks which were found to be due to EMF interference.

Identifying sources of EMF interference and removing them helps with these signals. Whilst the SBESD set-up was encased in a low electrical noise box and earthed, noise was still observed

in that data due to the need for wires to be fed to different parts of the experiment, and the requirement for light and highly flexible wires to limit mechanical interference from the electrical contact point limited the potential for the use of grounded coaxial cables to reduce this effect.

Other sources of transient potential differences

Up to this point, the only other source of potential difference considered has been that from the thermoelectric effect, which has been discounted for metallic glasses tested here as a negligible contributor. However the act of a sudden deformation event could conceivably produce a charge distortion in the otherwise smooth charge for in the experiment due to electrons being excited from the shear banding event. As it is the potential difference that is used to measure the state of charge flow in the sample rather than the current, then an event like this could foreseeably affect the detected signal in such a way that would mimic a shear band event. This being said, it is expected that the previous effects are likely to be more dominant than this due to the metallic nature of the tested material, which will not hold charge for long, and not build up a significant potential difference due to the release of a few valence electrons. In addition, this effect is very close to that of the effect that is being attempted to be detected in the experiment as it is, and similar parallels can be drawn from its effect if this is the source of the observed signals (i.e. the density of electrons perturbed by the event will be proportional to the enthalpy and entropy change of the system). Therefore whilst the values may not compare in their absolute, the general behaviours and trends will hold true for both cases.

7.6 Conclusions

Tests with the final iteration of the SBESD system developed for the work presented here have produced strong evidence that the processes involved with shear banding affect the resistivity behaviour of a BMG over detectable magnitudes. Whilst the SBESD system still requires further refinement and improvement in certain aspects of its design, the system has discovered the following:

- Resistance changes due to the shear banding process produce both weak and strong resistance changes termed W or S SBESD events.
- W events are commonly observed. Signals of this type are weak and are heavily influenced by background noise. Some tests return single W signals, whilst others return multiple observations, which appear uniform in both the SBESD and load response. Therefore it is possible that the process is caused by shear banding.
- S events are very rarely observed in tested materials, with only tests in $\text{Zr}_{50}\text{Cu}_{40}\text{Al}_{10}$ showing any degree of reproducibility of these events. All the observed signals showed a positive change in resistance, and features within the signal could be accommodated for by the shear banding process. Tests in the $\text{Zr}_{50}\text{Cu}_{40}\text{Al}_{10}$ alloy showed multiple S signals throughout a single test. The uniformity of the multiple W response and the linearity of the multiple S responses with respect to the observed load drop magnitudes hypothetically indicates a secondary factor other than shear banding affecting the SBESD observation, such as nanocrystallisation, which has been used to identify features in S signals and infer minimum rises in temperature from shear band events which are in agreement with literature.

In addition to the development of the SBESD system and the experimental detection of shear band events through changes in resistivity, modelling approaches in conjunction with proof-of-concept experiments were developed to determine the source of the resistivity changes beyond the general description of shear banding.

- Laser flash experiments showed that the SBESD system is capable of detecting minor changes in resistivity to the sudden input of thermal energy into an amorphous structure.
- SBESD compression experiments on a chromium powder- weak epoxy mix showed that the SBESD system, if sensitive enough, is capable of detecting structural changes in materials during shear banding and provided a signal morphology to seek during real BMG SBESD compression tests.

Based on the SBESD signals and the proof-of-concept experiments, models were developed to determine the effective contribution of entropic and enthalpic factors to both W and S SBESD events:

- W events were found to be impossible to characterise through purely enthalpic arguments due to the permanent changes in resistivity they implied. As such, W events can only be characterised through changes in structural state.
- S events were characterisable through both structural and thermal arguments and were subjected to rigorous data treatments as a result. It was found that the bulk of the resistance change required both thermal and entropic contributions to the resistance, whilst secondary decay features in the SBESD data could be attributed to purely thermal considerations only.
- Improvements to both the thermal and entropic models are required to strengthen the arguments behind the sources of the SBESD signals. These improvements include an understanding of the temperature and structural dependence of parameters that are at the core of both the enthalpic and entropic models, development of a 3 dimensional model for both enthalpic and entropic models, accommodation for fragile assumptions (such as the assumed adiabatic nature of shear bands) and extension of both models to predict the mechanics of shear band initiation.
- The models here have focused on SRO-MRO structures governing changes in resistivity behaviours. However the potentially fractal nature [256] of BMG structures allows for the potential application of the model to MRO clusters in place of the model atoms. With the increased separation values, this may prove to be more accurate in predicting structural change, especially given inferences of deformation behaviour of BMGs being focused on MRO cluster movements rather than individual atomic rearrangements [6].

Chapter 8

Conclusions

This thesis focuses on the exploration of novel testing methodologies to probe mechanical behaviours of BMGs. Chapters 5-7 summarise the experimental investigations performed throughout this work, exploring the 3 key modes of deformation: elastic/inelastic, homogeneous plastic and inhomogeneous plastic deformation. The conclusions of these chapters have been summarised as follows:

8.1 Local mechanical property assessments of BMGs through nano-indentation

An in depth study of the standard usage protocol of nano-indentation was performed with the aim to evaluate the capability of nano-indentation to measure fundamental mechanical properties of materials with limiting volumes and geometries. It was found that:

- As expected, tests in simple crystalline materials returned hardness and modulus values that corresponded well with literature.
- Modulus values of tested BMGs approached those reported in literature, but also show behaviours similar to those observed in crystalline materials. This observation could be justified by the presence of small volumes of crystalline material that are undetectable by XRD techniques, or through the act of nano-crystallisation during indentation.
- Hardness measurements of BMGs produced a range of behaviours from good agreement with the literature values to significant overestimates of literature measurements. Further verification of hardness values through micro-indentation tests revealed deviations from literature values to be a size effect, with micro-indentation measurements reflecting better agreement with literature for the cases where nano-indentation hardnesses were grossly over estimated.
- BMG hardness measurements showed no significant correlation with the indentation test loads ranging from 2 mN to 10 mN, however weak correlation was noted for loading rates ranging from 0.5 mNs^{-1} to 2 mNs^{-1} , explicable through high rates of free volume generation in the higher loading rate tests allowing for the facilitation of greater levels of plastic deformation. As such, a standardised sample preparation and test methodology is needed for the testing of BMGs through nano-indentation in order to obtain accurate values of hardness and modulus.

- Further observations of the raw nano-indentation data revealed the presence of 2 signal types, categorised based on the size, conditions for formation, abundance and morphology.
 - Weak signals were observed during all stages of loading and were attributed to STZ activation due to the apparent transient expansion of the material due to the generation of free volume from STZ activation
 - Strong signals were observed only during loading and were attributed to shear banding processes due to the sudden displacement bursts that preferentially occur in tests at high loading rate (conditions required for inhomogeneous deformation).
- Energies calculated through a mechanical work approach for each of the signal types during the different stages of loading were found to be heavily dependent on the smoothing treatment applied to the data required for an accurate calculation of the energy, and therefore require equipment with higher sensitivities and sampling rates. However energies plotted against different levels of smoothing treatment all show shear band events being the most energetic process and STZ processes during unloading being the least energetic.

It was noted that absolute measurements of elastic moduli of BMGs could not be achieved through nano-indentation alone, requiring additional information regarding the elastic behaviour of the material. To that end, the works of Teter, Chen, and Zorzi and Perottoni were applied to the measurements and literature data of BMG and crystalline materials to infer further elastic properties from hardness measurements from which absolute elastic modulus values could be derived. It was found that:

- For polycrystalline metals, predicted ν values through the equations and Teter, Chen and Zorzi and Perottoni approximated the values reported in the literature, but could not produce the level of accuracy required for successful use in the nano-indentation technique to measure absolute elastic moduli. The authors of these approaches suggested that deviation of the predicted values in pure polycrystalline materials is expected to be from micro-structural effects such as localised work hardening, and therefore warranted a similar assessment in BMGs.
- Tests were performed on literature data of BMGs and it was noted that hardness values predicted through Teter's simplified approach agreed better with reported values of hardness than the hardnesses predicted by Chen and Zorzi and Perottoni. This may be due to the use of literature data from multiple sources, which in the case of Chen's and Zorzi and Perottoni's approaches introduces more sources of error than that of Teter.
- Attempts at reducing the level of scatter were made through the evaluation of predicted hardnesses with data obtained from nano-indentation and the contribution of literature data for ν only. The same results were found, with Teter's approach producing predicted hardnesses near that reported, and Chen's and Zorzi and Perottoni's estimations showing significant deviations from the measured hardness. Deviations in these measurements could not be accounted for with variations in the measurement parameters indicating that the application of Chen's and Zorzi and Perottoni's work could not utilise hardness as an effective measure of elastic properties of metallic glasses.
- Based on the success of Teter's equation, elastic property measurements were predicted from hardness measurements for several alloys, which had no reported ν values. ν determined through nano-indentation measurements were below that expected of BMGs of that type.

This could be due bulk modulus not being considered in the the calculation, or due to the localised tests only sampling the elasticity of the densified structure and not regions of free volume. Further tests are required to determine the cause of this.

8.2 Probing creep behaviour in crystalline and BMG materials

Tests through nano-indentation were explored further to determine if the method could be used to rapidly and accurately measure creep. Investigations were performed using CLH indentation creep tests with a range of testing parameters in a range of crystalline and amorphous materials. It was found that:

- Reproducibility of tests in both crystalline and amorphous materials was poor. To that end, beyond the sample preparation considerations highlighted in the previous chapter, a list of factors was developed to produce the most reliable indentation creep test possible, including:
 - Use of high load.
 - Use of correct loading rate values (high for crystalline but low for BMGs)
 - Use of long thermalisation times
 - Use of an appropriate treatment of thermal drift in terms of correction and minimisation.

Despite poor reproducibility, an in depth analysis was performed on the test data for all alloys utilising a wide range of reported evaluation methodologies to determine the stress dependency of creep in both material types (as simple crystalline materials have well characterised stress dependencies, whilst BMG stress dependencies are determined by a single value due to their unique homogeneous flow mechanism). Results showed:

- Analysis methodologies heavily influenced the measurement of stress dependency of creep both as an overall value and as a time varying parameter. Data fitting analysis approaches were heavily dependent on the fitting equation used for seemingly similar fits, whilst numerical analysis approaches were heavily influenced by measurement scatter within the data, thus making detailed analysis of the signals dependent on the quality of the test data.
- The introduction of a combined analysis method in order to reduce the factors affecting the analysis of results still produced poor reproducibility as a consequence of the quality of the input data. However the combined method showed greater transparency in the mechanics behind the analysis and therefore is recommended as a means to evaluate indentation creep results.

8.3 Probing inhomogeneous yield behaviour in BMGs

Analysis of shear banding phenomena is still a highly contested topic, with the clarity of the mechanisms behind initiation and propagation of shear bands as well as the structural and temperature evolution of the process being poor. As such a new testing methodology, called SBESD, was hypothesised for probing shear banding behaviour of BMGs through indirect measurement of the phenomena through the dynamic measurement of electrical resistivity of BMG samples under compression. Evidence of shear banding behaviour was successfully detected through SBESD. The following outlines the key achievements and findings of this endeavour:

- A prototype SBESD system based on a Wheatstone bridge was developed and was used to detect small dynamic change of resistance associated with shear banding.
- Several SBESD events were observed and were grouped into 2 categories based on the signal strength and morphology; termed S and W signals. Both signal types were rationalised in terms of expected shear banding behaviour derived from theory and proof-of-concept experiments, with W signals being attributed to typical shear bands, and S signals being attributed to shear bands with a nano-crystallisation component.
- Quantitative analysis of the detected signals was performed in order to identify details surrounding the source of the observed signals and how they relate to the evolution of shear banding. Analysis was split into purely thermal and structural characterisation approaches in order to identify which mechanism was predominantly responsible for the signals observed. It is noted that both these variables are not independent of each other, even if the mechanism in which they affect electron transport is.
 - Assessment of SBESD signals through thermal arguments was based on the classic electron-phonon interaction formulae with a temperature coefficient of resistance determining the strength of the interaction. Due to the complex nature of shear banding and its potential effect on the temperature coefficient of resistance, an upper limit to this value for all alloys was evaluated through a rule of mixtures approach, as BMGs and liquids are reported to have a much weaker temperature coefficient of resistance than that of the crystalline phase.
 - Assessment of SBESD signals through entropic arguments was performed with the aid of 3 distinct modelling approaches. The first two models are based on a Monte-Carlo and Ising model approach, whereby 2 dimensional boxes of atoms were constructed and relaxed to structural states reflecting different temperatures. Measured changes in resistance were related to these structural temperatures based on the relative change in the work required to pass an electron from one atom to another across nearest neighbour atoms from the room temperature structure to a higher energy structure. One model utilised a hard-sphere model for the inter-atomic potentials, whilst the other utilises a soft-hard-sphere model, which allowed for some flexibility in the atomic position near the borders of the atom depending on the thermal energy state being considered but still had an absolute border defined by the larger of the radii of the atomic pair. The 3rd model utilised an extension of the thermal expansion model such that the thermal expansion coefficient of the material could be used to determine the average inter-atomic separation of different atomic pairs within the material from which structural states could be inferred based on a structural temperature value. This also used the change in inter-atomic potentials to relate changes in resistivity to the difference in work required to pass a charge across the pair potential.
- Application of the thermal and structural assessment methodologies were applied to both S and W SBESD signals in order to determine their validity:
 - The weakness of W signals made quantitative analysis of these signals difficult, requiring a greater model and experimental sensitivity and sampling rate. However the morphology of W based signals discounted these as having any thermal signal contributions associated with them, as such an assumption would imply the material to have undergone a permanent change in thermal state, thereby breaking the 2nd law of thermodynamics.

- Thermal contributions to SBESD signals was successfully determined for S signals. The dominant change in resistance in these signals were found to require temperature contributions of over 100,000,000K, far in excess of that explicable through any physical means. Therefore additional contributors to the bulk change in resistance are required. Detailed features of the S SBESD signals revealed a secondary decay feature which was hypothesised to be due to thermal cooling of nano-crystallites. As such, attempts were made at fitting these to a modified heat equation in order to extrapolate the temperature rise at the point of shear band initiation. This was found to be difficult due to scatter in the data, however a linear fit was found and was used to determine a lower temperature rise limit estimate. Results showed that the linear extrapolation signifies a temperature increase of the order of 100K, which is more in agreement with literature estimates. Noting this is an absolute lower limit to temperature change, further work is suggested to improve the fitting and quality of the SBESD data such that an accurate fitting of the modified heat flow equation could be used to for an accurate determination of the temperature rise at the point of shear band initiation, and how this temperature profile evolves with shear band propagation.
- Entropic contributions were also evaluated for S SBESD signals. HS and SHS models predicted temperature rises of these signals in excess and of the order of 50,000K respectively, again far in excess of that explicable through physical means. However the improvement of the estimation from the HS model to the SHS model indicates that changes to the inter-atomic potential to a more realistic form and the accommodation of a 3 dimensional atomic box may bring temperature estimates observed through this method in line with that of the literature. This is supported by the observation of the linear expansion model, which predicts structural temperatures of 10,000K, in agreement with results from the literature. Whilst it is recognised that such an observation cannot represent the inter-atomic spacing of every single atomic pair in a glassy structure, the agreement with literature estimates for this model indicates that with adjustments made in favour of more realistic models, reasonable measurements of temperature and structural evolution during shear band processes can be inferred. One such adjustment would be the replacement of atoms with MRO clusters in the atomic box models to reflect the current ideas of MRO affecting shear band behaviour. This is suggested as a direction for further work.

To summarise, this thesis has investigated the mechanical behaviours of BMGs through novel testing techniques. These techniques have ranged from new ways of applying standardised tests to the development of brand new methodologies. Whilst the results reported are open to interpretation, the insights provided here are believed to be valuable contributions to the effort in understanding mechanical behaviours of BMGs, from both a mechanistic and phenomenological point of view, both of which will be useful in the development of new BMG compositions and assessment of their performance whilst in service and in the laboratory.

Chapter 9

Appendix

9.1 Wheatstone bridge theory

The mechanics behind how the bridge circuit operates and gives measurements is based on Kirchoff's 2 laws and Ohms law:

- Kirchoff's 1st law: The sum of the current flowing into a node (labelled if Fig.(7.2a) as N_1 and N_2) must equate to the sum of the current flowing out of the node.

This statement is a conservation of charge statement that states the sum of all currents entering a node must equate to zero:

$$\sum_{k=1}^n I_k = 0 \quad (9.1)$$

This statement applies to a system where current flow is in equilibrium.

- Kirchoff's 2nd law: The sum of potential differences across a closed network must also equal zero.

This statement is an extension of conservation of energy rules, whereby energy cannot be created or destroyed within a closed system:

$$\sum_{k=1}^n V_k = 0 \quad (9.2)$$

- Ohm's law: If a potential difference is applied across a material, the current that flows through that material is proportional to the potential difference applied.

This definition of Ohm's law identifies that the proportionality constant between the potential difference and current variables is simply the resistance.

9.1.1 Calculations regarding the relationship between the Wheatstone bridge voltage, and changes in resistance

Referring to Fig.(7.2a), a small change at R_x can be measured through monitoring changes in V_g . The following shows how measurements of V_g can be used to determine values of R_x , thus justifying the use of the Wheatstone bridge for use in detecting small changes in resistance due to shear banding.

Lets assume that the gate voltage (V_g) is replaced with a wire of $R_g\Omega$ resistance. From Kirchoff's 1st law, the sum of the currents at the nodes leading to the gate voltage (N_1 and N_2 in Fig.(7.2a)) are as follows:

$$I_1 - I_2 - I_g = 0 : \text{ at node } N_1 \quad (9.3)$$

$$I_3 + I_g - I_x = 0 : \text{ at node } N_2 \quad (9.4)$$

By taking Kirchoff's 2nd law, and applying it to the 2 closed loops in the circuit (defined as L_1 and L_2 in Fig.(7.2a)), the following can be seen to be true:

$$I_x R_x - I_2 I_2 + I_g R_g = 0 \quad (9.5)$$

$$I_3 R_3 - I_g R_g - I_1 R_1 = 0 \quad (9.6)$$

If the values of R in Fig.(7.2a) are such the potential difference between N_1 and N_2 ($= V_g$) is zero, then the bridges is considered to be balanced. From Ohm's law, $I_G = 0$ for a balanced bridge, thereby allowing Eq.(9.3)-(9.6) to be written as:

$$I_1 = I_2 \quad (9.7)$$

$$I_3 = I_x \quad (9.8)$$

$$I_x R_x = I_3 R_x = I_2 R_2 \quad (9.9)$$

$$I_1 R_1 = I_2 R_1 = I_3 R_3 \quad (9.10)$$

Dividing (9.9) by (9.10) yields:

$$\frac{R_x I_x}{I_3 R_3} = \frac{I_2 R_2}{I_1 R_1} \quad (9.11)$$

$$R_x = \frac{I_2 R_2 I_3 R_3}{I_1 R_1 I_x} = \frac{I_{(1/2)} R_2 I_{(3/x)} R_3}{I_{(1/2)} R_1 I_{(3/x)}} = \frac{R_2 R_3}{R_1} \quad (9.12)$$

Finally, by reinstating an infinite resistance at the gate voltage, then it can be seen that 2 potential dividers have been set up within the circuit. Therefore the gate voltage can then be determined as the difference in the voltage between these potential dividers:

$$V_{G_{right}} = \frac{R_2}{R_1 + R_2} V_s \quad (9.13)$$

$$V_{G_{left}} = -\frac{R_x}{R_x + R_3} V_s \quad (9.14)$$

$$V_{G_{right}} + V_{G_{left}} = V_G = \left(\frac{R_2}{R_1 + R_2} - \frac{R_x}{R_x + R_3} \right) V_s \quad (9.15)$$

This equation relates measurements taken at the gate voltage to resistance values of R_x , providing values are known for R_1, R_2 and R_3 .

9.2 Kauzmann's paradox

Formation of metallic glasses produces a potential problem upon the formation of metallic glasses. The entropic state of a liquid state is inherently higher than that of a crystalline solid due to the higher degrees of freedom present in the liquid. Kauzmann noticed that by plotting the ratio of difference in entropies of liquid and crystalline states over a range of temperatures to that of the difference in entropies of the 2 states at T_m , a paradox forms.

$$\frac{S_{liq}(T) - S_{crys}(T)}{S_{liq}(T_m) - S_{crys}(T_m)} = \frac{\Delta S(T)}{\Delta S(T_m)} \quad (9.16)$$

This plot of the difference of entropies can be used to define a strong and fragile glass, with strong glasses having slopes less than one, and vice versa to the temperature T_m [257].

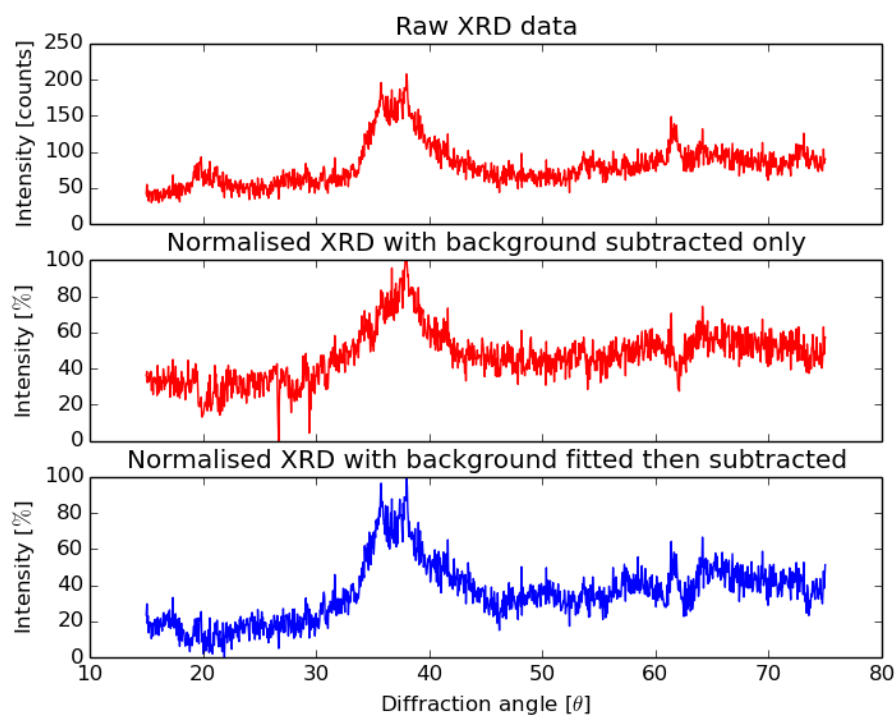
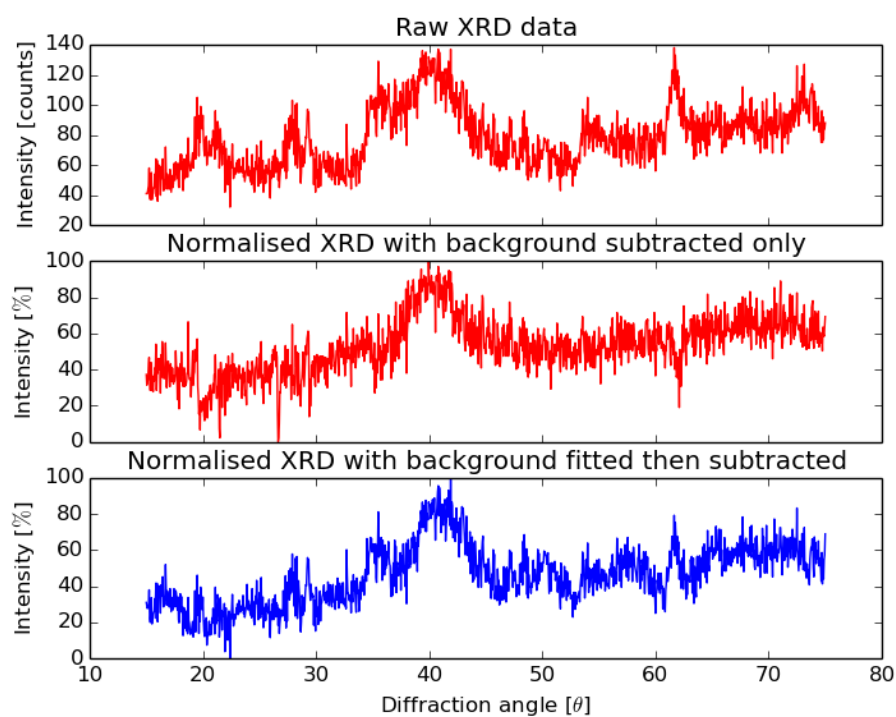
$$\left(\frac{\delta \Delta S(T) / \Delta S(T_m)}{\delta T / T_m} \right)_{T=T_m} = \frac{T_m}{\Delta S(T_m)} \left(\frac{\delta \Delta S(T)}{\delta T} \right)_{T=T_m} \quad (9.17)$$

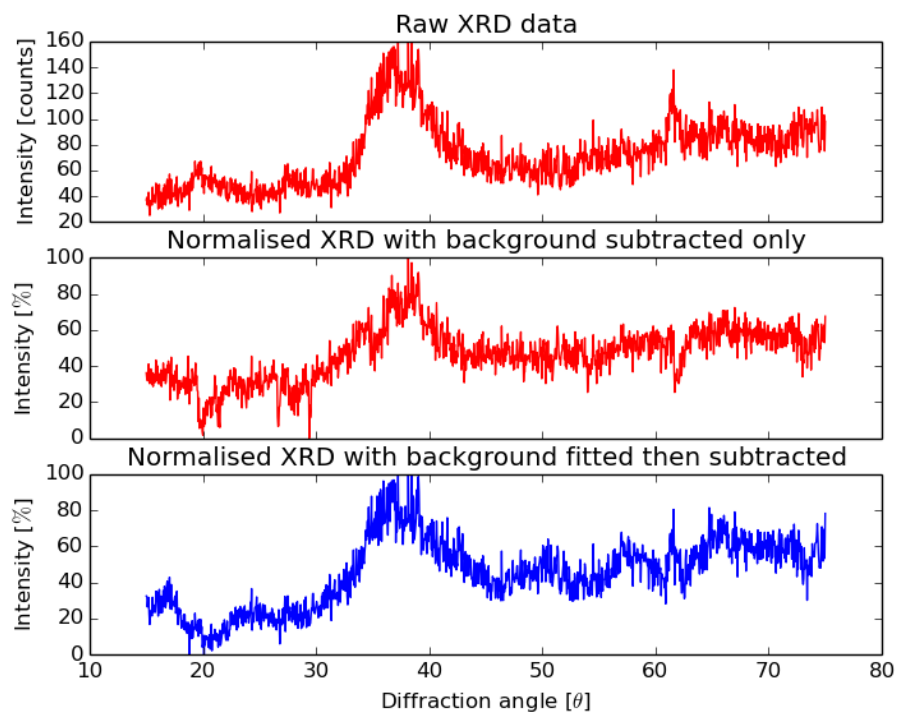
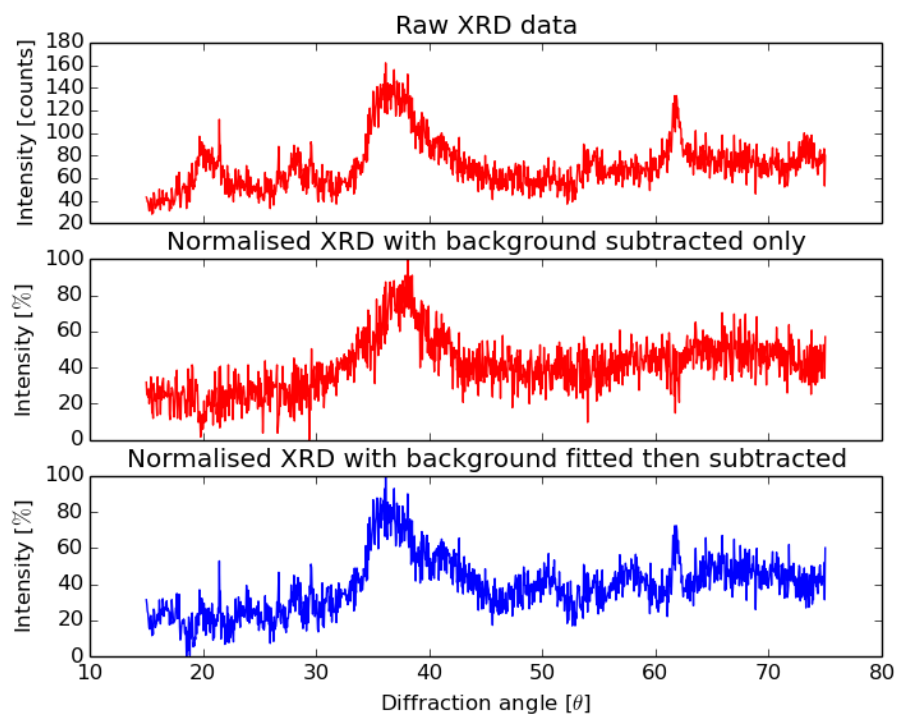
$$= \frac{T_m}{\Delta S(T_m)} \cdot \frac{\Delta C(T_m)}{T_m} = \frac{\Delta C(T_m)}{\Delta S(T_m)} \quad (9.18)$$

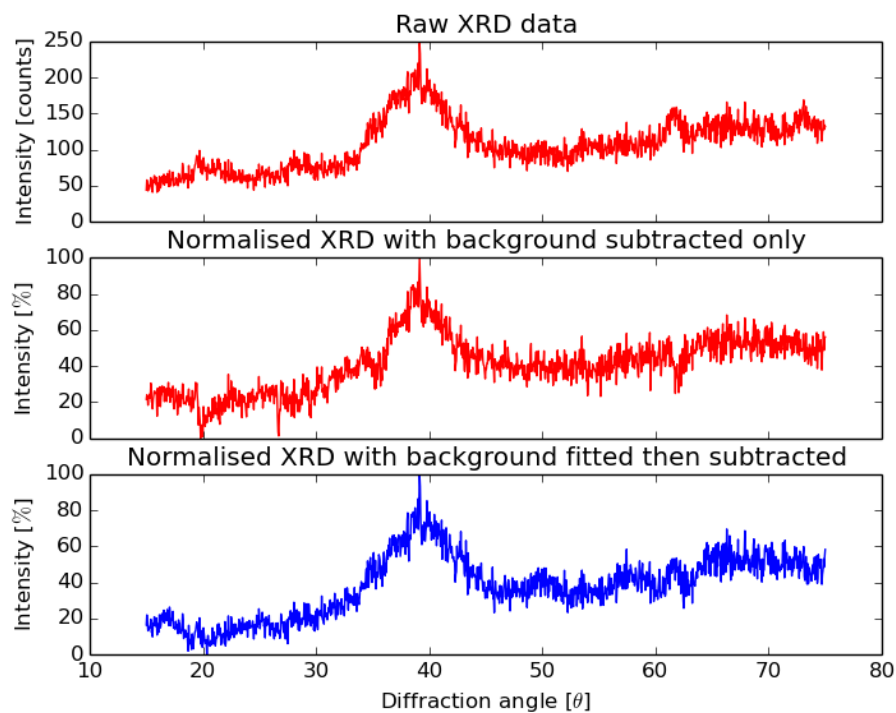
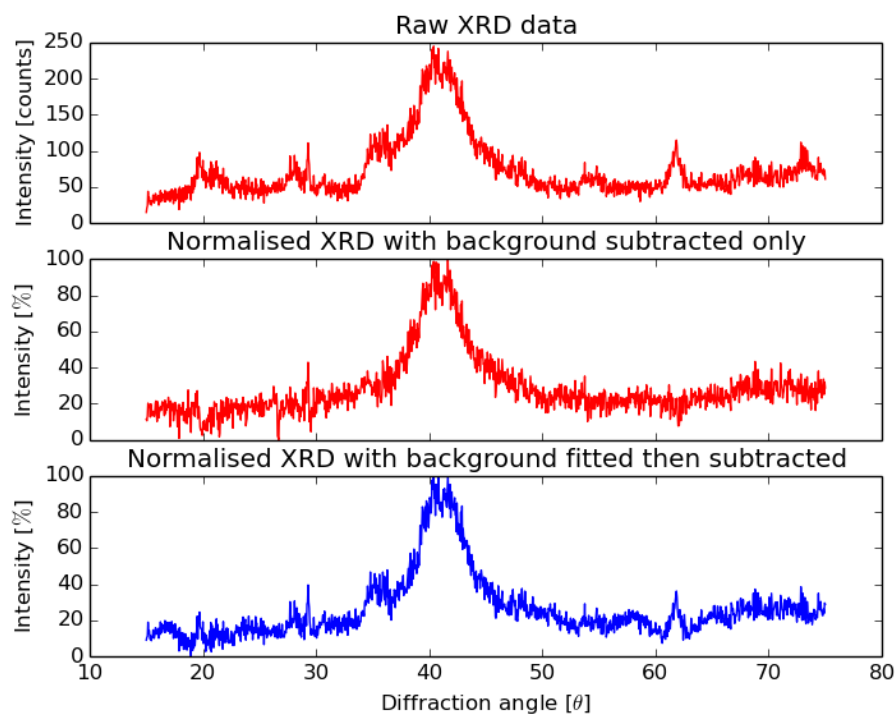
$$= \frac{\Delta C(T_m) T_m}{\Delta U(T_m)} \quad (9.19)$$

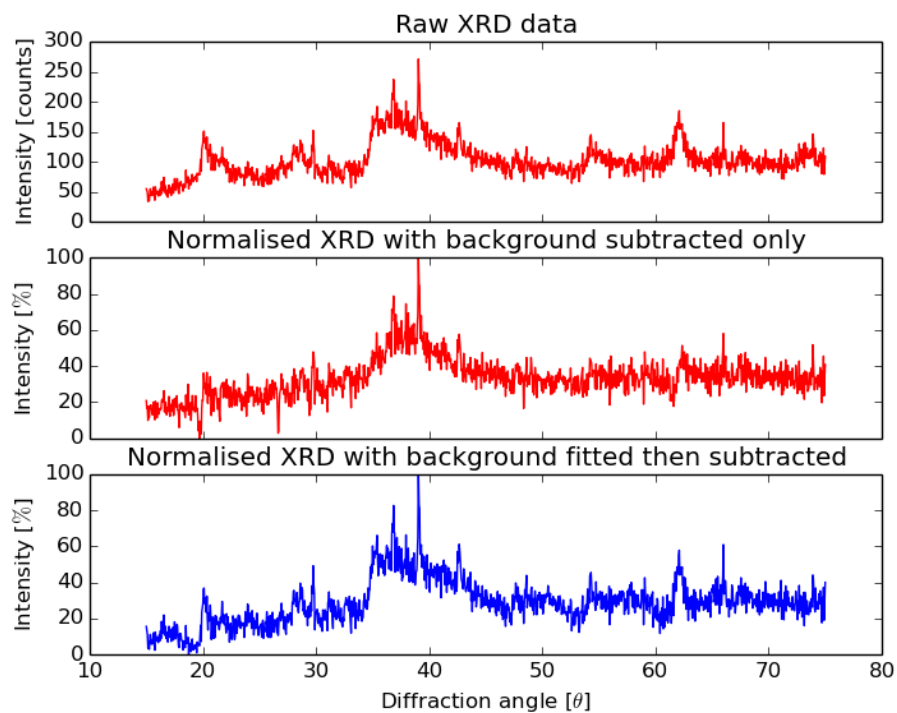
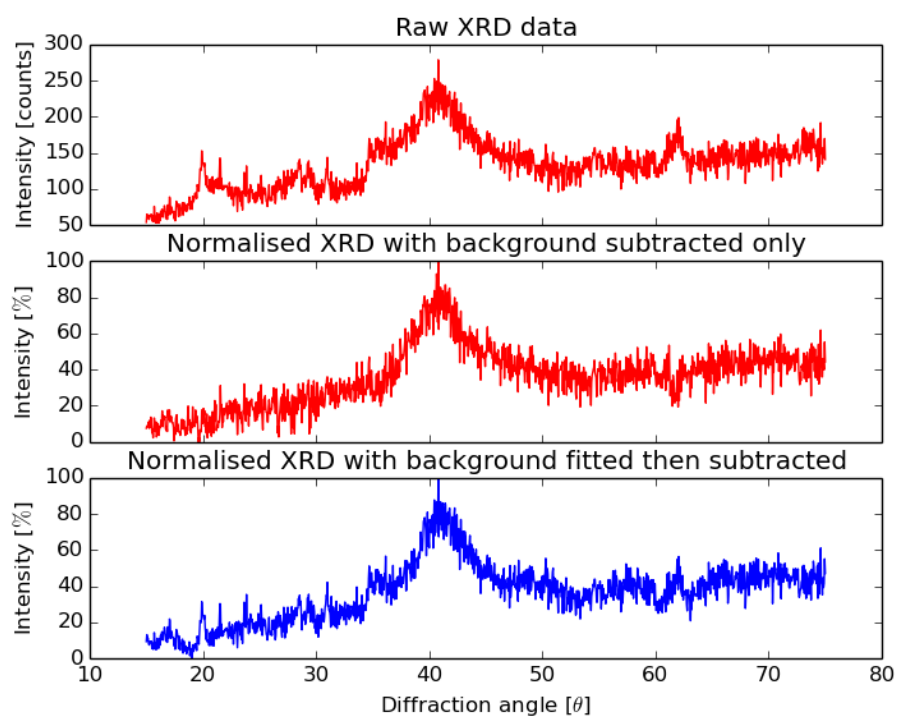
From Eq.(9.19), a fragile liquid must have a high T_m , high C_p or a small internal energy difference to maintain a gradient value greater than one.

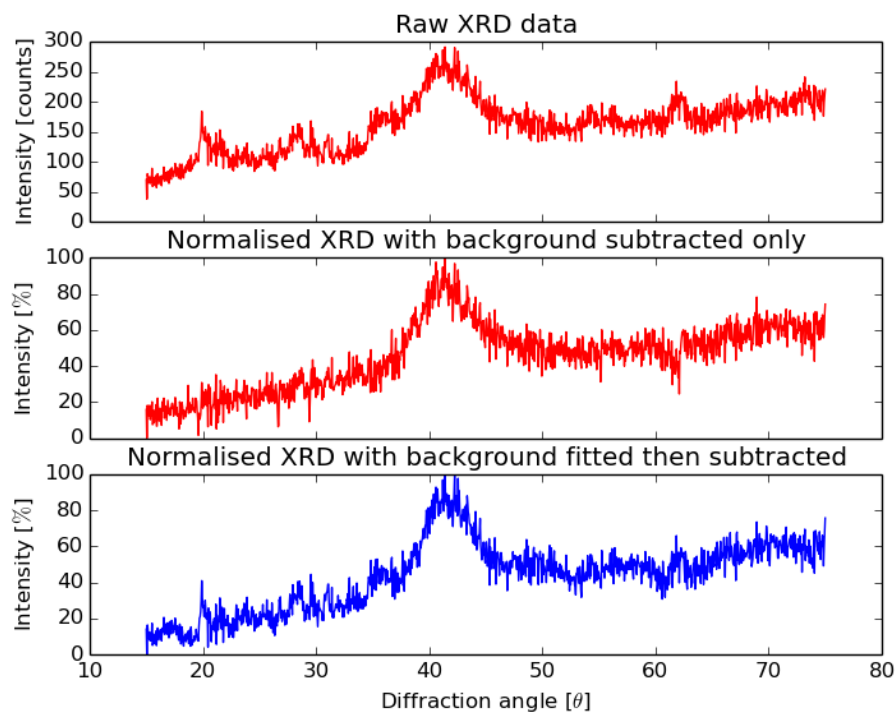
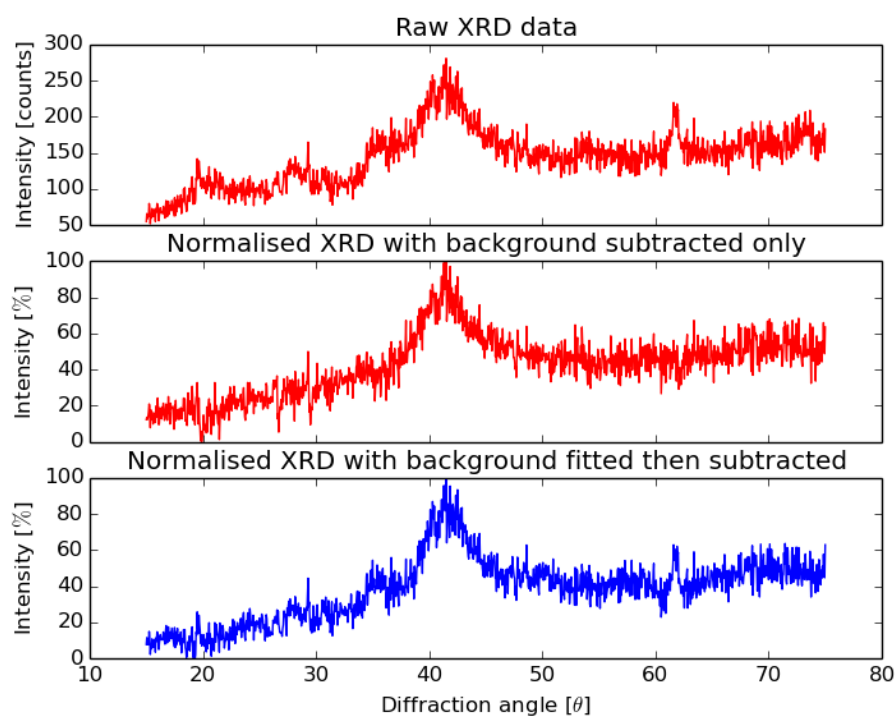
9.3 XRD results

Figure 9.1: XRD results for $\text{Zr}_{65}\text{Cu}_{15}\text{Al}_{10}\text{Ni}_{10}$.Figure 9.2: XRD results for $\text{Cu}_{57.5}\text{Hf}_{27.5}\text{Ti}_{15}$.

Figure 9.3: XRD results for $Zr_{57}Cu_{20}Al_{10}Ni_8Ti_5$.Figure 9.4: XRD results for $Zr_{57.5}Nb_5Cu_{15.4}Ni_{12}Al_{10}$.

Figure 9.5: XRD results for $\text{Zr}_{44}\text{Cu}_{44}\text{Al}_6\text{Ag}_6$.Figure 9.6: XRD results for $\text{Pd}_{77.5}\text{Si}_{16.5}\text{Cu}_6$.

Figure 9.7: XRD results for $Zr_{50}Cu_{40}Al_{10}$.Figure 9.8: XRD results for $Ti_{43.15}Zr_{9.59}Cu_{36.24}Ni_{9.06}Sn_{1.96}$.

Figure 9.9: XRD results for $\text{Ti}_{33}\text{Cu}_{47}\text{Zr}_9\text{Ni}_6\text{Sn}_2\text{Si}_1\text{Nb}_2$.Figure 9.10: XRD results for $\text{Ti}_{40}\text{Zr}_{10}\text{Pd}_{14}\text{Cu}_{34}\text{Sn}_2$.

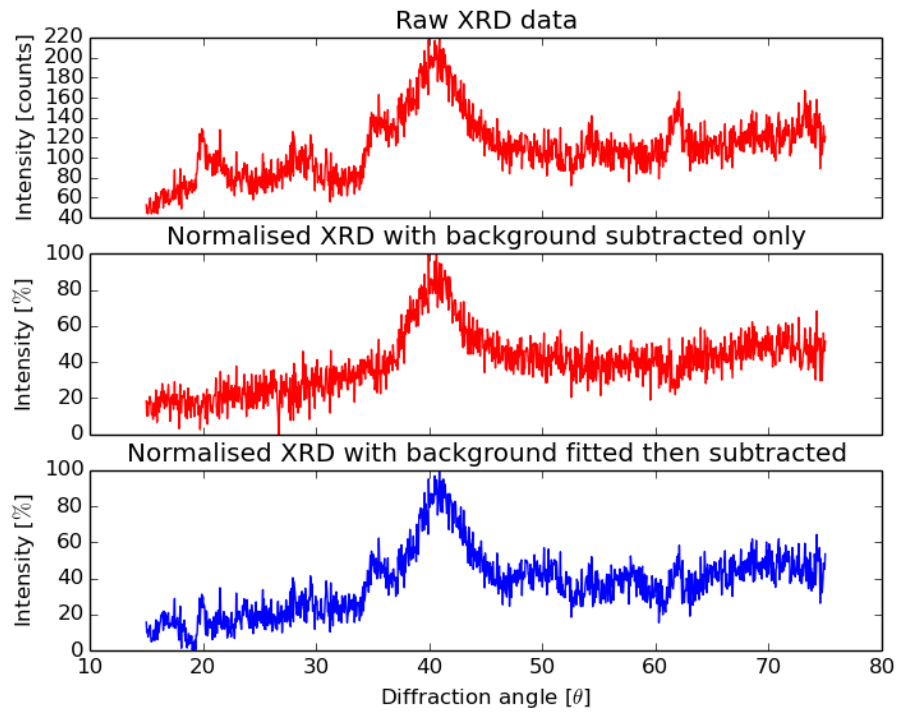


Figure 9.11: XRD results for $\text{Ti}_{33.85}\text{Cu}_{46.35}\text{Ni}_{8.4}\text{Zr}_{11.4}$.

9.4 LabView program

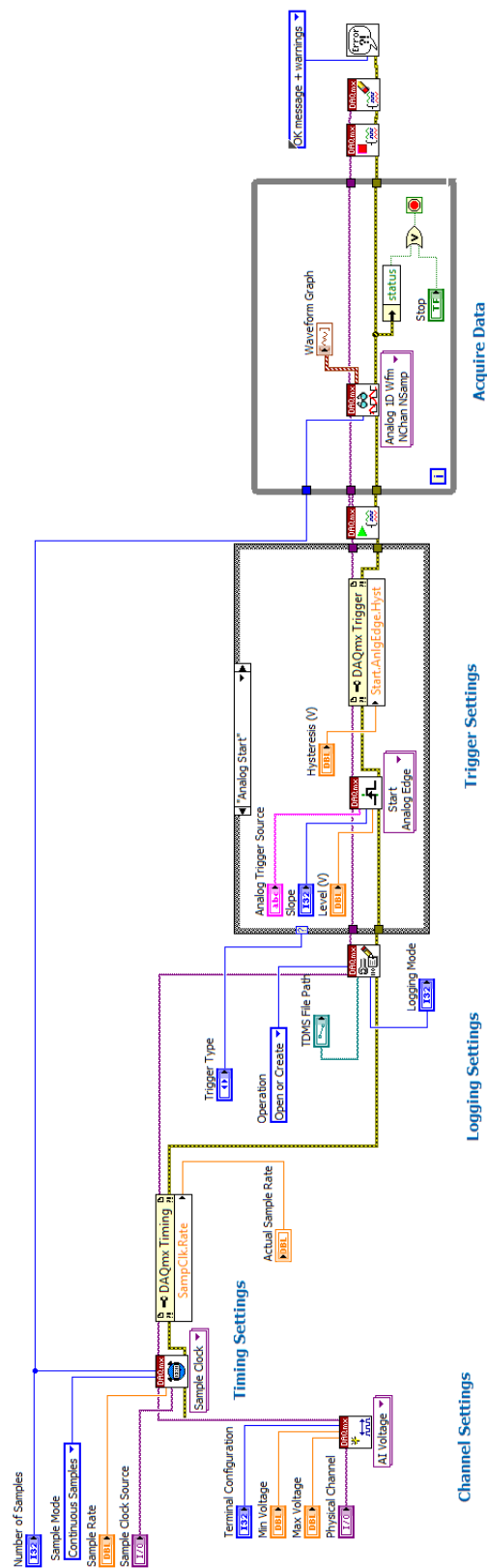


Figure 9.12: Graphical display of the LabView program developed for the rapid sampling of voltage data in the SBESD system.

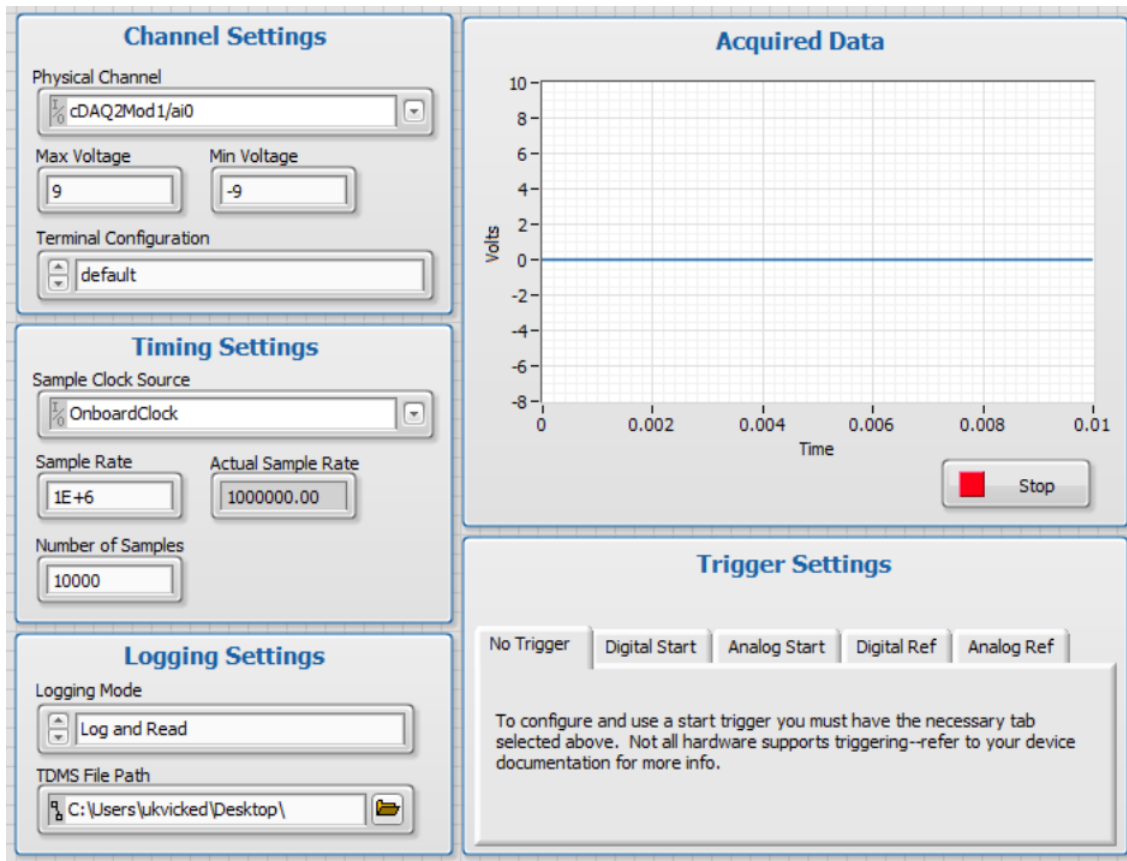


Figure 9.13: Control panel view of the LabView program developed for the rapid sampling of voltage data in the SBESD system.

9.5 Fitting resistivity data to a temperature profile equation

Samples tested in the SBESD compression experiment can be electrically modelled as a string of resistors of in series. Each resistor has a resistance $dR(x, t)$, and represents a cylindrical slice of material of thickness dx and facial area identical to that of the shear bands outlined in Fig.(7.18).

$$dR(x, t) = R_o \alpha_\Omega \Delta T = \frac{\rho_o}{\pi a^2 \sqrt{2}} \alpha_\Omega \Delta T dx \quad (9.20)$$

At time $t = 0$, a shear band is assumed to form adiabatically. At time $t = t_i$ the thermal energy generated during the shear band process has diffused into the surrounding material approximately according to the heat flow equation. As such, the resistance state of the material, after the initial shear band energy has been generated (section II of the S SBESD signal), can be determined from the sum of all the resistor elements that make up the material which have resistance values that depend on the temperature distribution of the material at any given time. Therefore:

$$\int_{-x}^x dR(x, t) dx = \Delta R(t) = R_o \alpha_\Omega \Delta T = \frac{1}{2} \int_{-x}^x \frac{A}{\sqrt{t}} \exp \left[\frac{-x^2}{Bt} \right] dx = \frac{A}{\sqrt{t}} \int_0^x \exp \left[\frac{-x^2}{Bt} \right] dx \quad (9.21)$$

where $A = \frac{HR_o \alpha_\Omega}{\rho C_p \sqrt{\pi \alpha_\theta}}$ and $B = 4\alpha_\theta$

The integral in this equation is a special integral with a fixed result. As such,

$$\Delta R(t) = A \sqrt{\pi B} \times \mathbf{erf} \left[\frac{x}{\sqrt{Bt}} \right], \quad (9.22)$$

where \mathbf{erf} is the error function. This describes the expected thermal resistance response of BMG having undergone shear banding, and provides an equation to which data from section II can be fitted, utilising A and B as fitting constants.

9.6 Chapter 7 results

9.6.1 Microstructure of Tin tested for indentation creep

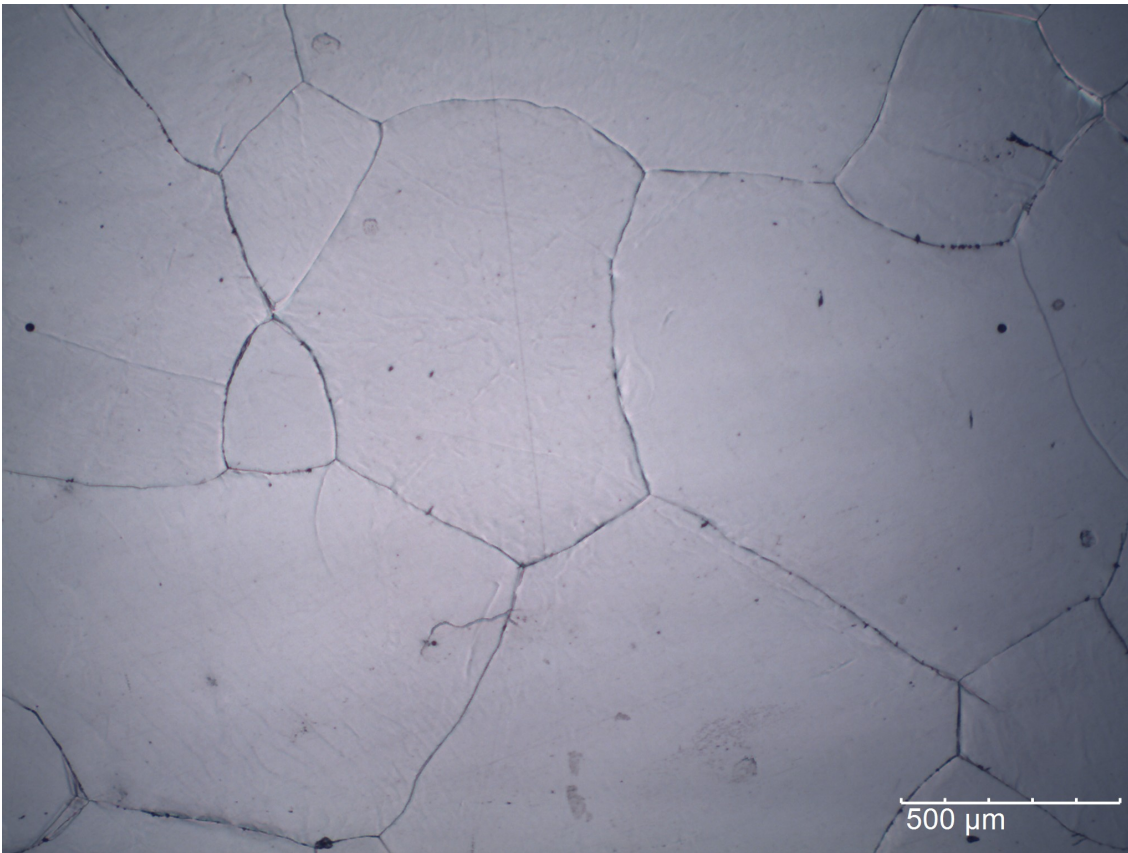


Figure 9.14: Microstructure of Tin tested for indentation creep showing that the size of the grains are far in excess of the size of the indent arrays performed.

9.6.2 Indentation creep results and fitting equations

Typical fitting parameters for the fitting equations

| Material | $h(t) = h_0 + A \ln(t - t_0) + kt$ | | $h(t) = h_0 + a(t - t_0)^m + kt$ | | $h(t) = a(1 - e^{-bt})$ | |
|-----------|------------------------------------|------------------------------------|------------------------------------|------------------------------------|------------------------------------|-----------------------------------|
| | h_0 | t_0 | h_0 | t_0 | a | b |
| Aluminium | $(65 \pm 7) \times 10^{-9}$ | $(81.2 \pm 1.7) \times 10^{-9}$ | $(195.6 \pm 6.8) \times 10^{-9}$ | $(41.0 \pm 1.4) \times 10^{-9}$ | $(5220.7 \pm 2.2) \times 10^{-10}$ | $(2027 \pm 6) \times 10^{-5}$ |
| Magnesium | $(2508.0 \pm 3.4) \times 10^{-10}$ | $(2646.9 \pm 9.5) \times 10^{-11}$ | $(2508.0 \pm 3.4) \times 10^{-10}$ | $(2646.9 \pm 9.5) \times 10^{-11}$ | $(4962.2 \pm 6.9) \times 10^{-10}$ | 0.01536 ± 0.00011 |
| Lead | $(-980.3 \pm 3.5) \times 10^{-8}$ | $(1543.7 \pm 5.3) \times 10^{-9}$ | $(-980.3 \pm 3.5) \times 10^{-8}$ | $(1543.7 \pm 5.3) \times 10^{-9}$ | $(4389.5 \pm 2.0) \times 10^{-10}$ | $(1544.4 \pm 3.5) \times 10^{-5}$ |
| Tin | $(-1317.3 \pm 3.0) \times 10^{-9}$ | $(2582.1 \pm 5.4) \times 10^{-10}$ | $(-1317.3 \pm 3.0) \times 10^{-9}$ | $(2582.1 \pm 5.4) \times 10^{-10}$ | $(4359.4 \pm 3.2) \times 10^{-10}$ | $(1271.1 \pm 3.9) \times 10^{-5}$ |
| Silver | $(2096.9 \pm 1.6) \times 10^{-10}$ | $(877.2 \pm 4.8) \times 10^{-11}$ | $(2096.9 \pm 1.6) \times 10^{-10}$ | $(877.2 \pm 4.8) \times 10^{-11}$ | $(340.8 \pm 1.2) \times 10^{-10}$ | $(1330.4 \pm 3.4) \times 10^{-5}$ |
| Tungsten | (55.5 ± 10^{-6}) | (-2.7 ± 6.1) | (55.5 ± 10^{-6}) | (-2.7 ± 6.1) | $(997.5 \pm 3.6) \times 10^{-13}$ | $(1961.6 \pm 5.7) \times 10^{-5}$ |

Typical fitting parameters for the fitting equations

| Material | $h(t) = h_0 + a(t - t_0)^m + kt$ | | | | | $h(t) = h_e + \sum_{i=1}^n h_i(1 - e^{-\frac{t}{\tau_i}})$ | | | | |
|-----------|----------------------------------|------------------------------------|-------------------|--------------------------|-----------------------------------|--|--------------------------------------|--------------------|------------------------------------|-------------------|
| | h_0 | a | t_0 | m | k | h_e | h_1 | τ_1 | h_2 | τ_2 |
| Aluminium | $(2.2 \pm 1.7) \times 10^{-7}$ | $(1.6) \times 10^{-7}$ | 63.0 ± 1.7 | 0.081 ± 0.057 | $(152.3 \pm 7.7) \times 10^{-12}$ | $(3703.9 \pm 3.6) \times 10^{-10}$ | $(898.1 \pm 8.1) \times 10^{-7}$ | 602316.2 ± 0.0 | $(1193.0 \pm 3.2) \times 10^{-10}$ | 107.12 ± 0.88 |
| Magnesium | $(-2.5 \pm 5.5) \times 10^{-6}$ | $(0.28 \pm 55.5) \times 10^{-6}$ | (62.8 ± 2.9) | 0.01 ± 0.10 | $(32.5 \pm 1.0) \times 10^{-11}$ | $(296.3 \pm 1.3) \times 10^{-9}$ | $(1172.6 \pm 6.5) \times 10^{-9}$ | (3038.5 ± 0.0) | $(918.4 \pm 7.7) \times 10^{-10}$ | 76.8 ± 1.6 |
| Lead | $(2.7 \pm 13.1) \times 10^{-6}$ | $(-2.7 \pm 13.0) \times 10^{-6}$ | 42.2 ± 6.1 | (-0.02 ± 0.12) | $(1.97 \pm 2.7) \times 10^{-11}$ | $(146.0 \pm 2.5) \times 10^{-8}$ | $(179.1 \pm 8.2) \times 10^{-8}$ | 21.443 ± 0.093 | $(267.0 \pm 2.1) \times 10^{-9}$ | 589.3 ± 8.3 |
| Tin | $(80.39) \times 10^{-5}$ | $(-1.41 \pm 80.38) \times 10^{-5}$ | (62.9 ± 2.67) | (-0.00157 ± 0.09326) | $(29.9 \pm 1.3) \times 10^{-11}$ | $(2304.2 \pm 2.6) \times 10^{-10}$ | $(1.12 \pm 12881.61) \times 10^{-7}$ | (243.8 ± 0.0) | $(1.7 \pm 12881.6) \times 10^{-7}$ | (243.8 ± 6.5) |
| Silver | $(7.9 \pm 340.9) \times 10^{-6}$ | $(-7.8 \pm 340.9) \times 10^{-6}$ | (62.6 ± 2.3) | (-0.00179 ± 0.08054) | $(104.9 \pm 6.9) \times 10^{-12}$ | $(1044.2 \pm 1.1) \times 10^{-10}$ | $(8.8 \pm 41741.8) \times 10^{-8}$ | (178.0 ± 0.7) | $(4.0 \pm 41741.8) \times 10^{-8}$ | (178.0 ± 0.0) |
| Tungsten | $(-4.6 \pm 87.3) \times 10^{-6}$ | $(4.8 \pm 87.3) \times 10^{-6}$ | (63.1 ± 1.3) | (0.00251 ± 0.04555) | $(80.8 \pm 3.5) \times 10^{-12}$ | $(62.7 \pm 3.5) \times 10^{-8}$ | $(149.0 \pm 2.5) \times 10^{-9}$ | (678.2 ± 18.6) | $(86.1 \pm 3.5) \times 10^{-8}$ | (19.5 ± 0.2) |

Table 9.1: Fitting parameters for all the fitted equations (except for Eq.(6.5)) STS tests across all materials. Some parameters return errors much greater than the estimated value. For the well fitted equations, this is accounted for by a degeneracy in the fitting parameters, whereby multiple combinations fitting parameters could produce the same fit.

| Material | Typical fitting parameters for the fitting equations | | | | | |
|-----------|--|------------------------------------|-------------------|-----------------------------------|----------------------------------|-----------------------|
| | h_0 | $h(t) = h_0 + A \ln(t - t_0) + kt$ | t_0 | k | $h(t) = a(1 - e^{-bt})$ | b |
| Aluminium | $(391.2 \pm 2.6) \times 10^{-9}$ | $(129.4 \pm 6.3) \times 10^{-10}$ | 7.21 ± 0.73 | $(212.4 \pm 3.2) \times 10^{-12}$ | $(518.1 \pm 2.7) \times 10^{-9}$ | 0.08579 ± 0.00651 |
| Tin | $(482.9 \pm 6.3) \times 10^{-9}$ | $(32.7 \pm 1.4) \times 10^{-9}$ | -0.84 ± 1.44 | $(89.4 \pm 5.2) \times 10^{-12}$ | $(683.2 \pm 2.5) \times 10^{-9}$ | 0.10756 ± 0.0068 |
| Tungsten | $(99.5 \pm 7.5) \times 10^{-8}$ | $(-10.5 \pm 1.0) \times 10^{-8}$ | -1647.8 ± 0.0 | $(179.3 \pm 5.4) \times 10^{-12}$ | $(246.9 \pm 1.2) \times 10^{-9}$ | 0.1289 ± 0.0131 |

| Material | Typical fitting parameters for the fitting equations | | | | | | | | | | |
|-----------|--|-------------------------------------|--------------------|---|------------------------------------|-------------------------------------|----------------------------------|----------------------------------|----------------------------------|---------------------------------|------------------|
| | h_0 | a | t_0 | m | k | h_e | t_1 | h_1 | τ_1 | h_2 | τ_2 |
| Aluminium | $(6.5 \pm 1841.0) \times 10^{-5}$ | $(6.5 \pm 1841.0) \times 10^{-5}$ | 1.0 ± 3.2 | 0.0002489 ± 0.0732021 | $(199.9 \pm 7.1) \times 10^{-12}$ | $(367.7 \pm 5.1) \times 10^{-9}$ | $(68.2 \pm 4.9) \times 10^{-9}$ | $(187.4 \pm 8.1) \times 10^{-9}$ | 13.7 ± 1.0 | $(32.6 \pm 1.3) \times 10^{-8}$ | 891.2 ± 50.3 |
| Tin | $(5.0 \pm 18441.6) \times 10^{-5}$ | $(5.0 \pm 18441.6) \times 10^{-5}$ | 0.050268 ± 0.0 | $1 \times 10^{-9} \pm 2.05920121796 \times 105 \frac{h_1}{h_0} \times 10^{-12}$ | $(265.5 \pm 2.7) \times 10^{-9}$ | $(543.9 \pm 2.7) \times 10^{-9}$ | $(187.4 \pm 8.1) \times 10^{-9}$ | 512.0 ± 52.8 | $(69.2 \pm 2.6) \times 10^{-9}$ | 32.7 ± 2.7 | |
| Tungsten | $(2.9 \pm 228763.1) \times 10^{-4}$ | $(2.9 \pm 228763.1) \times 10^{-4}$ | 0.030255 ± 0.0 | $(1.1 \pm 15222.0) \times 10^{-9}$ | $(1237.0 \pm 2.3) \times 10^{-13}$ | $(21492.0 \pm 8.3) \times 10^{-11}$ | $(64.0 \pm 3.4) \times 10^{-7}$ | 14896.6 ± 0.0 | $(-16.2 \pm 1.2) \times 10^{-7}$ | 5166.3 ± 0.0 | |

Table 9.2: Fitting parameters for all the fitted equations (except for Eq.(6.5))for LTS tests across all materials. Some parameters return errors much greater than the estimated value. For the well fitted equations, this is accounted for by a degeneracy in the fitting parameters, whereby multiple combinations fitting parameters could produce the same fit.

| Material | $h(t) = h_0 + A \ln(t - t_0) + kt$ | | $h(t) = h_0 + a(t - t_0)^m + kt$ | | $h(t) = h_0 + \sum_{i=1}^n h_i(1 - e^{-\frac{t}{\tau_i}})$ | | $h(t) = h_0 + h_1 t + h_2 t^2 \dots h_n t^n (n = 1, 2, \dots, 10)$ | |
|-----------|------------------------------------|--------------------|----------------------------------|--------------------|--|----------------------|--|--------------------|
| | $n(\chi_r^2 \approx 1)$ | $n(\Delta t = 5s)$ | $n(\Delta t = 300s)$ | $n(\Delta t = 5s)$ | $n(\Delta t = 5s)$ | $n(\Delta t = 300s)$ | $n(\chi_r^2 \approx 1)$ | $n(\Delta t = 5s)$ |
| aluminium | 13.2±16.1 | 6398.1±12758.1 | 5.3±2.2 | 11.9±17.2 | 9.3±6.5 | 4.7±1.6 | 22.1±58.0 | 4.8±1.8 |
| magnesium | 2.5±0.9 | 2.5±1.8 | 2.4±0.7 | 1.2±0.4 | 2.3±0.7 | 2.5±1.1 | 0.6±4.9 | 2.3±0.6 |
| lead | 1.3±1.0 | 1.0±0.7 | 2.0±1.7 | 1.7±1.9 | 1.1±0.8 | 1.2±0.8 | 19.9±20.0 | 1.9±1.6 |
| tin | 4.2±0.6 | 5.5±2.0 | 2.9±1.1 | 2.4±2.1 | 2.5±0.8 | 2.0±1.2 | -22.0 | 2.1 |
| tungsten | 2.0±1.1 | 1.4±0.7 | 4.0±2.1 | 1.7±1.2 | 1.9±1.1 | 2.0±1.2 | 17.1±50.1 | 22.5±61.1 |
| silver | 3.8±3.4 | 4.4±5.6 | 2.6±0.3 | 1.2±0.1 | 3.5±2.0 | 2.7±3.1 | 75.3±117.3 | 74.9±106.5 |

Table 9.3: Different evaluations of n depending on how $\ln \sigma$ vs. $\ln \dot{\epsilon}$ (evaluated Through the combined method of fitting and tangential analysis) is treated from STS data. Results are shown for when $\ln \sigma$ vs. $\ln \dot{\epsilon}$ becomes most linear from the end of the test ($\chi_r^2 \approx 1$), when only the last 2 seconds of the data is considered and when the entire data set is considered.

| Material | Peak load [μN] | Loading rate[μN/s] | h(t) = h ₀ + A ln(t - t ₀) + kt | | | h(t) = h ₀ + a(t - t ₀) ^m + kt | | | h(t) = h ₀ + Σ _{i=1} ⁿ h _i (1 - e ^{-$\frac{t}{\tau_i}$}) | | | |
|---------------------|----------------|--------------------|--|-------------|---------------|--|---------------|---------------|---|---------------|---------------|-----------|
| | | | n (X ² ≈ 1) | n (Δt = 2s) | n (Δt = 300s) | n (X ² ≈ 1) | n (Δt = 2s) | n (Δt = 300s) | n (X ² ≈ 1) | n (Δt = 2s) | n (Δt = 300s) | |
| Cu57.5Al10Zr7.5Ti15 | 2000 | 500 | 0.3±0.0 | 0.3 | 0.3 | 1990.1±3185.0 | 2328.0±3647.2 | 1.6±1.3 | 9.4±8.4 | 4918.3±8283.1 | 3656.7±6013.0 | 7.8±6.5 |
| Cu57.5Hf97.5Ti15 | 2000 | 1000 | 3.1±2.6 | 2.5±2.1 | 3.4±2.9 | 2.2±1.9 | 1.6±1.3 | 5.5±4.5 | 3.2±2.8 | 1.5±0.4 | 0.8 | 3.2±2.7 |
| Cu57.5Hf97.5Ti15 | 2000 | 2000 | 6.6±8.0 | 9.5±12.5 | 2.1±1.1 | 86.0±41.6 | 127.0±209.9 | 3.7±0.7 | 5.1±0.8 | 264.8±450.8 | 359.5±611.2 | 5.6±4.6 |
| Cu57.5Hf97.5Ti15 | 6000 | 500 | 12.7±0.2 | 19.0±1.0 | 5.4±0.8 | 4.2±0.1 | 0.6±0.1 | 0.8±0.7 | 0.8±0.7 | 37.4±38.7 | 57.2±61.9 | 0.9±0.4 |
| Cu57.5Hf97.5Ti15 | 6000 | 1000 | 0.8±0.6 | 1.0±0.7 | non-linear | 0.9±0.4 | 0.7±0.3 | 1.5±1.6 | 1.5±1.6 | 1.0±0.6 | 1.2±0.9 | 1.5±1.6 |
| Cu57.5Hf97.5Ti15 | 6000 | 2000 | 1.8±2.0 | 2.4±2.8 | non-linear | 0.9±0.7 | 0.7±0.3 | 2.3±2.3 | 2.3±2.3 | 2.1±1.4 | 3.0±1.6 | 3.0±1.6 |
| Cu57.5Hf97.5Ti15 | 10000 | 500 | 1.3±1.1 | 0.9±0.3 | 2.2±2.2 | 1.3±0.8 | 0.8±0.4 | 0.8±0.7 | 0.8±0.7 | 1.2±0.7 | 1.2±0.7 | 2.0±2.0 |
| Cu57.5Hf97.5Ti15 | 10000 | 1000 | 5.3±3.1 | 7.3±4.8 | 3.9±2.0 | 2.8±2.4 | 2.8±3.6 | 4.3±2.0 | 4.3±2.0 | 5.9±4.3 | 7.7±6.3 | 3.9±2.0 |
| Cu57.5Hf97.5Ti15 | 10000 | 2000 | 119.8±167.8 | 180.0±292.9 | 5.3±2.0 | 4.1±4.7 | 4.0±4.8 | 4.4±4.8 | 4.4±4.8 | 26.7±36.1 | 36.8±50.1 | 4.0±4.9 |
| Zr44Cu44Al6Ag6 | 2000 | 500 | 4.1±2.2 | 3.2±1.7 | 5.6±2.6 | 5.4±3.8 | 5.4±5.2 | 5.4±5.2 | 5.4±5.2 | 2.3±1.4 | 2.5±1.9 | 5.1±2.2 |
| Zr44Cu44Al6Ag6 | 2000 | 1000 | 36.0±68.6 | 52.9±103.2 | 3.4±2.5 | 3.2±3.6 | 3.5±5.2 | 3.3±2.2 | 3.3±2.2 | 8.7±15.5 | 11.3±21.6 | 3.3±2.4 |
| Zr44Cu44Al6Ag6 | 2000 | 2000 | 3.3±1.9 | 2.8±1.8 | 4.1±1.8 | 3.6±2.2 | 3.5±2.4 | 4.3±1.8 | 4.3±1.8 | 1.1±0.3 | 0.9±0.6 | 3.8±1.5 |
| Zr44Cu44Al6Ag6 | 6000 | 500 | 1.1±0.3 | 0.8±0.2 | 2.0±0.5 | 1.1±0.4 | 0.8±0.2 | 1.8±0.9 | 1.8±0.9 | 1.5±0.6 | 1.1±1.0 | 2.1±0.6 |
| Zr44Cu44Al6Ag6 | 6000 | 1000 | 1.6±0.5 | 1.1±0.4 | 2.8±1.0 | 1.6±0.6 | 1.2±0.5 | 2.8±1.0 | 2.8±1.0 | 2.7±1.3 | 3.6±1.9 | 3.0±1.1 |
| Zr44Cu44Al6Ag6 | 6000 | 2000 | 1.8±1.5 | 2.4±2.2 | 1.4±1.2 | 0.9±0.5 | 0.7±0.2 | 1.4±1.1 | 1.4±1.1 | 2.4±1.6 | 3.3±2.7 | 1.5±1.1 |
| Zr44Cu44Al6Ag6 | 10000 | 500 | 0.8±0.2 | 0.6±0.1 | 2.6±0.8 | 0.8±0.1 | 0.6±0.1 | 1.3±0.3 | 1.3±0.3 | 0.8±0.4 | 0.8±0.6 | 1.2±0.3 |
| Zr44Cu44Al6Ag6 | 10000 | 1000 | 1.6±0.6 | 1.2±0.4 | 2.6±0.8 | 1.6±0.5 | 1.2±0.4 | 2.5±0.8 | 2.5±0.8 | 2.2±1.0 | 2.9±1.4 | 2.6±0.8 |
| Zr44Cu44Al6Ag6 | 10000 | 2000 | 6.4±13.0 | 8.6±19.0 | 3.2±3.6 | 2.8±4.5 | 3.1±5.9 | 3.7±3.5 | 3.7±3.5 | 6.8±13.6 | 9.1±18.8 | 3.3±3.9 |
| Zr57Cu90Al10Ni8Ti5 | 2000 | 500 | 4.1±3.1 | 5.8±4.9 | 2.1±0.9 | 2.9±3.5 | 3.3±5.2 | 2.7±1.7 | 2.7±1.7 | 6.6±7.4 | 8.8±10.3 | 2.7±1.8 |
| Zr57Cu90Al10Ni8Ti5 | 2000 | 1000 | 34.1 | 52.2 | 3.5 | 7004.0±11842.1 | 4366.9±7136.7 | 13.7±11.3 | 7203.3±11919.1 | 4540.9±7102.7 | 13.4±9.8 | 13.4±9.8 |
| Zr57Cu90Al10Ni8Ti5 | 2000 | 2000 | 9.6 | 12.8 | 3.9 | 3.0 | 4.1 | 5.7 | 5.7 | 4.3 | 2.2 | 5.3 |
| Zr57Cu90Al10Ni8Ti5 | 6000 | 300 | 0.2±0.2 | 0.3±0.2 | 0.2±0.2 | 0.3±0.1 | 0.5 | 0.2±0.2 | 0.2±0.2 | -0.2±0.4 | -0.7±1.2 | 0.4±0.3 |
| Zr57Cu90Al10Ni8Ti5 | 6000 | 1000 | 0.6±0.5 | 0.8±0.6 | 0.5±0.6 | 0.3±0.3 | 0.5±0.1 | 0.4±0.6 | 0.4±0.6 | 1.1±2.1 | 1.7±3.6 | 0.6±0.8 |
| Zr57Cu90Al10Ni8Ti5 | 6000 | 2000 | 13.4±16.1 | 20.4±25.2 | 3.6±2.6 | 1.7±0.8 | 1.1±0.5 | 3.1±2.0 | 3.1±2.0 | 10.4±13.6 | 14.7±18.9 | 3.3±2.2 |
| Zr57Cu90Al10Ni8Ti5 | 10000 | 500 | -1.2 | -0.6 | -1.2 | -0.1 | 0.4 | -1.5 | -1.5 | 0.5 | 0.5 | 0.5 |
| Zr57Cu90Al10Ni8Ti5 | 10000 | 1000 | 7.3 | 10.6 | 6.2 | 4.8 | 3.1 | 6.0 | 6.0 | 6.7 | 9.1 | 6.2 |
| Zr57Cu90Al10Ni8Ti5 | 10000 | 2000 | 4.3 | 6.3 | 2.8 | 19.0±24.4 | 25.6±34.3 | 13.1±14.8 | 13.1±14.8 | 49.5±62.0 | 67.8±84.8 | 13.3±15.1 |

Table 9.4: The conventionally evaluated n values for the fitting equation analysis on the tested Metallic glass samples when data is considered at 2s, 300s from the end of the test and also when the data is approximated to be linear from X² analysis. Just as in the crystalline samples, these tests also show wide variability in the results represented by the larger errors associated with each n value. In addition, the creep behaviour was often not reproducible, resulting in some estimates of n from a single test (values with no errors).

| Material | n | $h(t) = h_0 + A \ln(t - t_0) + kt$ | | $h(t) = h_0 + a(t - t_0)^m + kt$ | | $h(t) = h_e + \sum_{i=1}^n h_i(1 - e^{-\frac{t}{\tau_i}})$ | | Tangential analysis | | | |
|-----------|-----|------------------------------------|--------------------|----------------------------------|-------------------------|--|----------------------|-------------------------|--------------------|----------------------|---|
| | | $n(\chi_r^2 \approx 1)$ | $n(\Delta t = 2s)$ | $n(\Delta t = 300s)$ | $n(\chi_r^2 \approx 1)$ | $n(\Delta t = 2s)$ | $n(\Delta t = 300s)$ | $n(\chi_r^2 \approx 1)$ | $n(\Delta t = 2s)$ | $n(\Delta t = 300s)$ | n (ln σ vs. ln $\dot{\epsilon} = 100s$) |
| aluminium | 4.4 | 13.2±16.1 | 40206.1±80373.0 | 5.3±2.2 | 9.0±11.2 | 12.2±17.8 | 4.8±1.6 | 9.3±6.5 | 12.2±9.6 | 4.7±1.6 | 3.8 ± 1.7 |
| magnesium | 5.0 | 2.5±0.9 | 2.5±1.9 | 2.4±0.7 | 1.6±0.3 | 1.2±0.4 | 2.5±0.8 | 2.3±0.7 | 2.5±1.1 | 2.5±0.8 | 1.5 ± 0.3 |
| lead | 5.0 | 1.3±1.0 | 1.0±0.7 | 2.0±1.7 | 1.8±1.8 | 1.7±1.9 | 2.0±1.7 | 1.1±0.8 | 1.2±0.8 | 1.9±1.6 | 0.1 ± 0.6 |
| tin | 5.0 | 4.2±0.6 | 5.5±2.1 | 2.9±1.1 | 2.5±1.8 | 2.4±2.1 | 2.9±1.2 | 2.5±0.8 | 2.6±2.3 | 2.8±1.0 | 2.0 ± 0.4 |
| tungsten | 4.7 | 2.0±1.1 | 1.4±0.7 | 4.0±2.1 | 2.4±1.6 | 1.7±1.2 | 3.9±2.1 | 1.9±1.1 | 2.0±1.2 | 3.8±1.9 | 1.5 ± 0.8 |
| silver | 4.3 | 3.8±3.4 | 4.5±5.7 | 2.6±0.3 | 1.6±0.1 | 1.2±0.1 | 2.6±0.3 | 2.5±2.0 | 2.7±3.2 | 2.5±0.3 | 1.6 ± 0.4 |

Table 9.5: Different evaluations of n depending on how $\ln \sigma - \ln \dot{\epsilon}$ (evaluated analytically from fitted equations) is treated from STS results. Results are shown for when $\ln \sigma$ vs. $\ln \dot{\epsilon}$ becomes most linear from the end of the test ($\chi_r^2 \approx 1$), when only the last 2 seconds of the data is considered and when the entire data set is considered. The errors associated with each estimate of n shows that whilst the value of n may sometimes coincide to the literature values, the error associated with it makes the estimate invalid for distinguishing between different creep behaviours in materials.

References

- [1] D. M. Teter, “Computational Alchemy: The Search for New Superhard Materials,” *MRS Bulletin*, vol. 23, no. January, pp. 22–27, 1998.
- [2] Liquidmetal, “Liquidmetal amorphous alloy in hybrid knife is 25% harder than stainless steel,” 2016.
- [3] T. Burgess and M. Ferry, “Nanoindentation of metallic glasses,” *Materials Today*, vol. 12, pp. 24–32, jan 2009.
- [4] C. Schuh, T. Hufnagel, and U. Ramamurty, “Mechanical behavior of amorphous alloys,” *Acta Materialia*, vol. 55, pp. 4067–4109, jul 2007.
- [5] Y. Q. Cheng and E. Ma, “Atomic-level structure and structure–property relationship in metallic glasses,” *Progress in Materials Science*, vol. 56, no. 4, pp. 379–473, 2011.
- [6] M. M. Trexler and N. N. Thadhani, “Mechanical properties of bulk metallic glasses,” *Progress in Materials Science*, vol. 55, pp. 759–839, nov 2010.
- [7] X.-Q. Chen, H. Niu, D. Li, and Y. Li, “Modeling hardness of polycrystalline materials and bulk metallic glasses,” *Intermetallics*, vol. 19, pp. 1275–1281, 2011.
- [8] J. Zorzi and C. Perottoni, “Estimating Young’s modulus and Poisson’s ratio by instrumented indentation test,” *Materials Science and Engineering: A*, vol. 574, pp. 25–30, jul 2013.
- [9] W. Klement, R. H. Willens, and P. Duwez, “Non-crystalline Structure in Solidified Gold-Silicon Alloys,” *Nature*, vol. 187, no. 4740, pp. 869–870, 1960.
- [10] M. Ashby and a. Greer, “Metallic glasses as structural materials,” *Scripta Materialia*, vol. 54, pp. 321–326, feb 2006.
- [11] A. Inoue and A. Takeuchi, “Recent development and application products of bulk glassy alloys,” *Acta Materialia*, vol. 59, pp. 2243–2267, apr 2011.
- [12] A. L. Greer, N. Karpe, and J. Bottiger, “Diffusional Aspects of the Solid-State Amorphization Reaction,” *Journal of Alloys and Compounds*, vol. 194, no. 2, pp. 199–211, 1993.
- [13] W. Johnson, “Thermodynamic and kinetic aspects of the crystal to glass transformation in metallic materials,” *Progress in Materials Science*, vol. 30, pp. 81–134, 1986.
- [14] A. O. Aning, Z. Wang, and T. H. Courtney, “Tungsten solution kinetics and amorphization of nickel in mechanically alloyed NiW alloys,” *Acta Metallurgica Et Materialia*, vol. 41, no. 1, pp. 165–174, 1993.
- [15] H. Chen, “The Glass Transition in Glassy Alloys: Effects of Atomic Sizes and the Heats of Mixing.,” *Acta Metallurgica*, vol. 22, pp. 897–900, 1974.

- [16] H. Chen and D. Turnbull, "Formation, stability and structure of palladium-silicon based alloy glasses," *Acta Metallurgica*, vol. 17, no. August, pp. 1021–1031, 1969.
- [17] J. Plummer, *On the physical aspects that control mechanical deformation in bulk metallic glasses*. PhD thesis, 2012.
- [18] Materion, "Bulk Metallic Glass," tech. rep., 2016.
- [19] S. Pauly, L. Löber, R. Petters, M. Stoica, S. Scudino, U. Kühn, and J. Eckert, "Processing metallic glasses by selective laser melting," *Materials Today*, vol. 16, no. 1-2, pp. 37–41, 2013.
- [20] G. Parisi and F. Sciortino, "Structural glasses: Flying to the bottom.," *Nature materials*, vol. 12, pp. 94–95, mar 2013.
- [21] M. D. Demetriou, M. E. Launey, G. Garrett, J. P. Schramm, D. C. Hofmann, W. L. Johnson, and R. O. Ritchie, "A damage-tolerant glass.," *Nature materials*, vol. 10, no. February, pp. 123–128, 2011.
- [22] D. C. Hofmann, J.-Y. Suh, A. Wiest, G. Duan, M.-L. Lind, M. D. Demetriou, and W. L. Johnson, "Designing metallic glass matrix composites with high toughness and tensile ductility.," *Nature*, vol. 451, pp. 1085–9, feb 2008.
- [23] A. Inoue, "Stabilization of metallic supercooled liquid and bulk amorphous alloys," *Acta materialia*, vol. 48, pp. 279–306, 2000.
- [24] S. Ding, Y. Liu, Y. Li, Z. Liu, S. Sohn, F. J. Walker, and J. Schroers, "Combinatorial development of bulk metallic glasses," *Nature Materials*, vol. 13, no. April, pp. 1–7, 2014.
- [25] Y. Li, Q. Guo, J. a. Kalb, and C. V. Thompson, "Matching glass-forming ability with the density of the amorphous phase.," *Science (New York, N.Y.)*, vol. 322, no. 5909, pp. 1816–1819, 2008.
- [26] R. Busch, J. Schroers, and W. H. Wang, "Thermodynamics and Kinetics of Bulk Metallic Glass," *MRS Bulletin*, vol. 32, no. August, pp. 620–623, 2007.
- [27] D. Porter, K. E. Easterling, and M. Sherif, *Phase Transformations in Metals and Alloys*. CRC Press, 3 ed., 2009.
- [28] M.-B. Tang, D.-Q. Zhao, M.-X. Pang, and W.-H. Wang, "Binary Cu–Zr Bulk Metallic Glasses," *Chinese Physics Letters*, vol. 21, no. 5, pp. 901–903, 2004.
- [29] D. Wang, Y. Li, B. B. Sun, M. L. Sui, K. Lu, and E. Ma, "Bulk metallic glass formation in the binary Cu–Zr system," *Applied Physics Letters*, vol. 84, no. 20, pp. 4029–4031, 2004.
- [30] D. Xu, B. Lohwongwatana, G. Duan, W. L. Johnson, and C. Garland, "Bulk metallic glass formation in binary Cu-rich alloy series - Cu 100-xZrx (x=34 , 36, 38.2, 40 at.%) and mechanical properties of bulk Cu64Zr36 glass," *Acta Materialia*, vol. 52, no. 9, pp. 2621–2624, 2004.
- [31] J. Lipton, M. E. Glicksman, and W. Kurz, "Dendritic growth into undercooled alloy metals," *Materials Science and Engineering*, vol. 65, no. 1, pp. 57–63, 1984.
- [32] C. A. Angell, "Formation of glasses from liquids and biopolymers.," *Science (New York, N.Y.)*, vol. 267, no. 5206, pp. 1924–1935, 1995.

- [33] H. Frost and M. Ashby, *Deformation-Mechanism Maps*. Pergamon Press, 1982.
- [34] P. G. Debenedetti and F. H. Stillinger, “Supercooled liquids and the glass transition.,” *Nature*, vol. 410, pp. 259–267, mar 2001.
- [35] M. Goldstein, “Viscous Liquids and the Glass Transition: A Potential Energy Barrier Picture,” *The Journal of Chemical Physics*, vol. 51, no. May 2013, pp. 3728–3739, 1969.
- [36] S. J. Poon, A. Zhu, and G. J. Shiftet, “Poisson’s Ratio and Intrinsic Plasticity of Metallic Glasses,” *Applied Physics Letters*, vol. 92, no. 26, p. 261902, 2008.
- [37] N. Nishiyama and A. Inoue, “Bulk Amorphous, Nano-Crystalline and Nano-Quasicrystalline Alloys IV. Direct Comparison between Critical Cooling Rate and Some Quantitative Parameters for Evaluation of Glass-Forming Ability in Pd-Cu-Ni-P Alloys.,” *Materials Transactions*, vol. 43, no. 8, pp. 1913–1917, 2002.
- [38] G. Adam and J. H. Gibbs, “On the Temperature Dependence of Cooperative Relaxation Properties in Glass-Forming Liquids,” *The Journal of Chemical Physics*, vol. 43, no. 1, p. 139, 1965.
- [39] O. N. Senkov, “Correlation between fragility and glass-forming ability of metallic alloys,” *Physical Review B - Condensed Matter and Materials Physics*, vol. 76, no. 10, pp. 1–6, 2007.
- [40] W. H. Wang, “Correlations between elastic moduli and properties in bulk metallic glasses,” *Journal of Applied Physics*, vol. 99, no. 9, p. 093506, 2006.
- [41] W. L. Johnson and K. Samwer, “A Universal Criterion for Plastic Yielding of Metallic Glasses with a $(T/T_g)^{2/3}$ Temperature Dependence,” *Physical Review Letters*, vol. 95, no. 19, pp. 2–5, 2005.
- [42] H. Wagner, D. Bedorf, S. Küchemann, M. Schwabe, B. Zhang, W. Arnold, and K. Samwer, “Local elastic properties of a metallic glass.,” *Nature Materials*, vol. 10, no. 6, pp. 439–442, 2011.
- [43] L.-M. Wang, Y. Tian, R. Liu, and W. Wang, “A “universal” criterion for metallic glass formation,” *Applied Physics Letters*, vol. 100, no. 26, p. 261913, 2012.
- [44] F. H. Stillinger, “A topographic view of supercooled liquids and glass formation.,” *Science*, vol. 267, no. 5206, pp. 1935–1939, 1995.
- [45] A. Greer, “Atomic transport and structural relaxation in metallic glasses,” *Journal of Non-Crystalline Solids*, vol. 61-62, pp. 737–748, jan 1984.
- [46] D. L. Malandro and D. J. Lacks, “Volume dependence of potential energy landscapes in glasses,” *October*, vol. d, no. June, pp. 5804–5810, 1997.
- [47] D. L. Malandro and D. J. Lacks, “Relationships of shear-induced changes in the potential energy landscape to the mechanical properties of ductile glasses,” *The Journal of Chemical Physics*, vol. 110, no. 9, p. 4593, 1999.
- [48] U. Mizutani, “Electronic Structure of Metallic Glasses,” *Progress in Materials Science*, vol. 28, p. 97, 1983.
- [49] M. Q. Jiang and L. H. Dai, “Short-range-order effects on intrinsic plasticity of metallic glasses,” *Philosophical Magazine Letters*, vol. 90, pp. 269–277, apr 2010.

- [50] E. Rutherford, “The scattering of α and β particles by matter and the structure of the atom,” *Philosophical Magazine*, vol. 92, no. 4, pp. 379–398, 1911.
- [51] T. Scopigno, G. Ruocco, F. Sette, and G. Monaco, “Is the fragility of a liquid embedded in the properties of its glass?,” *Science (New York, N.Y.)*, vol. 302, no. 5646, pp. 849–852, 2003.
- [52] D. B. Miracle, T. Egami, K. M. Flores, and K. F. Kelton, “Structural Aspects of Metallic Glasses,” *MRS Bulletin*, vol. 32, no. 8, pp. 629–634, 2007.
- [53] M. Lee, C.-M. Lee, K.-R. Lee, E. Ma, and J.-C. Lee, “Networked interpenetrating connections of icosahedra: Effects on shear transformations in metallic glass,” *Acta Materialia*, vol. 59, pp. 159–170, jan 2011.
- [54] H. Guo, J. Wen, N. Xiao, Z. Zhang, and M. Sui, “The more shearing, the thicker shear band and heat-affected zone in bulk metallic glass,” *Journal of Materials Research*, vol. 23, pp. 2133–2138, jan 2011.
- [55] D. B. Miracle, “A structural model for metallic glasses,” *Nature Materials*, vol. 3, no. 10, pp. 697–702, 2004.
- [56] F. Jiang, Y. Zhao, L. Zhang, S. Pan, Y. Zhou, L. He, and J. Sun, “Dependence of ductility on free volume in a Cu-Zr-based metallic glass,” *Advanced Engineering Materials*, vol. 11, no. 3, pp. 177–181, 2009.
- [57] X. Gu, K. J. T. Livi, and T. C. Hufnagel, “Structure of Shear Bands in Zirconium-Based Metallic Glasses Observed by Transmission Electron Microscopy,” *MRS Proceedings*, vol. 754, p. CC7.9, feb 2011.
- [58] P. E. Donovan and W. M. Stobbs, “The structure of shear bands in metallic glasses,” *Acta Metallurgica*, vol. 29, no. 8, pp. 1419–1436, 1981.
- [59] W. Nitz, “Principles of Magnetic Resonance Imaging,” pp. 1–52, 2006.
- [60] P. Jónvári, K. Saksl, N. Pryds, B. Lebech, N. P. Bailey, A. Mellergård, R. G. Delaplane, and H. Franz, “Atomic structure of glassy Mg60Cu30Y10 investigated with EXAFS, x-ray and neutron diffraction, and reverse Monte Carlo simulations,” *Physical Review B*, vol. 76, no. 5, p. 054208, 2007.
- [61] H. W. Sheng, E. Ma, H. Z. Liu, and J. Wen, “Pressure tunes atomic packing in metallic glass,” *Applied Physics Letters*, vol. 88, no. 17, p. 171906, 2006.
- [62] J. D. Bernal, “The Structure of Liquids,” *Scientific American*, vol. 203, no. July 1964, pp. 124–134, 1960.
- [63] J. F. Sadoc, J. Dixmier, and A. Guinier, “Theoretical calculation of dense random packings of equal and non-equal sized hard spheres applications to amorphous metallic alloys,” *Journal of Non-Crystalline Solids*, vol. 12, no. 1, pp. 46–60, 1973.
- [64] N. Barnett and U. Landman, “Structure and Dynamics of a Metallic Glass: Molecular-Dynamics Simulations,” *Physical Review Letters*, vol. 55, no. 19, pp. 2035–2038, 1985.
- [65] F. Frank, “Viscosity of Liquids,” in *Proceedings of the Royal Society of London. Series A, Mathematical and Physical Sciences*, vol. 215, pp. 43–46, Royal Society, 1952.

- [66] C. Fan, P. K. Liaw, and C. T. Liu, "Atomistic model of amorphous materials," *Intermetallics*, vol. 17, no. 1-2, pp. 86–87, 2009.
- [67] S. Torquato, T. M. Truskett, and P. G. Debenedetti, "Is Random Close Packing of Spheres Well Defined?," *Physical Review Letters*, vol. 84, no. 10, pp. 2064–2067, 2000.
- [68] H. W. Sheng and E. Ma, "Atomic packing of the inherent structure of simple liquids," *Physical Review E - Statistical, Nonlinear, and Soft Matter Physics*, vol. 69, no. 6 1, pp. 1–4, 2004.
- [69] J. P. K. Doye and D. J. Wales, "The Structure and Stability of Atomic Liquids: From Clusters to Bulk," *Science*, vol. 271, no. 5248, pp. 484–487, 1996.
- [70] P. J. Steinhardt, D. R. Nelson, and M. Ronchetti, "Icosahedral Bond Orientational Order in Supercooled Liquids," *Physical Review Letters*, vol. 47, no. 18, pp. 1297–1300, 1981.
- [71] P. J. Steinhardt, D. R. Nelson, and M. Ronchetti, "Bond-orientational order in liquids and glasses," *Physical Review B*, vol. 28, no. 2, pp. 784–805, 1983.
- [72] M. Dzugutov, "Glass formation in a simple monatomic liquid with icosahedral inherent local order," *Physical Review A*, vol. 46, no. 6, pp. 2984–2987, 1992.
- [73] J. P. K. Doye, D. J. Wales, F. H. M. Zetterling, and M. Dzugutov, "The favored cluster structures of model glass formers," *Journal of Chemical Physics*, vol. 118, no. 6, pp. 2792–2799, 2003.
- [74] P. H. Gaskell, "A new structural model for amorphous transition metal silicides, borides, phosphides and carbides," *Journal of Non-Crystalline Solids*, vol. 32, no. 1-3, pp. 207–224, 1979.
- [75] D. B. Miracle, "The efficient cluster packing model - An atomic structural model for metallic glasses," *Acta Materialia*, vol. 54, no. 16, pp. 4317–4336, 2006.
- [76] Y. Q. Cheng, H. W. Sheng, and E. Ma, "Relationship between structure, dynamics, and mechanical properties in metallic glass-forming alloys," *Physical Review B - Condensed Matter and Materials Physics*, vol. 78, no. 1, pp. 1–7, 2008.
- [77] L. Börjesson, R. L. McGreew, and W. S. Howells, "Fractal aspects of superionic glasses from Reverse Monte Carlo simulations," *Philosophical Magazine Part B*, vol. 65, no. 2, pp. 261–271, 1992.
- [78] C. Fan, P. Liaw, V. Haas, J. Wall, H. Choo, a. Inoue, and C. Liu, "Structures and mechanical behaviors of Zr₅₅Cu₃₅Al₁₀ bulk amorphous alloys at ambient and cryogenic temperatures," *Physical Review B*, vol. 74, no. 1, pp. 1–6, 2006.
- [79] J. C. Ye, J. Lu, C. T. Liu, Q. Wang, and Y. Yang, "Atomistic free-volume zones and inelastic deformation of metallic glasses," *Nature Materials*, vol. 9, no. 8, pp. 619–23, 2010.
- [80] F. C. Frank and J. S. Kasper, "Complex alloy structures regarded as sphere packings. I. Definitions and basic principles," *Acta Crystallographica*, vol. 11, no. 3, pp. 184–190, 1958.
- [81] F. C. Frank and J. S. Kasper, "Complex alloy structures regarded as sphere packings. II. Analysis and classification of representative structures," *Acta Crystallographica*, vol. 12, no. 7, pp. 483–499, 1959.

- [82] A. Takeuchi and A. Inoue, "Classification of Bulk Metallic Glasses by Atomic Size Difference, Heat of Mixing and Period of Constituent Elements and Its Application to Characterization of the Main Alloying Element," *Materials Transactions*, vol. 46, no. 12, pp. 2817–2829, 2005.
- [83] U. Mizutani, *Introduction to the Electron Theory of metals*. Cambridge University Press, 2001.
- [84] J. J. Lewandowski and A. L. Greer, "Temperature rise at shear bands in metallic glasses," *Nature Materials*, vol. 5, pp. 15–18, dec 2005.
- [85] H. Chen, J. Krause, and E. Coleman, "Elastic constants, hardness and their implications to flow properties of metallic glasses," *Journal of Non-Crystalline Solids*, vol. 18, pp. 157–171, 1975.
- [86] J. J. Lewandowski, M. Shazly, and A. S. Nouri, "Intrinsic and extrinsic toughening of metallic glasses," *Scripta Materialia*, vol. 54, no. 3, pp. 337–341, 2006.
- [87] G. N. Greaves, A. L. Greer, R. S. Lakes, and T. Rouxel, "Poisson's ratio and modern materials," *Nature materials*, vol. 10, no. October, pp. 823–838, 2011.
- [88] A. M. Brown and M. F. Ashby, "Correlations for Diffusion Constants.," *Acta Metallurgica*, vol. 28, no. 8, pp. 1085–1101, 1980.
- [89] U. Mizutani, "Electron Transport Properties of Amorphous Alloys," *IEEE Translation Journal on Magnetism in Japan*, vol. 1, no. 2, pp. 185–194, 1985.
- [90] H. Y. Bai, C. Z. Tong, and P. Zheng, "Electrical resistivity in Zr₄₈Nb₈Cu₁₂Fe₈Be₂₄ glassy and crystallized alloys," *Journal of Applied Physics*, vol. 95, no. 3, pp. 1269–1273, 2004.
- [91] D. Naugle, "Electron transport in amorphous metals," *Journal of Physics and Chemistry of Solids*, vol. 45, no. 4, pp. 367–388, 1984.
- [92] C. Kittel, *Introduction to Solid State Physics*. Berkeley: John Wiley & Sons, Inc, 8th ed., 2010.
- [93] M. Ziman, "A theory of the electrical properties of liquid metals. I: The monovalent metals," *Philosophical Magazine*, vol. 6, no. 68, 1961.
- [94] P. Anderson, "Absence of Diffusion in Certain Random Lattices," *Physical Review Letters*, vol. 109, p. 1492, 1958.
- [95] N. Mott, "The electrical resistivity of liquid transition metals," *Philosophical Magazine*, vol. 26, no. 6, pp. 1249–1261, 1972.
- [96] R. Y. Umetsu, R. Tu, and T. Goto, "Thermal and Electrical Transport Properties of Zr-Based Bulk Metallic Glassy Alloys with High Glass-Forming Ability," *Materials Transactions*, vol. 53, no. 10, pp. 1721–1725, 2012.
- [97] A. Dubach, K. E. Prasad, R. Raghavan, J. F. Loffler, J. Michler, and U. Ramamurty, "Free-volume dependent pressure sensitivity of Zr-based bulk metallic glass," *Journal of Materials Research*, vol. 24, no. 8, pp. 2697–2704, 2009.
- [98] J.-C. Lee, K.-W. Park, K.-H. Kim, E. Fleury, B.-J. Lee, M. Wakeda, and Y. Shibutani, "Origin of the plasticity in bulk amorphous alloys," *Journal of Materials Research*, vol. 22, pp. 3087–3097, jan 2007.

- [99] C. A. Schuh, A. C. Lund, and T. Nieh, “New regime of homogeneous flow in the deformation map of metallic glasses: elevated temperature nanoindentation experiments and mechanistic modeling,” *Acta Materialia*, vol. 52, no. 20, pp. 5879–5891, 2004.
- [100] M. Chen, “Mechanical Behavior of Metallic Glasses: Microscopic Understanding of Strength and Ductility,” *Annual Review of Materials Research*, vol. 38, pp. 445–469, aug 2008.
- [101] A. Argon and H. Kuo, “Plastic flow in a disordered bubble raft (an analog of a metallic glass),” *Materials Science and Engineering*, vol. 39, pp. 101–109, 1979.
- [102] A. S. Argon, “Plastic deformation in metallic glasses,” *Acta Metallurgica*, vol. 27, pp. 47–58, 1979.
- [103] D. Pan, A. Inoue, T. Sakurai, and M. W. Chen, “Experimental characterization of shear transformation zones for plastic flow of bulk metallic glasses,” *Proceedings of the National Academy of Sciences of the United States of America*, vol. 105, no. 39, pp. 14769–14772, 2008.
- [104] M. H. Cohen and D. Turnbull, “Molecular Transport in Liquids and Glasses,” *The Journal of Chemical Physics*, vol. 31, no. 5, p. 1164, 1959.
- [105] F. Spaepen, “A microscopic mechanism for steady state inhomogeneous flow in metallic glasses,” *Acta Metallurgica*, vol. 25, no. 4, pp. 407–415, 1977.
- [106] P. Müllner, “In-plane edge somigliana dislocation dipoles and quadrupoles,” *Scripta Metallurgica et Materialia*, vol. 33, pp. 1181–1186, oct 1995.
- [107] G. Cargill, “Dense random packing of hard spheres as a structural model for noncrystalline metallic solids,” *Journal of Applied Physics*, vol. 41, no. 5, p. 2248, 1970.
- [108] O. Bobrov and V. Khonik, “Inhomogeneous flow via dislocations in metallic glasses: a survey of experimental evidence,” *Journal of Non-Crystalline Solids*, vol. 193, pp. 603–607, 1995.
- [109] A. L. Greer, Y. Q. Cheng, and E. Ma, “Shear bands in metallic glasses,” *Materials Science and Engineering: R: Reports*, vol. 74, pp. 71–132, apr 2013.
- [110] W. H. Wang, “The elastic properties, elastic models and elastic perspectives of metallic glasses,” *Progress in Materials Science*, vol. 57, pp. 487–656, 2012.
- [111] A. Castellero, B. Moser, D. I. Uhlhaupt, F. H. D. H. D. Torre, and J. F. Löffler, “Room-temperature creep and structural relaxation of Mg–Cu–Y metallic glasses,” *Acta Materialia*, vol. 56, pp. 3777–3785, sep 2008.
- [112] D. D. Liang, X. D. Wang, Y. Ma, K. Ge, Q. P. Cao, and J. Z. Jiang, “Decoupling of pronounced beta and alpha relaxations and related mechanical property change,” *Journal of Alloys and Compounds*, vol. 577, pp. 257–260, nov 2013.
- [113] D. Weaire, M. Ashby, J. Logan, and M. Weins, “On the use of pair potentials to calculate the properties of amorphous metals,” *Acta Metallurgica*, vol. 19, no. 8, pp. 779–788, 1971.
- [114] A. Concustell, S. Godard-Desmarest, M. Carpenter, N. Nishiyama, and A. L. Greer, “Induced elastic anisotropy in a bulk metallic glass,” *Scripta Materialia*, vol. 64, pp. 1091–1094, jun 2011.

- [115] P. Yu, R. J. Wang, D. Q. Zhao, and H. Y. Bai, "Temperature dependence of elastic moduli in bulk metallic glasses down to liquid nitrogen temperature," *Applied Physics Letters*, vol. 90, no. 25, 2007.
- [116] C. E. Packard, J. Schroers, and C. a. Schuh, "In situ measurements of surface tension-driven shape recovery in a metallic glass," *Scripta Materialia*, vol. 60, pp. 1145–1148, jun 2009.
- [117] J. Lu, G. Ravichandran, and W. Johnson, "Deformation behavior of the Zr_{41.2}Ti_{13.8}Cu_{12.5}Ni₁₀Be_{22.5} bulk metallic glass over a wide range of strain-rates and temperatures," *Acta Materialia*, vol. 51, pp. 3429–3443, jul 2003.
- [118] P. S. Steif, F. Spaepen, and J. W. Hutchinson, "Strain localization in amorphous metals," *Acta Metallurgica*, vol. 30, no. 2, pp. 447–455, 1982.
- [119] M. L. Falk and J. S. Langer, "Dynamics of Viscoplastic Deformation in Amorphous Solids," vol. 57, no. 6, p. 16, 1997.
- [120] E. Pekarskaya, C. P. Kim, and W. L. Johnson, "In situ transmission electron microscopy studies of shear bands in a bulk metallic glass based composite," *Journal of Materials Research*, vol. 16, no. 9, pp. 2513–2518, 2001.
- [121] R. D. Conner, W. L. Johnson, N. E. Paton, and W. D. Nix, "Shear bands and cracking of metallic glass plates in bending," *Journal of Applied Physics*, vol. 94, no. 2, p. 904, 2003.
- [122] R. D. Conner, Y. Li, W. D. Nix, and W. L. Johnson, "Shear band spacing under bending of Zr-based metallic glass plates," *Acta Materialia*, vol. 52, no. 8, pp. 2429–2434, 2004.
- [123] D. Klaumünzer, R. Maaß, and J. F. Löffler, "Stick-slip dynamics and recent insights into shear banding in metallic glasses," *Journal of Materials Research*, vol. 26, no. 12, pp. 1453–1463, 2011.
- [124] S. X. Song and T. G. Nieh, "Direct measurements of shear band propagation in metallic glasses - An overview," *Intermetallics*, vol. 19, no. 12, pp. 1968–1977, 2011.
- [125] S. X. Song, X. L. Wang, and T. G. Nieh, "Capturing shear band propagation in a Zr-based metallic glass using a high-speed camera," *Scripta Materialia*, vol. 62, no. 11, pp. 847–850, 2010.
- [126] W. J. Wright, M. W. Samale, T. C. Hufnagel, M. M. LeBlanc, and J. N. Florando, "Studies of shear band velocity using spatially and temporally resolved measurements of strain during quasistatic compression of a bulk metallic glass," *Acta Materialia*, vol. 57, no. 16, pp. 4639–4648, 2009.
- [127] H. Neuhäuser, "Rate of shear band formation in metallic glasses," *Scripta Metallurgica*, vol. 12, no. 5, pp. 471–474, 1978.
- [128] C. Pampillo, "Localised shear deformation in a glassy metal," *Scripta Metallurgica*, vol. 6, pp. 915–917, 1972.
- [129] H. J. Leamy, T. T. Wang, and H. S. Chen, "Plastic flow and fracture of metallic glass," *Metallurgical Transactions*, vol. 3, no. 3, pp. 699–708, 1972.
- [130] W. J. Wright, R. B. Schwarz, and W. D. Nix, "Localized heating during serrated plastic flow in bulk metallic glasses," *Materials Science and Engineering A*, vol. 319-321, pp. 229–232, 2001.

- [131] F. H. D. Torre, A. Dubach, M. E. Siegrist, and J. F. Löffler, “Negative strain rate sensitivity in bulk metallic glass and its similarities with the dynamic strain aging effect during deformation,” *Applied Physics Letters*, vol. 89, no. 2006, pp. 91913–91918, 2006.
- [132] R. W. Cahn, N. A. Pratten, M. G. Scott, H. R. Sinning, and L. Leonardsson, “Studies of Relaxation of Metallic Glasses by Dilatometry and Density Measurements.,” in *Materials Research Society Symposia Proceedings*, vol. 28, pp. 241–252, Elsevier Science Publ Co, 1984.
- [133] K. M. Flores, “Structural changes and stress state effects during inhomogeneous flow of metallic glasses,” *Scripta Materialia*, vol. 54, no. 3, pp. 327–332, 2006.
- [134] A. Dubach, F. H. Dalla Torre, and J. F. Löffler, “Constitutive model for inhomogeneous flow in bulk metallic glasses,” *Acta Materialia*, vol. 57, pp. 881–892, 2009.
- [135] L. Anand and C. Su, “A theory for amorphous viscoplastic materials undergoing finite deformations, with application to metallic glasses,” *Journal of the Mechanics and Physics of Solids*, vol. 53, no. 6, pp. 1362–1396, 2005.
- [136] A. J. Cao, Y. Q. Cheng, and E. Ma, “Structural processes that initiate shear localization in metallic glass,” *Acta Materialia*, vol. 57, no. 17, pp. 5146–5155, 2009.
- [137] Y. Shi and M. L. Falk, “Does metallic glass have a backbone? the role of percolating short range order in strength and failure,” *Scripta Materialia*, vol. 54, no. 3, pp. 381–386, 2006.
- [138] A. Vinogradov, “On shear band velocity and the detectability of acoustic emission in metallic glasses,” *Scripta Materialia*, vol. 63, no. 1, pp. 89–92, 2010.
- [139] L. F. Liu, J. Yang, J. Hu, H. Q. Li, and S. B. Guo, “Effect of hydrostatic pressure on shear banding behaviors in bulk metallic glasses,” *Materials Letters*, vol. 93, pp. 289–292, feb 2013.
- [140] S. Ogata, F. Shimizu, J. Li, M. Wakeda, and Y. Shibutani, “Atomistic simulation of shear localization in Cu-Zr bulk metallic glass,” *Intermetallics*, vol. 14, no. 8-9, pp. 1033–1037, 2006.
- [141] E. R. Homer, “Examining the initial stages of shear localization in amorphous metals,” *Acta Materialia*, vol. 63, pp. 44–53, nov 2013.
- [142] National Instruments, “How to Choose the Right DAQ Hardware for Your Measurement System,” tech. rep., 2012.
- [143] H. Bruck, A. Rosakis, and W. Johnson, “The dynamic compressive behavior of beryllium bearing bulk metallic glasses,” *Journal of Materials Research*, vol. 11, no. 2, pp. 503–511, 1996.
- [144] J. Qiao, F. Yang, G. Wang, P. Liaw, and Y. Zhang, “Jerky-flow characteristics for a Zr-based bulk metallic glass,” *Scripta Materialia*, vol. 63, pp. 1081–1084, nov 2010.
- [145] F. Yang, “Plastic flow in bulk metallic glasses: Effect of strain rate,” *Applied Physics Letters*, vol. 91, no. 5, 2007.
- [146] Y. Yang, X. L. Fu, S. Wang, Z. Y. Liu, Y. F. Ye, B. a. Sun, and C. T. Liu, “Probing stochastic nano-scale inelastic events in stressed amorphous metal.,” *Scientific reports*, vol. 4, p. 6699, jan 2014.

- [147] W. Jiang, G. Fan, F. Liu, G. Wang, H. Choo, and P. Liaw, "Spatiotemporally inhomogeneous plastic flow of a bulk-metallic glass," *International Journal of Plasticity*, vol. 24, pp. 1–16, jan 2008.
- [148] J. Park, H. Lim, J.-H. Kim, H. Chang, W. Kim, D. Kim, and E. Fleury, "In situ crystallization and enhanced mechanical properties of the Zr_{41.2}Ti_{13.8}Cu_{12.5}Ni₁₀Be_{22.5} alloy by cold rolling," *Journal of Non-Crystalline Solids*, vol. 351, pp. 2142–2146, 2005.
- [149] Y. Yokoyama, "Ductility improvement of Zr-Cu-Ni-Al glassy alloy," *Journal of Non-Crystalline Solids*, vol. 316, pp. 104–113, 2003.
- [150] Q. P. Cao, J. F. Li, Y. H. Zhou, a. Horsewell, and J. Z. Jiang, "Effect of rolling deformation on the microstructure of bulk Cu₆₀Zr₂₀Ti₂₀ metallic glass and its crystallization," *Acta Materialia*, vol. 54, pp. 4373–4383, 2006.
- [151] "Shot Peening of Metal Parts," *AMS*, no. S-13165, pp. 1–26, 1997.
- [152] J. Fu, Y. Zhu, C. Zheng, R. Liu, and Z. Ji, "Effect of laser shock peening on mechanical properties of Zr-based bulk metallic glass," *Applied Surface Science*, vol. 313, pp. 692–697, 2014.
- [153] D. Tabor, *The hardness of metals*. Oxford University Press, 1951.
- [154] M. Wakeda, Y. Shibutani, S. Ogata, and J. Park, "Relationship between local geometrical factors and mechanical properties for Cu–Zr amorphous alloys," *Intermetallics*, vol. 15, pp. 139–144, feb 2007.
- [155] M. Wakeda and Y. Shibutani, "Icosahedral clustering with medium-range order and local elastic properties of amorphous metals," *Acta Materialia*, vol. 58, pp. 3963–3969, jun 2010.
- [156] D. Jang and J. Greer, "Transition from a strong-yet-brittle to a stronger-and-ductile state by size reduction of metallic glasses," *Nature Materials*, vol. 9, no. 3, pp. 215–219, 2010.
- [157] G. Subhash, R. J. Dowding, and L. J. Kecskes, "Characterization of uniaxial compressive response of bulk amorphous Zr-Ti-Cu-Ni-Be alloy," *Materials Science and Engineering A*, vol. 334, no. 1-2, pp. 33–40, 2002.
- [158] X. Gu, T. Jiao, L. J. Kecskes, R. H. Woodman, C. Fan, K. T. Ramesh, and T. C. Hufnagel, "Crystallization and mechanical behavior of (Hf, Zr)-Ti-Cu-Ni-Al metallic glasses," *Journal of Non-Crystalline Solids*, vol. 317, no. 1-2, pp. 112–117, 2003.
- [159] T. Mukai, T. G. Nieh, Y. Kawamura, A. Inoue, and K. Higashi, "Effect of strain rate on compressive behavior of a Pd₄₀Ni₄₀P₂₀ bulk metallic glass," *Intermetallics*, vol. 10, pp. 1071–1077, 2002.
- [160] H. Li, G. Subhash, X. L. Gao, L. J. Kecskes, and R. J. Dowding, "Negative strain rate sensitivity and compositional dependence of fracture strength in Zr/Hf based bulk metallic glasses," *Scripta Materialia*, vol. 49, no. 11, pp. 1087–1092, 2003.
- [161] H. Li, G. Subhash, L. J. Kecskes, and R. J. Dowding, "Mechanical behavior of tungsten preform reinforced bulk metallic glass composites," *Materials Science and Engineering A*, vol. 403, no. 1-2, pp. 134–143, 2005.
- [162] T. Masumoto and R. Maddin, "The mechanical properties of palladium 20 a/o silicon alloy quenched from the liquid state," *Acta Metallurgica*, vol. 19, no. 7, pp. 725–741, 1971.

- [163] T. C. Hufnagel, T. Jiao, Y. Li, L.-Q. Xing, and K. T. Ramesh, "Deformation and Failure of Zr₅₇Ti₅Cu₂₀Ni₈Al₁₀ Bulk Metallic Glass Under Quasi-static and Dynamic Compression," *Journal of Materials Research*, vol. 17, pp. 1441–1445, jan 2011.
- [164] A. Kelly, W. R. Tyson, and A. H. Cottrell, "Ductile and brittle crystals," *Philosophical Magazine*, vol. 15, pp. 567–586, mar 1967.
- [165] S. Pugh, "XCII. Relations between the elastic moduli and the plastic properties of polycrystalline pure metals," *The London, Edinburgh, and Dublin Philosophical Magazine and Journal of Science*, vol. 45, pp. 823–843, apr 1954.
- [166] J. R. Rice and R. Thomson, "Ductile versus brittle behaviour of crystals," *Philosophical Magazine*, vol. 29, pp. 73–97, jan 1974.
- [167] J. J. Lewandowski, W. H. Wang, and A. L. Greer, "Intrinsic plasticity or brittleness of metallic glasses," *Philosophical Magazine Letters*, vol. 85, no. 2, pp. 77–87, 2005.
- [168] R. D. Conner, H. Choi-Yim, and W. L. Johnson, "Mechanical properties of Zr₅₇Nb₅Al₁₀Cu₁₅.₄Ni₁₂.₆ metallic glass matrix particulate composites," *J. Mater. Res*, vol. 14, no. 8, pp. 3292–3297, 1999.
- [169] S. V. Madge, D. V. Louzguine-Luzgin, J. J. Lewandowski, a.L. Greer, and a.L. Greer, "Toughness, extrinsic effects and Poisson's ratio of bulk metallic glasses," *Acta Materialia*, vol. 60, pp. 4800–4809, jul 2012.
- [170] J. Chen, "Indentation-based methods to assess fracture toughness for thin coatings," *Journal of Physics D: Applied Physics*, vol. 45, p. 203001, may 2012.
- [171] X. Li and B. Bhushan, "A review of nanoindentation continuous stiffness measurement technique and its applications," *Science*, vol. 48, no. 1, pp. 11–36, 2002.
- [172] M. Sakai and R. C. Bradt, "Fracture toughness testing of brittle materials," *International Materials Reviews*, vol. 38, pp. 53–78, jan 1993.
- [173] V. Keryvin, V. H. Hoang, and J. Shen, "Hardness, toughness, brittleness and cracking systems in an iron-based bulk metallic glass by indentation," *Intermetallics*, vol. 17, pp. 211–217, apr 2009.
- [174] T. Zhang, Y. Feng, R. Yang, and P. Jiang, "A method to determine fracture toughness using cube-corner indentation," *Scripta Materialia*, vol. 62, pp. 199–201, feb 2010.
- [175] G. D. Quinn and R. C. Bradt, "On the Vickers Indentation Fracture Toughness Test," *Journal of the American Ceramic Society*, vol. 90, pp. 673–680, mar 2007.
- [176] A. Ghosh, A. S. Kobayashi, Z. Li, and C. H. H. Jr, "Vickers microindentation toughness of a sintered SiC in the median-crack regime," 1991.
- [177] A. G. Evans, "Fracture toughness determinations by indentation," *Journal of the American Ceramic*, pp. 371–372, 1976.
- [178] K. Niihara, "A fracture mechanics analysis of indentation-induced Palmqvist crack in ceramics," *Journal of materials science letters*, vol. 2, pp. 221–223, 1983.
- [179] B. R. Lawn and R. F. Cook, "Probing material properties with sharp indenters: a retrospective," *Journal of Materials Science*, vol. 47, no. 1, pp. 1–22, 2012.

- [180] G. R. Anstis, P. Chantikul, B. R. Lawn, and D. B. Marshall, "A Critical Evaluation of Indentation Techniques for Measuring Fracture Toughness: I, Direct Crack Measurements," *Journal of the American Ceramic Society*, vol. 64, no. 9, pp. 533–538, 1981.
- [181] P. Chantikul, G. R. Anstis, B. R. Lawn, and D. B. Marshall, "A Critical Evaluation of Indentation Techniques for Measuring Fracture Toughness: II, Strength Method," *Journal of the American Ceramic Society*, vol. 64, no. 9, pp. 539–543, 1981.
- [182] Z. Li, A. Ghosh, A. S. Kobayashi, and R. C. Bradt, "Indentation fracture toughness of sintered silicon carbide in the Palmqvist crack regime," *Journal of the American Ceramic Society*, vol. 72, no. 6, pp. 904–911, 1989.
- [183] C. B. Ponton and R. D. Rawlings, "Vickers indentation fracture toughness test Part 1 Review of literature and formulation of standardised indentation toughness equations," *Materials Science and Technology*, vol. 5, no. 9, pp. 865–872, 1989.
- [184] C. B. Ponton and R. D. Rawlings, "Vickers indentation fracture toughness test Part 2 Application and critical evaluation of standardised indentation toughness equations," *Materials Science and Technology*, vol. 5, no. 10, pp. 961–976, 1989.
- [185] M. He, F. Li, J. Cai, and B. B. Chen, "An indentation technique for estimating the energy density as fracture toughness with Berkovich indenter for ductile bulk materials," *Theoretical and Applied Fracture Mechanics*, vol. 56, no. 2, pp. 104–111, 2011.
- [186] J. Hay and G. Pharr, *Instrumented Indentation Testing. ASM Handbook, vol. 8: Mechanical Testing and Evaluation*. Ohio: ASM International, 2000.
- [187] W. C. Oliver and G. M. Pharr, "Improved technique for determining hardness and elastic modulus using load and displacement sensing," *Journal of Materials Research*, vol. 7, no. 6, pp. 1564–1583, 1992.
- [188] A. F. Bower, N. A. Fleck, A. Needleman, and N. Ogbonna, "Indentation of a power law creeping solid," *Proceedings of the Royal Society of London Series A Mathematical and Physical Sciences*, vol. 441, no. 1911, pp. 97–124, 1993.
- [189] V. Keryvin, Y. Gueguen, and C. Bernard, "Assessment of rheological and thermodynamic properties of the Pd40Ni40P20 bulk metallic glass around glass transition using an indentation creep technique," *Journal of Alloys and Compounds*, vol. 509, pp. S18–S22, jun 2011.
- [190] L. Shen, W. C. D. Cheong, Y. L. Foo, and Z. Chen, "Nanoindentation creep of tin and aluminium: A comparative study between constant load and constant strain rate methods," *Materials Science and Engineering: A*, vol. 532, pp. 505–510, jan 2012.
- [191] R. Goodall and T. W. Clyne, "A critical appraisal of the extraction of creep parameters from nanoindentation data obtained at room temperature," *Acta Materialia*, vol. 54, no. 20, pp. 5489–5499, 2006.
- [192] I.-C. Choi, B.-G. Yoo, Y.-J. Kim, and J.-i. Jang, "Indentation creep revisited," *Journal of Materials Research*, vol. 27, no. 01, pp. 1–9, 2011.
- [193] C. Y. S. Chang, W. C. J. Wei, and C. H. Hsueh, "Viscosity of Ba–B–Si–Al–O glass measured by indentation creep test at operating temperature of IT-SOFC," *Journal of Non-Crystalline Solids*, vol. 357, pp. 1414–1419, mar 2011.

- [194] G. Feng, a.H.W. Ngan, and a.H.W. Ngan, “Creep and strain burst in indium and aluminium during nanoindentation,” *Scripta Materialia*, vol. 45, pp. 971–976, oct 2001.
- [195] H. Li and A. H. W. Ngan, “Size effects of nanoindentation creep,” *Journal of Material Research*, vol. 19, no. 2, pp. 513–522, 2004.
- [196] ASTM E 139-06A, “Standard Test Method for Conducting Creep, Creep-rupture, and Stress-rupture Tests of Metallic Materials,” 2006.
- [197] J. Wu, Y. Pan, and J. Pi, “On indentation creep of two Cu-based bulk metallic glasses via nanoindentation,” *Physica B: Condensed Matter*, vol. 421, pp. 57–62, jul 2013.
- [198] J. Wu, Y. Pan, and J. Pi, “Nanoindentation study of Cu₅₂Zr₃₇Ti₈In₃ bulk metallic glass,” *Applied Physics A*, jul 2013.
- [199] B. Wei, T. Zhang, W. Li, D. Xing, L. Zhang, and Y. Wang, “Indentation Creep Behavior in Ce-Based Bulk Metallic Glasses at Room Temperature,” *Materials Transactions*, vol. 46, no. 12, pp. 2959–2962, 2005.
- [200] L. Shen, P. Septiwerdani, and Z. Chen, “Elastic modulus, hardness and creep performance of SnBi alloys using nanoindentation,” *Materials Science and Engineering: A*, vol. 558, pp. 253–258, dec 2012.
- [201] W. R. LaFontaine and B. Yost, “Indentation load relaxation experiments with indentation depth in the submicron range,” *Journal of Materials . . .*, vol. 5, no. 10, pp. 2100–2106, 1990.
- [202] M. J. Mayo, R. W. Siegel, A. Narayanasamy, and W. D. Nix, “Mechanical properties of nanophase TiO₂ as determined by nanoindentation,” *Journal of Materials . . .*, 1990.
- [203] C. Su, E. G. Herbert, S. Sohn, J. a. LaManna, W. C. Oliver, and G. M. Pharr, “Measurement of power-law creep parameters by instrumented indentation methods,” *Journal of the Mechanics and Physics of Solids*, vol. 61, pp. 517–536, feb 2013.
- [204] W. H. Li, K. Shin, C. G. Lee, B. C. Wei, T. H. Zhang, and Y. Z. He, “The characterization of creep and time-dependent properties of bulk metallic glasses using nanoindentation,” *Materials Science and Engineering: A*, vol. 478, pp. 371–375, apr 2008.
- [205] Astm, “ASTM E384: Standard Test Method for Knoop and Vickers Hardness of Materials,” *ASTM Standards*, pp. 1–43, 2012.
- [206] T. Chudoba and F. Richter, “Investigation of creep behaviour under load during indentation experiments and its influence on hardness and modulus results,” *Surface and Coatings Technology*, vol. 148, pp. 191–198, 2001.
- [207] J. R. Greer, W. C. Oliver, and W. D. Nix, “Size dependence of mechanical properties of gold at the micron scale in the absence of strain gradients,” *Acta Materialia*, vol. 53, no. 6, pp. 1821–1830, 2005.
- [208] H. Huang, H. Zhao, Z. Zhang, Z. Yang, and Z. Ma, “Influences of Sample Preparation on Nanoindentation Behavior of a Zr-Based Bulk Metallic Glass,” *Materials*, vol. 5, pp. 1033–1039, jun 2012.
- [209] Goodfellow, “Goodfellow: Interactive Periodic table (software),” 2016.
- [210] Granta Design Ltd, “Cambridge Materials Selector (software).”

- [211] J. J. Kim, Y. Choi, S. Suresh, and a. S. Argon, "Nanocrystallization during nanoindentation of a bulk amorphous metal alloy at room temperature.," *Science (New York, N.Y.)*, vol. 295, pp. 654–7, jan 2002.
- [212] Y. Q. Cheng, a.J. Cao, E. Ma, and a.J. Cao, "Correlation between the elastic modulus and the intrinsic plastic behavior of metallic glasses: The roles of atomic configuration and alloy composition," *Acta Materialia*, vol. 57, pp. 3253–3267, jun 2009.
- [213] L. Perrière, S. Nowak, S. Brossard, M.-T. Thai, M. Blétry, and Y. Champion, "Nanoindentation study of chemical effects on the activation volume controlling shear band initiation in metallic glasses," *Scripta Materialia*, vol. 68, pp. 183–186, feb 2013.
- [214] S. Zhu, X. Wang, and a. Inoue, "Glass-forming ability and mechanical properties of Ti-based bulk glassy alloys with large diameters of up to 1cm," *Intermetallics*, vol. 16, pp. 1031–1035, aug 2008.
- [215] S. T. Liu, Z. Wang, H. L. Peng, H. B. Yu, and W. H. Wang, "The activation energy and volume of flow units of metallic glasses," *Scripta Materialia*, vol. 67, pp. 9–12, jul 2012.
- [216] Z. Suo, K. Qiu, Q. Li, Y. Ren, and Z. Hu, "Effect of Nb on glass forming ability and plasticity of (Ti–Cu)-based bulk metallic glasses," *Materials Science and Engineering: A*, vol. 527, pp. 2486–2491, apr 2010.
- [217] B. Moser, J. Kuebler, H. Meinhard, W. Muster, and J. Michler, "Observation of instabilities during plastic deformation by in-situ SEM indentation experiments," *Advanced Engineering Materials*, vol. 7, no. 5, pp. 388–392, 2005.
- [218] K. Li, X. Wang, F. Zhang, and D. Xue, "Electronegativity identification of novel superhard materials," *Physical Review Letters*, vol. 100, no. June, p. 235504, 2008.
- [219] V. A. Mukhanov, O. O. Kurakevych, and V. L. Solozhenko, "Thermodynamic aspects of materials' hardness: prediction of novel superhard high-pressure phases," *High Pressure Research*, vol. 28, no. 4, pp. 531–537, 2008.
- [220] F. Gao, J. He, E. Wu, S. Liu, D. Yu, D. Li, S. Zhang, and Y. Tian, "Hardness of Covalent Crystals," *Physical Review Letters*, vol. 91, no. 1, p. 015502, 2003.
- [221] A. Šimůnek and J. Vackář, "Hardness of Covalent and Ionic Crystals: First-Principle Calculations," *Physical Review Letters*, vol. 96, no. 8, p. 085501, 2006.
- [222] M. M. Smedskjaer, J. C. Mauro, and Y. Yue, "Prediction of Glass Hardness Using Temperature-Dependent Constraint Theory," *Physical Review Letters*, vol. 105, no. 11, pp. 10–13, 2010.
- [223] J. Gilman, "Hardness – a strength microprobe," in *The science of hardness testing and its research applications*, ch. 4, 1973.
- [224] A. Y. Liu and M. L. Cohen, "Prediction of new low compressibility solids.," *Science*, vol. 245, no. 4920, pp. 841–842, 1989.
- [225] P. M. Sargent and M. F. Ashby, "Indentation creep," *Materials Science and Technology*, vol. 8, no. 7, pp. 594–601, 1992.

- [226] F. Gao, H. Nishikawa, T. Takemoto, and J. Qu, “Mechanical properties versus temperature relation of individual phases in Sn–3.0Ag–0.5Cu lead-free solder alloy,” *Microelectronics Reliability*, vol. 49, pp. 296–302, mar 2009.
- [227] J. Dean, J. M. Wheeler, and T. W. Clyne, “Use of quasi-static nanoindentation data to obtain stress–strain characteristics for metallic materials,” *Acta Materialia*, vol. 58, pp. 3613–3623, jun 2010.
- [228] J. Dean, A. Bradbury, G. Aldrich-Smith, and T. W. Clyne, “A procedure for extracting primary and secondary creep parameters from nanoindentation data,” *Mechanics of Materials*, vol. 65, pp. 124–134, 2013.
- [229] Y. Liu, B. Wang, M. Yoshino, S. Roy, H. Lu, and R. Komanduri, “Combined numerical simulation and nanoindentation for determining mechanical properties of single crystal copper at mesoscale,” *Journal of the Mechanics and Physics of Solids*, vol. 53, pp. 2718–2741, dec 2005.
- [230] Y. Liu, S. Varghese, J. Ma, M. Yoshino, H. Lu, and R. Komanduri, “Orientation effects in nanoindentation of single crystal copper,” *International Journal of Plasticity*, vol. 24, pp. 1990–2015, nov 2008.
- [231] O. Casals, J. Ocenasek, and J. Alcala, “Crystal plasticity finite element simulations of pyramidal indentation in copper single crystals,” *Acta Materialia*, vol. 55, pp. 55–68, jan 2007.
- [232] S. Bouvier and a. Needleman, “Effect of the number and orientation of active slip systems on plane strain single crystal indentation,” *Modelling and Simulation in Materials Science and Engineering*, vol. 14, pp. 1105–1125, oct 2006.
- [233] H. Pelletier, “Predictive model to estimate the stress–strain curves of bulk metals using nanoindentation,” *Tribology International*, vol. 39, pp. 593–606, jul 2006.
- [234] C. Heinrich, a.M. Waas, and a.S. Wineman, “Determination of material properties using nanoindentation and multiple indenter tips,” *International Journal of Solids and Structures*, vol. 46, pp. 364–376, jan 2009.
- [235] B. Guelorget, M. François, C. Liu, and J. Lu, “Extracting the plastic properties of metal materials from microindentation tests: Experimental comparison of recently published methods,” *Journal of Materials Research*, vol. 22, pp. 1512–1519, jan 2007.
- [236] Y. J. Huang, Y. L. Chiu, J. Shen, J. Chen, and J. F. Sun, “Indentation creep of a Ti-based metallic glass,” *Journal of Material Research*, vol. 24, no. 3, p. 994, 2009.
- [237] Y. J. Huang, J. Shen, Y. L. Chiu, J. J. J. Chen, and J. F. Sun, “Indentation creep of an Fe-based bulk metallic glass,” *Intermetallics*, vol. 17, no. 4, pp. 190–194, 2009.
- [238] Y. H. Chen, J. C. Huang, L. Wang, and T. G. Nieh, “Effect of residual stresses on nanoindentation creep behavior of Zr-based bulk metallic glasses,” *Intermetallics*, vol. 41, pp. 58–62, oct 2013.
- [239] I. C. Choi, B. G. Yoo, Y. J. Kim, and M. Y. Seok, “Estimating stress exponent of nanocrystalline nickel: sharp versus spherical indentation,” *Scripta Materialia*, vol. 65, no. 4, pp. 300–303, 2011.

- [240] Y. Liu, C. Huang, H. Bei, X. He, and W. Hu, "Room temperature nanoindentation creep of nanocrystalline Cu and Cu alloys," *Materials Letters*, vol. 70, pp. 26–29, mar 2012.
- [241] C. L. Wang, M. Zhang, and T. G. Nieh, "Nanoindentation creep of nanocrystalline nickel at elevated temperatures," *Journal of Physics D: Applied Physics*, vol. 42, p. 115405, jun 2009.
- [242] S. a. Hackney, K. E. Aifantis, a. Tangtrakarn, and S. Shrivastava, "Using the Kelvin-Voigt model for nanoindentation creep in Sn-C/PVDF nanocomposites," *Materials Science and Technology*, vol. 28, pp. 1161–1166, oct 2012.
- [243] V. M. F. Marques, B. Wunderle, C. Johnston, and P. S. Grant, "Nanomechanical characterization of Sn–Ag–Cu/Cu joints—part 2: Nanoindentation creep and its relationship with uniaxial creep as a function of temperature," *Acta Materialia*, pp. 1–10, feb 2013.
- [244] P. Kral, J. Dvorak, S. Zharebtsov, G. Salishchev, M. Kvapilova, and V. Sklenicka, "Effect of severe plastic deformation on creep behaviour of a Ti–6Al–4V alloy," *Journal of Materials Science*, vol. 48, pp. 4789–4795, jan 2013.
- [245] J. Terlouw and M. Vogelaar, *Kapteyn Package, version 2.2*. Kapteyn Astronomical Institute, Groningen, apr 2012.
- [246] C. Schuh and T. Nieh, "A nanoindentation study of serrated flow in bulk metallic glasses," *Acta Materialia*, vol. 51, pp. 87–99, 2003.
- [247] J. Qiao, H. Jia, Y. Zhang, P. Liaw, and L. Li, "Multi-step shear banding for bulk metallic glasses at ambient and cryogenic temperatures," *Materials Chemistry and Physics*, vol. 136, pp. 75–79, sep 2012.
- [248] S. Ekelof, "The genesis of the Wheatstone bridge," *Engineering Science and Education Journal*, vol. 10, no. 1, p. 37, 2001.
- [249] ASTM E9-09, "Standard Test Methods of Compression Testing of Metallic Materials at Room Temperature," *ASTM International*, 2009.
- [250] W. J. Parker, R. J. Jenkins, C. P. Butler, and G. L. Abbott, "Flash method of determining thermal diffusivity, heat capacity, and thermal conductivity," *Journal of Applied Physics*, vol. 32, no. 9, pp. 1679–1684, 1961.
- [251] Goodfellow, "Molybdenum - Lump."
- [252] K. Krishnanand and R. Chan, "Recovery from plastic deformation in a Ni/Nb alloy glass," *Scripta Metallurgica*, vol. 9, pp. 1259–1261, 1975.
- [253] T. Egami, "Understanding the properties and structure of metallic glasses at the atomic level," *JOM*, vol. 62, no. 2, pp. 70–75, 2010.
- [254] E. Matsubara, T. Ichitsubo, K. Itoh, T. Fukunaga, J. Saida, N. Nishiyama, H. Kato, and A. Inoue, "Heating rate dependence of T_g and T_x in Zr-based BMGs with characteristic structures," *Journal of Alloys and Compounds*, vol. 483, pp. 8–13, 2009.
- [255] J. Lennard-Jones, "Cohesion," in *The proceedings of the Physical Society*, vol. 43, 1931.
- [256] D. Ma, a. D. Stoica, and X.-L. Wang, "Power-law scaling and fractal nature of medium-range order in metallic glasses," *Nature materials*, vol. 8, no. 1, pp. 30–4, 2009.

- [257] D. Wales, *Energy Landscapes With Applications to Clusters, Biomolecules and Glasses*. Cambridge: Cambridge Univ Press, 2003.